Advanced Reactor Safety Research
Quarterly Report October – December 1982

Volume 24

Advanced Reactor Research Program

Prepared for
U. S. NUCLEAR REGULATORY COMMISSION

8406210433 840430
PDR NUREG
CR-2679 R   PDR

NOTICE

This report was prepared as an account of work sponsored by an agency of the United States Government. Neither the United States Government nor any agency thereof, or any of their employees, makes any warranty, expressed or implied, or assumes any legal liability or responsibility for any third party's use, or the results of such use, of any information, apparatus product or process disclosed in this report, or represents that its use by such third party would not infringe privately owned rights.

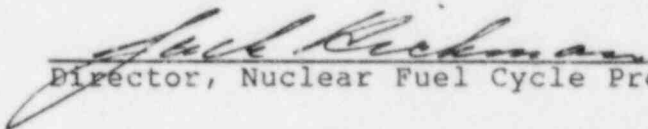ADVANCED REACTOR SAFETY RESEARCH
QUARTERLY REPORT
October-December 1982

Advanced Reactor Research Program
Sandia National Laboratories
Albuquerque, NM 87185

Printed: April 1984

APPROVED:

_____
Manager, Advanced Reactor Research

_____
Director, Nuclear Fuel Cycle Programs

Sandia National Laboratories
Albuquerque, New Mexico 87185
operated by
Sandia Corporation
for the
U.S. Department of Energy

FOREWORD

Sandia National Laboratories is conducting, under USNRC's sponsorship, phenomenological research related to the safety of commercial nuclear power reactors.

The overall objective of this work is to provide NRC a comprehensive data base essential to (1) defining key safety issues, (2) understanding risk-significant accident sequences, (3) developing and verifying models used in safety assessments, and (4) assuring the public that power reactor systems will not be licensed and placed in commercial service in the United States without appropriate consideration being given to their effects on health and safety.

Together with other programs, the Sandia effort is directed at assuring the soundness of the technology base upon which licensing decisions are made.

This report describes progress in a number of activities dealing with current safety issues relevant to both light water reactors (LWRs) and breeder reactors. The work includes a broad range of experiments to simulate accidental conditions to provide the required data base to understand important accident sequences and to serve as a basis for development and verification of the complex computer simulation models and codes used in accident analysis and licensing reviews. Such a program must include the development of analytical models, verified by experiment, which can be used to predict reactor and safety system performance under a broad variety of abnormal conditions.

Current major emphasis is focused on providing information to NRC relevant to (1) its deliberations and decisions dealing with severe LWR accidents and (2) its safety evaluation of the proposed Clinch River Breeder Reactor.

CONTENTS

ILLUSTRATIONS

ILLUSTRATIONS (Continued)

ILLUSTRATIONS (Continued)

ILLUSTRATIONS (Continued)

TABLES

1. Core Debris Behavior

1.1 Ex-Vessel Core Debris Interactions

If core debris formed during a severe reactor accident is not coolable, the debris will penetrate the reactor vessel and interact with structural material in the reactor cavity. This interaction could lead to gas generation, production of flammable species, and intense emission of radioactive aerosols, in addition to erosion of the reactor basemat.

Study of the phenomena associated with ex-vessel interaction of core debris with structural material found in the reactor cavity is the purpose of the Ex-Vessel Core Debris Interactions program. In the recent past, the major part of this program was the study of core debris interaction with concrete. Penetration of core debris through steel liners has also been examined. Other associated phenomena are currently undergoing study.

The effects of sudden additions of water to molten core debris interacting with concrete are very uncertain features of severe reactor accidents. Such additions are likely to occur in many of the accident scenarios hypothesized for most nuclear power plants. Clearly, water additions could be a deliberate accident-mitigation strategy. Water addition may also occur as an inadvertent consequence of an accident. Discharge of accumulators or erosion of weir walls could cause water flooding of core debris interacting with concrete.

The principal questions of the combined coolant/core-debris/ concrete interactions are:

a. Does the debris quench and fragment into a coolable bed of particulate?

b. What are the rates of steam and hydrogen generation?

c. Is aerosol production suppressed significantly by the coolant pool?

d. Is attack on the concrete affected if the debris is not quenched by water?

This progress report describes the experiments (the TWT Test Series) planned to explore the issure of combined coolant/core-debris/ concrete interactions. Project personnel plan four scoping tests. Each will involve a melt of 45 kg formed by metallothermic reaction

and sustained by inductive heating. Tests with and without a water pool over the melt will be run to assess the effect of water on melt behavior. A test with water, but with magnesium oxide instead of concrete, will be run. Investigators will use this test to evaluate arguments, which have appeared in the literature, on the ability of concrete gases to facilitate melt quenching.

Results of these tests will constitute the basis for larger-scale tests involving more prototypic melts.

1.2 Core Retention Materials Assessment

Core Retention Materials Assessment is a program, involving both experiments and analysis, designed to (1) determine the fundamental limitations of candidate core-retention materials and concepts, and (2) develop a data base for use by the NRC in the licensing review of proposed ex-vessel core retention materials. The program is currently focused on magnesia brick crucibles, thoria and alumina particle beds, and high alumina concrete liners.

In earlier quarterly reports, the PLUGM code was described in detail. The sample calculations presented here illustrate the application of PLUGM to the particle-bed core-retention concept. The calculations demonstrate the need for a layered structure to control initial penetration of a particle bed by molten core debris.

For producing 200-kg UO_2 melts, project personnel considered three alternative designs based on the scaling up of the results from the Sustained Oxide Test (SOT) series. One has been chosen as a preliminary design for the first application of the Inductive Ring Susceptor (IRIS) Technique at the Large-Scale Melt Facility (LMF). The test is scheduled for May 1983. The melt will be dropped onto a layered alumina particle bed.

A series of tests, in which stainless steel rings were heated in the LMF coil, indicated a coupling efficiency of 50%, and demonstrated the feasibility of the proposed IRIS test.

Manufacturing details for producing two tungsten liners, one by plasma spraying and one by chemical vapor deposition (CVD), are described. One or both of these liners will be used in future LMF tests. The better of the two will be used in the test scheduled for April 1983. The melt in this test will be dropped into a magnesia brick crucible.

Finally, two Ultrasonic Thermometer (UT) reliability tests were conducted in the LMF. These tests revealed several ways in which the reliability and performance of UTs can be improved and erratic behavior can be reduced significantly.

1.3 Sodium Containment and Structural Integrity

The Sodium Containment and Structural Integrity program is an investigation of safety phenomena that will develop should molten sodium contact structural or shielding concrete during a reactor accident. Quantitative evaluation of these phenomena, leading to development of models for use in predicting the ways in which these phenomena might threaten the reactor containment, is a major goal of this program. Quantitative evaluation of structural flaws in reactor cell liners is also sought in this program because these flaws can provide pathways for sodium to contact concrete.

During this quarter the Sodium Containment and Structural Integrity program addressed the following areas:

a. Completion of a mechanistic model of sodium interactions with concrete.

b. Laboratory-scale experiments to define the nature of chemical attack by sodium on concrete.

c. Posttest examination of the HEDL/Sandia AA/AB tests of sodium interactions with limestone and dolomite concrete.

The Sodium/Limestone Concrete Ablation Model (SLAM) is the mechanistic model of sodium interactions with concrete, and was developed from results obtained in this program. The model has been completed. It calculates the onset, magnitude, and termination of sodium/concrete interactions. The required input data are material properties and geometry information.

SLAM includes a detailed description of the chemistry of sodium attack on concrete. A summary of recent laboratory-scale tests to elucidate this chemistry is presented. Two important conclusions from this work are: (1) sodium hydroxide need not be present to initiate the energetic sodium reaction with concrete, and (2) the characteristics of the energetic attack, such as onset temperature and rate of reaction, depend on the particle size of the concrete.

The AA/AB tests involved a direct comparison of sodium interaction with both limestone and dolomite concretes. Externally available data such as hydrogen generation rates, sodium pool temperatures, and concrete temperature, were similar in the two tests. Posttest examination of the concretes showed that the nature of the attack on limestone concrete was quite different from that of attack on dolomite concrete. The interaction zone observed in the test with limestone concrete was quite narrow (~2 mm). The interaction zone observed in the test with dolomite concrete was about 7 cm thick. The spread in the interaction zone may explain why the much higher thermodynamic potential of the sodium reaction with dolomite concrete was not realized.

EXECUTIVE SUMMARY

A topical report entitled Large-Scale Exploratory Tests of Sodium/Magnetite Concrete Interactions, by E. Randich and R. U. Acton, NUREG/CR-3189, SAND83-0356, was completed this quarter.

1.4. Debris Bed Coolability

The Debris Bed Coolability program addresses issues concerned with the deposition of solid fuel debris on horizontal surfaces within the containment vessel and its subsequent coolability. This debris remains capable of generating significant power through the decay of fission products. Should natural processes fail to provide sufficient cooling, the debris could remelt and threaten containment. The Debris Bed Coolability program seeks to determine the natural cooling of such debris.

The joint USNRC/JRC, Ispra/PNC debris bed experiment D9 was conducted October 17-27, 1982, in Sandia's Annular Core Research Reactor (ACRR). Several dryouts at various subcoolings, power-step tests, channel events, superheat flashing events, nonboiling (conduction) control runs, and other tests were performed.

In most of the categories, the number of events exceeds the combined total of similar events from all previous D-series experiments because of the duration and successful operation of virtually all features of the D9 experiment package. None of the 53 thermocouples failed (in spite of temperatures on some up to 1150°C), the crucible remained intact and well-insulating throughout the experiment, the cover gas expansion tank opened as designed and the capsule pressure decreased with minimal bed disturbance, and three experiment shutdowns and restarts were successful, allowing periods of data assessment and formation of extended experiment test plans. (A dominant factor in the longevity of D9 was the experience gained from the previous experiment (D7) which was the same design as D9.) Considerable verification and refinement of ideas on debris phenomena were accomplished and new regimes of bed behavior were investigated.

The D9 experiment consisted of four sessions. The first session showed that the dryout powers, which ranged from 0.10 to 0.65 W/g, were very close to incipient boiling, even at a low subcooling of 70°C. Sandia's one-dimensional boiling and dryout model predicted this. The saturation temperature experienced sudden drops at the lowest subcooling only. These events occurred at about the same subcooled-zone thickness as predicted for channel formation. However, they did not lead to an increase in bed coolability. Investigators postulate that the bed may have loosened because of capillary pressure at that point, but vapor did not penetrate the subcooled zone. However, higher powers subsequently yielded a thinner dry zone. This is believed to indicate channel penetration of the subcooled zone because such behavior was predicted for the channeled state. Note that channel penetration occurred only after dryout began, and that channeling did not cause a large increase in coolability.

Session 2 was devoted primarily to large power steps to simulate better the heating history in an accident bed. Steps up to 1.43 W/g were made (with higher steps in later sessions). Even though the steps exceeded the incipient dryout power by a factor of as much as 5 (and 10 in session 3), the dry-zone thickness was less than 20 mm in most of the cases. Channel penetration is believed to have been responsible for this more coolable behavior. The dry-zone thickness in the channeled state was predicted to be limited to 20 mm. Despite the many step tests, the incipient dryout power remained close to incipient boiling.

Session 3 investigated steady-state extended dryout. The dry-zone thicknesses were fairly close to those predicted by the one-dimensional model. In addition, a small increase in power yielded a collapse of the dry zone with low subcooling. This was the most direct indication of channeling in the experiment. It was repeatable, and occurred at powers only slightly higher than predicted.

At the end of session 3, 373 K (100°C) of liquid superheat was deliberately induced in the bed. This superheat was reduced and flashed at 90°C (for safety considerations), resulting in a permanent change in the bed, which increased the dryout flux (by a factor of 20) up to 4.4±0.6 W/g. The investigators believe that the flash mixed the bed sufficiently to overcome the detrimental effects of stratification.

The final session was devoted to the investigation of superheat flashing. Superheat could be achieved at the predicted levels only if the bed was sufficiently boiled and was boiled between each superheat flash. However, superheat in excess of 30°C could not be achieved with a large power step prototypic of heating in accident debris. Thus the benefits of flashing may not be applicable to reactor accidents.

1.5 Dry Debris Coolability

After a major reactor accident, if the core material debris is uncoolable it will progress to a molten state. The progression of the debris to a molten state and the interaction of the core melt with structural and core retention material are being investigated experimentally. This program, the follow-on to the Molten Pool Studies, interfaces closely with both the Ex-Vessel Core Debris Interactions and the Debris Bed Coolability programs. High-temperature, laboratory-furnace tests and the first-of-a-kind, neutronically heated experiments are providing significant data on melt progression phenomena, including the thermal response of dry UO_2 and steel particulate beds to internal decay heating, the formation of crusts and voids in pools of internally heated molten fuel material, and the interaction of hot fuel debris with core structure and retention material. As with other safety research programs, investigators are using the experimental results to develop and verify analytical models that will be used to study reactor behavior under a wide variety of accident conditions.

EXECUTIVE SUMMARY

The next in-pile experiment, DC 1, will investigate the thermal characteristics of an internally heated UO_2 debris bed from 1273 K (1000°C) to melt and the phenomenology and thermal characteristics of a molten UO_2 pool. The bed will consist of 2 kg of UO_2 particulate and will be top- and bottom-cooled and side-insulated. The maximum molten mass during the experiment is estimated to be from 0.7 kg to 1.0 kg.

During this quarter, project personnel completed the stress analysis on the containment design, the experiment plan was written and approved, and the fabrication of the experiment hardware was completed. Work began on the development of a one-dimensional model for analyzing the postdryout behavior of debris beds. The model will include both heat transfer and material redistribution.

2. HIGH TEMPERATURE FISSION-PRODUCT CHEMISTRY AND TRANSPORT

The purpose of the High-Temperature Fission-Product Chemistry and Transport program is to establish the data base necessary to predict properly fission-product behavior during severe accidents. This experimental task is being pursued by three interrelated activities:

a. Definition of thermodynamic data and chemical-reaction characteristics of particular fission products of interest.

b. Examination of the transport properties of fission products in prototypic environments of steam and hydrogen.

c. Comparison of the observed behavior of the fission products with predictions made by purely thermodynamic considerations.

Transport properties of the fission products are under study in the Fission-Product Reaction Facility (FPRF), developed as part of this program. The FPRF allows moderately volatile fission products to be generated in flowing steam and hydrogen mixtures at temperatures up to 1273 K (1000°C). The fission-product stream passes over alloys representative of structural materials in reactor cores. A Raman spectroscopy unit has been developed that allows determination of the chemical form of fission products in the vapor state.

During this quarter, project personnel conducted the test to conclude the study of cesium hydroxide reactions with structural materials. The final test involved exposure of Inconel 600 to CsOH vapors in steam and hydrogen at 1273 K (1000°C). A small amount of the cesium did react and did bind to the Inconel in a water insoluble chemical form.

Investigators also conducted experiments to determine the effects of boron carbide control-rod material on cesium and cesium iodide behavior. These investigators found that boron carbide is aggressively attacked by steam to yield B_2O_3 and boric acid vapors. The cesium compounds react with the boron corrosion products to yield cesium borate which is less volatile than cesium iodide. When cesium iodide reacts with the boric acids, gaseous HI is liberated, but its final disposition is unknown.

Results of the tests with boron carbide introduce a new dimension to the problem of fission-product transport in the primary system. Especially in boiling water reactors, boron carbide could represent an important source of nonradioactive aerosols. As aerosols, the boric acid products of steam corrosion of boron carbide will accentuate deposition and agglomeration of radioactive aerosols. The chemical reactions of CsI with boric acid could be a pathway to releasing iodine in a gaseous form.

3. CONTAINMENT ANALYSIS

The Containment Analysis programs are centered on the development, testing, and application of the CONTAIN code. CONTAIN is NRC's general-purpose computer code for modeling containment response to a severe accident and for determining the consequences thereof. It provides models, for both LWR and LMFBR systems, of phenomena occurring outside the reactor primary system and inside the containment building, including interactions between core debris and coolant or concrete, hydrogen combustion, thermal hydraulics of the gases in the various compartments of the containment building, aerosol behavior, and fission-product transport. Major parts of CONTAIN are being tested and applied to reactor accident analysis.

Papers on CONTAIN were presented at the 10th LWR Safety Research Information Meeting in Gaithersburg, Maryland, and the BMFT/USNRC Core Melt Information Exchange Meeting in Karlsruhe, Germany. A meeting took place at NRC to review CONTAIN's treatment of aerosol and radio-isotope behavior in containment.

3.1 CONTAIN Code Development

Accomplishments in code development during this quarter include:

a. A meeting at Culham, UK, to exchange information useful in the development of MEDICI.

b. Writing of a skeleton version of MEDICI.

c. Contracting with Drs. M. Corradini and G. Moses to assist in the MEDICI development.

d. Completing a major revision to the model for vapor condensation on structures.

e. Completing the basic structure for the new version of SINTER.

f. Refining the containment-spray model in CONTAIN.

g. Completing a version of CONTAIN with a CORCON option.

h. Initiating a review of MELCOR's treatment of reactor-cavity phenomena.

i. Converting the input portions of CONTAIN to FORTRAN 77.

3.2 CONTAIN Testing and Validation

Testing of SINTER during this period concentrated on pool chemistry, pool sources, and pool-heat transfer. CONTAIN's aerosol calculations were compared with QUICK. CONTAIN's sodium-aerosol predictions were validated with the ABCOVE experiment AB5 at HEDL. The CONTAIN models relevant to the initial phases of a steam blowdown were validated by German experiments at the HDR facility. Finally, the washout features of CONTAIN's containment-spray model were validated in an experiment at PNL.

3.3 Clinch River Containment Analysis

Sandia collaborated with NRC on a technical assistance plan for using CONTAIN to address a number of CRBRP licensing issues. CONTAIN was compared with HAA-3B's prediction of aerosol behavior in selected TMBDB scenarios for CRBR; the two codes had significant differences.

3.4 LWR Containment Analysis

A study of the effects of coupling between thermal-hydraulics and aerosol behavior was initiated. The problem of modeling radionuclide-release-plume rainout is being addressed. The LWR Sample Problem is ready for use by holders of CONTAIN.

4. ELEVATED TEMPERATURE MATERIALS ASSESSMENT

The primary objectives of the Elevated Temperature Materials Assessment studies are (a) to determine how microstructures evolve due to thermomechanical history that results in mechanical property changes, (b) to evaluate the validity of material damage rules used in design, and (c) to develop and evaluate nondestructive evaluation techniques.

4.1 Inconel 718 Characterization

Transmission electron microscopy examination of the creep-deformed and thermally aged specimens of Inconel 718 from ORNL showed that neither time at temperature nor creep deformation at 866 K (593°C) produces significant changes in the fine-scale strengthening substructure. By contrast, exposure for approximately 1000 hr at either 977 K (704°C) or 1033 K (760°C) was enough to alter the strengthening substructure. Specimens tested at 922 K (649°C) were requested from ORNL, and a series of thermally aged specimens has arrived from INEL.

4.2 Biaxial Testing

The elastic response of the tubular biaxial specimen was measured under numerous multiaxial loading conditions to provide confirmation of the stress and strain measuring and calculating methods. Computer programs have been written to impose several different biaxial loading paths on the specimen. These will control the test while the graphics terminal shows the actual test history plotted in biaxial stress space. The first exercise for these programs will be to develop yield surfaces at room temperature. Elevated temperature measurements will follow.

4.3 Deformation Modeling

Work in this area has shown that a back stress or kinematic hardening variable can be unambiguously determined from the strain transient dip test. Tests conducted on both an MTS servo-controlled hydraulic test machine and the specially designed dip test machine produced consistent results. These data are necessary for application of any of the unified creep plasticity models that incorporate a kinematic hardening variable.

5. ADVANCED REACTOR ACCIDENT ENERGETICS

The Advanced Reactor Accident Energetics program is directed toward developing a data base for the understanding of the key in-core events in a core disruptive accident, which determine the progression and severity of a reactor accident. For the advanced reactor, understanding in-core events is particularly important because significant energy release from the core is possible. The magnitude of this energy release, and therefore the ultimate threat to the containment, is determined by the competing positive and negative reactivity effects caused by the motion and temperature of fuel, cladding, and coolant.

This program, currently focused on postulated CRBR accidents, involves experimental and analytical efforts to determine the magnitude and characteristics of these reactivity effects in the three phases of a core disruption accident in an advanced reactor. These phases are:

1. Initiation Phase -- Fuel Dynamics

2. Disassembly Phase -- Energetics

3. Transition Phase -- Fuel Freezing and Streaming.

5.1 Initiation Phase -- Fuel Dynamics

The final four experiments in the FD 2/4 series were performed this quarter to complete the FD 2/4 series. The experiments performed were FD 2.7, FD 2.8, FD 4.4, and FD 4.5. These experiments investigated the effects of the power history and fuel burnup on disruption. Fuel burnup is an important parameter because it strongly affects the amount of retained fission gas that can influence the time and mode of fuel disruption. Experiments FD 2.7 and FD 2.8 used fuel that had a burnup of 8.3 atomic percent (a/o). Experiment FD 2.7 reproduced the CRBR LOF-accident heating conditions, while experiment FD 2.8 examined the SNR-300 conditions.

The behavior of fuel disruption for this high-burnup fuel was indeed different from that observed in the moderate-burnup (4.0 to 5.0%) fuel that was used in previous experiments. In both experiments, fuel disruption began quite early in the form of solid-state swelling. Copious amounts of volatile fission products were released as aerosols during the disruption process. In FD 2.7, the solid-state swelling was followed by liquid-state frothing, which produced large increases in volume. In FD 2.8, fuel sputtering began shortly after the solid-state swelling. Investigators believe that this sputtering is analogous to the solid-state cracking and dispersion observed in earlier experiment FD 4.3. In the high-burnup case, the solid-state swelling relieved the fission-gas pressurization; therefore, the cracking was milder and appeared as sputtering rather than energetic dispersal.

Experiments FD 2.7 and FD 2.8 are described this quarter; FD 4.4 and FD 4.5 will be described in the January-March 1983 quarterly report.

Experiment FD 2.7 used an ACRR power history very similar to that of experiment FD 2.6. However, because of the lower coupling factor, and the high burnup and low linear heat rating of the fuel, this experiment reproduced the LOF accident heating conditions of the intermediate subassemblies in CRBR. The fuel disruption began as solid-state swelling, observed as a vertical crack about 10 mm long in the clad, and indicating that the fuel had swollen enough to contact the clad. Because the clad was about 90% through the heat of fusion and essentially molten, this contact caused it to separate. As the swelling continued, it began to accelerate. Subsequently, the fuel surface cracked, probably because of interior liquid-state frothing caused by fuel melting. The outer regions of the fuel began to slump, in the form of a collection of solid chunks about 2 to 3 mm in diameter. This breakup and cracking is attributed to the massive swelling or frothing that occurred in the interior of the fuel pin when fuel began to melt. This type of disruption was predicted by SANDPIN, but SAND-PIN apparently underpredicted the magnitudes of the disruption of solid and molten fuel settling. SAS-type settling was observed in the experiment, but the observed settling was preceded by massive swelling. The swelling is enough to cause pin-to-pin interactions that would probably prevent further settling in a bundle geometry. This, in turn, would probably reduce the predicted power burst dramatically, and would increase the amount of fuel remaining in the core when the core entered the transition phase.

Experiment FD 2.8 used an ACRR power history very similar to that of experiment FD 4.3. However, the pin power was slightly less because of the lower coupling factor. The purpose of this experiment was to investigate fuel-disruption behavior in cases where fuel and clad are expected to disrupt coherently for high-burnup fuel and at relatively high power levels. The disruption began as solid-state fuel swelling, just as it did in experiment FD 2.7. Again, the swelling first appeared as a vertical crack in the clad. It continued for a short time when sputtering began and was superimposed on the swelling. Both swelling and sputtering proceeded to a point at which very rapid swelling began, probably the result of fuel melting. The fuel had swollen to 5 or 6 times its original volume by this time, and slumping began shortly thereafter. SANDPIN predicted all three modes of fuel behavior, but, just as in the previous experiment, it apparently underpredicted the magnitudes of the disruption phenomena. The sputtering observed in FD 2.8 is believed to have resulted because early solid-state swelling relieved the fission-gas pressurization, therefore reducing the potential for energetic cracking.

In terms of reactor safety analysis, the most important point is that if the observed fuel behavior is typical for an LMFBR LOF accident, then the swelling is enough to close up the flow channels, thus

removing paths for fuel to be ejected rapidly from the reactor. The nature of fuel movement under these conditions is not addressed by these experiments. However, it must be addressed in some mechanistic manner before the amount of fuel remaining in the core upon entering the "transition phase" can be estimated.

5.2 Disassembly Phase--Energetics

This program is directed toward identifying the phenomena dominating the conversion of thermal energy into work energy and accurately modeling those phenomena for inclusion in accident analysis. The results of this work will be used to determine the work potential associated with core disruptive accidents (CDA) and to assess the magnitude of the threat to reactor containment from CDA energetics. This program currently emphasizes the Effective Equation-of-State (EEOS) and fuel coolant interaction (FCI) tasks. The jointly sponsored USNRC-KfK EEOS program is intended to characterize the pressure sources arising from fresh UO_2 and mixed oxide fuels.

During this quarter, work in the Disassembly Phase focused on completing the current series of EEOS experiments, planning for the coarse dispersed mixture (CDM) experiments, and development and documentation of the TEXAS multifield hydrodynamics code.

The fifth and sixth experiments in the current EEOS series were conducted in late November. EEOS-5 provided confirmatory data on vapor pressure of high-purity UO_2. The EEOS-6 experiment was the first test to examine fresh "reactor-typical" UO_2. The last three experiments in the EEOS experiment series were completed at the end of the quarter. EEOS-7 was a second experiment using reactor-typical UO_2 fuel and was the confirmatory repeat of EEOS-6. Experiments EEOS-8 and EEOS-9 were performed using reactor-typical fresh mixed oxide fuel (UO_2-PuO_2). Data reduction and analysis must be completed before the implications of these results for the timing and magnitude of a CDA disassembly phase can be assessed.

Planning and analysis activities for the CDM experiments continued, but because of resource constraints imposed late in the quarter, design and development activities for the CDM experiments were phased down considerably, postponing indefinitely the first three CDM experiments.

Resource constraints have also curtailed work on the TEXAS multifield hydrodynamics code, except for documentation. Further reporting of the Disassembly Phase in this series of documents will occur on an "as-appropriate" basis only.

5.3 Transition Phase

The use of pure fuel/steel melts in Transition Phase experiments is of great interest because no data on the freezing and streaming of fuel and steel have been obtained with pure reactor materials (UO_2/Mo thermites differ significantly in microscopic thermal properties from UO_2/steel melts). When a nuclear reactor is used to melt the fuel/

steel load, a radial variation of energy deposition results from neu-
tron self-absorption in the fuel. When experiments are being per-
formed at low driving pressures, this radial variation of energy
deposition could cause transient steel-vapor pressures at the outer
radius of the pellet that are larger than the driving pressure.
Therefore, during this quarter, much effort was put into designing
fuel/steel loads that would have an acceptably uniform energy deposi-
tion. The two main approaches considered for reducing steel vapor
production in fuel/steel melts were described in the April-June 1982
Quarterly Report in this series (separation of steel from very hot
fuel until the turbulent flow is established or use of radial zones of
different enrichment to minimize variations in energy deposition).
For reasons that do not need statement here, the second approach,
using graded fuel enrichment to compensate for neutron absorption, was
chosen.

Measuring the fuel flow up the freezing channel has been diffi-
cult because of the high initial temperatures involved, the large
radiation backgrounds present, and the need for thick containment
walls. The Series II design offers more flexibility for diagnostic
measurements because the freezing-channel wall and the containment
wall are now separate.

For the case in which rapid plugging keeps essentially all the
fuel in the melting chamber, project personnel investigated the
problem of thermal stress in the walls of the melting chamber more
closely. Elastic calculations show the possibility of wall rupture,
so a plastic yield will have to be calculated. This calculation will
help determine the desirability of reduced initial temperature in the
fuel-melting-chamber area.

The nature of the leading-edge plugs observed in TRAN Series I
experiment TRAN-2 has been of interest because their location at the
leading edge suggests a bulk-freezing mechanism, yet the fuel pene-
tration distance, about 90 cm, disagrees strongly with the bulk-
freezing model. During this quarter, TRAN-2 was disassembled and
studied in the hot cell facility, yielding information on the plug
composition and details of the crust observed in TRAN-2. Sections
near the channel entrance show steel melting and ablation and a sheet
of melted and refrozen steel surrounding a thick fuel crust. A longi-
tudinal section through the two plugs at the end of the TRAN-2 crust
shows isolated areas of steel distributed throughout the fuel plug,
suggesting an ablation-freezing type of mechanism with reduced heat
transfer between the fuel and the steel, as compared to the tradi-
tional ablation-freezing model. More complete studies of the crusts
and the plugs are underway.

In the area of PLUGM code development and application, PLUGM is
in use for pretest analysis of the annular channel experiment (TRAN
Series II). The first TRAN Series II experiment is scheduled for
February 1983. This test will use an annular freezing channel to

investigate the stability of fuel crusts on steel surfaces of opposite curvature. The resulting information will help determine the applicability of stable-crust, conduction-freezing models to the freezing and plugging of fuel in noncircular flow channels.

The TRAN Series III (GAP) experiments are designed to study downward fuel penetration through planar channels representative of the gaps between adjacent blanket subassembly walls in a heterogeneous-core LMFBR. One of the major safety questions in such an experiment is survival of the containment if the channel plugs rapidly and the hot fuel remains in the cylindrical form. Preliminary heat-calculations showed that melting of the containment walls depends critically on the thickness of the fuel cylinder. Therefore more detailed neutronic design of the experiment is required.

6. LIGHT WATER REACTOR (LWR) DAMAGED FUEL PHENOMENOLOGY

Sandia's LWR Damaged Fuel Phenomenology program includes analyses and experiments that are part of the integrated NRC Severe Fuel Damage (SFD) Research Program. Sandia is investigating, both analytically and in separate-effects experiments, the important "in-vessel" phenomenology associated with severe LWR accidents. This investigative effort provides for three related research programs, the Melt-Progression Phenomenology (MPP) program, the Damaged Fuel Relocation (DFR) program, and the Damaged-Core Coolability (DCC) program. These programs are key elements in the NRC research effort to provide a data base to assess the progression and consequences of severe core-damaging accidents.

6.1 Melt Progression Phenomonology

The objective of this program is to provide balanced perspectives and capabilities applicable to that phase of severe LWR accidents starting with initial core damage and progressing through breach of the reactor vessel and discharge of core materials into the containment environment.

The formal elements comprising this program are:

a. Core Damage Sensitivity Studies.

b. Severe Accident Uncertainty Analysis.

c. Melt Progression Model (MELPROG) Development.

The core-damage sensitivity studies are directed toward identifying the most influential phenomena that govern the in-vessel core degradation process. Project personnel designed a sensitivity matrix, during this quarter, that led to a two-level factorial approach to the sensitivity studies. The two-level factorial approach was designed to investigate the influence of six "external" factors:

a. Oxidation kinetics.

b. Void fraction model.

c. Sequence pressure.

d. Power level.

e. Hydrogen blanketing.

f. Axial power distribution.

Most of the two-level factorial study on the six external factors was completed and much of the preparation of the report documenting this work was also completed.

Sandia staff members have begun to analyze the air oxidation tests of K. T. Stalker (Sandia) using a modified version of the experiment code. The purpose of the analysis is to verify the heat transfer and oxidation models used in the DFR experiment design codes. Although the air oxidation test series is primarily intended for diagnostic development, the tests have achieved temperatures, under rapid oxidation conditions, of up to 2500 K (2227°C), providing a useful data base for design code verification.

The goal of the Severe Accident Uncertainty Analysis (SAUNA) work is the quantification of the impact of phenomenological uncertainty on probabilistic risk analysis (PRA). It is a multiprogram effort at Sandia with a single working group. The effort will ultimately result in a report entitled, Identification of Severe Accident Uncertainties.

In the area of Melt Progression (MELPROG) Code Development, the report, Modeling of LWR Coolant Systems During Severe Accidents: MELPROG Prospective, was completed. Draft copies are currently undergoing review by Sandia management and the NRC.

6.2 Light Water Reactor (LWR) Fuel Damage Experiment Program

This program is directed toward examining the key phenomena that determine the core-damage configuration during the progression of a core melt sequence in an LWR core-uncovering accident. This program uses the information and perspectives gained in current LWR safety programs and focuses on the design of experiments that can contribute to the resolution of important severe-damage issues.

The two major areas of interest regarding in-vessel phenomena are:

a. The behavior of fuel and cladding during the stages of major core deformation from rod-bundle geometry to a severely degraded geometry and

b. The response of the severely damaged fuel to reintroduction of coolant from the emergency core cooling system (ECCS), especially the questions of redistribution of quenched material, short-term cooldown, increased steam generation, and oxidation reaction kinetics.

Information on the first item is necessary to predict the course and duration of core meltdown, fission-product release and transport, and associated effects in containment; resolution of the second provides the essential information to guide action that would terminate the accident and/or mitigate its consequences and to preclude action that could exacerbate the accident.

Current work under this subtask focuses on the in-pile applications because neutronic heating allows prototypic heat generation under severely damaged conditions.

A series of ACRR experiments is planned that addresses the above-described severe core damage issues:

a. Damaged Fuel Relocation Experiments (DF) -- Visually observed fuel damage in a flowing steam environment using neutronic heating in rod sections and multirod configurations.

b. Damaged Fuel Quench Experiments (DQ) -- Postmortem observation of damage configuration after ECCS flooding of damaged core materials.

c. Damaged Core Coolability Experiments (DCC) -- Coolability studies using DQ configurations.

During this quarter, calculations were performed to determine the operating parameters for the first in-pile experiment. The effect of several steam oxidation and hydrogen blanketing models on steam and thermal conditions for DFR tests were also investigated. Calculations were performed to determine the conditions necessary to precrack DFR test fuel pellets by pulsing the test rod bundle in the ACRR. Pre-cracked fuel may be used to represent, to some degree, the effect of the degraded mechanical properties of irradiated fuel on the fuel damage process. DFR personnel have also examined the use of irradiated fuel in later DFR tests to allow correlation of fission-product release with damage configuration. A preliminary evaluation has determined that if the bundle dose is kept relatively low (below 500 R/hr at 1 ft) and the capsule length does not increase substantially, current handling facilities may be used for preirradiated fuel, with relatively minor modifications.

The design for almost all out-of-pile and in-pile experiment hardware has been completed and purchasing of components has begun.

6.3 Light Water Reactor (LWR) Degraded-Core Coolability (DCC) Program

Sandia National Laboratories is conducting a program to determine the coolability of LWR degraded cores. The main purpose is to provide an experimental data base for use in evaluating the applicability of LMFBR coolability models to LWR-specific conditions. This will be accomplished by performing a limited number of in-pile experiments using fission heating of UO_2 rubble to simulate the source of decay power in a severe-fuel-damage accident. For FY83, the scope of the DCC program encompasses the following:

a. Continue design, acquisition of parts, and assembly of the first two DCC experiment packages.

b. Perform DCC-1, the first in-pile coolability experiment con-
    taining a UO_2 rubble bed in a water bath.

c. Analyze the DCC-1 results compared to current coolability
    models and develop and improve models where necessary.

6.3.1 LWR DCC Program - Experimental Activity

During this quarter, the DCC experimental effort focused on the
following activities:

a. The liquid nitrogen storage tank and heat exchanger were
    assembled. Performance tests were completed and showed that
    the heat exchanger satisfied all required specifications.

b. The DCC fuel development testing program was completed. Of
    the candidate thermal neutron poisons studied, gadolinium
    oxide (Gd_2O_3) had the best retention ($>97\%$ during UO_2 pro-
    cessing) and also had the least impact on the mechanical and
    chemical properties of the fuel. Neutronics calculations
    show that 1.0 a/o Gd_2O_3 is sufficient to decouple the bed
    power density from the liquid fraction in the bed.

c. All package hardware for the DCC-1 experiment was ordered.
    Some components, such as the thermocouples, were received and
    initial testing and assembly were started.

6.3.2 LWR DCC program - Analysis and Modeling

Particle bed fluidization phenomena relevant to LWR coolability
questions were surveyed briefly during this quarter. The survey
emphasized determining the main sources of uncertainty affecting the
long-term coolability of degraded cores. The main conclusions are:

a. For bottom-blocked heated beds in steady state, the liquid
    flows downward and the vapor flows upward. Thus, only the
    vapor has the potential to fluidize the bed particles. For
    beds of single-size particles in steady state at powers below
    or near the dryout power, the vapor flow is not large enough
    to fluidize the beds (except locally). Several questions
    have arisen about uncertainties in dealing with these beds.

b. For heated beds with forced flow of liquid through the bottom
    of the bed, both the liquid and the vapor can fluidize the
    bed. If the flow of liquid and vapor is large enough, the
    entire bed can be fluidized. The liquid flow required to
    fluidize a bed of either single- or mixed-particle size in
    the presence of flowing vapor can probably be estimated
    fairly accurately. Uncertainties exist in dealing with these
    beds also.

c. The greatest uncertainty as well as potentially the most important fluidization phenomena probably occur during transient processes.

Since September 1981, the DCC program and the Sandia University Research Program (SURP) have supported jointly a series of particle bed experiments being conducted under Dr. Mohamed El-Genk at the University of New Mexico. The experiments conducted thus far are particularly relevant to LWR severe accident analysis. They include measurements of the porosity of debris beds made from different size and shape particles, some of which are commonly used to investigate coolability limits of particle beds (i.e., spheres) experimentally and others of which are believed to be typical in shape and size to those that will be found in a degraded LWR core.

The results clearly show that:

1. Stratified beds of spherical particles will form with lower porosity than will beds of uniformly sized particles having irregular shape.

2. In a stratified bed of irregularly shaped particles, the porosity of the small-particle layers will generally be larger than that of the large-particle layers.

3. Homogeneous beds of particles of different sizes always form with a smaller porosity than they would if the same particles were strictly stratified in layers according to size.

Under the same funding programs as were described in the previous section, the capillary head of water in particle beds was measured. The particulate used for the beds was the same type as that used to measure porosity. Capillary head is an indication of the ability of a particle bed to pull a liquid (in this case, water) into it. The expression developed to predict capillary head shows it to vary directly as the surface tension of the liquid and inversely as the liquid density, the contact angle between the particle and the liquid, the particle shape factor, and the bed porosity. Comparing model results and experimental data shows that capillary head is greater than predicted by the expression when shape factors are set at 1.0 for particles of less uniform shape. An adjustment of shape factors for irregular particles would improve the agreement between the model and experimental results.

7. TEST AND FACILITY TECHNOLOGY

7.1 ACRR Status

This section contains comments on the general status of overall ACRR operation and remarks concerning experimental activities involving the ACRR.

The ACRR is operating normally in support of weapons program research and advanced reactor safety experiments.

ADVANCED REACTOR SAFETY RESEARCH
QUARTERLY REPORT
OCTOBER-DECEMBER 1982

1. CORE DEBRIS BEHAVIOR

1.1 Ex-Vessel Core Debris Interaction
(D. A. Powers, 6422; W. W. Tarbell, 6422; J. E. Gronager, 6422;
J. E. Brockmann, 6422)

If core debris formed during a severe reactor accident is not
coolable, the debris will penetrate the reactor vessel and interact
with structural material in the reactor cavity . This interaction
could lead to gas generation, production of flammable species, and
intense emission of radioactive aerosols, in addition to erosion of
the reactor basemat.

Study of the phenomena associated with ex-vessel interaction of
core debris with structural material found in the reactor cavity is
the purpose of the Ex-Vessel Core Debris Interactions program. In the
recent past, the major part of this program was the study of core
debris interaction with concrete. Penetration of core debris through
steel liners has also been examined. Other associated phenomena are
currently undergoing study.

1.1.1 Introduction

Sandia project personnel have initiated an experiment program to
address quenching of molten core debris interacting with concrete.
The transient-water-test (TWT) experiments are designed to provide
preliminary data on water-quenching of molten debris interacting with
water where the decay heats range from 1.0 to 0.1 W/g. The data
generated will address questions about:

a. The global effects of an overlying pool on melt/concrete
interactions.

b. Gas generation and composition during the quenching process.

c. Effects on the aerosol and fission-product source terms in
the presence of an overlying water pool.

d. Coolability of the resulting debris bed.

The sections that follow describe the experiment apparatus, test
procedures, test matrix, and schedules.

1

1.1.2 Experiment Apparatus

The apparatus for the TWT series, shown in Figure 1.1-1, consists of a crucible, induction coil, instrument chamber, expansion chamber, instrumented "top hat," and overflow tank. Crucibles will be constructed of limestone/common sand concrete or magnesium oxide (MgO) castable ceramic. Both crucible types will be instrumented with Type K, 1.6-mm-diameter, stainless-steel-sheathed thermocouples to infer heat flux and monitor erosion. The crucible shown in Figure 1.1-2 has dimensions of 40.6-cm OD x 76.2-cm height, with a cylindrical cavity of 21.6-cm ID x 61.0-cm depth. The outside of each crucible will be fitted with a 3.3-mm-thick, laminated fiberglass shell having a minimum yield strength of 10 ksi. This shell will provide structural strength for stresses induced in the concrete by thermal shock and pressurization caused by gas and steam generation. Two copper tubes will be cast into the sides of the crucible to act as inlet and overflow for supply water. The tubes will be 1.6-cm OD x 1.2-cm ID. Each tube will be equipped with two thermistors to measure differential temperature.

An induction coil will be placed around the crucible and connected to a 125-kW induction power supply. The coil consists of 12 turns of 3.5-cm-OD copper tubing and will be connected to the power supply in a four-conductor-lead configuration. A thermistor will be placed in each of the four leads at the coil to monitor heating of the cooling water as it passes through the coil.

The experiment chamber will be sealed to the top of the crucible with 3.2-mm-thick Graphfoil* gasket. The instrument chamber is 40.6-cm OD x 38.5-cm ID x 30.5-cm high. A gas sampling port, thermocouples, pressure transducer, safety burst diaphragm, chamber purge inlet, ignitors, and electrical feedthroughs will be installed in the chamber. The chamber will also incorporate two pairs of pneumatic cylinders that will be used to deliver resistance temperature devices (RTDs) to the cavity during the experiment.

The expansion chamber will be bolted to the top of the instrument chamber using a flange connection and eight 1/2-13 UNC hex head bolts with nuts. Each flange will be sealed using an O-ring having a cross-section of 7.0 mm. The dimensions of the expansion chamber are 40.6-cm OD x 39.4-cm ID x 137.2-cm high with a 58.8-cm OD x 1.3-cm-thick bolted flange at each end. The expansion chamber is connected to two vertically-mounted pneumatic cylinders (not shown in Figure 1.1-1), having a stroke of about 2 meters. Activating these air cylinders lifts the entire apparatus, allowing access to the crucible.

The lower flange of the instrumented "top hat" is bolted to the upper flange of the expansion chamber and sealed with an O-ring. The dimensions of the top hat are 40.6-cm OD x 39.4-cm ID x 30.5-cm high. Three 10.2-cm-diameter, gas-purged quartz glass view ports are located

---

*
A product of Union Carbide Corporation, Carbon Products Division, P.O. Box 1661, Cleveland, OH, 44101.
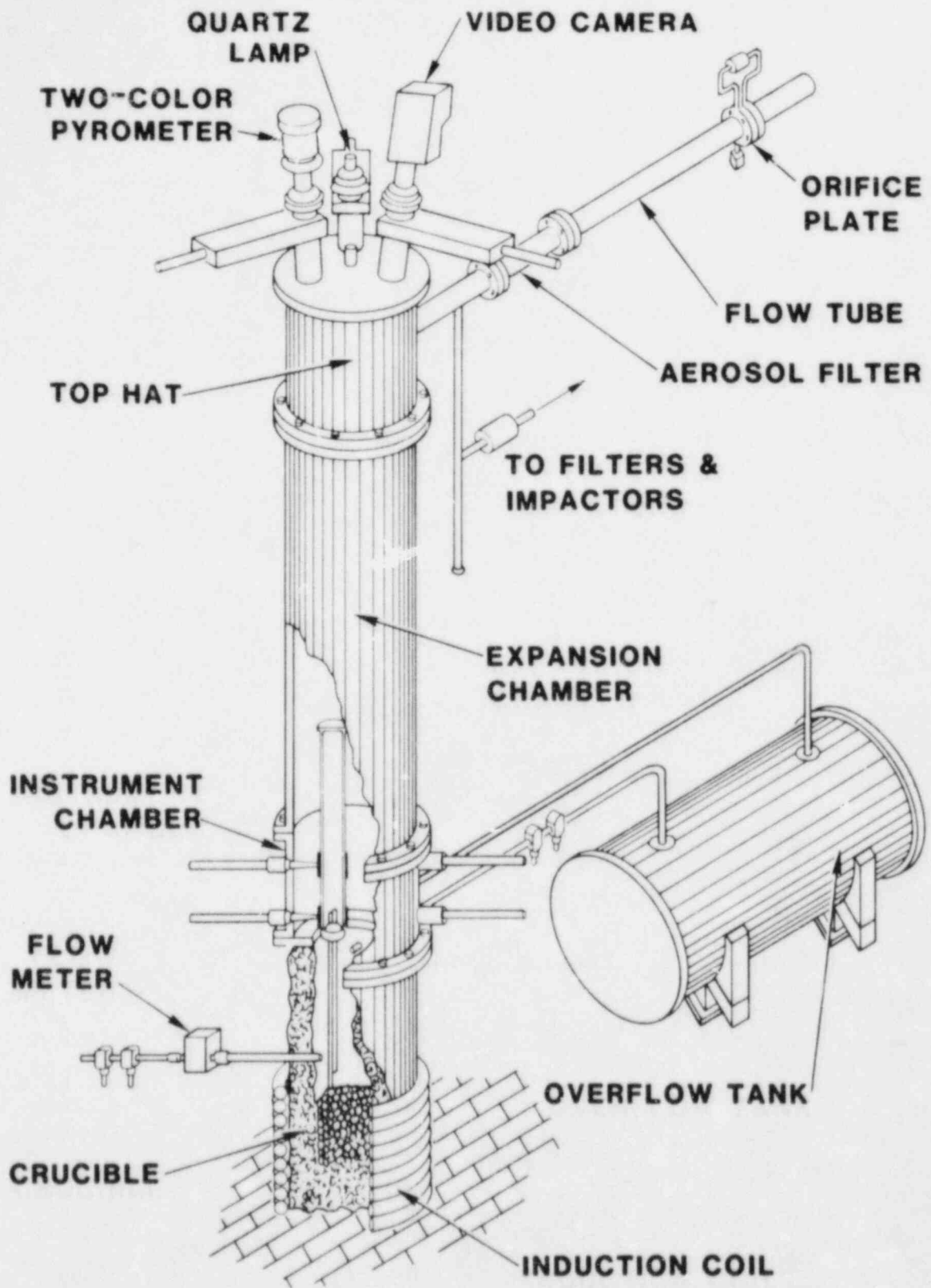
Figure 1.1-1. Experiment Apparatus

3
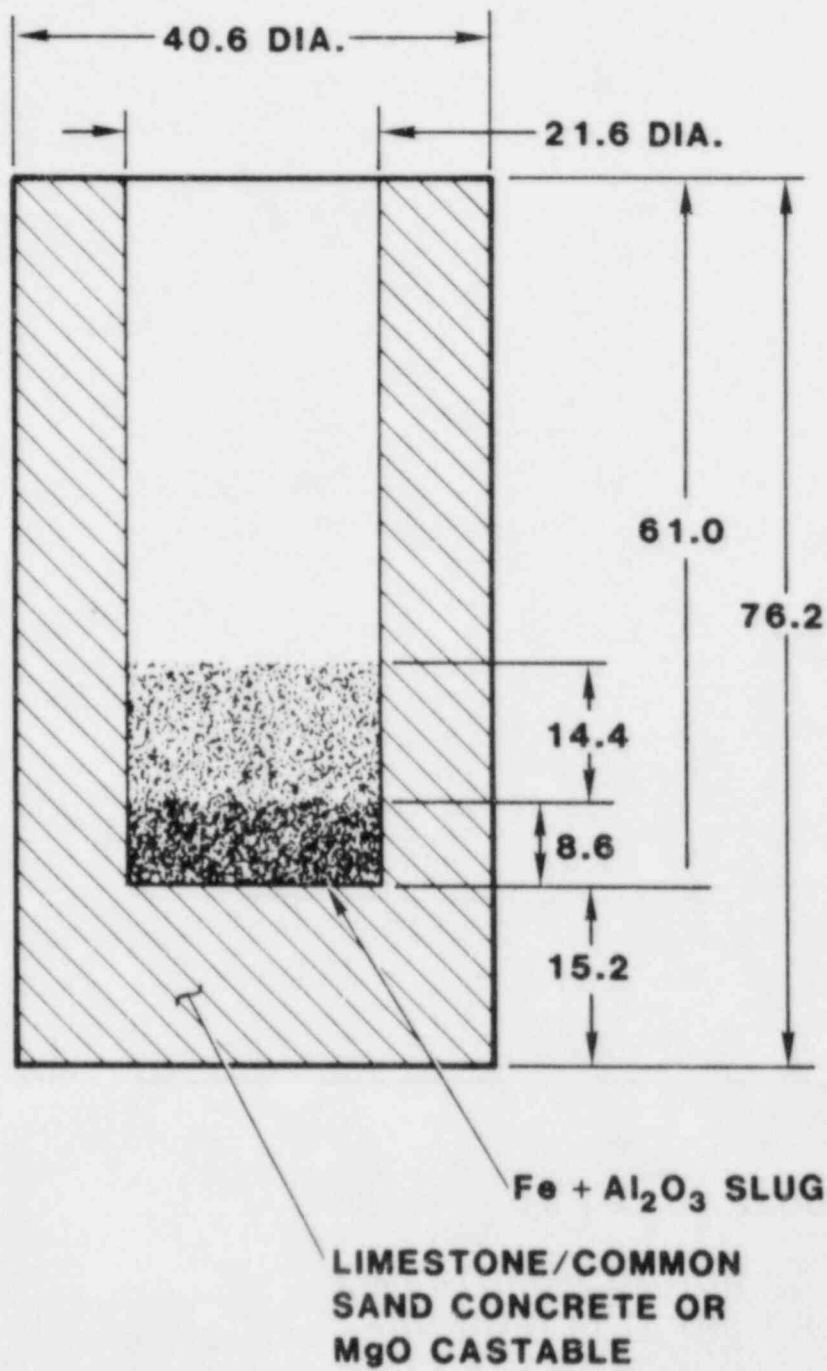
Figure 1.1-2.   Test Article Geometry (dimensions in cm.)

4

on the cover of the top hat. A video camera, a quartz lamp, and a two-color pyrometer will be mounted above the ports. Each port will be protected by a gate valve actuated with a two-way pneumatic cylinder. The instrumented top hat will incorporate a flow tube, orifice, thermocouples, pressure transducers, aerosol dilution system, cascade impactors, filters, dew point sensor, and chamber purge outlet. The entire apparatus, including the instrument chamber, expansion chamber, and instrumented top hat will be wrapped with heating tapes and insulated to maintain a temperature above 373 K (100°C), preventing condensation of water vapor.

The 159-liter overflow tank will be mounted on two 100-kg load cells to measure the difference between the weight of water supplied to the crucible and the weight collected. The tank will be sealed to the test apparatus, maintaining a pressure equilibrium. A large drain will be incorporated to empty the tank when it is filled.

Investigators have tentatively planned to run the tests at Sandia's 10 MeV X-ray facility. The X-ray beam is produced from a Linatron model 1500 pulsed X-ray source. Real-time X-ray imaging could provide visual information related to the interaction of water, melt, and concrete. Image collection will be done with a Decalix-SI image intensifier. The resulting video image will be recorded on video cassette tape.

1.1.3 Test Procedure and Measurements

The test procedure begins with unreacted thermite powder having a density of approximately 2.2 g/cm^3. This powder will fill the cavity to a height of 55.9 cm. Simulants representing fission products will be mixed into the thermite prior to ignition. D. A. Powers and J. E. Brockmann[1-1] addressed the condition of the degraded core at vessel failure and ranked the first 12 fission products according to potential overall safety hazard for a 1- and 10-hour time interval. Table 1-I shows these rankings.

Selection of fission product mocks is based on matching chemical activity with the radioactive fission products, and compatibility with the thermite reaction (i.e., the presence of the fission-product simulant material will not appreciably alter the thermite reaction). The materials to be used are given in Table 1-II.

Forty-five kg of iron oxide/aluminum thermite, doped with fission-product mocks, will be ignited in either a limestone/common sand crucible or a MgO ceramic crucible. Project personnel will start the reaction by passing a high current through a low-resistance wire (Pyrofuse)* placed in the thermite, causing instantaneous heating and ignition of the thermite powder. A 6.6-mm disk of mild steel, 21.3 cm in diameter, will be placed on top of the thermite powder before ignition. The disk will help minimize the ejection of molten debris into the chambers mounted above the crucible. Type K stainless-steel-sheathed thermocouples, 1.6-mm-diameter, cast into the crucible will

---

* A product of Pyrofuse Corporation, Affiliate of Sigmund Cohn Corporation, Mt. Vernon, NY.

TABLE 1-I

Importance Ranking of Fission Products
(Total Dose)

Rank	1 Hour	10 Hours
1	I	I
2	Np	Np
3	Te	Te
4	Tc	Mo
5	Mo	Tc
6	Sr	Cs
7	Ba	Nb
8	Cs	Ba
9	Y	Sr
10	La	Y or La
11		Ru

TABLE 1-II

Fission-Product Simulants

Fission Product	Simulant
Ba	Ba
Sr	Sr
Y	La or Y
Ce	Ce
U	U
Te	Te or PbTe
Ru	Ru
Mo	Mo

6

be used to infer heat flux and monitor erosion. The position of each thermocouple is estimated to be known within 1.5 mm relative to the apparatus. Temperature data measured by the embedded thermocouples will be put into an inverse-heat-conduction computer code to calculate heat flux. Erosion rates will be measured by monitoring the failure of the thermocouples as the molten debris contacts them.

A Type K thermocouple case flush with the bottom surface of the cavity will be used to indicate completion of the thermite reaction. Approximately 10 to 15 s after completion, a 125-kW inductive power supply will be used to supply heat to the molten debris. Simultaneously, water will be added through a tube cast into the side of the curcible. At this point in the experiment, conditions could exist such that a steam explosion could occur with resulting melt fragmentation. Hydrostatic pressures as high as 180 bars[1-2] can develop in the water pool and, when combined with thermal stresses, could cause the crucible to fail. Estimates of chamber pressures range between 28 and 122 bars. These values were calculated based on converting the thermal energy of the thermite into explosive work using a conversion ratio of 1% and 5%, respectively. The FITSA experiments[1-2] report conversion ratios in the range of 1% to 2%, but suggest that they are underestimated. For the purpose of these calculations, the mass of the thermite was assumed to be 45 kg and the thermal energy of the melt was 2.8×10^6 J/kg. The values of explosive work were then converted to the pressure that would be created in the apparatus, assuming a volume of 280 liters and using graphical data presented in the Sandia Laboratories Pressure Safety Practices Manual[1-3]. If a steam explosion occurs, but the pressures are insufficient to cause crucible failure, the event will be detected by an absolute pressure transducer located in the instrumentation section. Visual posttest observation would verify whether fragmentation had occurred provided remelt of the debris had not taken place. Real-time X-ray imaging could be used to indicate a steam explosion and melt fragmentation, given good image contrast and sharpness.

Power introduced to the debris to simulate decay heat will be adjusted to maintain a constant value near 1.0 W/g. The value will depend upon the coupling efficiency of the system. The coupling efficiency is equal to the resistance of the work piece reflected into the coil circuit and the resistance of the coil itself given by reference 1-4:

$$\eta_e = \frac{R_{2eq}}{R_1 + R_{2eq}} , \qquad (1.1)$$

where

η_e = coupling efficiency,

R_{2eq} = reflected resistance of the work piece,

R_1 = resistance of the heating coil.

7

The equivalent resistance of the work piece (R_{2eq}) is given by reference 1-4:

$$R_{2eq} = \frac{\rho_2 \pi a_o \, K_{R2} N_1^2 \, K_{S2}}{d_2 W} ,$$ (1.2)

where

$$d_2 = \sqrt{\frac{\rho_2}{\mu f}}$$

and

ρ_2 = resistivity of the work piece,

a_o = diameter of the work piece,

N_1 = number of coil turns,

d_2 = reference depth of work piece,

μ = magnetic permeability,

f = frequency of the power supply,

W = length of the work piece,

K_{R2} = resistance factor, and

K_{S2} = work piece shortness factor.

The coil resistance is defined by reference 1-4:

$$R_1 = \frac{\rho_1 \pi (b_1 - d_1) N_1^2}{d_1 L(sf)} ,$$ (1.3)

where

$$d_1 = \sqrt{\frac{\rho_1}{\mu f}} ,$$

$$sf = \frac{t N_1}{L} ,$$

and

ρ_1 = resistivity of the coil material,

b_1 = inside diameter of the coil,

8

d_1 = reference depth of coil,

 L = length of the coil,

 t = space between coil turns, and

 sf = space factor.

The actual power delivered to the coil is obtained from reference 1-5 and is:

$$P = EI \cos \theta, \tag{1.4}$$

where

 E = coil voltage,

 I = coil current,

 θ = phase angle between the voltage and current, and

 $\cos \theta$ = power factor

Equation (1.4) shows that when the phase angle is 0 deg (power factor = 1.0), all the volt-amperes become the actual power, while if the phase angle is greater than 0 deg (power factor < 1.0), only part of the volt-amperes becomes actual power. Because only the actual power does useful work, the power factor should be as near to unity as possible. Combining two facts, (1) that only resistance takes power, and (2) that impedance is the combined effect of resistance and the capacitive and inductive reactances of a circuit, permits the power factor (PF) to be expressed in terms of the resistance and impedance of a circuit[1-5]:

$$PF = \frac{R}{Z}, \tag{1.5}$$

where

 R = resistance of the circuit and

 Z = impedance of the circuit.

In induction heating, the impedance of the circuit strongly affects the power delivered to the coil. It is not unrealistic for only 30% of the rated power of an inductive power supply to be delivered to the coil. Based on product data for the 125 kW power supply to be used in the TWT experiments, 190 kg of steel can be melted and raised to 1923 K (1650°C) in 1 hour. The actual power input to the steel to get this type of heating is equal to 41 kW. Assuming a coupling efficiency of 100% for this case, the power at the coil is also 41 kW. This is a conservative assumption because, in reality, the efficiency would be less, thereby increasing the required coil power. The resultant debris configuration for the TWT experiments for calculation purposes assumes a two phase cylindrical slug of

9

alumina over iron. A calculation of the reflective resistance (Eq. 1.2) of the alumina resulted in a value of 0, indicating that alumina does not couple with the inductive field. The actual power applied to the composite slug will go into heating the iron. The reflective resistance of the iron phase and coil was calculated using Eqs. (1.2) and (1.3), respectively, and a coupling efficiency of 90% was calculated using Eq. (1.1). The actual power delivered to the iron phase is, therefore, 37 kW. A power density of 1 W/g is desirable in the actual experiments. If the thermite reaction goes to completion, 24.75 kg of the original 45 kg will be iron, resulting in a power density of 1.5 W/g. This is sufficient to achieve the power-density goal in the experiment.

Water will be added to the cavity at the rate of 45 l/min through a copper tube cast into the crucible 48.3 cm above the base. Water will continue to flow out the overflow tube into the overflow tank. The flow will then be reduced to maintain a subcooled water pool (2 to 5 l/min). The overflow tube is cast into the crucible 71.1 cm above the base and 180 deg from the supply tube. The supply tube is installed well below the overflow tube to insure that the supply water is thoroughly mixed before it leaves the cavity. Two thermistors will be installed in the supply tube and two in the overflow tube and will be connected to form a bridge circuit to measure differential water temperature. Project personnel will use this temperature data to calculate the heat flux to the water pool. This heat flux data will be compared to the subcooled critical heat flux models (CHF) such as that used in the ZPSS, as discussed in Tong[1-6] and correlated by Ivey and Morris[1-7]. The CHF model suggests that a subcooled water pool has a major influence on the critical heat flux, i.e., the greater the pool subcooling, the greater the critical heat flux.

Just as the water pool begins forming over the melt, two pairs of pneumatic cylinders will be actuated. Each pair of cylinder rods supports a vertical tube located in the instrumentation section. Inside each tube is a slider with two 6.3-mm-diameter stainless-steel-sheathedresistance temperature devices (RTDs) of varying lengths, attached by a set screw. Also attached to the slider is a stainless-steel rod approximately 2.5-cm longer than the longest RTD. When the air cylinders are actuated, the piston rods extend, moving the tube over the opening of the crucible cavity. As the stainless rod slips over the edge of the cavity, the slider moves down the tube and delivers the RTDs to the water pool to measure temperature. The rod makes initial contact with the debris, thereby establishing the elevation of each of the RTDs in the pool. Each RTD will be monitored separately. The individual temperatures will be averaged and used in the subcooled critical heat flux equations to calculate heat flux.

Thermistors and RTDs are used rather than thermocouples because they produce a greater output voltage for small changes in temperature. Also, configuring these devices into bridge circuits reduces the common-mode electrical interference produced by the inductive power supply.

Crust formation is based on the physics of the experiment; the probability of existence of the crust is inferred from other experiments such as the FRAG tests[1-8] and TWT-1. The formation of a crust during the course of the experiment could be inferred by temperatures measured by thermocouples cast into the side walls and base of the cavity. If an insulating crust forms, isolating the water above it from the molten debris below, water temperatues would be near 373 K (100°C); the temperature below the crust should be an order of magnitude greater. Real-time X-ray imaging could also show the formation of a crust.

A device built by Inductotherm Corporation will measure the power delivered to the coil and will provide an output voltage proportional to that power. Power lost by heating the cooling water in the coil will be calculated by measuring the differential water temperature at the inlet and outlet of the coil with a thermistor bridge. The power introduced to the debris is difficult to measure because the melt temperature cannot be measured directly. This power is the one variable in the experiment that needs to be controlled because all the data produced will be related to the decay heat of the debris. A steady-state power input to the debris, maintained between 0.1 and 1.0 W/g, is desired. Because the power to the debris cannot be measured directly, a heat balance will be performed to offset heat gain and loss terms to quantify the power input.

Consider a controlled volume around the coil and crucible. An equation can be written for the heat/power gain and loss terms:

$$\dot{q}_m = \dot{q}_c - \dot{q}_{cw} - \dot{q}_{cc} - \dot{q}_w - \dot{q}_s , \qquad (1.6)$$

where

$\dot{q}_m$ = power delivered to the debris,

$\dot{q}_c$ = power at the coil,

$\dot{q}_{cw}$ = power lost to heating coil cooling water,

$\dot{q}_{cc}$ = heat loss to concrete,

$\dot{q}_w$ = heat loss to water pool, and

$\dot{q}_s$ = heat loss to steam production.

The power loss to heating the coil cooling water will be calculated by reference 1-9:

$$\dot{q}_{cw} = \dot{m} C_p (T_{out} - T_{in}) , \qquad (1.7)$$

where

$\dot{m}$ = mass flow rate of coil water,

c_p = specific heat of water,

T_{out} = outlet water temperature, and

T_{in} = inlet water temperature.

Heat is lost to the concrete $(\dot{q}_{cc})$ from the molten debris by a combination of conduction, convection, and radiation. If the composite slug resulting from this heat transfer is assumed to be a short circular cylinder of some height, heat will be lost to the concrete in both the radial and downward axial direction. The total contribution of the heat transferred by these three mechanisms can be measured by considering a small control volume in the concrete adjacent to the melt/concrete interface. Figure 1.1-3 shows the control volumes for the radial and axial orientations. For the purpose of analysis, two nodal points are shown which represent actual thermocouple locations. An energy balance can be written for each of the control volumes[1-10].

$$\dot{E}_{in} + \dot{E}_{g} - \dot{E}_{out} = \dot{E}_{st} , \qquad (1.8)$$

where

$\dot{E}_{in}$ = energy entering the control volume,

$\dot{E}_{out}$ = energy leaving the control volume,

$\dot{E}_{g}$ = energy generated (equals 0 for this case), and

$\dot{E}_{st}$ = energy stored within the control volume.

For a steady-state condition, $q_{in} = q_{out}$ and $q_{st} = 0$. Equation (1.8) can be expanded to define the heat conduction through both the radial and axial control volumes.

For the radial control volume[1-10],

$$\dot{q}_{r}(in) = \dot{q}_{r}(out) + \dot{q}_{r}(st) , \qquad (1.9)$$

and

$$\dot{q}_{r}(out) = \frac{2kLA_{rs}}{\ln \frac{r_{o}}{r_{i}}} \; T_{r_i} - T_{r_o} , \qquad (1.10)$$

$$\dot{q}_{r}(st) = \rho V_{r} c_{p} \frac{\Delta T_{r_i}}{\Delta t} , \qquad (1.11)$$

where

k = thermal conductivity of the concrete,

L = height of iron phase of composite slug,

12
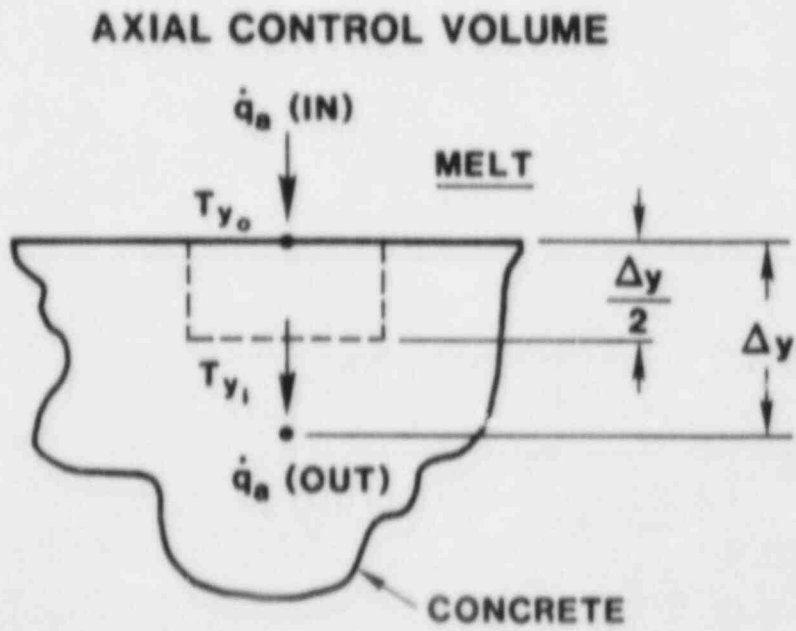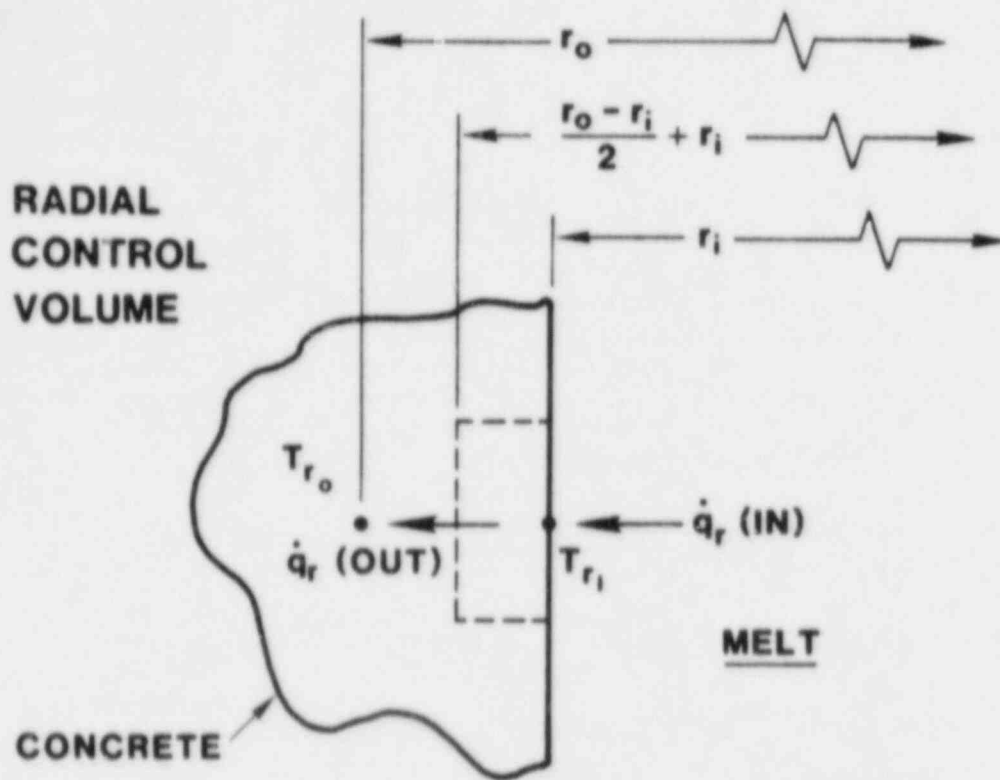
Figure 1.1-3. Description of the Control Volume for Heat-Loss Calculations for Concrete

A_{rs} = surface area of the iron phase in the radial direction ($A_{rs} = 2\pi r_i L$),

r_i = radial distance to the thermocouple closest to the melt,

r_o = radial distance to the thermocouple adjacent to r_i,

T_{r_i} = temperature of thermocouple at r_i,

T_{r_o} = temperature of thermocouple at r_o,

ρ = density of the concrete,

V_r = volume of mass associated with the control volume

$$\left(V_r = A_{rs} \, \pi \left[\left(\frac{r_o - r_i}{2} + r_i \right)^2 - r_o^2 \right] \right),$$

c_p = specific heat of concrete, and

$\Delta T_{r_i} / \Delta t$ = time rate of change of temperature measured at r_i.

For the downward axial control volume[1-10],

$$\dot{q}_a(in) = \dot{q}_a(out) + \dot{q}_a(st) , \tag{1.12}$$

and

$$\dot{q}_a(out) = \frac{kA_{as}\left(T_{y_o} - T_{y_1}\right)}{\Delta y} , \tag{1.13}$$

$$\dot{q}_a(st) = \rho V_a c_p \left(\frac{\Delta T_{y_o}}{\Delta t}\right) , \tag{1.14}$$

where

A_{as} = surface area of the iron phase in the axial direction

$$\left(A_{as} = \pi r_i^2 \right),$$

V_a = volume of mass associated with the control volume

$$V_a = \frac{2A_{as}}{\Delta y} ,$$

14

Δy = distance between the two measuring thermocouples

$(\Delta y = y_1 - y_0)$,

T_{y_0} = temperature of the thermocouple nearest the melt at depth y_0,

T_{y_1} = temperature of the thermocouple at depth y_1, and

$\Delta T_{y_0} / \Delta t$ = time rate of change of the temperature measured at y_0.

The heat to the concrete ($\dot{q}_{cc}$) at a particular instant equals the heat entering the surface of the control volume. This is equal to the sum of the heat leaving and stored within the control volume in both the radial and axial orientations given by:

$$\dot{q}_{cc} = \dot{q}_r(\text{out}) + \dot{q}_r(\text{st}) + \dot{q}_a(\text{out}) + \dot{q}_a(\text{st}) , \qquad (1.15)$$

and substituting

$$\dot{q}_{cc} = \frac{2kLA_{rs}}{\ln \frac{r_o}{r_i}} \left(T_{r_i} - T_{r_o}\right) + \rho V_r c_p \left(\frac{\Delta T_{r_i}}{\Delta t}\right)$$

$$+ \frac{kA_{as}\left(T_{y_0} - T_{y_1}\right)}{\Delta y} + \rho V_a c_p \left(\frac{\Delta T_{y_0}}{\Delta t}\right) \qquad (1.16)$$

The following assumptions have been used for the development of these equations:

a. One-dimensional conduction,

b. Semi-infinite medium,

c. Constant material properties,

d. Uniform temperature over the entire area for any instant,

e. No internal heat generation,

f. Distance between nodal points is small.

Heat loss to the water pool will be calculated using Eq. (1.7). The mass flow rate of water delivered to the crucible will be measured with a water flow meter that provides a voltage analogous to flow rate. The differential temperature at the inlet and outlet of the crucible will be measured with a thermistor bridge.

Heat lost to steam production will be calculated by measuring the instantaneous difference between the mass of water flowing into the crucible and the mass collected in the overflow tank. This difference is assumed to be the total steam produced,

$$q_s = m \, h_{fg} \, , \qquad\qquad (1.17)$$

where

m = mass of steam, and

h_{fg} = latent heat of vaporization.

Some miscellaneous power losses occur, primarily associated with the coil coupling to adjacent structures. These losses are difficult to measure and are assumed to be negligible when compared to the others.

Gases will be sampled periodically and the noncondensable components of these samples will be analyzed using gas chromatography. Samples will be obtained through a 6.4-mm-diameter stainless-steel tube mounted just above and slightly away from the opening of the crucible cavity. Several samples will be taken during the initial quenching process. The temperature and pressure at which the gases are sampled will be recorded and measured, with a Type K thermocouple and an absolute pressure transducer located in the instrument chamber.

A high-temperature dew-point probe located in the instrumented "top hat" will measure the amount of water vapor present in the chamber. The probe can operate at stream temperatures up to 443 K (170°C) and humidity limits up to saturation. The instrument provides a direct measurement of dew point between 252 K and 443 K (-15°C and 170°C). It has a slew rate of 23 K/min ascending dew point and 43 K/min descending dew point. It is also insensitive to dust, gases or aggressive materials in the concentrations expected in these experiments.

The 159-liter overflow tank is mounted on two 100-kg load cells. The time-resolved amount of steam produced can be calculated by taking the difference between the weight of water collected and the weight of water supplied to the crucible. The entire apparatus, except for the overflow tank, will be heated above 373 K (100°C) with resistance-heating tapes and insulated with 2.5-cm-thick fiberglass with aluminized backing to prevent condensation of water vapor.

Aerosols and fission-product mocks will be taken into a collection system through a sampling port located in the flow tube facing upstream (not shown in Figure 1.1-1). The flow tube is constructed of 2-inch, Schedule 40 pipe. Aerosol and fission-product mocks will be collected on filters; particle sizing will be determined by collection with cascade impactors. The aerosols are assumed to be wet, therefore a system has been designed to dry the particles prior to their being collected. Figure 1.1-4 is schematic representation of the collection system. Assuming that the aerosols have the same velocity as the

16
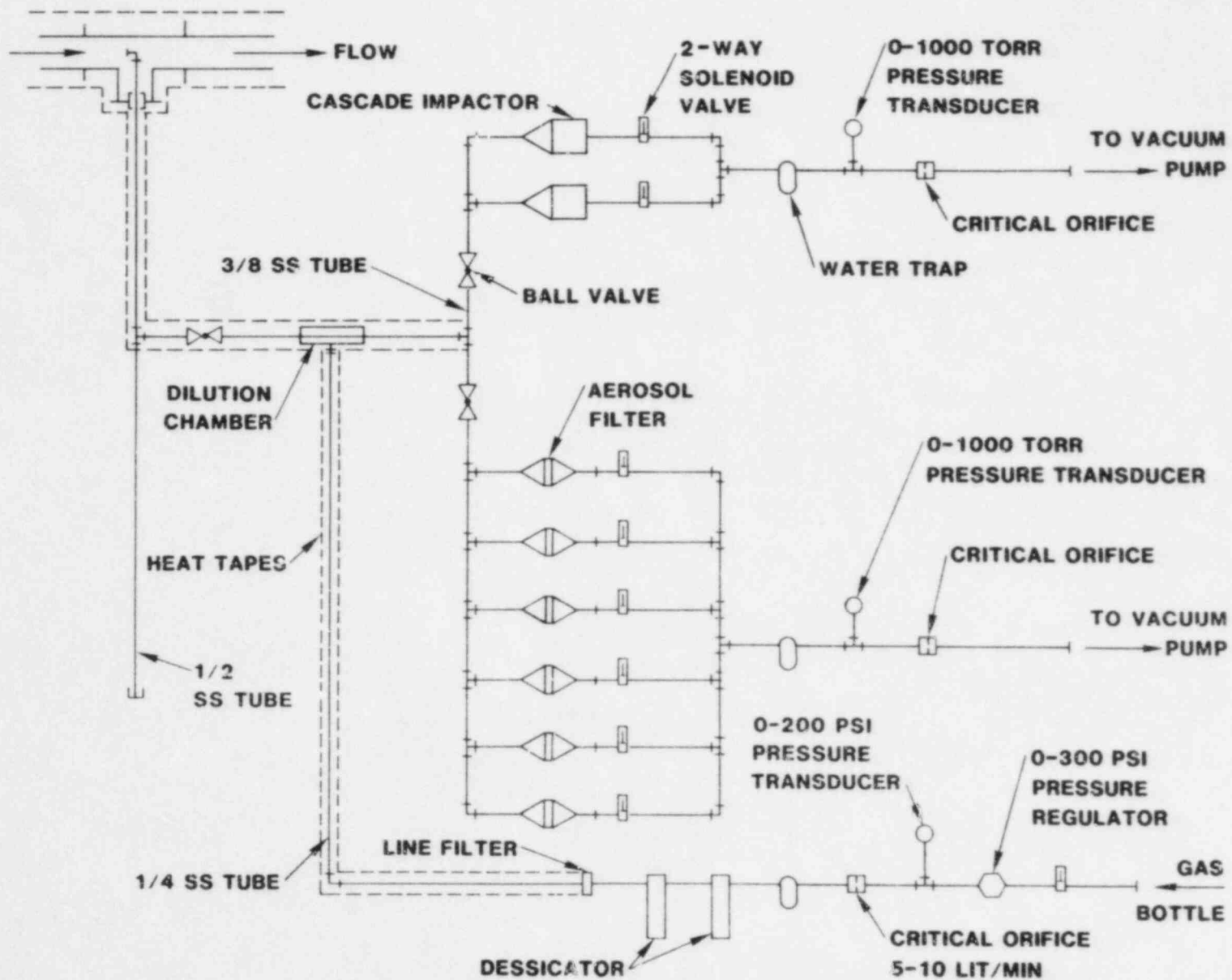
Figure 1.1-4. Aerosol Dilution System

gases, the density of the aerosols in suspension can be calculated from filter-sample data. The volumetric flow rate of reaction gases can be calculated from flow data measured at the sharp-edge concentric orifice. The mass of aerosol collected on the filter paper sampled over a specific period of time can be weighed. Dividing the mass of aerosol collected per sample time by the volumetric flow rate gives the density of aerosol in suspension by:

$$\rho = m/t/Q_v, \tag{1.18}$$

where

ρ = density of aerosols in suspension,

t = sample time,

Q_v = volumetric flow rate of gases, and

m = mass of aerosol collected.

Periodic sampling can provide information regarding the rate of aerosol production at different phases of the experiment.

Aerosol-mass concentration will be measured by weighing the particle deposits on the filter paper. The fission-product mocks, also collected on the same filter but in small mass quantities, will be analyzed with an electron microprobe and X-ray fluorescence techniques. Water from the overflow tank will be sampled periodically to examine the effectiveness of the water pool to capture and retain the aerosol and fission-product particulate.

By measuring the differential pressure at flange tops across a sharp-edge concentric orifice, and using Bernoulli's equation, flow rates of gases from the melt/concrete interaction and water quench will be calculated. The orifice is located at the end of the flow tube attached to the instrumented top hat. A particulate filter will be located 20 pipe diameters upstream of the orifice to remove any particles suspended in the flow stream. Particle deposition on an orifice can change the calibration, causing errors in flow calculations. A Type K thermocouple located 18 pipe diameters upstream of the orifice will measure gas temperature. An absolute-pressure transducer will be mounted at one of the upstream flange taps. Data from the thermocouple, pressure transducer, and gas samples will be used to calculate gas density.

Posttest analysis of the grab samples will measure, in percent, the composition of each gas species in the mixture. The density of the mixture will be calculated by the equation shown below (reference 1-11):

$$\rho_{gas} = \sum_{i=1}^{n} \frac{R_i M_i}{C} \times \frac{T}{T_{REF}} \times \frac{P_{REF}}{P}, \tag{1.19}$$

where

ρ_{gas} = density of the gas mixture,

i = individual gas species,

M_i = molecular weight of the individual species,

R_i = volumetric percent of the individual species in the mixture,

C = molecular gas volume constant (22.4 liters/mole at STP),

T = absolute temperature of gas,

T_{REF} = absolute reference temperature (273°C)

P = pressure of gas, and

P_{REF} = reference pressure (1 atm).

The instrumented "top hat" is equipped with a 10.2-cm-diameter, gas-purged, quartz glass view port with pneumatically actuated gate valves. A quartz lamp, a video camera, and a two-color pyrometer will be mounted above the three ports. The gate valves will be closed to protect the glass ports from molten debris ejected from the crucible during the thermite reaction. The quartz lamp will provide light inside the chamber for monitoring the experiment with the video camera. The two-color pyrometer will be used to measure the temperature of the molten debris just before water addition. The ability of the pyrometer to provide accurate temperature data amid the suspended aerosol and particulate matter is questionable. All the quartz view ports are clamped with a quick-release V-band retainer allowing rapid assembly and disassembly for cleaning the quartz glass during the experiment. The gate valve to the port being cleaned will be closed during the operation, allowing the experiment to proceed without shutdown.

The experiments are tentatively planned to be conducted at Sandia's 10-MeV X-ray facility if feasibility experiments prove that it can produce a sharp video image with good contrast. Real-time X-ray imaging could be used to observe the initial thermite reaction, debris configuration, effect of water quenching, occurrence of a steam explosion, and resulting fragmentation, vapor film interface, erosion rates and patterns, and crust formation. However, several inherent characteristics of these experiments exist that make real-time X-ray imaging difficult. First, the ability of X-rays to penetrate or be absorbed by a certain material depends on its thickness, its density, the atomic nature of the material, and the X-ray generation voltage. Relative absorption of different materials is not constant, but varies inversely as kilovoltage. In other words, as the kilovoltage is increased, the radiographic absorption of a material is progressively less dependent on the atomic number of its constituents. For this reason, the boundary between the melt and concrete may be difficult to define, resulting in poor contrast on the video image.

19

Second, the "fuzzy" boundary in a radiographic image is called "geometric unsharpness." It is defined by the equation shown below[1-12]:

$$U_g = F\left[\frac{t}{D_o}\right],$$ (1.20)

where

U_g = geometric unsharpness,

F = size of the radiation source,

D_o = source to object distance, and

t = distance from source side of the specimen to the film.

The size of the radiation source is nominally 2 mm. Clearly, if t becomes large or D becomes small with everything else held constant, the geometric unsharpness increases. A typical value for U for the TWT experiments would be 0.28 mm, assuming t = 510 mm and D^g = 3650 mm. This value is not unreasonable for a flat, uniformly thick specimen. The geometric unsharpness could be an order of magnitude larger than that calculated above for the TWT experiments because of the thickness and geometry effects.

Third, X-ray energy decreases as the inverse square of the source-to-object distance. The test apparatus will be set up outside the building that houses the X-ray source. Some question arises concerning whether the Linatron can be located close enough to the apparatus so that the emitted X-rays have enough energy to penetrate the crucible to produce an adequate video image.

Fourth, the inductive coil is in the same field of view as the debris. The resulting X-ray image will have the tubes of the inductive coil superimposed on the image of the debris. This could add to the problems with contrast and sharpness.

A major effort will be required to set up and conduct these experiments away from the normal test site. It will be well worth the effort if the X-ray imaging proves feasible. Therefore, several diagnostic tests will be performed at the X-ray facility to address the concerns previously mentioned.

To summarize this section, Table 1-III lists the measurements required together with the method for making them.

The experiment will be terminated if the melt breaches the crucible because of erosion, power to the debris is insufficient to cause an interaction between the melt water and concrete, goals of the experiment have been achieved, or safety becomes questionable.

TABLE 1-III

Measurements in TWT Experiments

Measurements	Device or System Used
Power applied to coil	Power transducer
Power input to debris	Energy balance
Coil differential water temperature	Thermistor bridge
Molten debris temperature	Two-color pyrometer
Heat flux to concrete	Type K thermocouples
Concrete erosion rate	Type K thermocouples
Flow rate of water	Water flow meter
Heat flux to water pool	Thermistor bridge, RTDs water flow meter
Steam explosion	X-ray imaging,* pressure transducer
Melt fragmentation	X-ray imaging,* posttest observation
Crust formation	X-ray imaging,* Type K thermocouples, posttest observation
Pool boiling regime	Video camera
Gas species and composition	Grab samples
Water vapor	Dewpoint probe
Steam generation	Water flow meter, overflow tank w/load cells, video camera
Gas flow rate	Concentric orifice
Gas density	Grab sample, Type K thermocouple, pressure transducer
Aerosol mass concentration	Aerosol filters
Particle size	Cascade impactors
Chamber pressure	Pressure transducer

* Dependent on feasibility of X-ray techniques

1.1.4 Test Matrix

Project personnel have designed the test matrix to provide data addressing the interaction of high-temperature melts with concrete in the presence of water. The data collection exists in three areas of interest: (a) the interaction between melt, concrete, and water; (b) gas generation, and (c) aerosol and fission-product source term. Table 1-IV shows the test matrix.

The TWT-1 test took place in June 1982 as a scoping test to assess the important phenomena of this type of event. It was intended to provide data of a qualitative nature to form the design basis for the subsequent tests in the series.

The TWT-2 test is designed to generate baseline data on a dry cavity. The results of this test will be compared directly to results

TABLE 1-IV

TWT Test Matrix

Test	Description	Purpose
TWT-1	Crucible - CRBR water quench conducted June 1982	Scoping Test - Preliminary qualitative study of quenching phenomena
TWT-2	Crucible - Limestone/common sand no water quench	Generate baseline data on the melt concrete interaction
TWT-3	Crucible - MgO water quench	Analyze the quenching process without concrete decomposition
TWT-4	Crucible - Limestone/common sand water quench	Analyze the quenching process with concrete decomposition
TWT-5		Corium composition

from the TWT-4 test using a water-quenched cavity. This comparison should show directly the effect of water on quenching of molten debris, gas generation, and aerosol and fission-product source term.

Investigators speculate that gas generation during the melt/concrete interaction can affect the quenching process. Therefore, they designed test TWT-3, substituting an MgO ceramic crucible for the prototypic limestone/common sand. the reaction of the thermite with the MgO will not produce a significant amount of gas when compared to concrete test TWT-4. The results of these two tests will be compared, examining the effect of gas generation on the quenching process and H_2 production.

The TWT-5 test will use a corium-composition prototype of actual core debris. This experiment will take place after investigators obtain a better understanding of the quenching process of the iron oxide/aluminum system. The iron oxide/aluminum system is used because of its availability and ease of use, lack of toxic health hazard, high initial reaction temperatures, coupling with an inductive field, metallic and oxide phases, and because it serves as a good model to characterize the quenching process.

The experiments do not attempt to address scaling effects such as mass or geometry. The experiments assume that an unlimited supply of water is available for cooling the debris when, in fact, it may not be. Assuming that the side walls of the cavity contribute very little to the resulting melt/concrete interaction, the experiment could represent a small area in the reactor cavity. However, the density of the resulting debris bed would be approximately 70% of actual core

22

debris and the bed thickness would be approximately 40%. These percentages assume no porosity together with deposition of all the material in the reactor vessel into the reactor cavity. For the numbers obtained above, the masses of core debris and the iron/alumina debris were assumed to be 8.6 g/cm^3 and 6.1 g/cm^3, respectively. The total mass of debris available and the reactor cavity area for the Zion Reactor were used for calculation purposes and were 1.45 x 10^5 kg and 32.1 m^2, respectively[1-13].

The test matrix has been designed to provide quantitative data to aid in answering questions about the interactions of molten debris, concrete, and water. Only a few experiments have been proposed. This proposed matrix represents an initial investigation into studying these interactions. The data from these tests could be used to design larger-scale tests (0.5- to 1.0-m-diameter cavities) that would incorporate scaling effects such as mass and geometry.

1.1.5 Program Schedule

A tentative schedule for the TWT program is shown in Table 1-V. Based on expected deliveries of instrumentation and support apparatus, the schedule should be reasonable. A diagnostic test will be conducted in late April with 45 kg of thermite to check out crucible integrity, water delivery, orifice sizing, apparatus temperatures, and timing critical to the actual tests.

Assembly and check out of the main apparatus should begin in late June 1983. Set-up for the TWT-2 test should begin in late July/early August. The data will be analyzed after each test to evaluate data-acquisition problem areas. Test TWT-3 should be run by the end of September, and TWT-4 by mid-November. Project personnel will try to produce a computer model characterizing the quenching process for the iron oxide/aluminum system. All the data will be compiled and analyzed and a topical report will be issued by January 1984.

1.2 Core Retention Materials Assessment
(J. D. Fish, 6422; M. Pilch, 6425; E. R. Copus, 6422; T. Y. Chu, 7537; M. E. Field, 6426; F. E. Arellano, 6422; J. H. Bentz, 7537)

1.2.1 Introduction

Core Retention Materials Assessment is a program, involving both experiments and analysis, designed to (1) determine the fundamental limitations of candidate core-retention materials and concepts, and (2) develop a data base for use by the NRC in the licensing review of proposed ex-vessel core retention materials. The program is currently focused on magnesia brick crucibles, thoria and alumina particle beds, and high alumina concrete liners.

1.2.2 Sample PLUGM Calculations[1-14]

The sample calculations that follow illustrate the application of PLUGM to the particle-bed core-retention concept. The first set of calculations assumes that the particle bed is composed of alumina

TABLE 1-V

TWT Program Schedule - 1983

ACTIVITY	JAN	FEB	MAR	APR	MAY	JUN	JUL	AUG	SEPT	OCT	NOV	DEC	
FINISH DESIGN	→⊢												
ORDER PARTS			→⊢										
FABRICATE APPARATUS				→————————→⊢									
READY POWER SUPPLY				→————————→⊢								
DIAGNOSTIC TESTS				→————————→⊢								
FABRICATE MgO				→————→⊢								
APPARATUS CHECK OUT						→———→⊢						
SITE SET UP								→⊢	→⊢	→⊢		
TEST							TWT-2 →⊢	TWT-3 →⊢	TWT-4 →⊢			
DATA ANALYSIS								→⊢	→⊢	→————————→⊢		
TOPICAL REPORT												JAN ----→ "84"

24
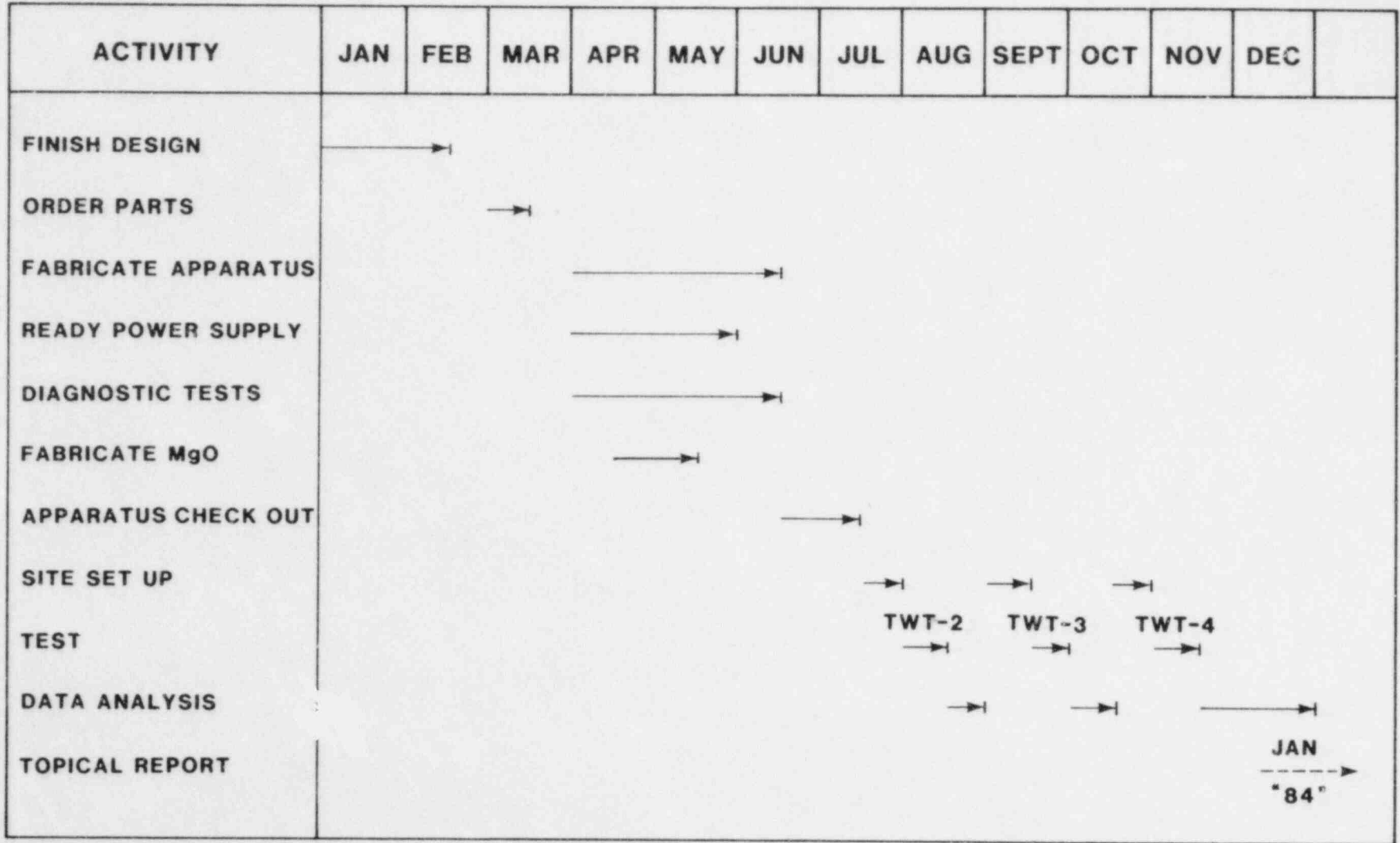
particles with a diameter of 2.0 cm. The porosity of the bed is taken
to be 40%. Molten core debris (primarily UO_2, ZrO_2, and Zr metal) is
ejected from the reactor primary vessel onto the particle bed in 4 s.
The total quantity of melt corresponds to a depth of 33 cm averaged
over a typical light water reactor cavity. Thermophysical properties
of the melt, the crust, and the alumina particles are listed in Table
1-VI.

TABLE 1-VI

Material Properties Used in PLUGM Calculations

	Corium Melt	Corium Crust	Al_2O_3 Particle
Thermal Conductivity (W/m/K)	11.0	2.31	8.9
Density (kg/m^3)	7000	7070	4000
Specific Heat (J/kg/K)	485	402	1213
Melting Temperature (K)	---	2225	2345
Heat of Fusion (J/kg)	2.08×10^5	___	___
Viscosity (P)	4.34×10^{-3}	---	---
Surface Tension (W/m)	0.5	---	---

Figure 1.2-1 shows penetration depth as a function of the temper-
ature of the melt. Even with a saturated melt, the penetration is 37
cm. With 200 K of superheat, the melt penetrates 54.7 cm.

One of the advantages of a particle-bed core-retention device is
the inherent ability to supply coolant to the bottom of the melt. The
bed depth, therefore, must exceed the expected melt penetration.
Otherwise, some of the melt will reach the concrete below the bed and
prevent coolant flow in that region and in any region for which the
coolant supply is on the other side of the point of maximum penetra-
tion. In some reactors, where space is extremely limited, a bed depth
of more than 20 to 25 cm in some locations is impractical. the calcu-
lations presented below indicate a more effective solution to the
problem of initial penetration.

Penetration depths for a layered particle bed have been calcu-
lated. The material properties are the same as those used above (see
Table 1-VI). The calculations are performed with a melt superheat of
200 K. The bed consists of three layers: (1) a top layer 25 cm deep;
(2) a middle layer 5 cm deep; and (3) a bottom layer 20 cm deep. The
top and bottom layers are composed of particles with diameters of 2
cm. The diameter of the particles in the middle layer is treated as a
parameter.
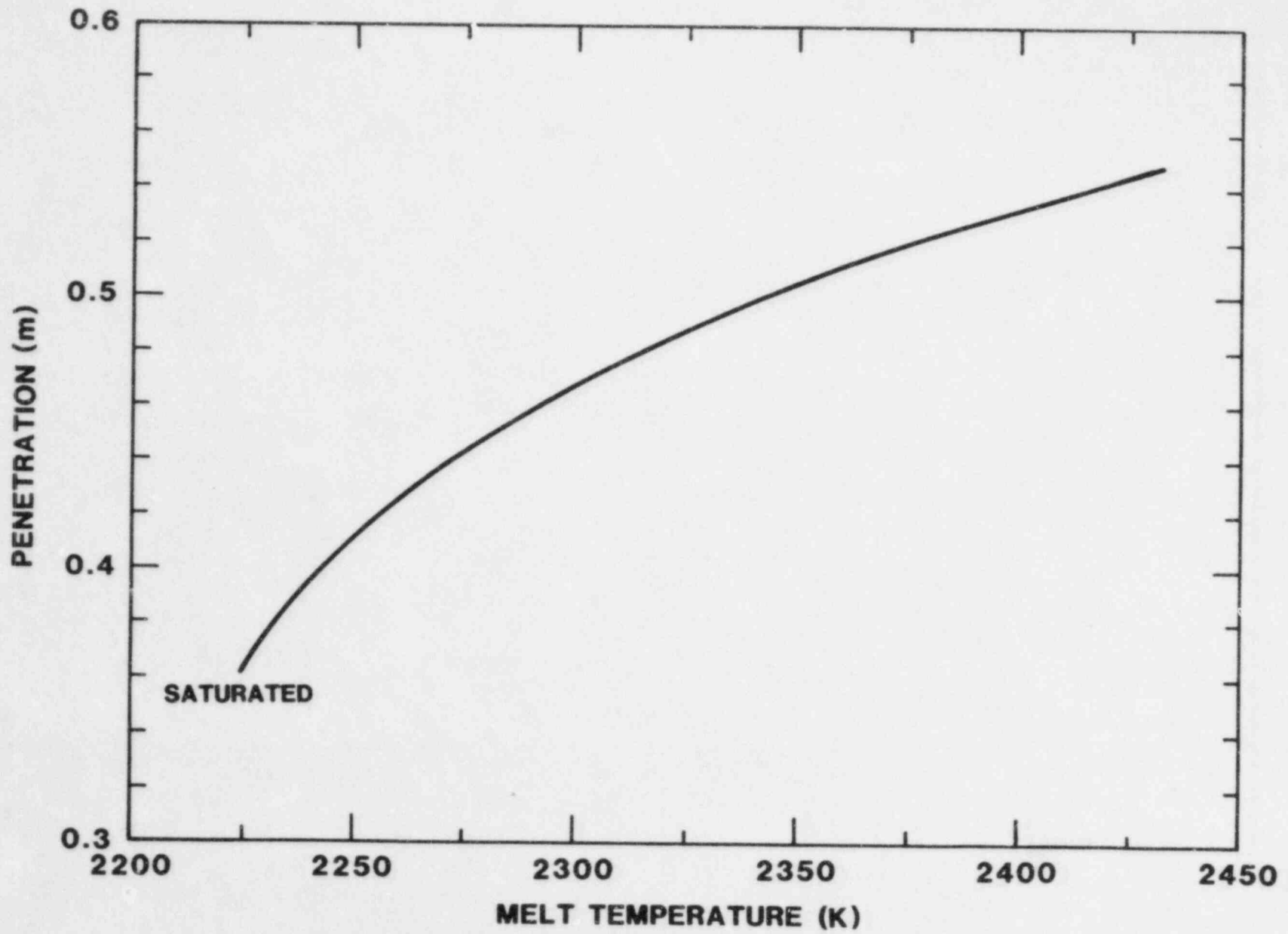
Figure 1.2-1. Melt Temperature vs. Penetration Depth

Figure 1.2-2 shows the melt penetration into the bed as a function of the middle-layer particle size. Melt reaches the concrete basemat for particles in the middle layer larger than about 1.65 cm. The melt is stopped in the middle layer for particles smaller than about 0.7 cm.

Note that the top layer need not be 25 cm thick throughout the cavity for the calculations to apply. In fact, penetration for any region greater than 25 cm from the point of melt deposition will be less than that shown in Figure 1.2-2 provided the top layer of the bed is at least 25 cm thick at the point of melt deposition. This consideration is particularly important for those reactors in which the instrumentation tubes severely limit the available space in the keyway of the cavity. A deep bed can still be placed directly under the primary vessel without interfering with motion of the instrumentation tubes.

1.2.3 Inductive Ring Susceptor (IRIS) Technique Development

The first application of the IRIS Technique at the Large-Scale Melt Facility (LMF) is scheduled for April or May 1983. The 200-kg melt will be dropped onto a layered alumina particle bed. Three design options for this test have been generated and are presented below. The designs are based on the scaling up of results of the Sustained Oxide Test (SOT) series. Also presented are the results of a series of tests in which stainless steel rings were heated in the LMF coil. The tests, which indicated a coupling efficiency of 50%, demonstrated the feasibility of the proposed IRIS test.

1.2.3.1 IRIS Scale-up Designs

Three designs for melting large quantities of UO_2 using the IRIS Technique are discussed below. Design One uses a 40-cm coil and a standard stock alumina crucible on hand at the Sandia experiment site. Design Two uses the 80-cm LMF coil but would require a special-order crucible. Design Three requires that both a crucible and a coil be ordered. In addition, all three designs would require custom made tungsten rings.

Design Three has been chosen for preliminary design of the IRIS test scheduled for April or May 1983. It will provide a larger molten pool (200 kg) in less time and with less thermal shock to the Al_2O_3 crucible.

The designs are extrapolated from the SOT series in which the IRIS Technique was used to melt moderate quantities (5-15 kg) of several oxides. Figures 1.2-3 and 1.2-4 show the results from the latest SOT experiment. Approximately 86% of a 13-kg UO_2 charge was melted in under three hours at an average power level of 5 kW. Table 1-VII shows details of the test.

Figures 1.2-3 and 1.2-4 also show the results of thermal modeling using the TAC2D computer code. Note the good agreement between the

27
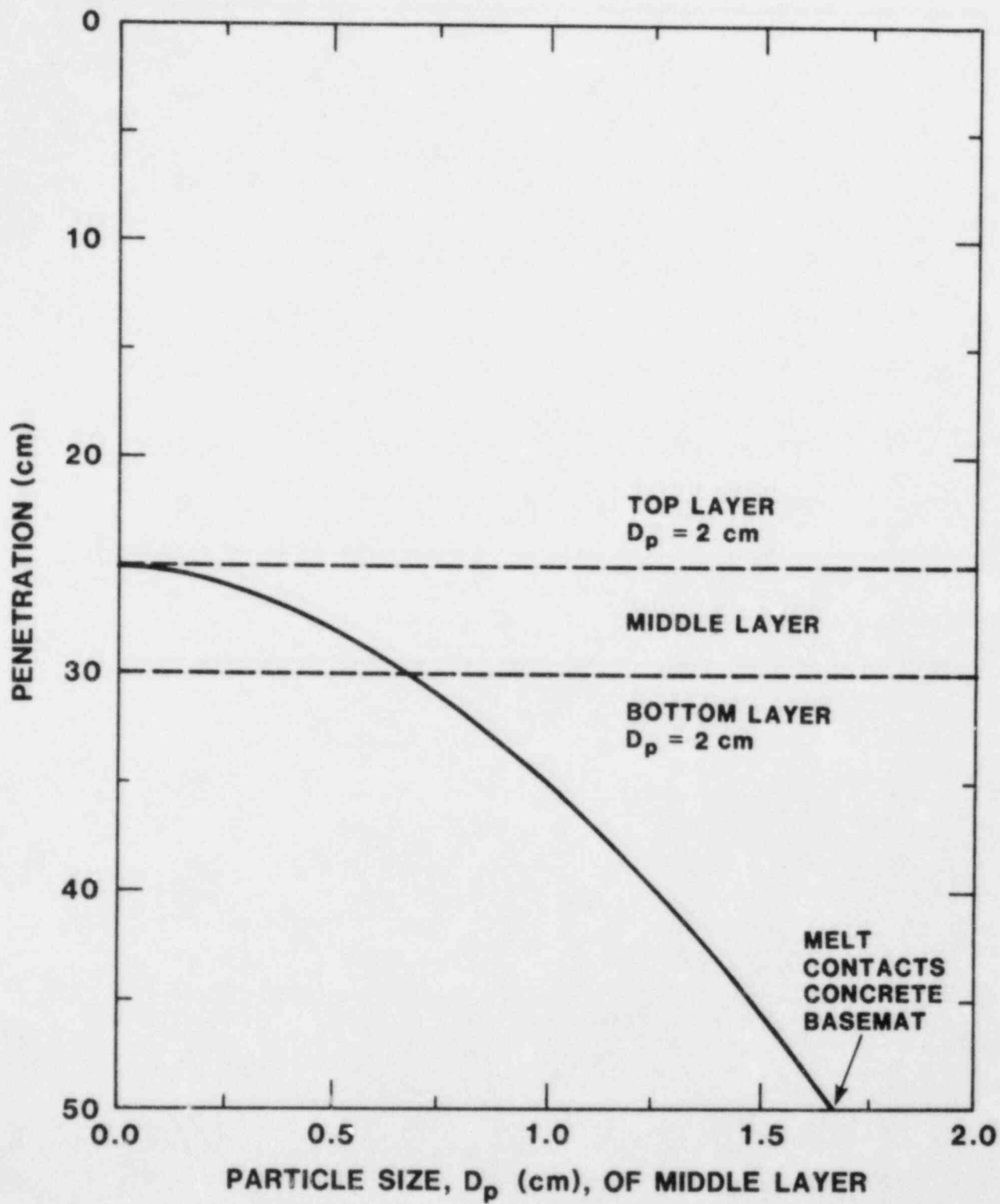
Figure 1.2-2. Penetration of Layered Particle Bed by Molten Corium
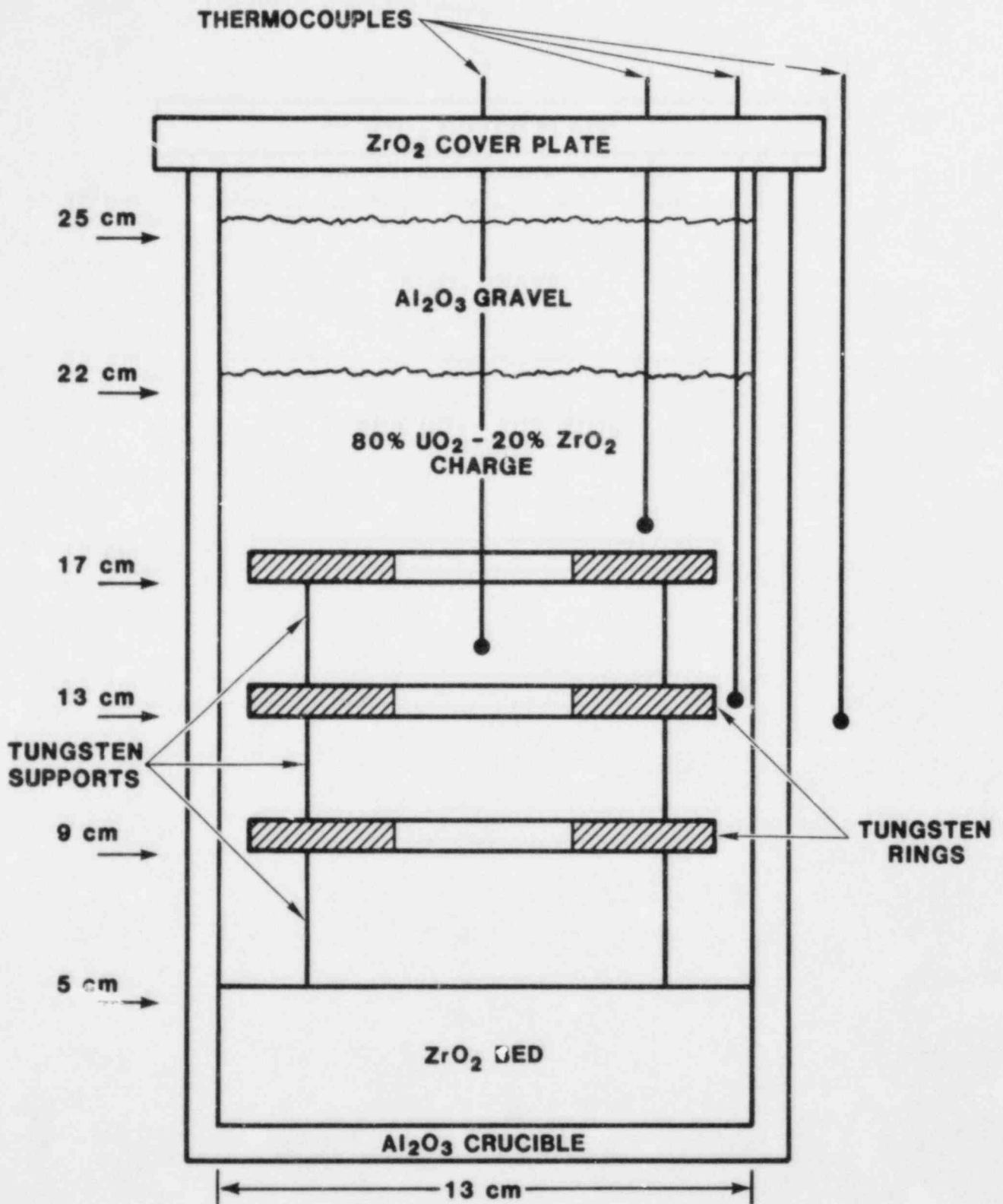
Figure 1.2-3. Medium-Scale (13 kg) Test Configuration
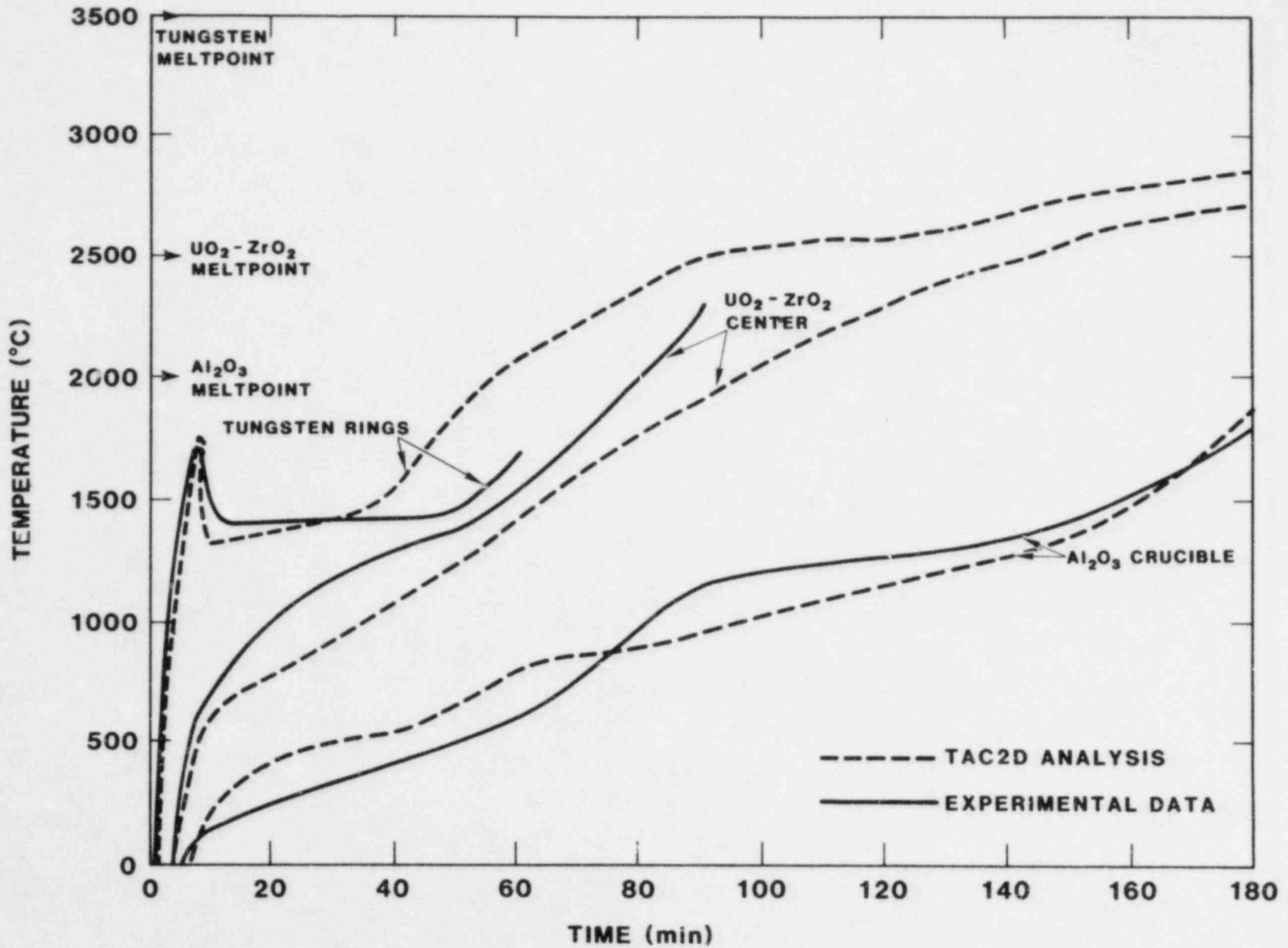
Figure 1.2-4. Thermal Analysis for Medium-Scale Test (13.8 kg charge 5 kW average power input)

TABLE 1-VII

Details of SOT on Which Scaled-up Designs are Based

Mass of charge: 13.8 kg   Ring O.D. = 10 cm

Vol. of charge: 2400 cm^3 Ring I.D. = 5 cm

Surface area/ring: 118 cm^2

Total input heat transfer area: 353 cm^2

Total heat loss area: 1296 cm^2 (sides)
                        212 cm^2 (ends)
                       1508 cm^2

Total heat losses at 60% melt: 4.2 kW (84%)

Gap between ring and crucible: 1.5 cm

SOT test results and the code predictions. Each of the three scaled-up designs is based on a thermal analysis using the same material properties and heat transfer coefficients as the medium-scale experiment.

a. Design ONE

Design ONE (Figure 1.2-5) uses a 40.6-cm coil in conjunction with a standard stock 227-kg Al$_2$O$_3$ crucible. This allows for a 1.3-cm gap between the crucible and the coil. The ring susceptors have a 30.5-cm outside diameter and a 10.1-cm inside diameter. Other design data are given below and the thermal analysis is shown in Figure 1.2-6. Here the input power is set at 10 kW per ring for a total input power of 50 kW. Melt would begin at one hour and would be about 60% complete in 3 hours.

Design ONE Data:

Mass of charge: 200 kg

Vol. of charge: 35,000 cm^3

Surface area per ring: 1256 cm^2

Total input heat transfer area: 6253 cm^2

Total heat loss area: 5776 (sides)
                       1140 (ends)
                       6916 Total

Gap between ring and crucible: 1.5 cm

Heat losses at 60% melt: 30 kW (60%)

31

Figure 1.2-5. Design ONE Configuration
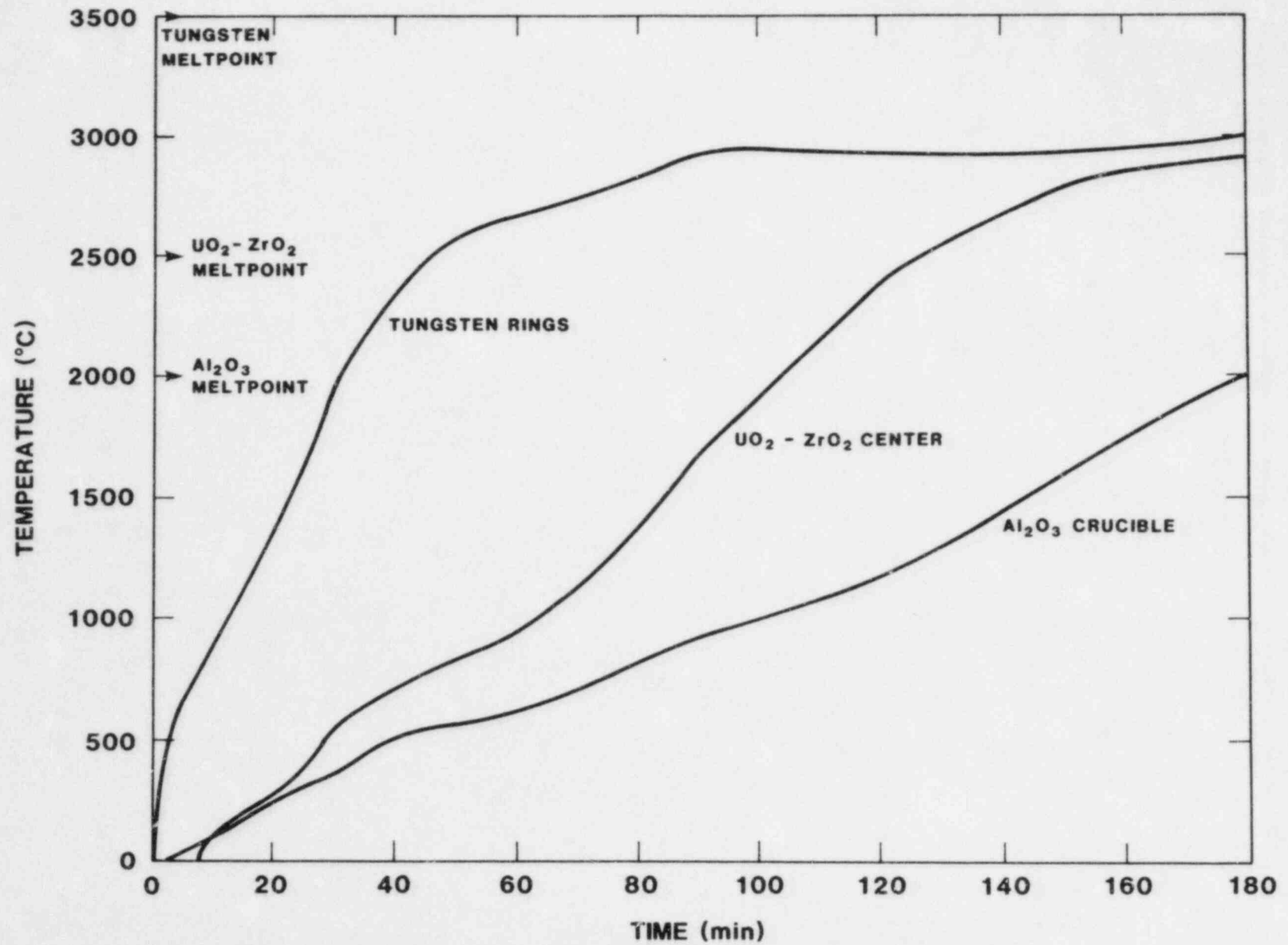
Figure 1.2-6. TAC2D Thermal Analysis for Design ONE (200 kg charge, 50 kW total power input)

33

b. Design TWO:

Design TWO uses the 81.3-cm LMF coil in conjunction with a non-standard 61-cm-diameter crucible. Here the rings were designed to have an outside diameter of 50.8 cm and an inside diameter of 25.4 cm. Steel rings of this size were found to be able to develop a maximum total power of approximately 80 kw at the LMF (see Section 1.2.3.2). For this case, an input power of 86 kW (total) would begin to melt the charge in 30 minutes, but total melt would not be achieved for at least another three hours. The pertinent details are below and in Figures 1.2-7 and 1.2-8.

Design TWO Data:

Mass of charge: 285 kg

Vol. of charge: 49,260 cm^3

Surface area/ring: 2865 cm^2

Total input surface area: 8595 cm^2

Total heat loss area: 3770 cm^2 (sides)
                       2827 cm^2 (ends)
                       _____
                       6597 cm^2 TOTAL

Gap between ring and crucible: 2.5 cm

Heat losses at 60% melt: 25 kW (30%)

c. Design THREE

Design THREE uses a custom-made coil and crucible. The ring susceptors have a 35.6-cm OD and a 10.1-cm ID. It is similar to Design ONE in that five rings are used and the bed height is identical, but the tungsten rings, crucible, and coil are all somewhat larger than design One and the gaps between ring, crucible, and coil are roughly doubled. A power of 10 kW per ring (50 kW total) will initiate melt at 90 min and be 60% complete in three and a half hours. Additional data is given below and in Figures 1.2-9 and 1.2-10.

Design THREE Data:

Mass of charge: 340 kg

Vol. of charge: 59,411 cm^3

Surface area per ring: 1878 cm^2

Total input surface area: 9393 cm^3

Total heat loss area: 6500 cm^2 sides
                       1661 cm^2 ends
                       _____
                       8160 cm^2 TOTAL

34
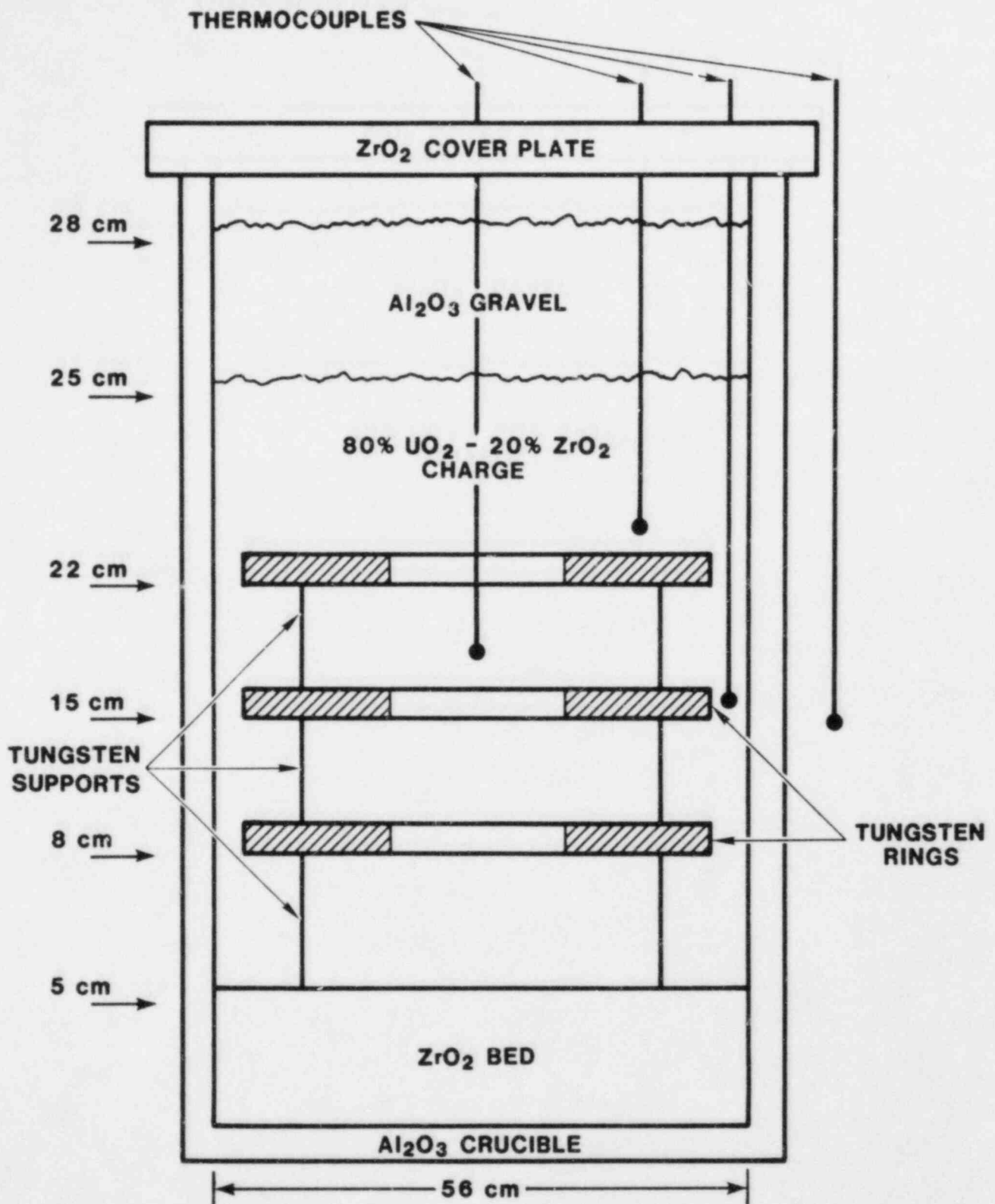
Figure 1.2-7. Design TWO Configuration

35
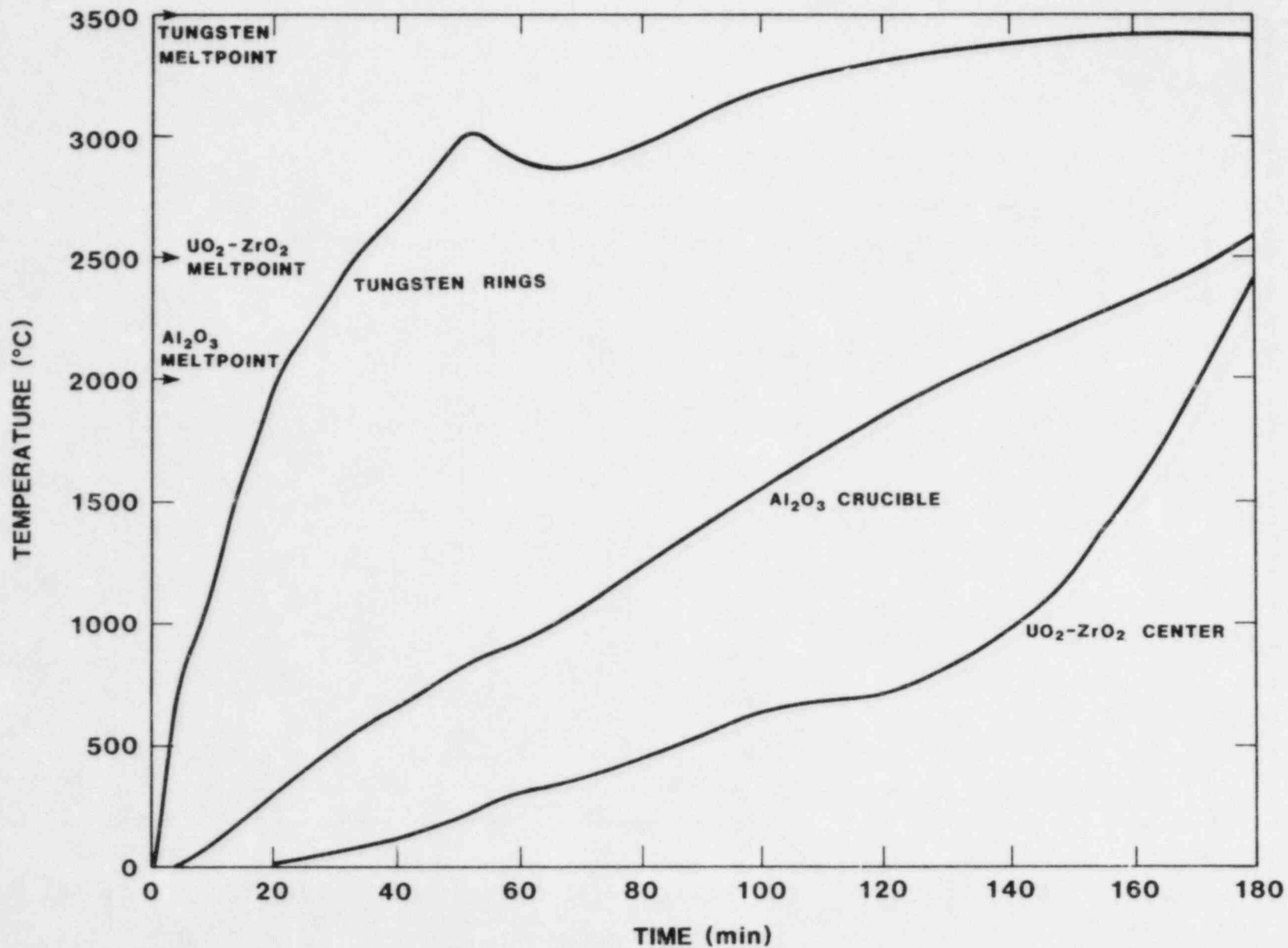
Figure 1.2-8.   TAC2D Thermal Analysis for Design TWO (86 kW total
                input power, 285 kg charge)
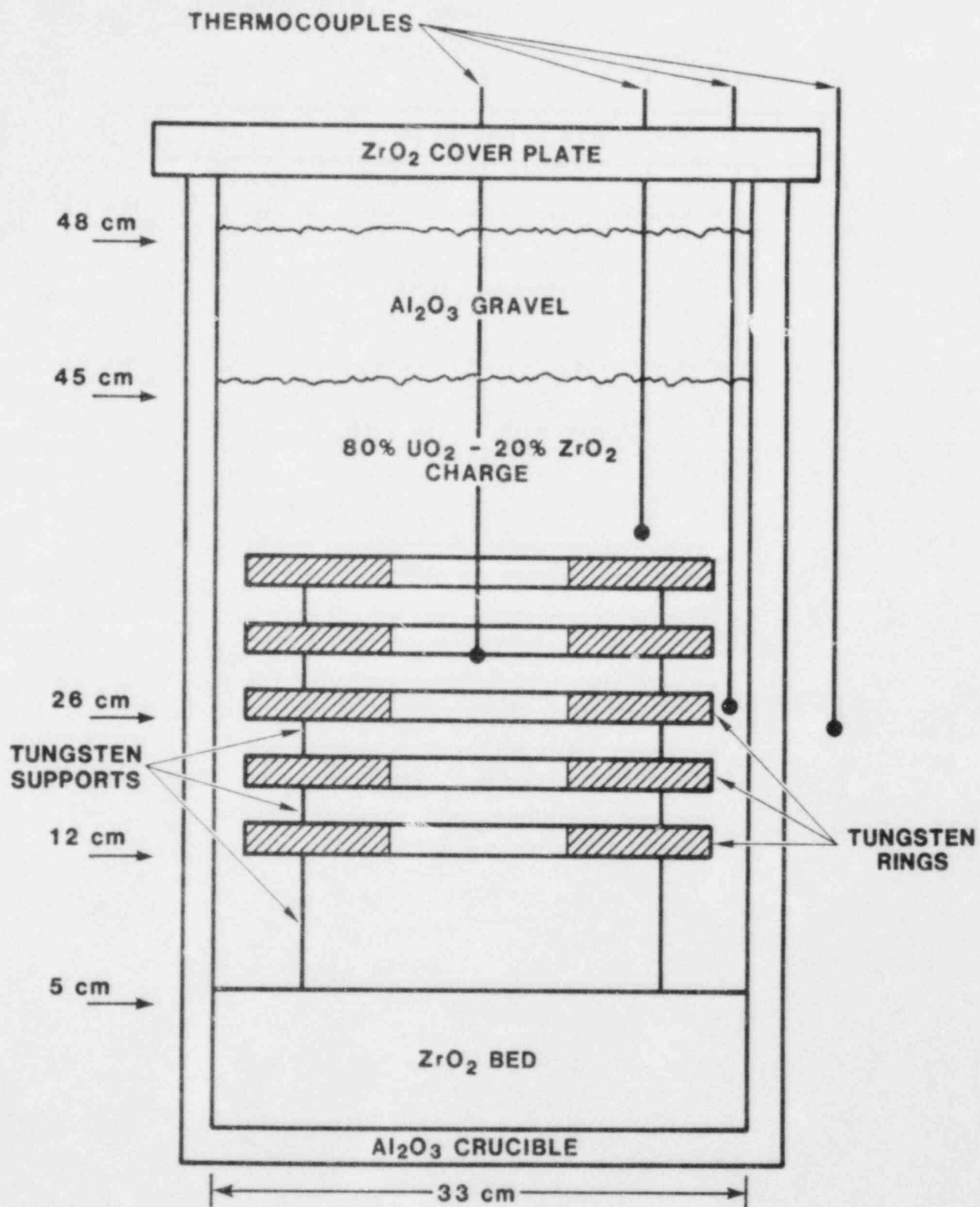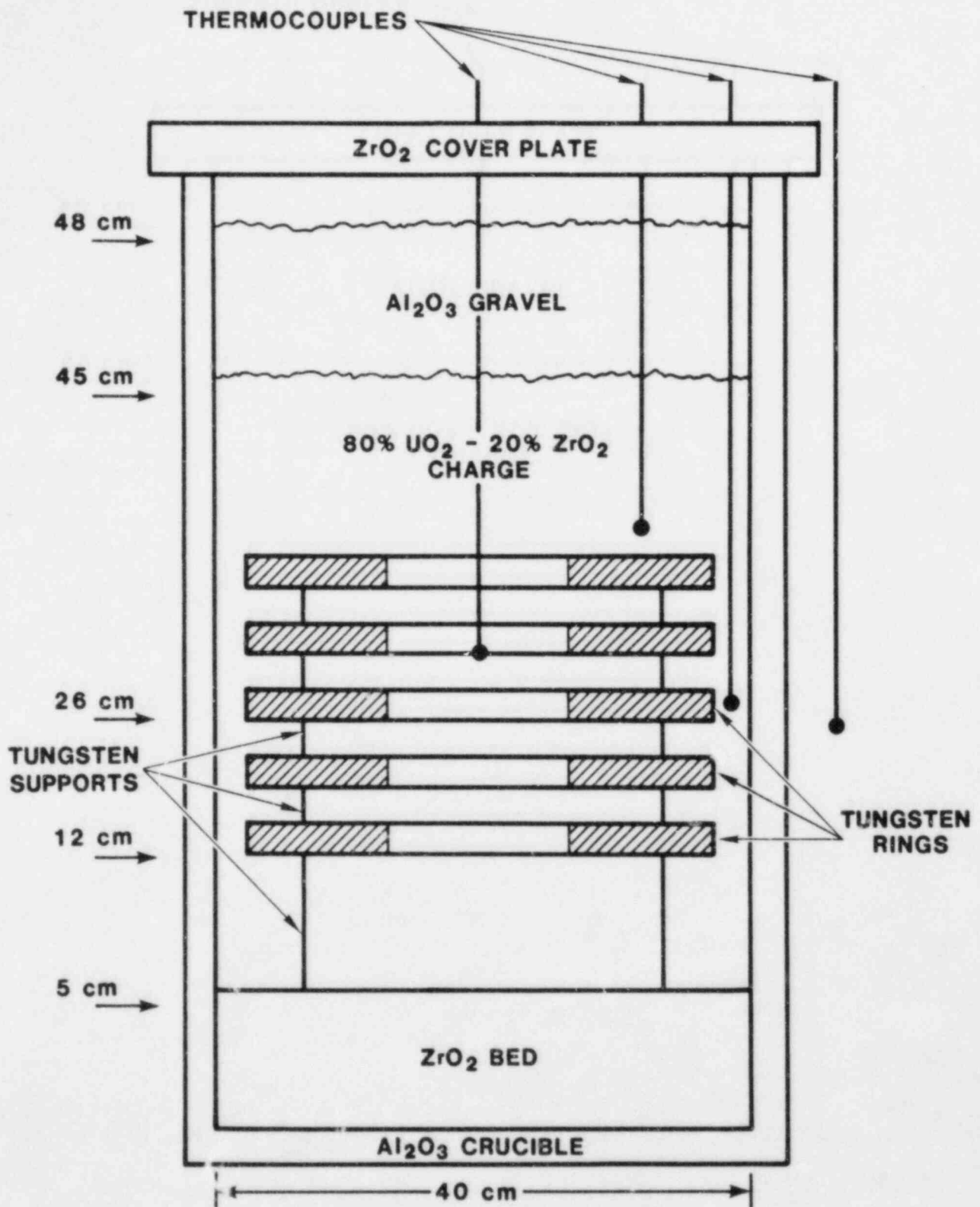
Figure 1.2-9. Design THREE Configuration
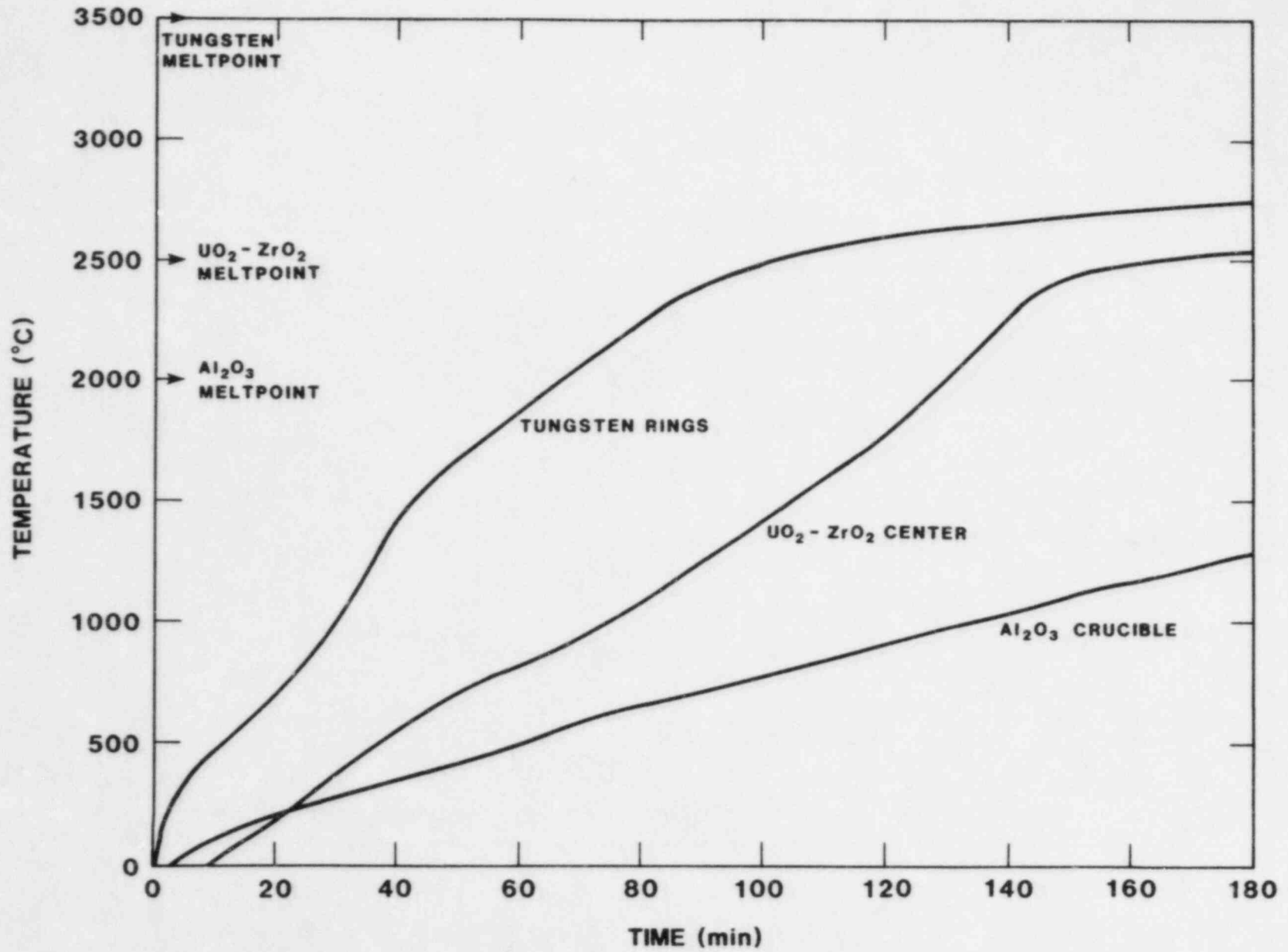
Figure 1.2-10. TAC2D Thermal Analysis for Design THREE (340 kg charge, 50 kW total power input)

38

Gap between crucible and ring: 2.5 cm

Heat losses at 60% melt: 25   kW (50%)

A comparison of the three scaled-up designs shows that all three
have overall input-heat-transfer characteristics which are similar to
the medium scale design, and that all three have considerably better
heat loss characteristics than the previous SOT experiments. For the
medium-scale experiment, the ratio of "input surface area to charge
volume" was 1:7 and the ratio of "input surface area to heat-loss
area" was 1:4. Each of the three scaled-up designs has an "input
surface to volume ratio of 1:6 and an "input area to loss area ratio
of 1:1. Consequently, all three scaled-up designs lose much less of
the input power at 60% melt than the medium scale design does. This
allows for a fast melt at a relatively low power density (0.2 kW/kg).
All three designs will provide about 150 kg of molten UO_2 in about
three hours, as Figure 1.2-11 shows. A comparison of the tungsten
ring, UO_2 centerline, and Al_2O_3 crucible at that time favors Design
THREE slightly over Deisgn ONE as the optimum configuration. Design
TWO is unacceptable because the center of the UO_2 is still quite solid
while the crucible has begun to melt. (See Table 1-VIII.)

TABLE 1-VIII

Design Temperature Profiles at Three Hours

	Design ONE	Design TWO	Design THREE
Tungsten Ring (M.P. 3600°C)	3000°C	3400°C	2750°C
UO_2 Center (M.P. 2500°C)	2900°C	2450°C	2500°C
Al_2O_3 Crucible (M.P. 200°C)	2000°C	2600°C	1250°C
Percent UO_2 Melt	80%	55%	75%

At three hours, the Design ONE configuration had reached its
maximum potential of 80% melt (160 kg) while Design THREE was at 75%
of its maximum melt of 200 kg. The increased gap between the ring and
crucible wall allowed the alumina crucible to be cooler in Design
THREE at the expense of a quicker, more complete melt which could be
achieved with Design ONE. This feature of reduced thermal shock to
the UO_2 containment will assure an adequate safety margin for a large
scale experiment and is the deciding factor for Design THREE over
Design ONE or Design TWO.
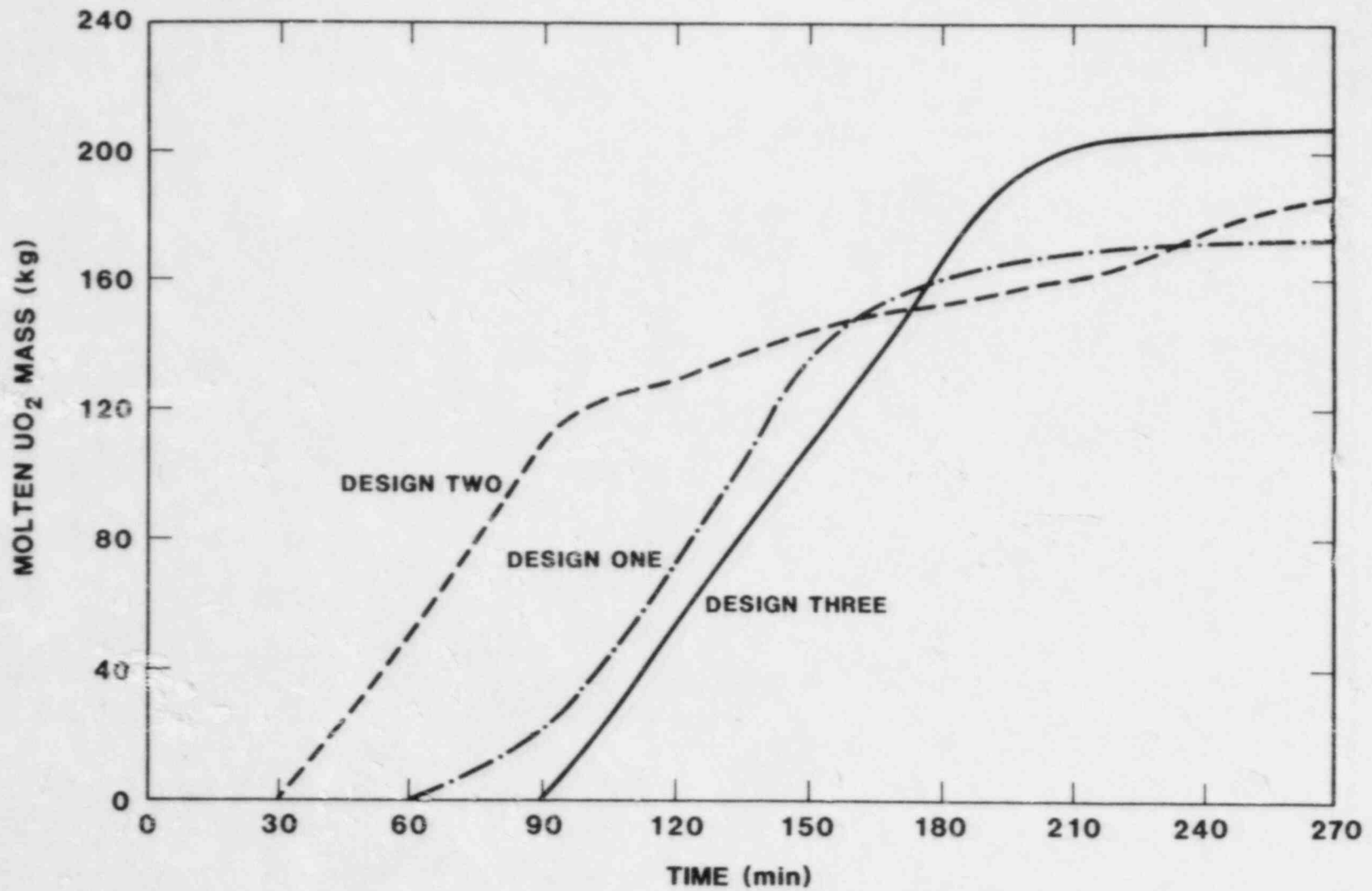
Figure 1.2-11. Mass of UO_2 - ZrO_2 Melt vs. Time

1.2.3.2 Ring Susceptor Tests at the LMF

A series of experiments, in which 304 stainless steel* rings were heated in the LMF coil, demonstrated the feasibility of the IRIS design described above.

Three sizes of rings were used: 50.8-cm OD/35/6-cm ID, 35.6-cm OD/20.3-cm ID, and 25.4-cm solid. All rings were 3.6 mm thick. Experiments were carried out with one, two, and five rings. Each ring was instrumented with four Chromel-Alumel thermocouples except for the five-ring tests in which only the top three rings were instrumented. Thin-walled stainless tubing served as supports to separate the rings by 7.5 cm. The ring structure was centered in an induction coil with a height of 94 cm and an inside diameter of 78.7 cm. A silica-alumina blanket, 5.1 cm thick insulated the ring assembly. Figure 1.2-12 is a schematic of the test configuration.

In each experiment, the furnace power was set and the temperature of the rings monitored. The four thermocouples provided an average temperature for each ring. Typical results are shown in Figures 1.2-13 and 1.2-14. The temperature rise below 873 K was essentially linear, indicating that the heat loss was small. Assuming adiabatic conditions, a value for the power to the rings can be calculated. Comparison of this value to the power at which the furnace power supply is set yields an efficiency for the configuration.

The general trend (see Figure 1.2-15) is increasing efficiency with increasing ring diameter and increasing number of rings. The results also indicated that the efficiency scales approximately with the square of the ratio of the diameter of the ring to the diameter of the coil. Applying these results to Design THREE above gives an efficiency of 50%.

The LMF power supply is rated at 280 kW. At 50% efficiency, the available power is well above the 50 kW on which the Design THREE calculations are based.

1.2.4 Crucible Assembly for LMF Applications

The LMF test of 27 May 1982 is scheduled to be rerun in April 1983. To reduce the probability of crucible failure, a tungsten liner will be included in the crucible assembly. Two methods for producing the liner are under consideration: plasma spraying and chemical vapor deposition (CVD). Manufacturing details for the two techniques are presented below.

1.2.4.1 Plasma Sprayed Tungsten Liner

One full-size graphite mandrel and two half-size graphite mandrels were ordered. Project personnel have designed the associated fixtures for mounting the mandrel in the G. E. low pressure spray facility and the fixtures are being fabricated.

---

*In the temperature range 273 to 873 K, 304 stainless has similar resistance characteristics as tungsten in the range 2273 to 3273 K.
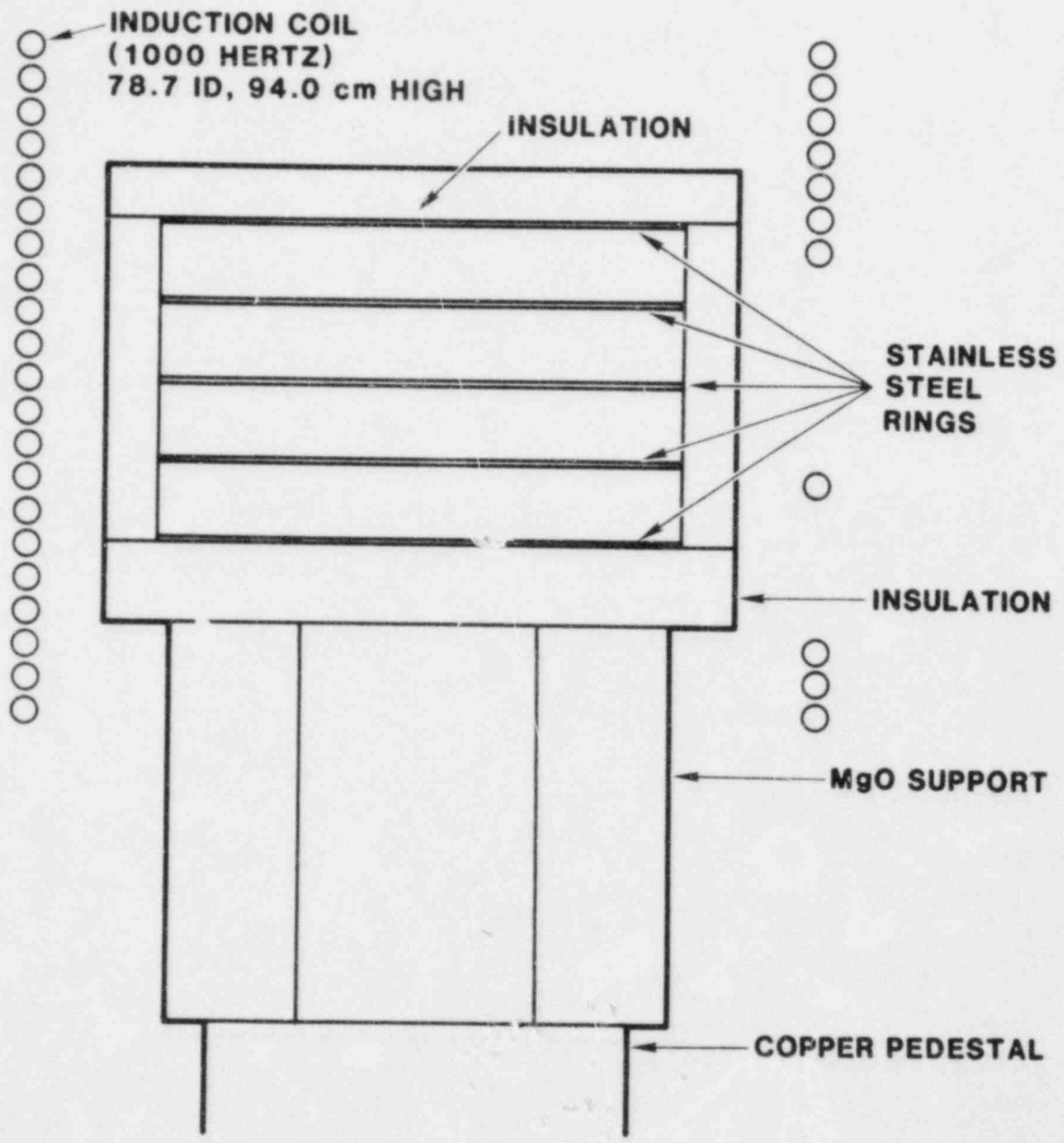
Figure 1.2-12. Susceptor Ring Test Setup
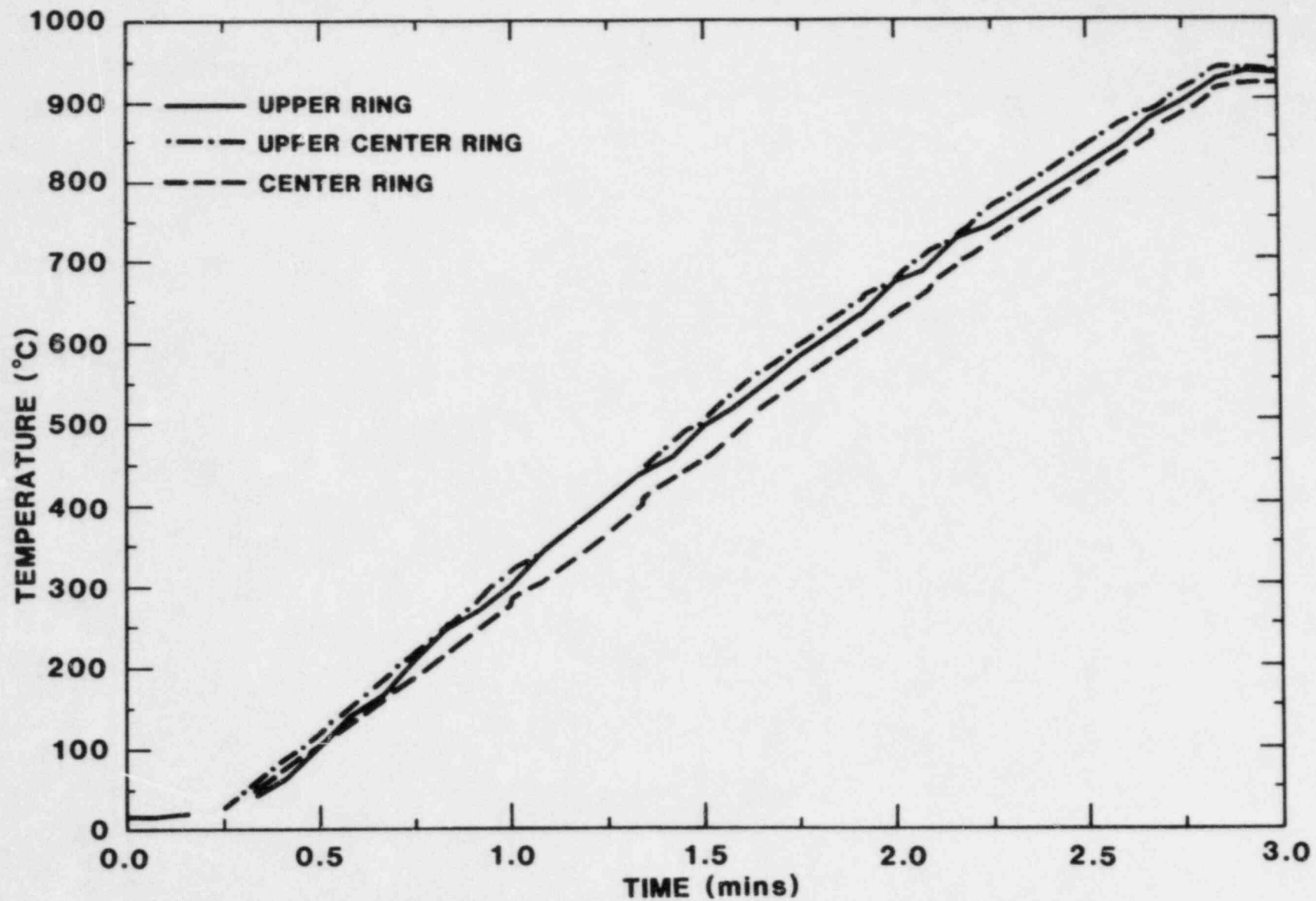
Figure 1.2-13. Susceptor Ring Test, 35.6-cm O.D., 20.3-cm I.D.
(Power = 100 kW, 5 rings)

43
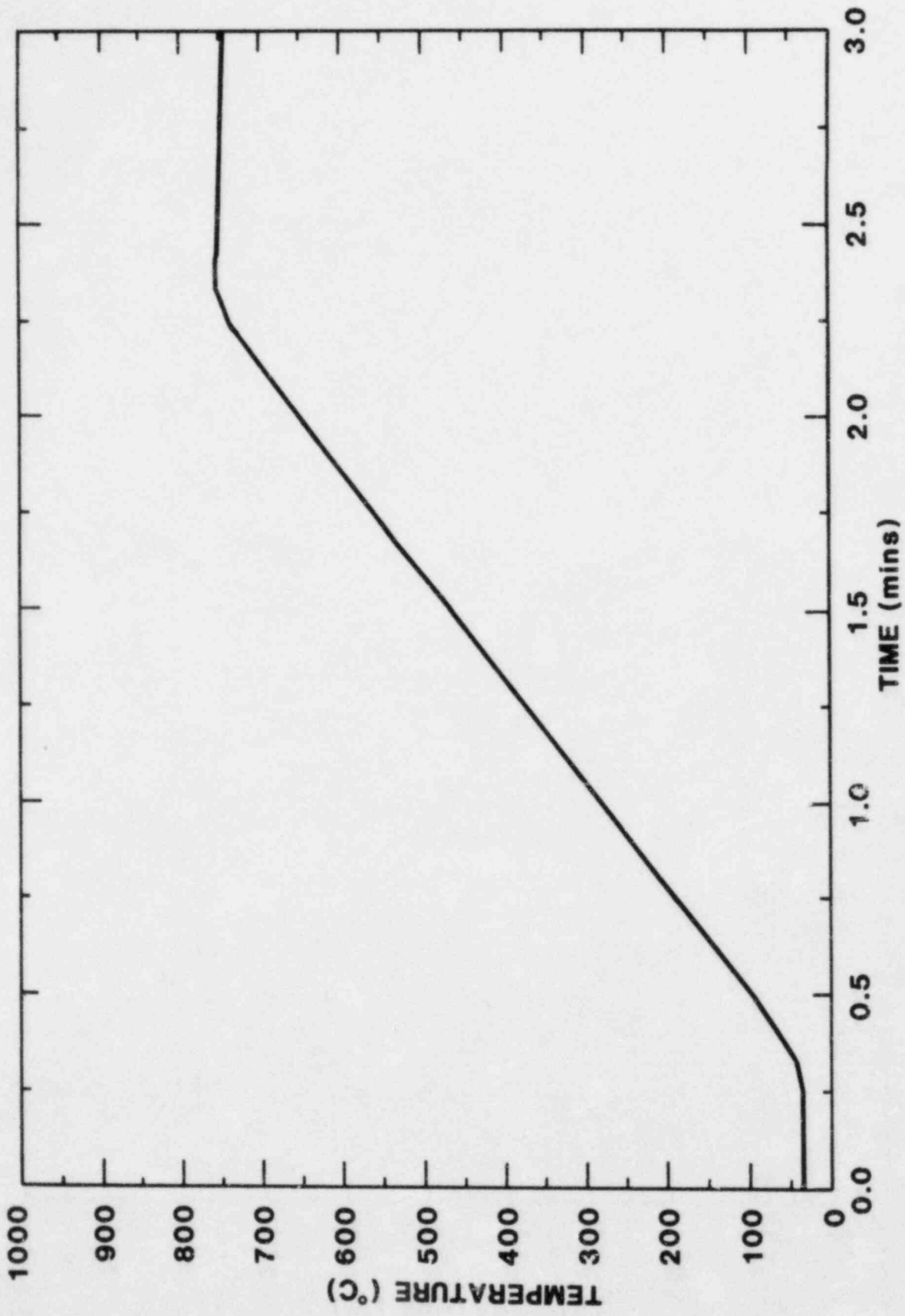
Figure 1.2-14.   Susceptor Ring Test, 50.8-cm O.D., 35.6-cm I.D.
(Power = 100 kW, 5 rings, Center Ring Average)
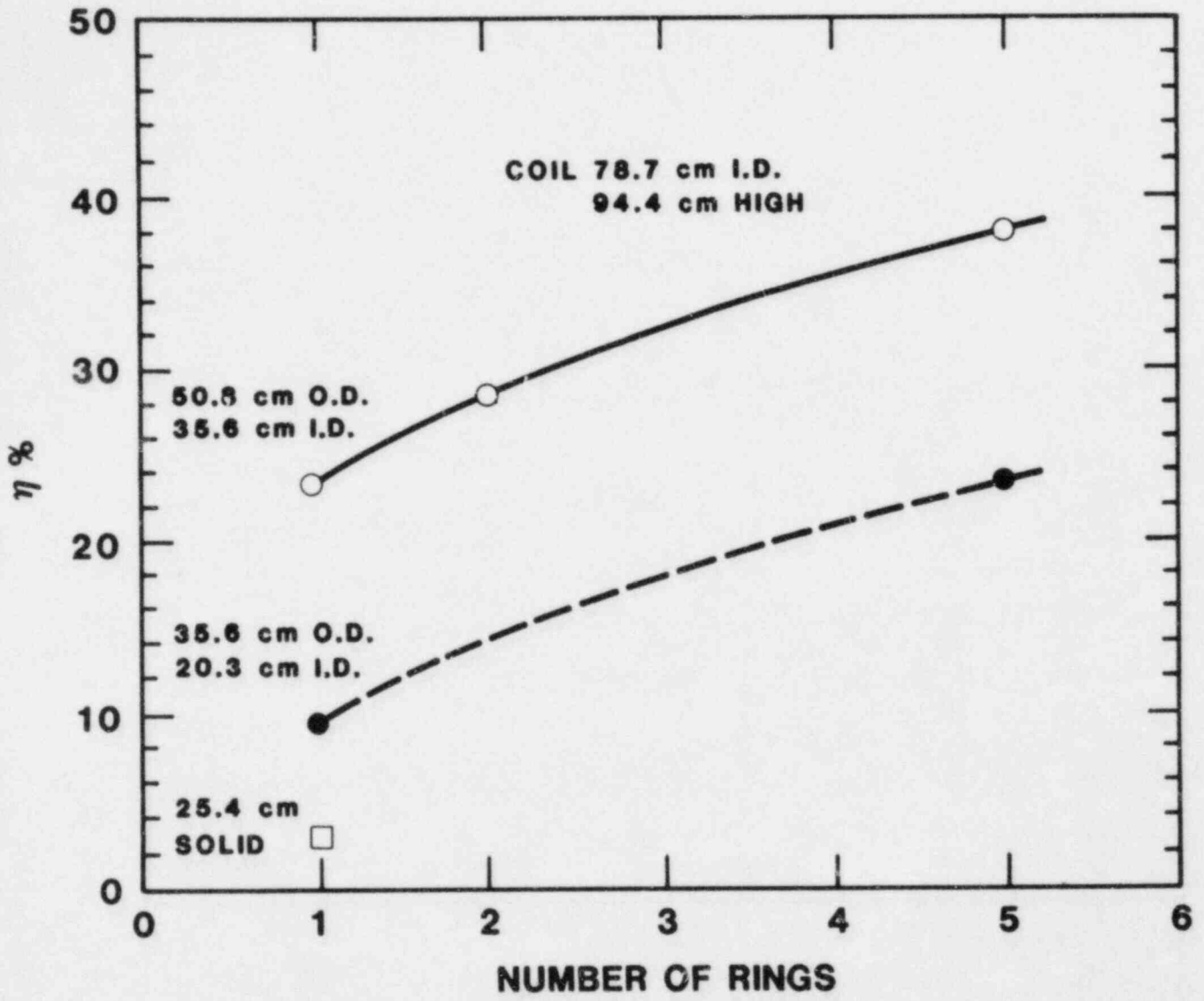
Figure 1.2-15.   The General Trend of Efficiency as a Function of Ring Diameter and Number of Rings

To make the liner, the mandrel must be pre-sprayed with ZrO_2 as a barrier against carburization of the tungsten spray. ZrO_2 was sprayed onto graphite in two practice runs at Sandia. One run used a 7.6-cm-diameter graphite cylinder and the other used a cylinder of 12.7-cm diameter. In both cases, the sprays were about 1.5 mm thick. The sprays adhered well to the graphite. The sprays were also heated to 1273 K (1000°C) in a furnace to simulate the thermal environment during the tungsten spray. Again, the sprays were satisfactory. Investigators observed no cracking or delamination. The next step will be to spray tungsten on these specimens.

1.2.4.2 CVD Tungsten Liner

The liner will be made by depositing tungsten on a male molybdenum mandrel. The mandrel has the shape of the inside configuration of the liner. The cylindrical portion of the mandrel is rolled from sheet stock, and the bottom hemisphere is deep drawn and machined into final shape. All the joints are riveted butt joints. Figure 1.2-16 is a representation of the mandrel. The liner is made about 2.5 cm longer than necessary to provide a material specimen for later inspection. The liner is expected to be complete by the end of the quarter and will be shipped to Ultramet for tungsten deposition.
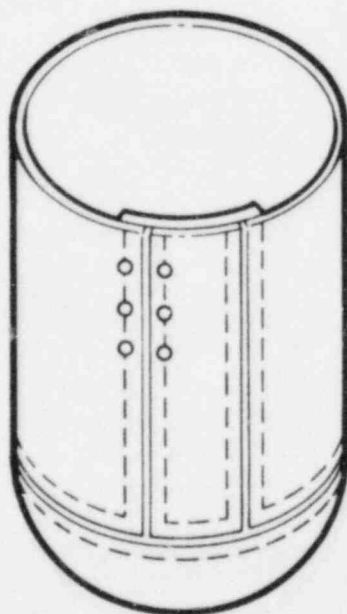
Figure 1.2-16.   The Mandrel

The tungsten will be built up to 1.5 mm in three runs. Between runs, the part will be cooled from the deposition temperature, 1173 K (900°C), to room temperature for inspection and to smooth over abnormal, nodule-like growths. If they were to be left unchecked, these nodular growths would eventually cause regions that would grow independently at a higher rate than the surroundings and would bond only

weakly to the surrounding deposits. After the required thickness is achieved, the liner will be cut to length by mechanical grinding, and the mandrel will be etched away with nitric acid.

1.2.5 Development of Ultrasonic Thermometers (UT)

Two UT reliability tests took place in the LMF. The same two UTs were used in both tests. They were placed vertically in a graphite susceptor block having an 11-in. radius, and in positions diametrically opposite each other at a radius of 8 in. Each UT has seven 1.9-cm-long measured zones. The central zone of each UT was located approximately 10 inches axially into the graphite block. At that location, each UT was instrumented with two tungsten-rhenium thermocouples (TC), one on each side of the UT at the same radius, and each 1/4 inch from the UT. In addition, two pyrometers were used to monitor the susceptor temperature, one along the axis of the graphite cylinder, and the other parallel to the axis at a radius of 9.5 inches. The pyrometer along the axis was focused at a point 20 inches inside the graphite block, representing the location of the bottom of a crucible used in UO_2 melt tests. The side pyrometer was focused at a point 3 1/2 inches inside the graphite block. Tungsten-rhenium TCs also monitored the temperatures at these two locations, for comparison. The basic UT-sensor design and electronics system are essentially identical to those used in previous tests. However, one UT was prepared using Sandia's normal cleaning procedure, and the other using a cleaning procedure similar to one that HEDL uses for high reliability, high temperature thermocouples. The details and encouraging results are discussed later. Improvements in the electronics and their performance follow.

Problems which occurred earlier with the servo systems not maintaining a locking condition with the corresponding signals from the UTs have been corrected. This was accomplished by replacing the integrated circuit operational amplifier used in the integrator with one of different design and manufacture. A redesigned preamplifier and RF-noise filter removed all effects of the 1 kHz induction power supply pickup. The signal loss attributable to the input filter was compensated by increased preamp gain at the expense of increased preamp noise figure (which is now near the practical limit achievable). At maximum preamp gain of 40 dB (voltage gain of 100), the output noise is approximately 100 mv, which easily sets the limit for the noise figure of the complete electronics system. The system has operated with the signal-to-noise ratio at the preamp output near unity. Operation under these conditions is undesirable; increasing the output signal from the sensor is the only reasonable alternative. This low signal-to-noise ratio generates a certain amount of data scatter. Fortunately, at high temperatures, where signal attenuation by the sensor material occurs, the sensitivity of the calibration curve increases. At high temperatures, the data from these tests indicate that total scatter from all sources appears to be less than ±50°C. At a temperature hold at 2953 K (2680°C) (as indicated by the UT), the steady-state variation in the UT readings for each segment was observed to be less than ±5°C. This is a good estimate of the effect of noise.

The computer software has undergone many changes to speed up the system and provide maximum useful information in real time during the test. Between each cycle of readings, the recent prior history of each UT is displayed on the CRT for a few seconds without interrupting the data gathering. The data from each element is received in less than three second intervals. The total cycle time for two UTs is about 67 seconds.

In all previous tests, the sensor wire itself has experienced changes, during the tests, which resulted in calibration changes or signal distortion at temperatures about 2573 K (2300°C). This ultimately has been the fundamental problem limiting the usefulness of the UT. Weak or false signals resulting from attenuation or distortion have challenged the performance of the electronics system. Project personnel have observed that false signals which appear presumably because of sensor changes, although small, often effectively override the real signals, causing shifts in servo lock that result in severe errors. In addition, the real signals, although large in amplitude, may suffer distortion, significantly altering the calibration. Investigators believe that these mechanisms, which have yet to be investigated thoroughly, are caused by contamination and impurities, at least in the high temperature regions of the device. Thus, for this test, one UT (UT-1) was fabricated using the normal procedure of solvent cleaning (trichloroethylene, acetone, and methanol (in sequence)), particularly of the high temperature metallic parts. The other UT (UT-2) was prepared using a more intensive procedure that uses different chemicals and techniques. This procedure is similar to that used at HEDL for high reliability, high temperature thermocouples. As Sandia uses it, it involves washing the sensor wire and inside surface of the protective sheath with a mix of Pierce's solution by means of a recirculating loop for 48 hours, followed by an 8-hour rinse with distilled water, followed by 8 hours of washing with very high purity ethanol. These pieces are then baked at 323 K to 673K (150°C to 400°C) for several hours. For both UTs, the thoria spacers were fired above 2473 K (2200°C) in argon and then were fired for several hours at 1373 K (1100°C) in air just before assembly.

The test was performed by increasing the temperature of the furnace at a rate of approximately 500°C/hour with holds of about one-half hour each near 773 K (500°C), 1273 K (1000°C), 1773 K (1500°C), and 2273 K (2000°C). The furnace temperature was then increased at a rate of approximately 250°C/hour with similar holds near 2523 K (2250°C), 2623 K (2350°C), and 2823 K (2550°C). The test then was stopped after about three hours above 2873 K (2600°C) because of failure of the UT cables within the furnace.

Figures 1.2-17 and 1.2-18 show the comparisons of UT-1 and UT-2 with their respective themocouples. During the temperature ramping period, the thermal response of the UTs shows a noticeable lag of up to 50°C with reference to the TC temperatures. the temperature hold periods are noted as the small circles in the plots, and these are interpreted to be caused by this temperature lag. Apparently, the temperature lag is significantly less for UT-2, although the reason is not definitely known at this time.

48

Figure 1.2-17. Thermocouple Temperature vs. UT-1 Corresponding
Element Temperature. Ideal agreement indicated by
straight line.

49
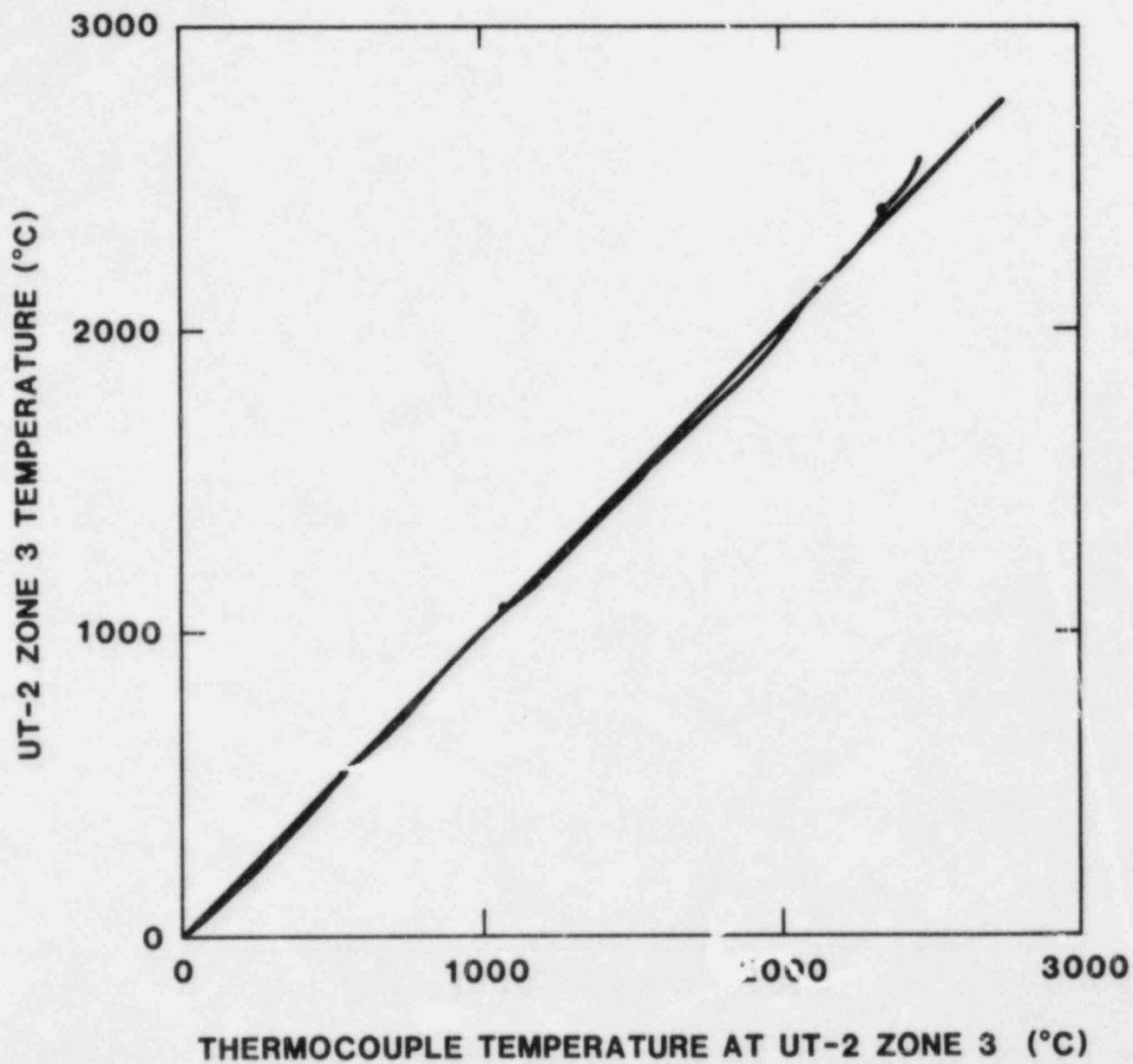
Figure 1.2-18. Thermocouple Temperature vs. UT-2 Corresponding Element Temperature. Ideal agreement indicated by straight line.

At the steady-state temperature regions (hold points) below 2473 K (2200°C), the agreement between the UTs and their TCs is certainly within 50°C. UT-2 is significantly better than UT-1. The largest deviation occurs only at low temperatures in UT-1. In this temperature range, the UTs agreed with each other in the central zone to within 10°C. Note that the agreement between the four TCs used to monitor the UTs was sometimes no better than 40°C.

In Figures 1.2-17 and 1.2-18, the agreement above 2523 K (2250°C) is worse because of degradation of the thermocouples. Also, at this point, as expected from previous tests, UT-1 began experiencing signal degradation, and the deviations were larger than for UT-2. Above 2523 K (2250°C), the agreement between UTs was typically 40°C.

Figure 1.2-19 is a comparison of the side pyrometer and UT-2. the pyrometers presented difficulties throughout this test. At the steady state points near 2273 K (2000°C), 2523 K (2250°C), and 2623 K (2350°C), UT-2 typically agreed with the side pyrometer (viewing through clean windows) to within 25°C. Perfect agreement would not be expected, however, because the temperature monitored by the pyrometer is at a different depth and radius than the UT.

The sudden shift of the curve to the left at 2823 K (2550°C) could result from pyrometer changes or calibration changes within UT-2. UT-2 was heat-treated only to 2823 K (2550°C) for one-half hour and calibration drift was expected (and indeed was confirmed after the test) above this temperature. However, the sudden shift to the left may also have been caused by a pyrometer problem. Disregarding this sudden shift, clearly some upward calibration shift of the UT occurred.

Figure 1.2-20 is a comparison of the performance of the two UTs. Note that different thermal lag is evident at the steady-state temperature points; the reason is not known at this time. Above 2573 K (2300°C), some unpredictable behavior is evident. The sudden change above 2923 K (2650°C) is believed to be the result of the calibration change of UT-2 caused by heating above the heat-treat temperature, fortuitously bringing it into better agreement with UT-1 which was heat treated near 2973 K (2700°C).

The erratic behavior between 2573 K and 2923 K (2300°C and 2650°C) is believed to result from sensor-material changes occurring in UT-1. During this time, distortion and unknown reflections appeared on UT-1. These distortions changed with time and are believed to have been caused by impurities or contamination on the sensor wire. Staff members were encouraged to note that much less difficulty was experienced with UT-2, presumably because the sensor was much cleaner. Some minor changes did take place in UT-2, however.

Even in the region of unpredictable behavior, the largest deviation in the readings is about 75°C. In all further experiments, the cleaning procedure used for UT-2 will be used until its effectiveness is verified. Project personnel anticipate that the erratic behavior will be significantly reduced.
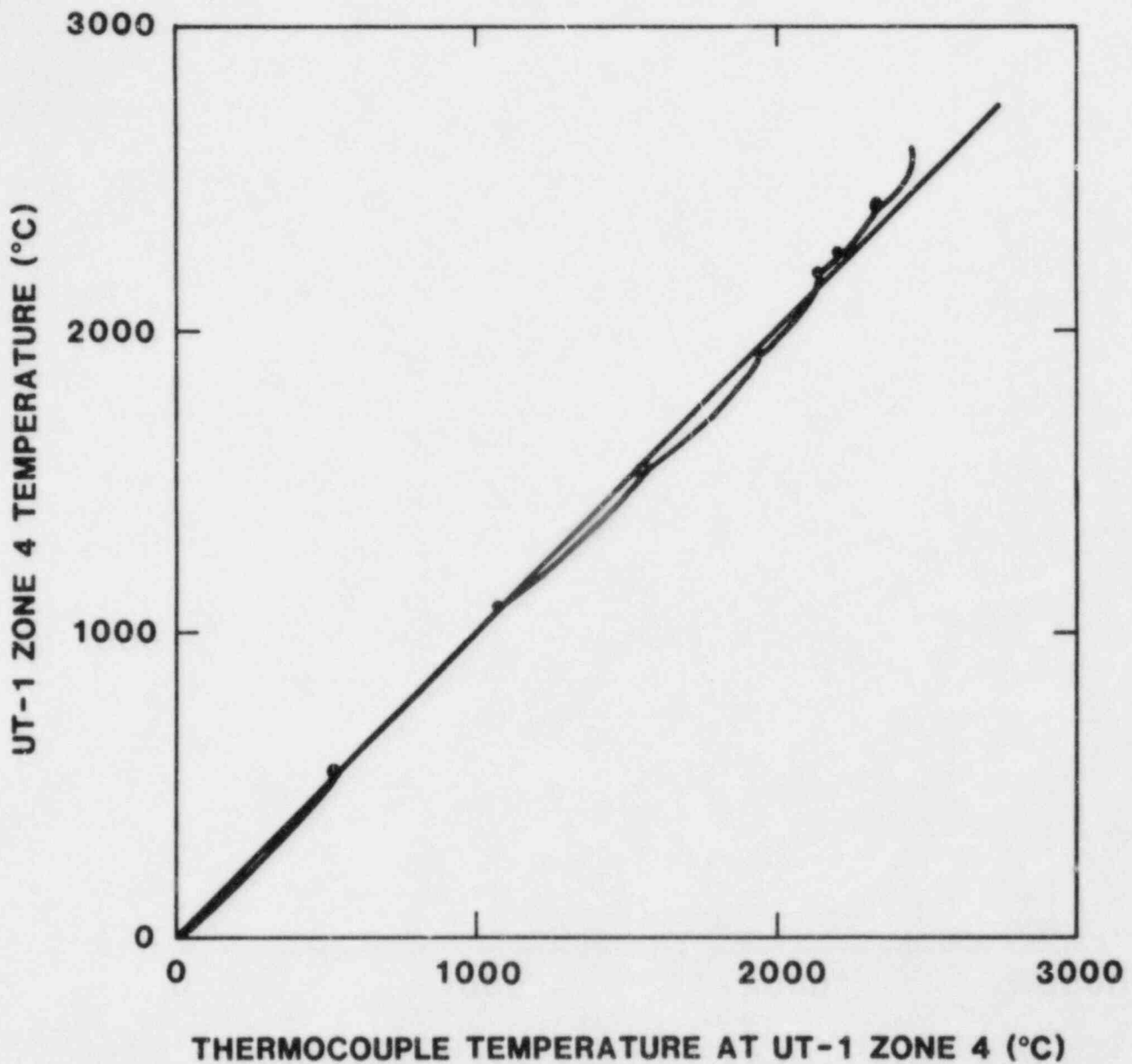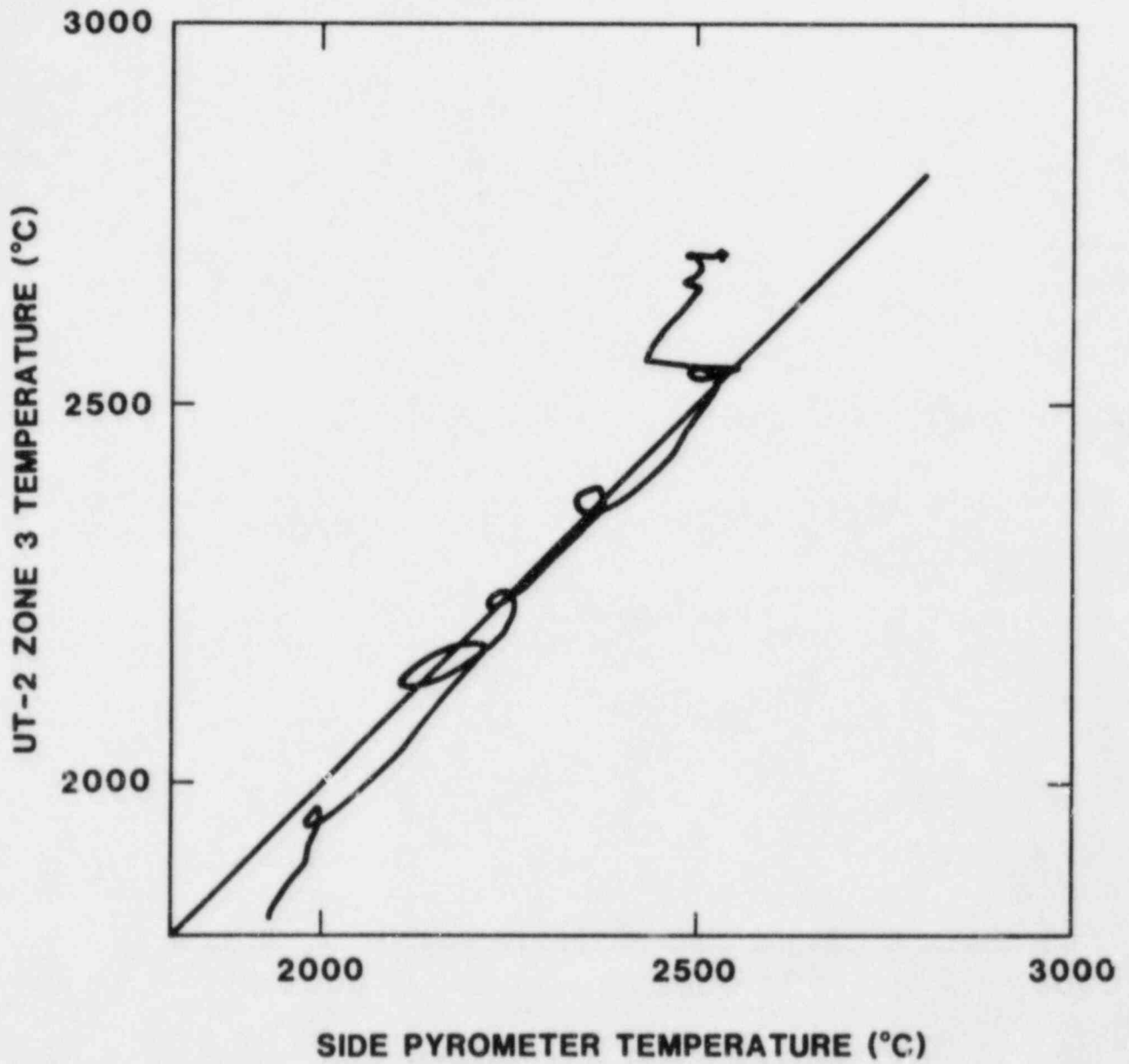
Figure 1.2-19.   Pyrometer Temperature vs. UT-2 Corresponding Element
Temperature.   Ideal agreement indicated by straight
line.
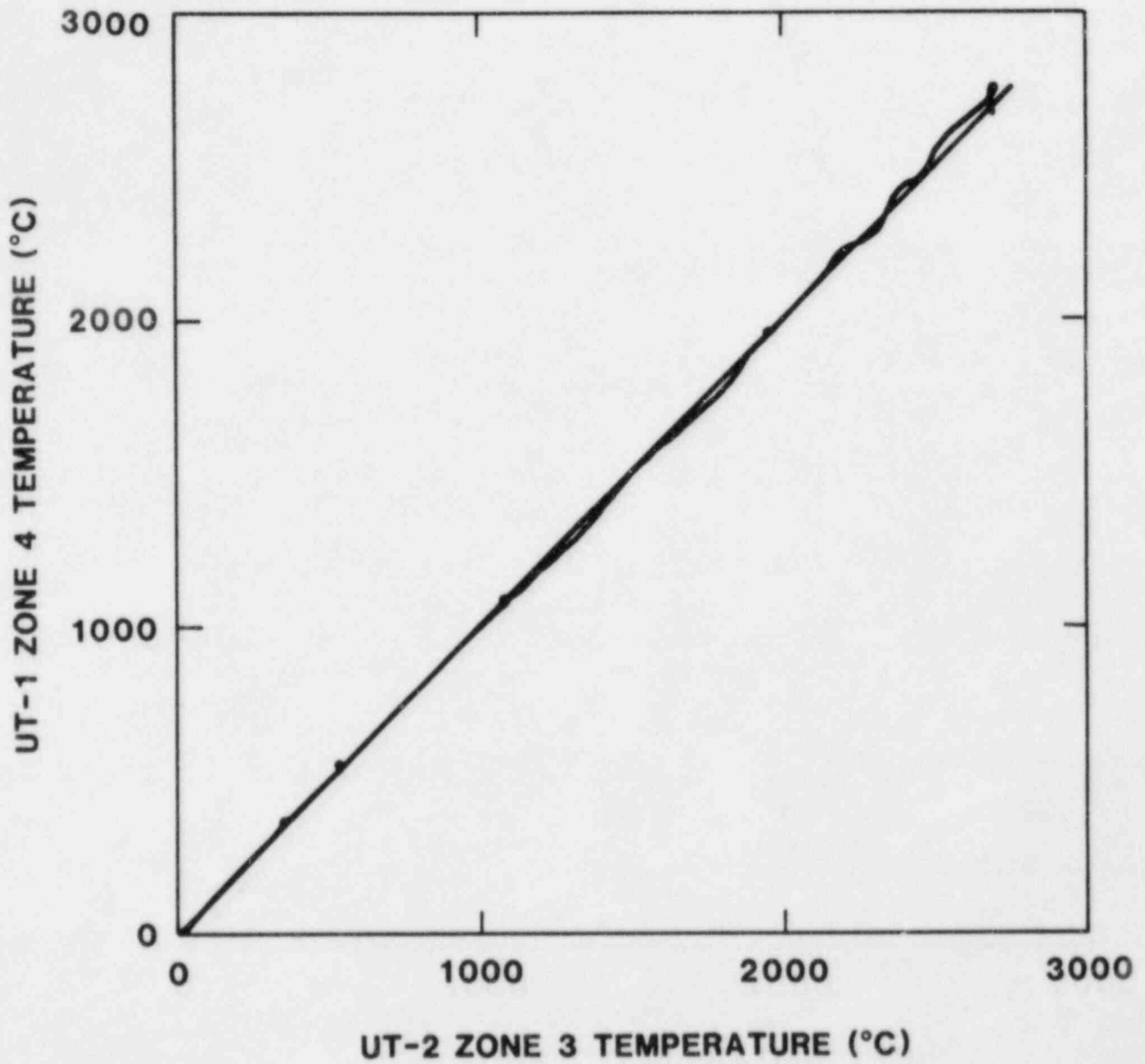
Figure 1.2-20.   Temperature Comparisons, UT-1 vs. UT-2.   Ideal agreement indicated by straight line.

After the cable failures (insulation melted), the furnace was allowed to cool for several days to room temperature. Upon replacement of the cables with high temperature cables, the room temperature calibration was checked. A drift was detected corresponding to a velocity change of 2 percent, corresponding to a temperature drift of about 150°C in the high temperature range (>2300°C). This drift will be alleviated by heat-treating the sensor at higher temperatures for longer periods of time in the future.

A check also showed that UT-2 had five notch signals that were very good while the rest were deteriorated and of questionable value. However, UT-1 had only four notch signals which were detectable, and all were somewhat deteriorated. The remaining notch signals were completely undetectable. In both cases, signal deterioration appeared at the bottom end of the sensor, and progressed up the sensor but to a decreasing degree. The mechanism producing this effect is not known at this time. In any case, UT-2 was vastly superior to UT-1.

A week later, the UTs were rerun without having disturbed the experimental arrangement resulting at the end of the first test. A temperature-time history similar to the earlier run was used. Both UTs were held at 2773 K (2500°C) for more than six hours. UT-1 underwent progressively severe deterioration, but UT-2 showed only slow deterioration. Data for this last test have not yet been analyzed and a room temperature check of the system calibration must still be performed. The latter will be a test of the theory that higher temperature, longer-duration heat-treatment (more crystallization) of the sensors, as occurred during the first test, is necessary.

Investigators believe that the cleaning procedure used for UT-2 will alleviate severe problems previously encountered with the UTs. Further, they believe that they can use slightly deeper notches successfully, if the sensor holds together, to increase the system signal-to-noise ratio, thereby reducing some of the data scatter.

These rerun tests indicated that temperature measurements above the 2873 K (2600°C) range can be performed reliably with the UT with errors of less than ±50°C.

1.3 Sodium Containment and Structural Integrity
(E. Randich, 6422; R. U. Acton, 7537; A. Suo-Anttila, 6425; H. R. Westrich, 1543; H. W. Stockman, 1543)

1.3.1 Introduction

The Sodium Containment and Structural Integrity program is an investigation of safety phenomena that will develop should molten sodium contact structural or shielding concrete during a reactor accident. Quantitative evaluation of these phenomena, leading to the development of models for use in predicting the ways in which these phenomena might threaten the reactor containment, is a major goal of this program. Quantitative evaluation of structural flaws in reactor cell liners is also sought in this program because these flaws can provide pathways for sodium to contact concrete.

54

This program has shown that sodium/concrete interactions proceed in two phases. The first phase is relatively mild and is character-ized by the reaction of water from the concrete with sodium to yield hydrogen and NaOH. The second phase of the interaction is more ener-getic and involves erosion of the concrete as well as hydrogen generation.

When sodium first contacts the concrete, the interaction is relatively mild and consists mostly of the reaction of water from the concrete with sodium. At the temperatures and hydrogen partial pres-sures encountered in the experiments, the condensed product of re-action is NaOH, which is partially soluble in sodium. After this mild phase of interaction has progressed for a while, it abruptly evolves into a very energetic interaction in which concrete is actually eroded. During this energetic phase, sodium pool temperatures rise to near boiling.

During this quarter, work in the Sodium Containment and Struc-tural Integrity program fell into the following categories:

a. Completion of a predictive computer model of sodium inter-actions with limestone concrete (SLAM).

b. Laboratory-scale studies of the chemical processes that occur between sodium, sodium hydroxide, and limestone concretes.

c. Posttest analysis of the HEDL/Sandia AA/AB tests which compared sodium interactions with calcite and dolomite concretes.

d. Preparation of a topical report outlining the results of two large-scale tests which examined the interaction between molten sodium and magnetite concrete.

1.3.2 Sodium/Limestone Concrete Ablation Model

The basic version of the sodium/limestone concrete ablation model (SLAM) was completed this quarter with the inclusion of variable thermal conductivity. As reported last quarter, SLAM is a predictive code which requires only material properties and initial conditions as inputs. Additional work must still be done to adjust internal emperi-cal parameters in the code for proper results. These parameters will be adjusted in the near future in conjunction with laboratory-scale tests now being performed.

The variations in thermal conductivity for sodium/concrete abla-tion problems can be very large. The extreme values range from the high conductivity of liquid sodium (approximately 50W/m.k) to the low conductivity of hot dehydrated concrete (0.2W/m.k). Even lower ther-mal conductivities are possible if vapor-phase reactions occur. Variable conductivities must be used in SLAM if the proper chemical response of the system is to be calculated.

The rate of chemical reaction, and the consequent heat production, is a function of the reactant concentration and the temperature. If the thermal conductivity is high, such as when a significant amount of liquid sodium is present, then any heat that is generated will be conducted away rather than causing a temperature rise. In contrast, if the thermal conductivity is low, high temperatures and reaction rates will result, possibly leading to reactant depletion which terminates the interaction. Thus, the behavior of the sodium concrete interaction is very sensitive to the thermal conductivity of the reaction zone.

The thermal conductivity of the reaction zone (boundary layer) is a function of the materials present. In turn, the materials that are present depend upon other phenomena such as chemical reaction, diffusion, and the ablation rate. Thus, changing a single parameter, such as the diffusion coefficient, can lead to a calculated behavior that is significantly different than what may be expected.

Several calculations have indicated that the response of the sodium/concrete interaction is very sensitive to the mixture rule that is used in calculating the thermal conductivity. Several mixture rules have appeared in the literature, however, project personnel do not know if the rules apply to the case at hand.

The current version of SLAM uses a simple-volume-fraction, α_i, weighting method of calculating the thermal conductivity. Initially the following formula was used:

$$K_{mix} = \sum (\alpha_i (K_i + \tau \rho_I C_i))$$

where

α_i is the volume fraction of material i

K_i is the thermal conductivity of material i

ρ_i is the macroscopic density of material i

C_i is the specific heat of material i

τ is the diffusion coefficient.

The term $\tau \rho_i C_i$ accounts for the turbulent mixing of the materials. This term assumes that the turbulent Schmidt number is equal to unity.

The result of using the volume-fraction weighting formula above was that the liquid sodium dominated the thermal conductivity and kept the thermal conductivity of the system significantly higher than the conductivity of the concrete. Calculations indicated that temperatures never rose more than a few degrees above the pool temperature regardless of the chemical reaction rate. However, the experimental data indicated that temperatures sometimes exceeded the boiling point of sodium and were often several hundred degrees higher than those in the pool. Investigators concluded that a method using materials in

parallel was not the correct method during the active part of the concrete ablation.

An alternative to the above method is a method using materials in series, i.e.:

$$K_{mix}^{-1} = \sum \frac{1}{\alpha_i (K_i + \tau \rho_i C_i)}$$

This formula yields better results because the low conductivity materials tend to dominate during the active part of the ablation, and hence higher temperatures are predicted.

At the present time, the best rule, or combination of rules, is not known. Because the model is still being verified, the final set of mixture rules that is used in the computer code may be modified somewhat from the series rule.

1.3.3 Laboratory-Scale Tests with Limestone Concretes

Investigators ran 22 additional laboratory-scale sodium/concrete tests during this quarter. The tests placed emphasis on evaluating the following effects upon the sodium/concrete reaction: (1) dehydration (water content) of the reactants, (2) particle size of the reactants, (3) heating rate, and (4) fluxing effect of sodium hydroxide. Project personnel are preparing a topical report describing the detailed findings of these experiments; a synopsis of the results follows.

1.3.3.1 Effect of Dehydration on Sodium/Concrete Reactions

The reaction between sodium and water to form sodium hydroxide and hydrogen (where water is derived from the dehydration of the cement) was previously postulated to be a necessary precursor of the very exothermic behavior observed at reaction temperatures above 823 ±30 K (550 ±30°C). Several experiments performed this quarter suggest that this reaction is actually subordinate to direct reactions between sodium and the limestone aggregate. Further, several experiments suggest that the presence of water in the cement matrix may actually delay the exothermic sodium/cement reactions. Investigators found that limestone concrete that had been dehydrated at 948 K (675°C) reacted with sodium to produce an exothermic peak in the time-temperature profile. The reaction had a threshold temperature of approximately 773 K (500°C) and a temperature rise of ~300°C above the 873 K (600°C) test temperature. The size of the peak was comparable to the peak produced by hydrated concrete/sodium interactions. Sodium reacting with calcite and dolomite aggregate material alone (with no cement binder) was also found to produce exothermic peaks with threshold temperatures and sizes similar to the peaks produced by hydrated concretes. Investigators suspected initially that the hydrous inclusions in the aggregate materials (e.g., clays, etc.) might be producing the exothermic peaks. Tests with dehydrated aggregate, however, reacted in the same manner as nondehydrated aggregate. Reactions between dehydrated portland cement and sodium produced exothermic peaks

with threshold temperatures of approximately 773 K (500°C). The reaction was less intense than the sodium/limestone aggregate reactions. Project personnel concluded that the presence of sodium hydroxide is not necessary for exothermic reactions to occur.

1.3.3.2 Effect of Aggregate Particle Size

Large limestone and dolomite clasts (> 1-cm diameter) reacted sluggishly with sodium, producing small exothermic peaks with ill-defined threshold temperatures of approximately 873 K (600°C) and maximum temperature rises of 30 to 50°C. Posttest analysis showed that the coarse aggregate clasts were coated with a black material (later identified by X-ray diffraction analysis as sodium carbonate, calcium oxide and carbon) which apparently inhibited the reaction. Finer aggregates (crushed coarse aggregate ranging from 0.08mm to 0.9 in diameter) reacted more completely with threshold temperatures of 808 K to 853 K (535°C to 580°C) and temperature rises of approximately 300°C. The reaction products were largely sodium carbonate, calcium oxide, magnesium oxide, and amorphous carbon. For the dolomite aggregate, some evidence indicated a lowering of the threshold temperature with decreasing particle size from 858 K (585°C) for 0.0-mm to 1.7-mm aggregate to 823 K (550°C) for aggregate of 0.08mm to 0.20mm.

1.3.3.3 Effect of Heating Rate

For internal consistency, all laboratory-scale experiments have been performed at an average sample heating rate of 1.8°C/s between 373 K (100°C) and 773 K (500°C). To test the effect of heating rate on threshold temperature, samples of sized dolomite aggregate (0.20 to 0.30-mm diameter) were heated at 1.8°C/s and 0.6°C/s. The threshold temperature for the exothermic reaction was 833 K (560°C) for the higher heating rate and 803 K (530°C) for the lower heating rate.

1.3.3.4 Fluxing Effect of Sodium Hydroxide

Additional experiments performed during this quarter failed to show any obvious exothermic reaction between molten sodium hydroxide and concrete or limestone aggregate at temperatures up to 943 K (670°C). The molten sodium hydroxide attacked the cement binder readily but had less affect on the aggregate. Slight exothermic reactions were observed, but the extent of these reactions was much less than those noted between sodium and the respective concretes or aggregates at similar temperatures.

1.3.4 Posttest Analysis of the Debris from the AA/AB Tests

Debris samples from the calcite and dolomite AA/AB tests were submitted for chemical and X-ray diffraction analyses. The chemical analyses will include determination of calcium, magnesium, sodium, free carbon, and CO_2. The X-ray diffraction analysis will include the identification of major crystalline phases.

Aerosol samples collected from the vent pipe of the calcite test were analyzed by X-ray diffraction techniques. The aerosol was mostly

metallic sodium. The X-ray spectrum contained only very weak peaks
corresponding roughly to the most intense lines of sodium hydride.
Investigators concluded that the sample contained a small amount (less
than 10%) of sodium hydride.

Project personnel attempted microprobe analysis of debris from
the calcite and dolomite tests. Satisfactory microprobe mounts of the
debris were obtained through careful dry polishing of selected
samples. Microprobe-wavelength dispersive X-ray analysis showed that
sodium hydroxide and sodium carbonate phases could be distinguished
through quantitative sodium analysis. A red-colored phase which was
evenly distributed in the dolomite debris was identified as a dendri-
tic growth of an iron/sodium-rich phase having a sodium/iron ratio of
approximately 3 by weight. Microprobe analysis also verified that the
starting materials were indeed calcite and dolomite. The limestone
clasts contained about 10% clays by volume. The presence of these
clays is noted because they are a potential source of additional water
for reaction with sodium. A topical report containing a detailed
discussion of these analyses is being prepared.

1.3.5 Large-Scale Sodium/Magnetite Concrete Interaction Tests

A topical report entitled Large-Scale Exploratory Tests of
Sodium/Magnetite Concrete Interactions (NUREG/CR--3189, SAND83--0356)
was completed during this quarter. Two large-scale tests examining
the interaction between molten sodium at 825 K (552°C) and magnetite
concrete were performed. In the first test, bare magnetite concrete
was exposed to molten sodium and in the second test, the concrete was
partially protected by a flawed steel liner and a layer of dense
silica fire brick. The results of the tests demonstrated that ener-
getic chemical reactions can occur between molten sodium and magnetite
concrete. In the unprotected concrete tests, reaction zone tempera-
tures exceeded 1150 K (877°C), and the maximum heat generation rate
was $1.3 \times 10^5 J/m^2 s$. The maximum observed penetration rate in this
test was 2.5 mm/min. In the flawed-liner test, the silica fire brick
provided little protection for the underlying concrete. The reaction
debris, which formed between the steel liner and the concrete, caused
gross deformation of the liner and extensive cracking and spalling of
the reinforced magnetite-concrete crucible.

1.4. Debris Bed Coolability
(G. W. Mitchell, 6421; C. A. Ottinger, 6421; J. E. Kelly, 6425;
R. J. Lipinski, 6425)

1.4.1 Introduction

The Debris Bed Coolability program addresses issues concerned
with the deposition of solid fuel debris on horizontal surfaces within
the containment vessel and its subsequent coolability. This debris
remains capable of generating significant power through the decay of
fission products. Should natural processes fail to provide sufficient
cooling, the debris could remelt and threaten containment. The Debris
Bed Coolability program seeks to determine the natural cooling of such
debris. During this period, experiments and analysis of debris bed
studies continued.

1.4.2 Debris Bed Experiment D9 - Results and Analysis

The joint USNRC/JRC(Ispra)/PNC debris bed experiment D9 was conducted October 17-27, 1982 in Sandia's Annular Core Research Reactor (ACRR). Several dryouts at various subcoolings, power-step tests, channel events, superheat flashing events, nonboiling (conduction) control runs, and other tests were performed. These are summarized in Table 1-IX. In most of the categories, the number of events exceeds the combined total of similar events from all previous D-series experiments because of the duration and successful operation of virtually all features of the D9 experiment package. None of the 53 thermocouples failed (in spite of temperatures on some up to 1150°C), the crucible remained intact and well-insulating throughout the experiment, the cover gas expansion tank opened as designed and the capsule pressure decreased with minimal bed disturbance, and three experiment shutdowns and restarts were successful, allowing periods of data assessment and formation of extended experiment test plans. (A dominant factor in the longevity of D9 was the experience gained from the previous experiment (D7) which was the same design as D9). Considerable verification and refinement of ideas on debris phenomena were accomplished, and new regimes of bed behavior were investigated.

TABLE 1-IX

D9 Summary

Sessions	4
Hours of Nuclear Heating	74
Subcooling Range (°C)	70-415
Incipient Dryout Measurements	30
Extended Dryout Measurements	12
Channeling Events	32
Superheat Flashing Events	19
Large Power-Step Tests	28
Nonboiling Control Runs	20
Power/Porosity Calibrations	11
Maximum Power (W/g)	5.0
Maximum Temperature (°C)	1150

1.4.2.1 Experiment Apparatus Description

The objective of the D9 experiment was to investigate the coolability of a shallow, stratified debris bed with an extended UO_2 particle size distribution. The experiment was conducted over a wide range of subcooling (70°C to 415°C) with the capability of low subcooling to aid in the investigation of channeling.

The UO_2 particulate was held in a double walled, insulated crucible suspended from the primary containment cover plate (Figure 1.4-1). To limit the possibility of pressurization of the crucible
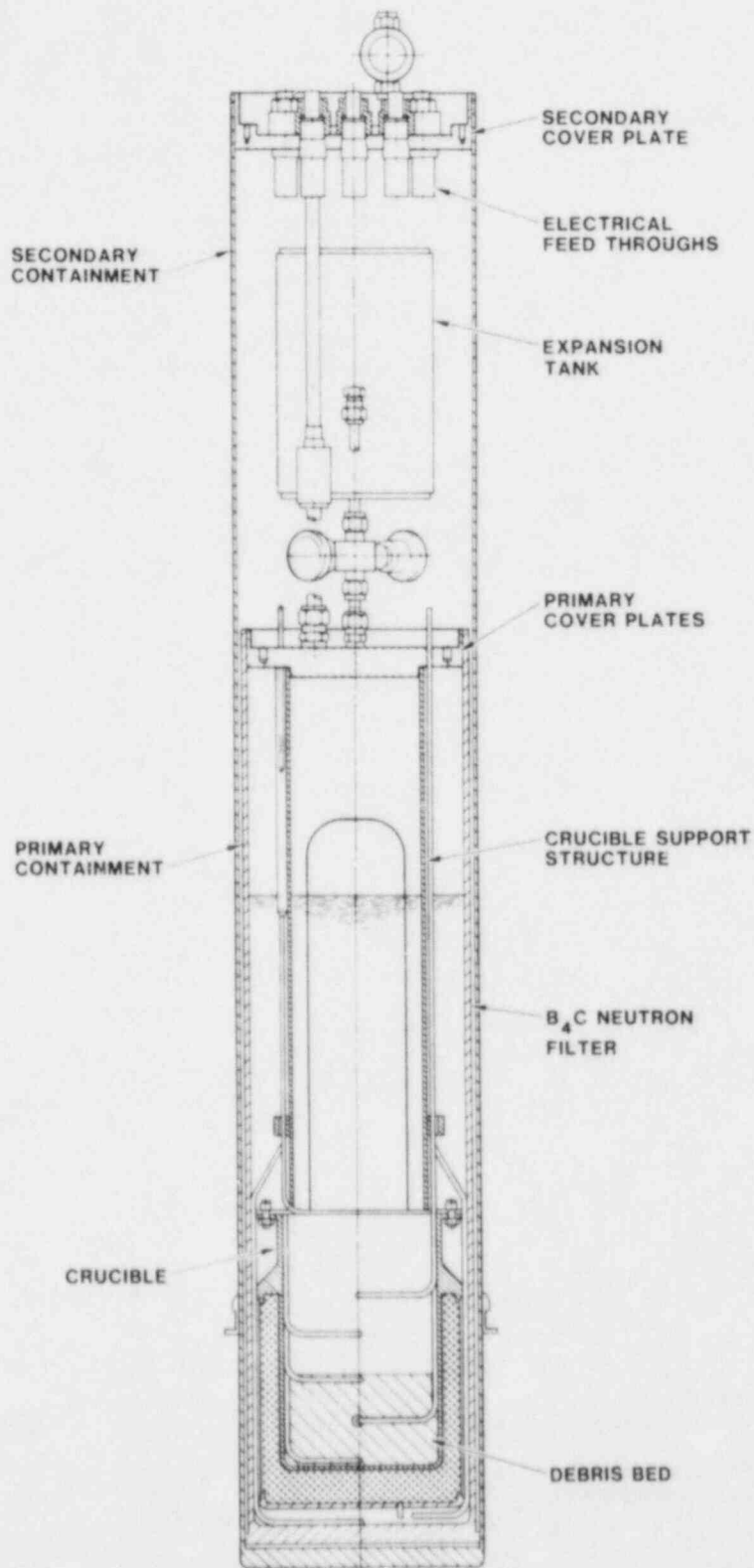
Figure 1.4-1. D9 Primary and Secondary Containment Assembly

caused by water vapor in the insulation, the crucible was baked-out
under vacuum at 973 K (700°C) for 11 hours before it was sealed. The
primary containment assembly served as the primary radiological con-
tainment as well as the sodium containment. During the experiment, an
evacuated expansion tank, which served to reduce the cover gas pres-
sure and extend the subcooling range, was opened to the primary con-
tainment remotely.

Electric heaters were located in the bulk sodium above the debris
bed and served to melt the sodium at the start of the experiment. The
heaters also helped to achieve high bulk sodium temperatures when the
bed was at low powers. These heaters were operational during the
first 13 hours of the experiment.

A secondary radiological containment assembly surrounded the
primary. Powdered B_4C was placed between the containments to harden
the neutron spectrum and flatten the power profile within the debris
bed. A helium cooling system surrounded the secondary containment and
removed heat from the bulk sodium above the debris bed. Insulation
surrounded the helium system to reduce heat losses from the experi-
ment.

The debris bed consisted of UO_2 particulate with an extended size
distribution (particle size ranges from 0.038 mm to 4.0 mm). The
particles were separated into 14 groups and loaded into the crucible
with the largest particles on the bottom. The weight and size of each
group are listed in Table 1-X. Bed porosity was calculated to be
43.5%. After loading, the UO_2 was baked-out under vacuum for 6 hours
at 573 K to 663K (300 to 390°C). The bed height was determined from
X-rays taken following sodium filling and ranged from 80 mm down to 70
mm (where the sodium entered the bed during filling). Other bed
parameters are given in Table 1-XI.

Inconel-sheathed K-type thermocouples provided the primary in-
strumentation for the D9 experiment. Both single- and multi-junction
thermocouples were used in the experiment. The glass-to-metal seals
on the ends of the thermocouples were removed and the thermocouples
were baked-out at 773 K (500°C) under vacuum for 5 hours. (These
actions may have aided in their longevity.) Sixteen thermocouple
junctions were located in the bed at axial locations of 1.5 (B0X), 10
(B1X), 20 (B2X), 35 (B3X), 50 (B4), 65 (B5) mm with respect to the
bottom of the bed. Three thermocouples were located in the sodium
above the bed to monitor bulk sodium temperatures. Five were located
in the sodium surrounding the crucible to monitor heat losses radially
and downward from the bed and to monitor containment boundary tempera-
tures. Eighteen thermocouple junctions were located in the insulation
around the helium chamber and next to the outer shell to monitor heat
losses from the experiment. Eleven more TC's were located elsewhere
in the package.

The thermocouple data were scanned at 5 s intervals for real-time
display and for storage on an HP-1000 system. The data were sampled
at 1 s intervals by an analog-to-digital converter and stored on a
disk by an HP-9845B computer.

TABLE 1-X

D9 UO$_2$ Loading

Particle Size Range (μm)	Mass of UO$_2$ (g)	Height to Top of Layer (mm)	Layer Depth (mm)
2800-4000	126	3	3
2000-2800	165	8	5
1400-2000	228	11	3
1000-1400	273	16	5
710-1000	322	21	5
500-710	364	29	8
355-5( )	374	37	8
250-355	378	44	7
180-250	326	53	9
125-180	318	58	5
90-125	238	65	7
63-90	199	69	4
45-63	133	72	3
38-45	56	75	3

TABLE 1-XI

D9 Bed Characteristics

Height (mm)	70-80
Average Porosity	0.435
Diameter (mm)	101.6
Mass of UO$_2$ (kg)	3.500
Density (kg/m^3)	5645.
Loading (kg/m^2)	432.
Power Coupling (W/g/MW$_{ACRR}$)	2.50

63

1.4.2.2 Experiment Operation and Overview

The experiment was conducted over the period October 17-27, 1982 with approximately 74 hours of nuclear heating and 30 dryout investigations. The experiment was conducted in 4 sessions. The first session, October 17-18, investigated incipient dryout as a function of sodium subcooling. Subcoolings as low as 70°C were achieved after the evacuated expansion tank was opened. Dryout occurred near incipient boiling, with incipient dryout powers of 0.10 to 0.64 W/g. The second session, October 19, investigated the effect of large rapid powers steps (up to 2.5 W/g) on the dryout powers. These step changes had minimal effect on the incipient dryout powers. The third session, October 21-22, investigated extended dryouts to a maximum temperature of 1423 K (1150°C), and superheat effects. Repeatable channel formation, which decreased the dry zone thickness, was observed. After prolonged boiling, a large-superheat flashing event (approximately 90°C) was triggered. Following this event, the dryout power was 4.4 ±0.6 W/g. The fourth session, October 26-27, investigated superheat phenomena. Superheat was achieved following boiling in the bed. Large power steps produced only small (approximately 20°C) superheat flashes.

1.4.2.3 Session 1

The first session was concerned basically with investigating the incipient dryout powers and channeling behavior of stratified debris beds. As in all sessions, calibration and control runs were made first in order to define the bed power and geometry. After these runs were completed, incipient dryout measurements were made for a wide range of subcoolings. While some channeling may have occurred during these studies, the dryout power remained quite low (<0.64 W/g). Following the dryout study, the bed was heated rapidly using relatively small power steps. The rapid heating, which simulates the heating of an actual debris bed upon formation, caused channels to form, but dryout still occurred.

a. Session 1 Bed Power Coupling Determination

The specific power of the fuel (W/g-UO$_2$) relative to the ACRR power may be determined by the heat-up rate of the bed in response to a step increase in power. Eleven such power calibrations were performed during the experiment (sometimes in conjunction with a large power-step test), always starting from a near-steady-state nonboiling condition. The initial calibration test resulted in a coupling of 2.50 W/g-UO$_2$/MW$_{ACRR}$. This value remained constant throughout the experiment. Future analysis of the subsequent step tests may yield information about changes in bed structure (e.g. bed porosity).

b. Session 1 Nonboiling Control Runs

The state of the bed can be determined, in part, by comparing the bed temperatures with expected temperatures based on conductive heat flow. Figure 1.4-2 shows the temperatures from the control runs made at the start and end of each session. The runs shown were all made
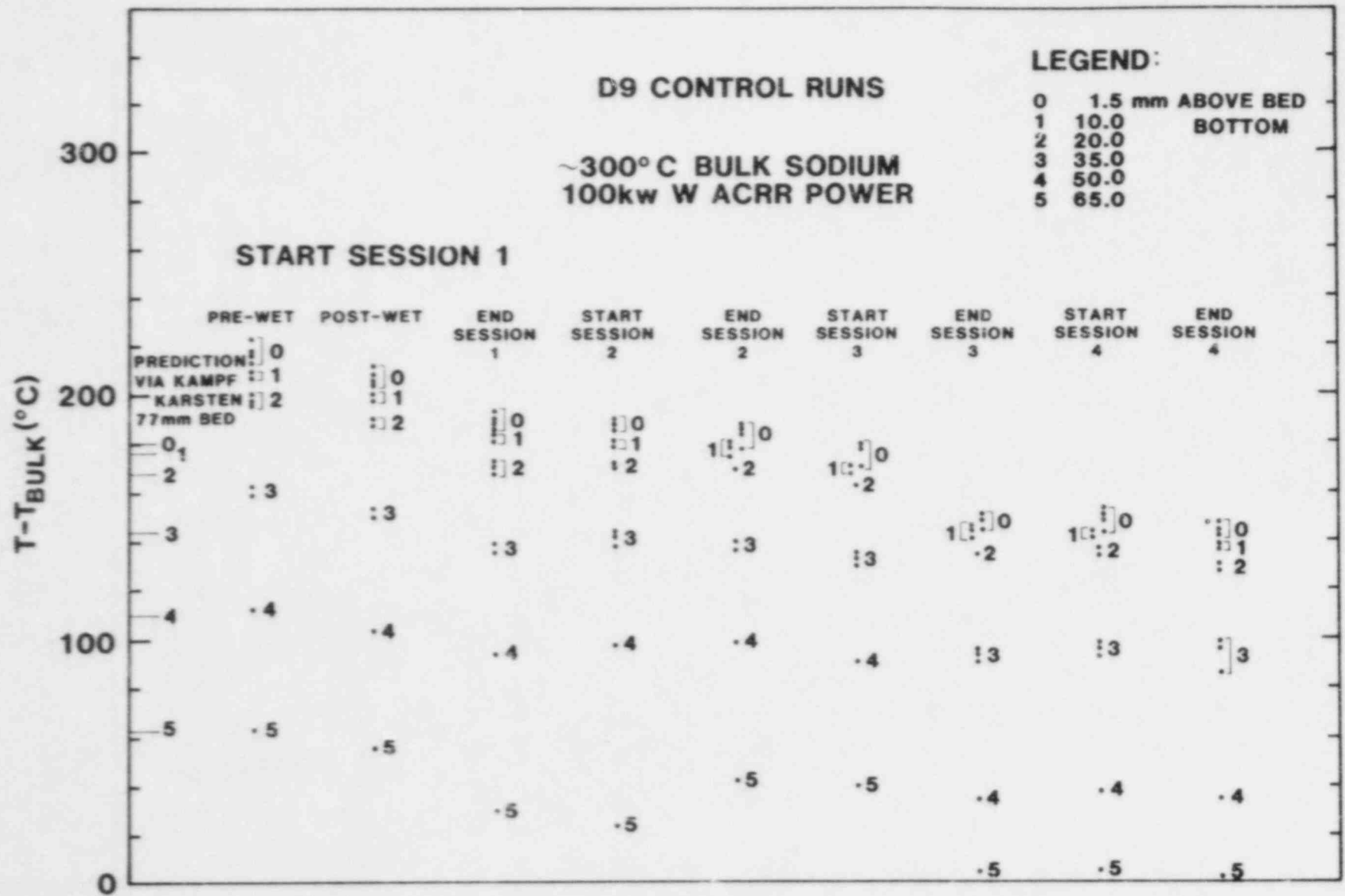
Figure 1.4-2. Nonboiling Control Run Bed Temperatures

with 573 K (300°C) bulk sodium and 0.250 W/g-UO$_2$ (except for those at the end of session 3 which were with 0.500 W/g-UO$_2$ and which have been normalized to 0.250 W/g-UO$_2$, allowing a more direct comparison of the data).

c. Bed State at the Start of Session 1

Experimenters made two control runs near the start of session 1. The first run showed that, while the temperatures in the top of the bed were as predicted, the temperatures in the bottom of the bed were higher than predicted.[1-15] This discrepancy could have been caused by trapped gas or porosity variations. After heating the bed for a period to encourage wetting and gas release, the second control run was made. In the second run, a slight decline in temperatures occurred. This decline may be evidence of release of gas. However, the agreement with the conduction predictions was still poor. Hence, some additional resistance remained in the bed.

d. Bed State after Tank Opening

Before the discussion of the dryout measurements (next section), note that the D9 package had an evacuated tank connected to the primary containment vessel (Figure 1.4-1). Opening this tank during the experiment would cause a decrease in the package pressure during operation, subsequently decreasing the saturation temperature and allowing a smaller subcooling with low bulk sodium temperatures, which would keep the primary containment within certain temperature limitations. Thus, after obtaining some dryout measurements with large subcoolings, experimenters would open the tank and conduct the rest of the experiment with lower pressures and subcoolings.

A similar tank, used in the D7 experiment, opened somewhat unexpectedly and the rapid boiling associated with the pressure decrease caused an increase in bed thickness of about 15 mm. In D9, the tank was opened as planned and under controlled conditions. The impact on bed structure was minimal and the increase in bed height was estimated to be about 2 mm or less.

e. Session 1 Incipient Dryout Measurements

Altogether, 30 incipient dryout measurements were performed with 10 being made in the first session. In most cases, the dryout power was determined by bracketing the incipient condition between two power levels. The dryout powers for all of D9 are given in Table 1-XII along with the bulk sodium and saturation temperatures and subcoolings. (The tank opening occurred just after dryout 5). Project personnel estimate the error in the power to be about ±0.02 W/g unless otherwise specified. Some dryouts (labeled T) were not stable, as the section on session 2 results will describe.

The dryout points are plotted in Figure 1.4-3. Also shown are the predicted incipient boiling powers and dryout powers determined with the series conduction model and the one-dimensional dryout model described in reference 1-16. The data from the entire experiment

66

TABLE 1-XII

Incipient Dryout Powers in D9

Dryout Number	T_{bulk} (°C)	T_{sat} (°C)	Subcooling (°C)	Power (W/g-UO$_2$)
Session 1:				
1	305	717	412	0.46
2	400	730	330	0.36
3	405	730	325	0.35
4	500	747	247	0.26
5	355	728	367	0.40
6	355	695	340	0.36
7	460	700	240	0.24
8	540	708	168	0.15
9	625	716	91	0.10
10	530	706	176	0.20
Session 2:				
11	375	698	323	0.43
12	370	692	322	0.44
13	460	700	240	0.35
14	550	702	152	0.29
15	650	720	70	0.50 T
16	605	714	109	0.38 T
17	645	720	75	0.38 T
18	640	719	79	0.20
19	640	720	80	0.23
20	370	700	330	0.50
21	500	700	200	0.36
22	560	710	150	1.0 ± 0.1 T
23	305	690	385	0.58
Session 3:				
24	360	695	335	0.49
25	400	700	300	0.44
26	552	708	156	0.21
27	548	708	162	0.38
28	550	708	158	0.24
29	560	709	149	0.30
30	660	720	60	4.4 ± 0.6
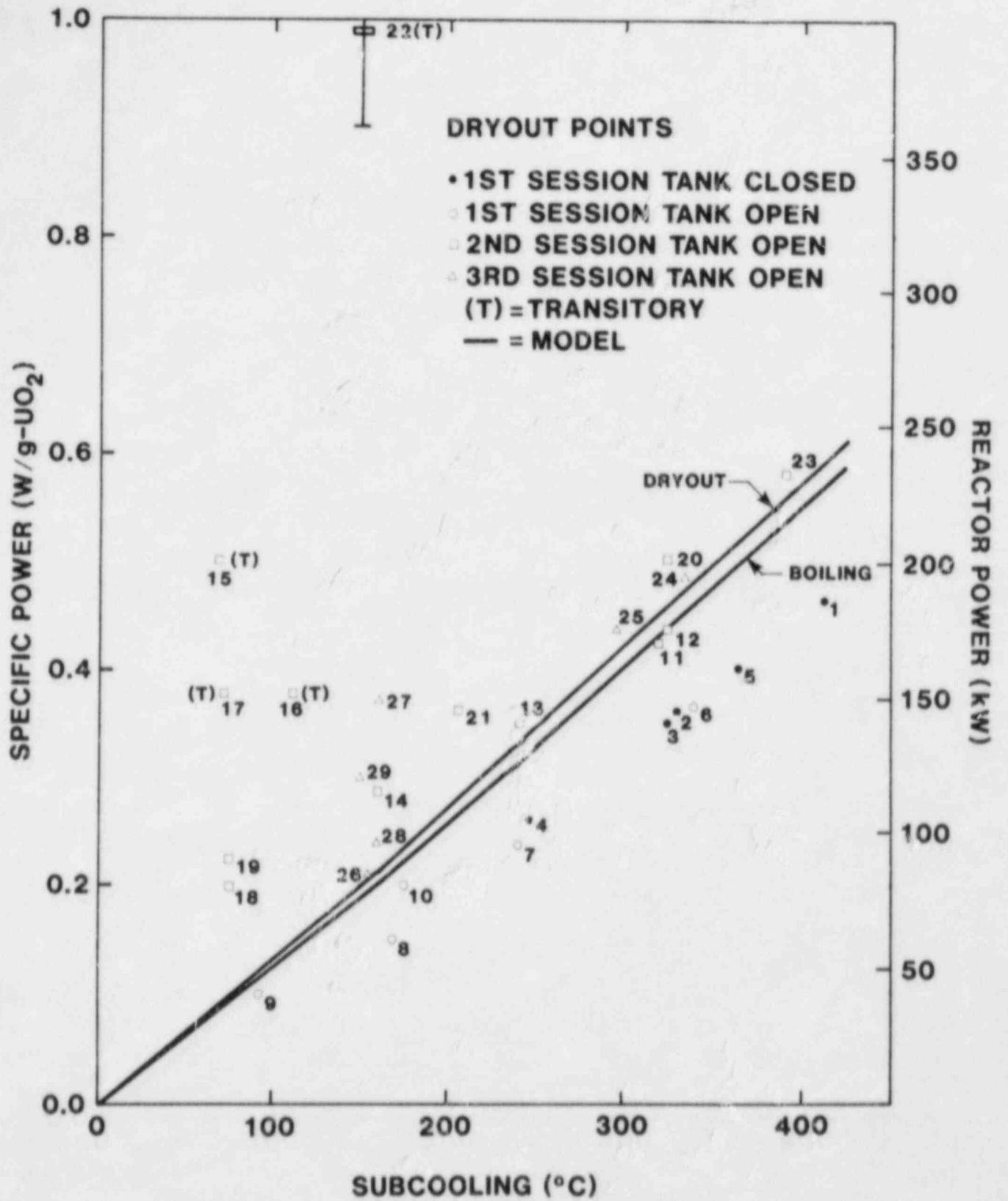
Figure 1.4-3.   Incipient Dryout Measures

58

appear somewhat scattered because of bed changes during later sessions. However, the data from session 1 (points 1 to 10) are very consistent and reproducible, and indicate that the dryout power is consistently lower than predicted.

The overprediction is a direct result of the error in the conduction calculations because the dryout predictions depend implicitly on the correctness of the conduction calculations. However, the one-dimensional boiling and dryout model[1-16] predicts that dryout will occur very close to incipient boiling,[1-15] and the data agree well with this. The first dryout point in session 1 occurred within 5% of the incipient boiling power.

The reason for such low dryout predictions is the effect of capillary force in stratified beds. Capillary force tends to keep the liquid in the region with the smallest particles. This impedes the downward flow of the liquid and causes dryout almost as soon as boiling begins.

Note that because of the strong surface tension in sodium, not much stratification is required to induce low dryout powers. For example, the first dryout point occurred with the boiling zone extending only over the bottom 10 mm of the bed. Above that, heat was removed in the subcooled zone by conduction. The particle diameters in the boiling zone ranged from 4.0 to 1.4 mm (bottom to top). The particle diameters spanned a factor of 3 in size. (The average size spanned only a factor of 2.) Yet this small amount of stratification was sufficient to induce a low dryout power. Only a dryout model which includes the influence of stratification on capillary forces within the bed[1-16] can come anywhere close to predicting such a low dryout power in a boiling zone 10 mm thick with such large particles.

The dryout power in D9 did not increase dramatically at very low subcoolings as it did in D4. Channel penetration of the thinner subcooled zone at low subcoolings was postulated to allow the higher dryout power in D4[1-17]. In D9, dryout occurred before channel penetration at all subcoolings investigated (except for the last dryout, as will be described later). This was predicted by the one-dimensional model[1-16] and again is a consequence of stratification: the dryout power in a stratified bed is so close to the incipient boiling power that the subcooled zone is thick and channels cannot penetrate. Such behavior was also seen in D6 and D7[1-18, 1-19].

f. Session 1 Channel Formation

Detection of channel formation was one of the objectives of the experiment. The pretest predictions indicated that channeling would occur, but only after dryout. Consequently, channeling was not expected to provide an increase in the incipient dryout power. Furthermore, once the channels formed, they would not be long enough to extend to the bottom of the bed and would only serve to decrease the size of the dry zone. The pretest predictions showed that with channeling the dry zone would be less than 20 mm thick, but certainly greater than 10 mm thick.

Experimentally, the occurrence of a channel was detected by a sudden reduction in the boiling temperature. This reduction occurred because of pressure relief caused by the channel. Drops of about 7°C are predicted by the one-dimensional boiling model[1-15, 1-16]. Unfortunately, a superheat flashing event produces a similar thermocouple response. The difference between the two is that channel formation must occur after boiling is initiated, while by definition a superheat flashing event must occur before boiling. Hence, careful observation of the thermocouple readings will permit investigators to differentiate between a channel formation and a superheat flashing event.

Unfortunately, experimenters must also be able to detect the onset of boiling in order to distinguish channeling from flashing. This is sometimes difficult because the saturation temperature is a function of vapor fraction and location in the bed because of varying capillary pressure. (Such behavior was first noted in D5 and was also seen in D7[1-19, 1-20]). However, the onset of boiling can be detected by noting when the temperature difference between two levels in the bed begins to decrease in response to a power increase.

Several sudden decreases in saturation temperature occurred in the first session (Figure 1.4-4). The power was held constant and the bulk sodium temperature allowed to increase in order to cause the temperature of the subcooled zone in the bed to decrease. The 20-mm (B2X) level was definitely boiling during the first two decreases because the temperature there remained nearly constant while the 35-mm (B3X) level temperature increased. Thus the saturation temperature drops indicated channel formation or a bed loosening of some kind. These events occurred after dryout, as predicted, and at about the same subcooled-zone thickness as predicted for channel penetration. However, they did not lead to a state of increased coolability. The dry zone temperatures did not decrease and the 20-mm (B2X) level later became dry indicating that the bed was still behaving as a packed bed. These events may have implied the formation of small internal channels that did not penetrate through the subcooled zone.

Following these events, a small power step was made, and channeling was again observed (Figure 1.4-4 again). In this case, the 20-mm (B2X) level did not dry out, and the dry zone temperatures were cooler than they had been previously with a lower power. This indicates that the bed was in a more coolable state and that channels may have penetrated the subcooled zone. Thus the subcooled-zone thickness required for channel penetration was slightly less than predicted, but the basic phenomenon was supported by these results. (More direct support occurred in session 3 and will be described later).

g. Session 1 Flashing

Superheat flashing was also investigated in the experiment. Flashing events result from deactivation of boiling nucleation sites. Before boiling can be initiated, the liquid temperature must exceed the saturation temperature in order to have vapor-bubble growth. The degree to which the liquid temperature must exceed the saturation

70
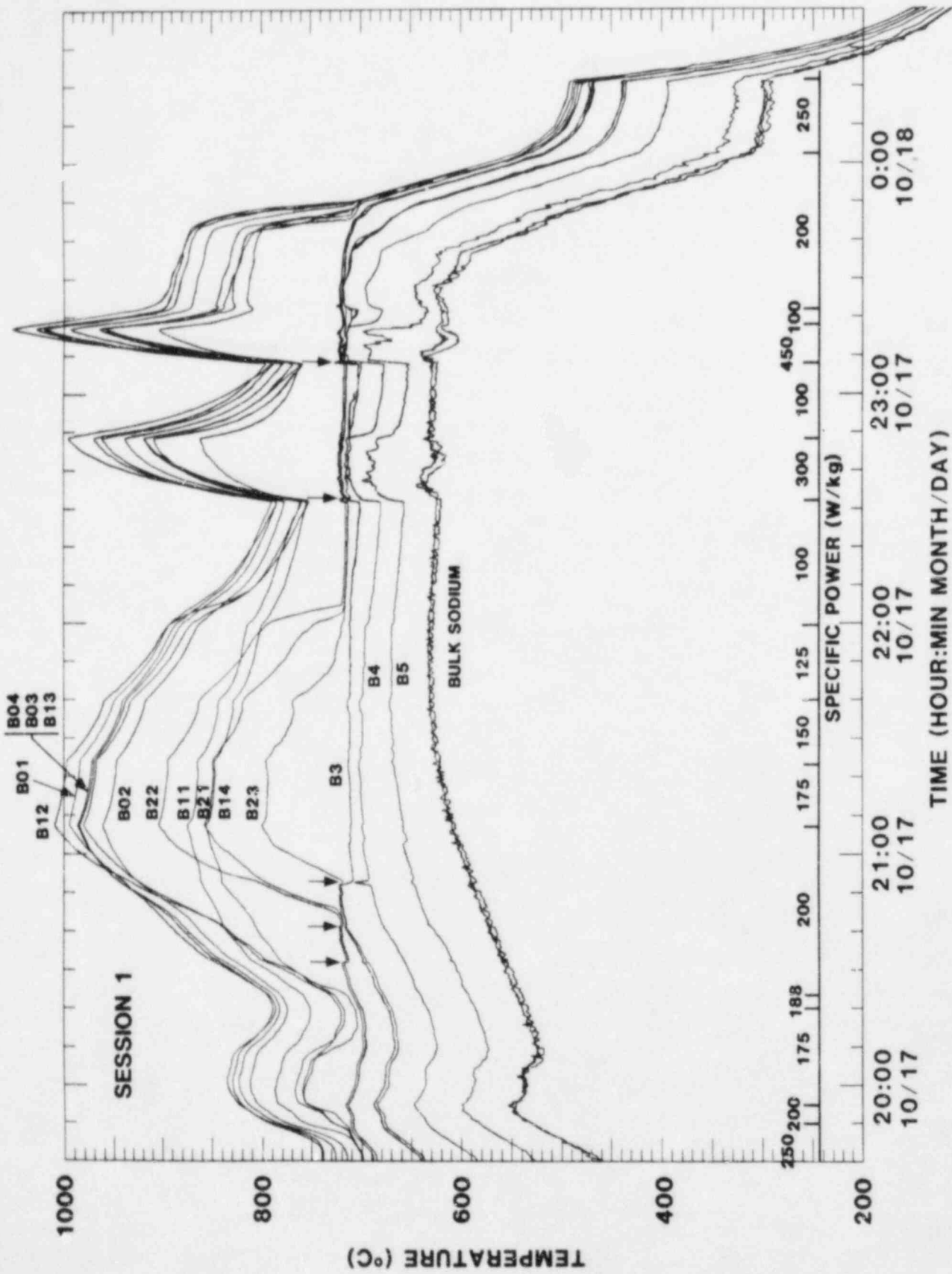
Figure 1.4-4. Session 1 Dryout and Channel Formation

temperature is called the superheat. The superheat needed to initiate boiling is inversely proportional to the radius of a nucleate bubble in a cavity. Current theory suggests that as boiling proceeds, gas trapped in the cavities escapes. If boiling ceases and the liquid becomes subcooled, the liquid may penetrate into the cavities deeper than before. The part of the cavity near the liquid will then be wetted, and the nucleate bubble for starting boiling will be smaller. Upon reheating, the amount of superheat needed for boiling will be greater. Without trapped gas, the amount of superheat is primarily a function of the amount of subcooling prior to heating[1-21].

While no direct study of flashing was undertaken in the first session, one unusual event occurred that is related to the superheat flashing phenomenon. Shortly after the first dryout was attained, and after 75 minutes of boiling, the reactor scrammed causing a loss of power and rapid temperature decrease. The bed became completely subcooled and upon heating, a superheat flashing event was antici- pated. However, no such event occurred. Apparently, in this case, the bed had not been boiling long enough to outgas fully the nuclea- tion sites.

h.   Bed State at the End of Session 1

A nonboiling control run was made at the end of session 1. Bed temperatures were found to be considerably lower than they were at the beginning of session 1 (Figure 1.4-2), indicating that the bed was about 4 mm shorter at the end of the session. Consideration of the subcooled zone temperatures during steady-state-boiling runs shows that this reduction in bed height occurred during the two small power steps near the end of this session.

1.4.2.4   Session 2

The second session was concerned primarily with subjecting the bed to a number of power steps. The purpose of these tests was to scope the range of anticipated conditions that a bed might experience upon forming. Steps up to 1.4 W/g were imposed with both boiling and subcooled initial conditions. The main result from these tests was that the dryout power was not significantly increased.

a.   Bed State at the Start of Session 2

The nonboiling control run at the start of the second session was essentially identical to the one at the end of the first session (Figure 1.4-2). This indicated that no major bed changes had occurred during the freezing and reheating cycle between the first two ses- sions, and also that the decrease in bed height during session 2 was permanent and not just caused by temporary suspension of fines in the overlying sodium pool. Later control runs showed no significant changes during any of the freezing and reheating cycles.

b.   Session 2 Large Power-Step Test

Essentially all dryout investigations, both in the D-series and elsewhere, have used small power increments so as to locate the

incipient dryout power with precision and to minimize disturbances in the bed so that the bed state at dryout is characterized better. However, debris formed in an accident is at a decay power level around 1 to 3 W/g-UO_2 immediately, and the power decays very slowly. When the bed is formed by falling through liquid sodium, the particles are well-cooled. Heatup calculations indicate that the bed could easily form before it heated to the boiling point. Thus a more prototypic heating method than slow power increases would be a single power step of 1 W/g or more (starting with a partially heated bed). Fifteen such large power steps were performed in session 2 to determine the behavior of the bed under these more prototypic conditions.

All the power steps of D9 are summarized in Table 1-XIII. Most of the power steps started with the bed below dryout, and some with the bed below boiling. Initial powers ranged from 0.05 to 0.45 W/g. Final powers ranged from 0.30 to 2.50 W/g. All step tests resulted in dryout (except for the last four, which were either deliberately terminated early or occurred after a significant bed change; these will be addressed in section 1.4.2.5b). However, in most of the tests, the dry zone was less than 20 mm thick. Experimenters postulate that in these cases the bed was channeled. Only large subcooling enabled dryout of the 20-mm (B2x) level, presumably because of channel suppression. (Although steady state was never achieved at these high powers, the dry-zone thickness was usually established and nearly steady well before temperature limits forced a power reduction). Some examples will demonstrate the features of these tests.

Figure 1.4-5 shows the bed temperatures for power step 4. The bulk sodium temperature was 638 K (365°C), and the initial subcooled zone was about 60 mm thick. A step to 0.90 W/g yielded very rapid dryout of the 1.5-mm (B0X), 10-mm (B1X), and 20-mm (B2X) levels. A slow decrease in the saturation temperature suggests some bed loosening, but it may only have been a nonpenetrating channel as described in section 1.4.2.4f.

Figure 1.4-6 shows the bed temperatures for power step 10. The bulk sodium temperature was 813 K (540°C), and the initial subcooled zone was only 40 mm thick. A power step to the same level as the previous example (0.90 W/g) produced dryout in the 1.5-mm (B0X) and 10-mm (B1X) levels only. Thus the bed was more coolable with reduced subcooling. This increased coolability may have been caused by the formation of penetrating channels.

Figure 1.4-7 shows the bed temperatures for power step 14. The bulk sodium was at nearly the same temperature as in the first example, but the bed power was chosen to be lower so as to start the step well below boiling. When the power was increased to the same level as in the previous two cases, a sharp drop in temperatures occurred just before dryout. In this case, the drop represented flashing of superheated liquid sodium. Comparing the response of the temperatures in the subcooled zone to that in the first example indicated that the flash released a large amount of vapor. This very large vapor flow may have disrupted the bed and established a penetrating channel. Evidence for this was that the dry-zone temperatures were much lower

TABLE 1-XIII

Large Power-Step Tests

Step Number	T_{bulk} (°C)	Initial T_{max} (°C)	Initial Power (W/g)	Final Power (W/g)	20-mm Dryout?
Session 1:					
1	625	792	0.10	0.30	No
2	625	797	0.10	0.45	No
Session 2:					
3	375	698	0.40	0.60	No
4	365	700	0.40	0.90	Yes
5	360	703	0.40	1.20	Yes
6	360	705	0.40	1.20	Yes
7	465	707	0.35	0.75	No
8	460	703	0.38	1.13	No
9	545	710	0.28	0.60	No
10	540	710	0.28	0.90	No
11	550	712	0.28	1.20	No
12	640	725	0.15	0.75	No
13	640	725	0.25	1. ?	No
14	355	537	0.23	0.90	No
15	360	546	0.23	1.43	No
16	445	630	0.23	1.43	No
17	550	657	0.08	1.38	No
Session 3:					
18	365	640	0.35	1.43	?
19	375	700	0.45	0.90	No
20	375	700	0.45	0.60	No
21	550	690	0.15	2.00	No
22	550	682	0.15	2.00	No
23	620	698	0.05	2.00	No
24	605	700	0.08	2.50	No
25	390	740	0.38	0.60	−
Session 4:					
26	500	748	0.28	0.90	−
27	500	552	0.05	2.50	−
28	360	560	0.38	1.50	−

74
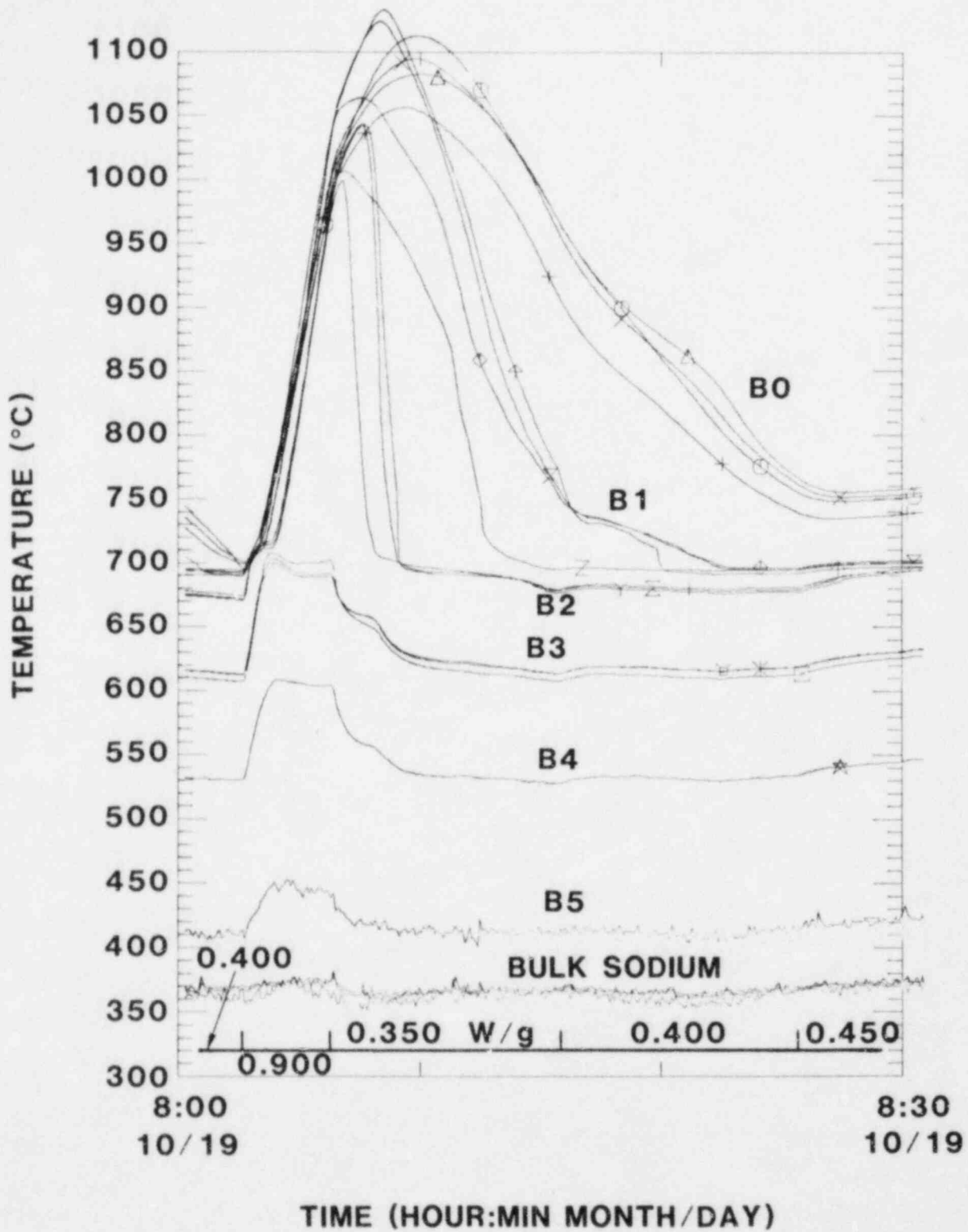
Figure 1.4-5.   Session 2 Bed Response to Power Step (Power Step 4)
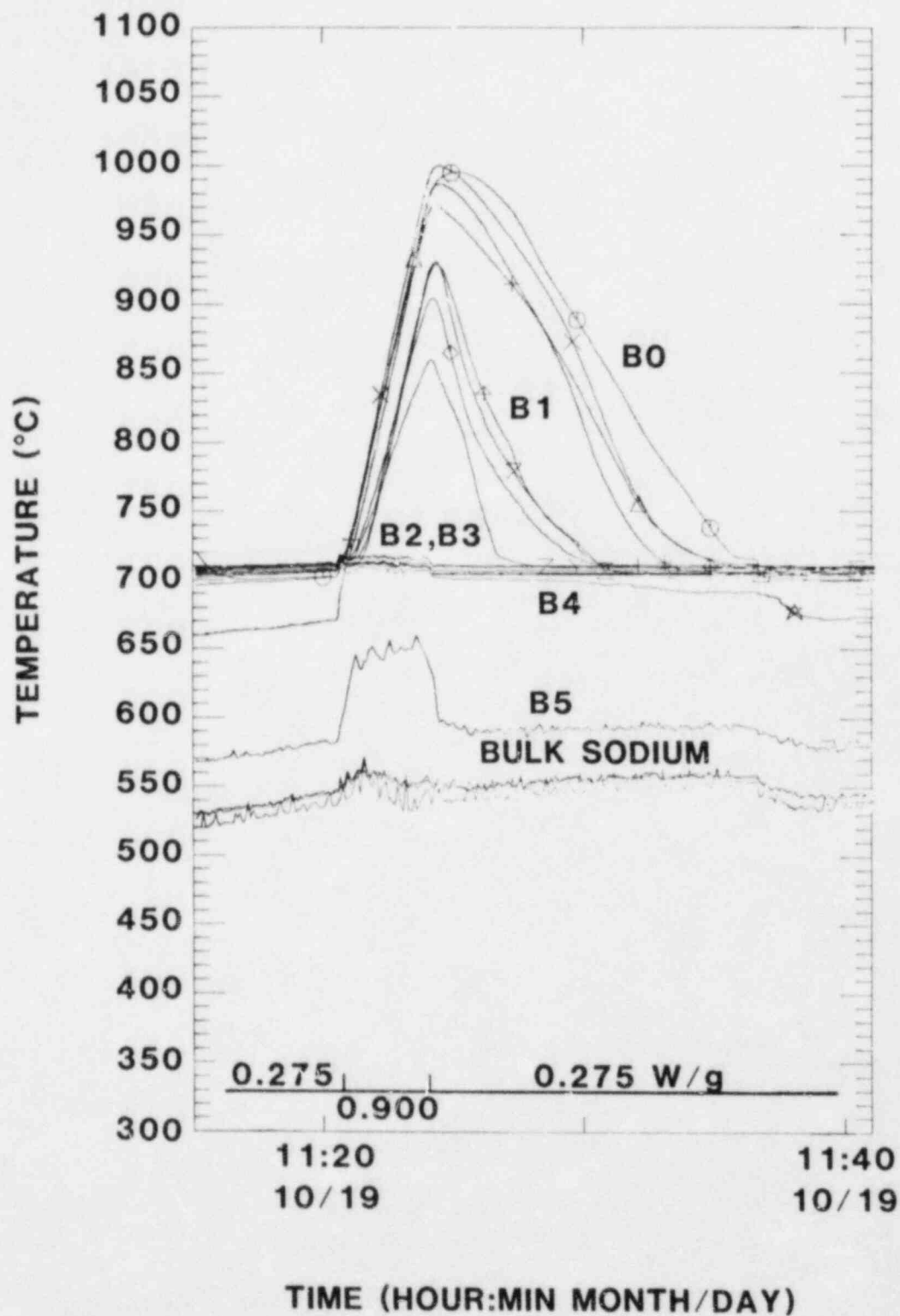
Figure 1.4-6. Session 2 Bed Response to Power Step (Power Step 10)
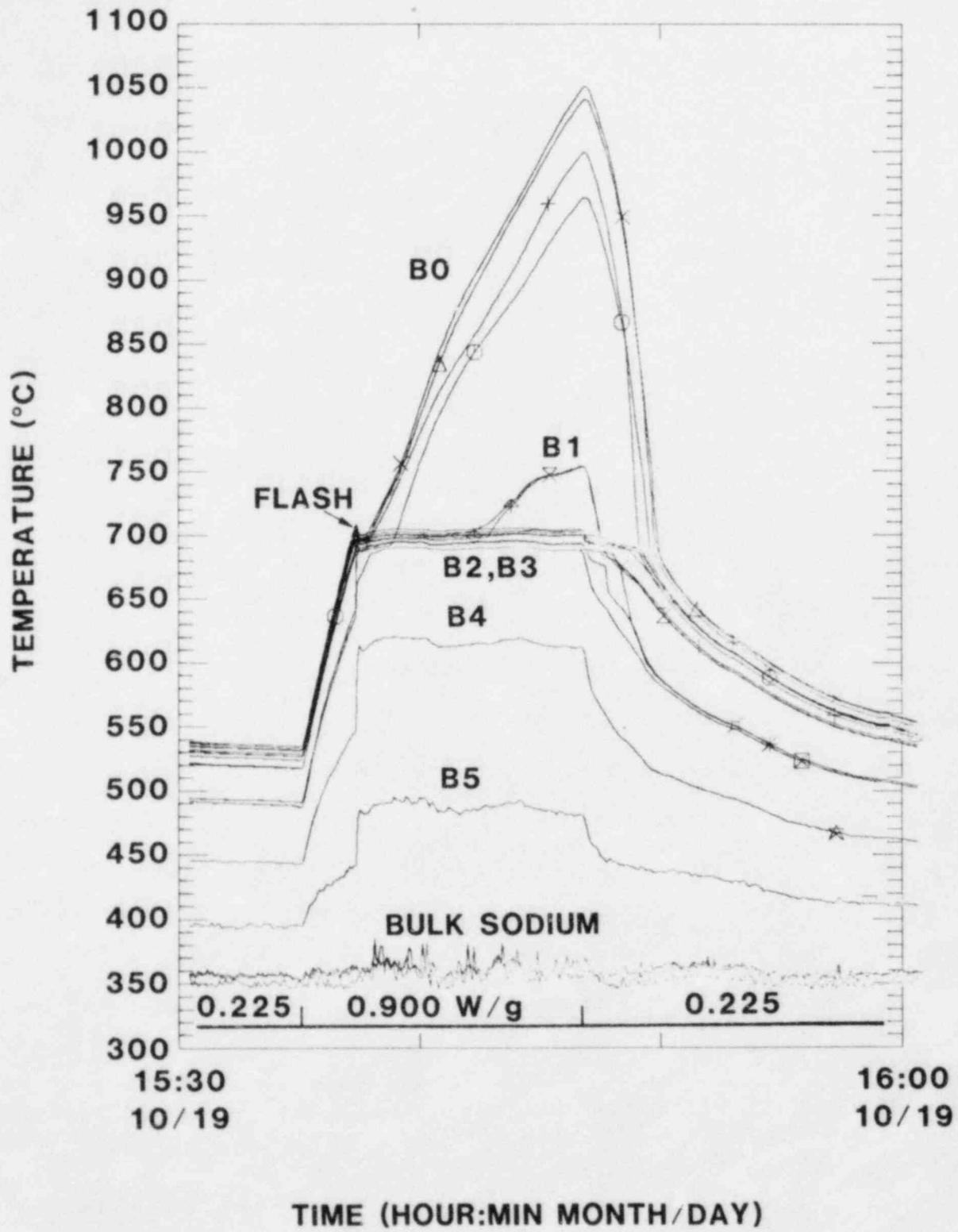
Figure 1.4-7. Session 2 Bed Response to Power Step (Power Step 14)

than in the first example and the 20-mm (B2X) level did not dry out. Thus, with the additional effect of flashing, a highly subcooled bed may channel and be more coolable.

The implication of having a dry zone limited to 20 mm under prototypic heating is that the maximum temperature will be lower than the melting point of UO_2. Unfortunately, it will be above the melting point of steel. Furthermore, this result applies only to the D9 bed. Thicker stratified beds, which channel, will have a larger limit to their dry zones. This is because the dry zone is limited by the bottom of the channels, and channel lengths are limited by the particle diameter at a given level and the weight of the bed above that level. Thus, although the power-step series indicated a state of increased coolability with more prototypic heating, the increase was not much.

c. Session 2 Dryout Measurements

In the second session, 13 incipient dryout points were determined between the large power-step tests. As Figure 1.4-3 shows, the dryout powers were slightly higher (about 30%) than during the first session. These differences may be attributed to minor changes in the bed structure, manifested primarily by an increase in the power required for incipient boiling. Dryout still occurred within 20% of incipient boiling, indicating that in spite of the many large-power-step tests, the bed still remained sufficiently stratified to suppress the dryout power severely.

Even though most of the dryout points indicated low dryout powers, some showed abnormally high powers. These dryout points were transitory in nature and are labeled "T" in Table 1-XII and in Figure 1.4-3. These measurements were made shortly after a large-power-step test and experimenters believe that the bed had not settled completely. The sequence of points 15 through 18 shows how the dryout flux decreased over a period of 90 min. The one-dimensional model predicts that the dryout power in a stratified bed will increase if the porosity increases with elevation so as to compensate for the decreasing particle size. The power step may have expanded the bed in such a fashion, causing an increased dryout flux, followed by bed compacting with time and boiling.

d. Session 2 Channel Formation

During the many power steps in the second session, channels formed in all cases except those with the highest subcooling. Apparently, the channels can be suppressed if the subcooling is large enough and the power low enough. When the channels formed, the 20-mm (B2X) level remained in the boiling zone, as predicted by the pretest calculations.

e. Session 2 Flashing

Because some of the power steps were made from subcooled initial conditions, a superheat flashing event was anticipated. The pretest predictions had indicated that the amount of superheat should be

nearly equal to the degree of subcooling if the subcooling were not too large. However, in all cases, the amount of the superheat was 30°C or less (Figure 1.4-7) even though the degree of subcooling was large and the bed had been boiled continuously for over 8 hours before the first flash. The rapid heating of the bed possibly caused the boiling to begin near the middle of the bed where active nucleation sites still existed.

Another unexpected result was obtained at the first onset of boiling in the second session. Because the bed was subcooled after boiling during the first session, a superheat flashing event was again anticipated. However, when the bed was heated to the boiling temperature, boiling started and no flash was observed. The lack of a flash was probably caused by cover gas leaking into the bed along shrinkage cracks which formed when the bed was frozen between sessions. The gas then provided nucleation sites which reduced the superheat to undetectable levels. Flashing never occurred at the beginning of any of the sessions. This result is important for future tests which need to run over many days.

f.   Bed State at the End of Session 2

The control run at the end of session 2 indicated that the bed thickness was essentially unchanged during session 2.

1.4.2.5   Session 3

The third session was concerned mainly with performing extended dryout studies. In these studies, incipient dryout was first attained and then the power was slowly increased. In this way, project personnel could monitor the growth of the dry zone. Also, the pretest predictions had shown that at a certain power level, channels would form, which would subsequently reduce the size of the dry zone. Hence, by performing very careful extended dryout studies, investigators hoped that these phenomena could be observed.

In addition to the dryout studies, a very careful attempt was also made to produce a superheat flashing event. As detailed below, this attempt was successful and a 90°C flash was produced. After the flash, experimenters tried to find the incipient dryout power. The dryout power was found to be approximately 4.4 W/g, 20 times larger than previous dryout powers at the same subcooling.

a.   Session 3 Dryout and Channeling Investigation

During the third session, extended dryout was investigated. This study carefully explored the growth of the dry zone as power increased and the shrinkage of the dry zone as channels formed.

Incipient dryout measurements made in this study were slightly higher than in previous sessions. Again, these differences were probably caused by changes in the bed structure (i.e., porosity and height changes).

The pretest predictions had indicated that channeling would occur only after dryout and, when it occurred, the dry-zone thickness would decrease. Figure 1.4-8 illustrates the anticipated thicknesses of the subcooled, boiling, and dry zones as a function of power (based on a 77-mm-thick bed).

During the extended dryout study, channeling occurred after dryout and did reduce the dry-zone thickness. This phenomenon can be seen more clearly in Figure 1.4-9 (18:00 to 20:00 hrs). The thermocouple readings before the channel formation show that the dry zone extended above the 20-mm (B2X) level. After the channel formed, the temperatures dropped rapidly and the 20-mm level was then in the boiling zone. This drop in temperature is a clear indication that the dry-zone thickness decreased. Indeed, apparently the dry zone would have disappeared entirely with sufficient time. This is greater coolability than predicted, but Figure 1.4-8 shows the channeling after dryout behavior was qualitatively predicted correctly.

Further study showed that the channel-formation phenomenon was reversible and repeatable. Figure 1.4-9 (20:00 to 23:00 hrs) shows that initially the channel was suppressed, and the bed dried out at approximately the same power. Furthermore, at essentially the same power level, a channel formed and the bed temperatures dropped. The temperatures after channel formation were slightly higher in this case, indicating some hysteresis, but this is probably a minor point. The observation of repeatable channel formation and collapse suggests that the bed was wetted and that the hypothesis of channel suppression by subcooling (as evolved from and supported by previous D-series experiments) is correct.

b. Session 3 Flashing

In the previous sessions, the superheat flashing events were either nonexistent or significantly reduced relative to their anticipated values. At the start of the third session, again, no flash occurred when boiling was first attained. Hence, after the extended dryout study was completed, a careful attempt was made to produce a superheat flashing event.

To perform this study, the bed was first substantially subcooled (100°C) and then slowly raised to the boiling temperature. The power was increased slowly and temperatures rose above the boiling temperature. A maximum superheat of 100°C was obtained before reducing power for safety discussions. Attempts were then made to initiate the flashing event. After several attempts, a 90°C flash was initiated (see Figure 1.4-10). A flash of this magnitude was higher than anticipated and may be a result of the long boiling times before the flash. After the flash was achieved, the incipient dryout power was investigated. The bed appeared to be packed at first, as evidenced by the large span of saturation temperatures in the bed (see Figure 1.4-10). (Similar behavior was seen in D5.[1-20]) As the power was increased, a channel formed before dryout was reached. Subsequent power increases yielded more channels, and the dryout power was eventually determined to be approximately 4.4 W/g. This was the last dryout
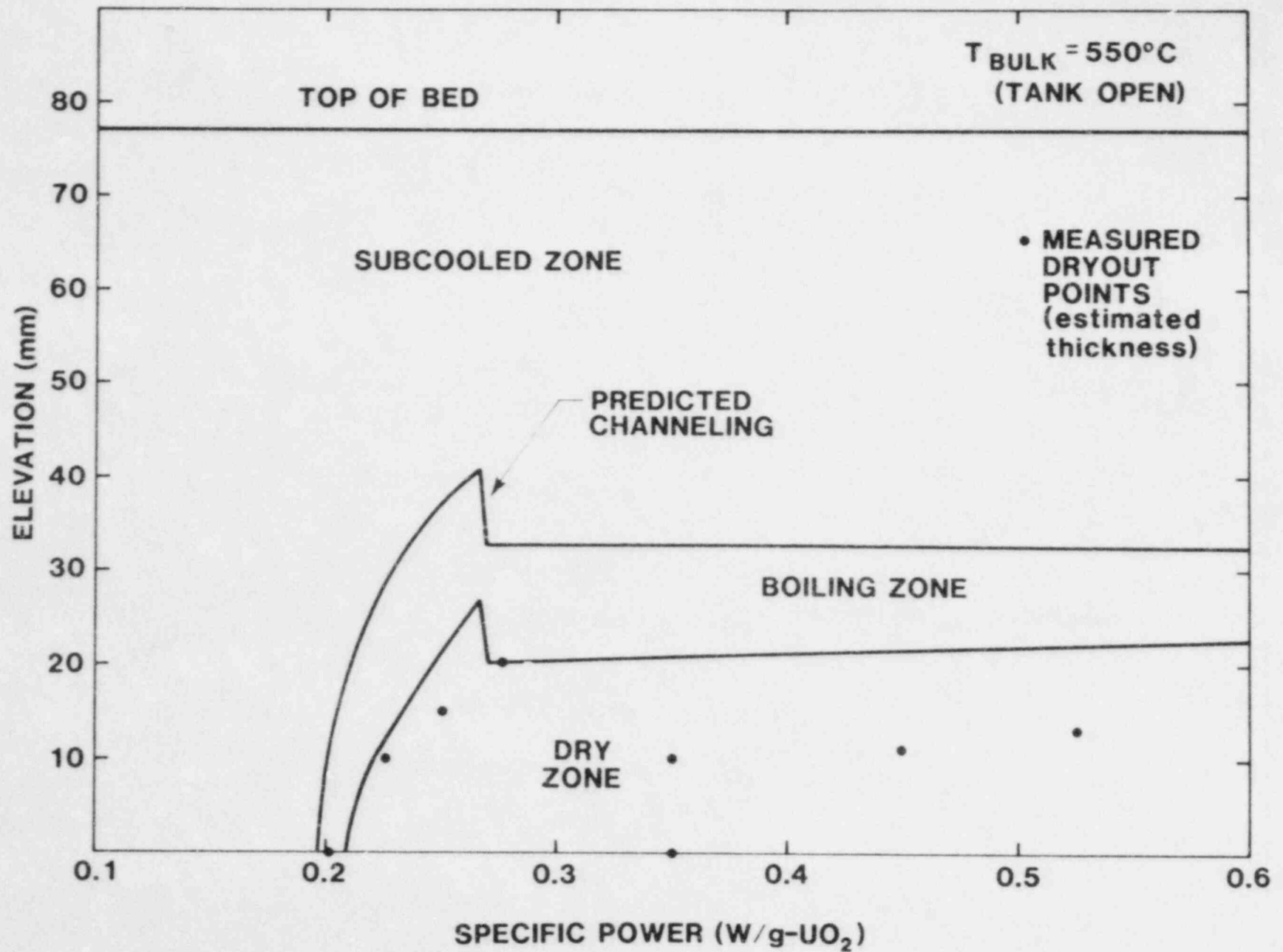
Figure 1.4-8.   Session 3 Zone Thickness Predictions and Measurements
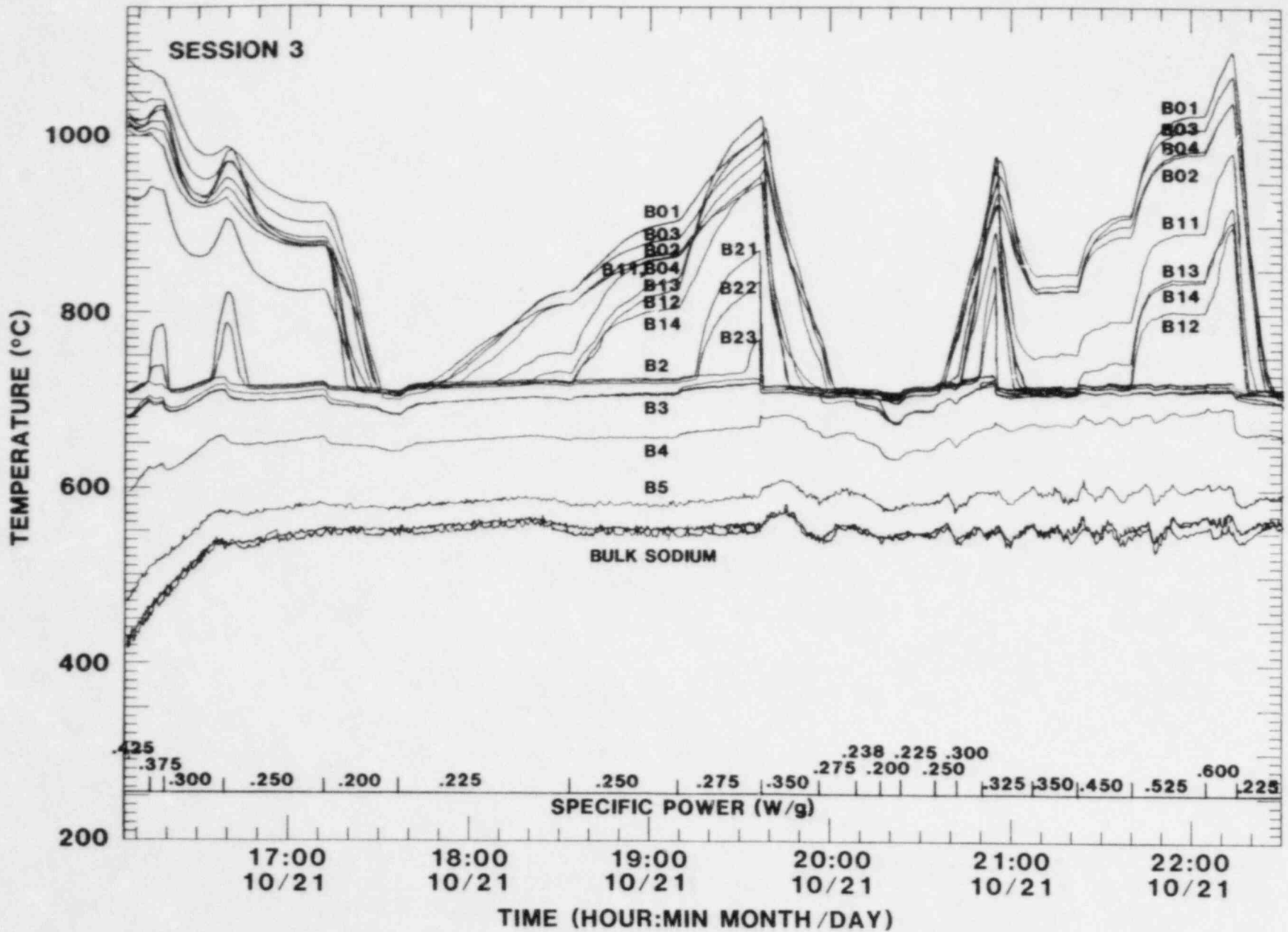
Figure 1.4-9.   Session 3 Dryout and Channel Formation
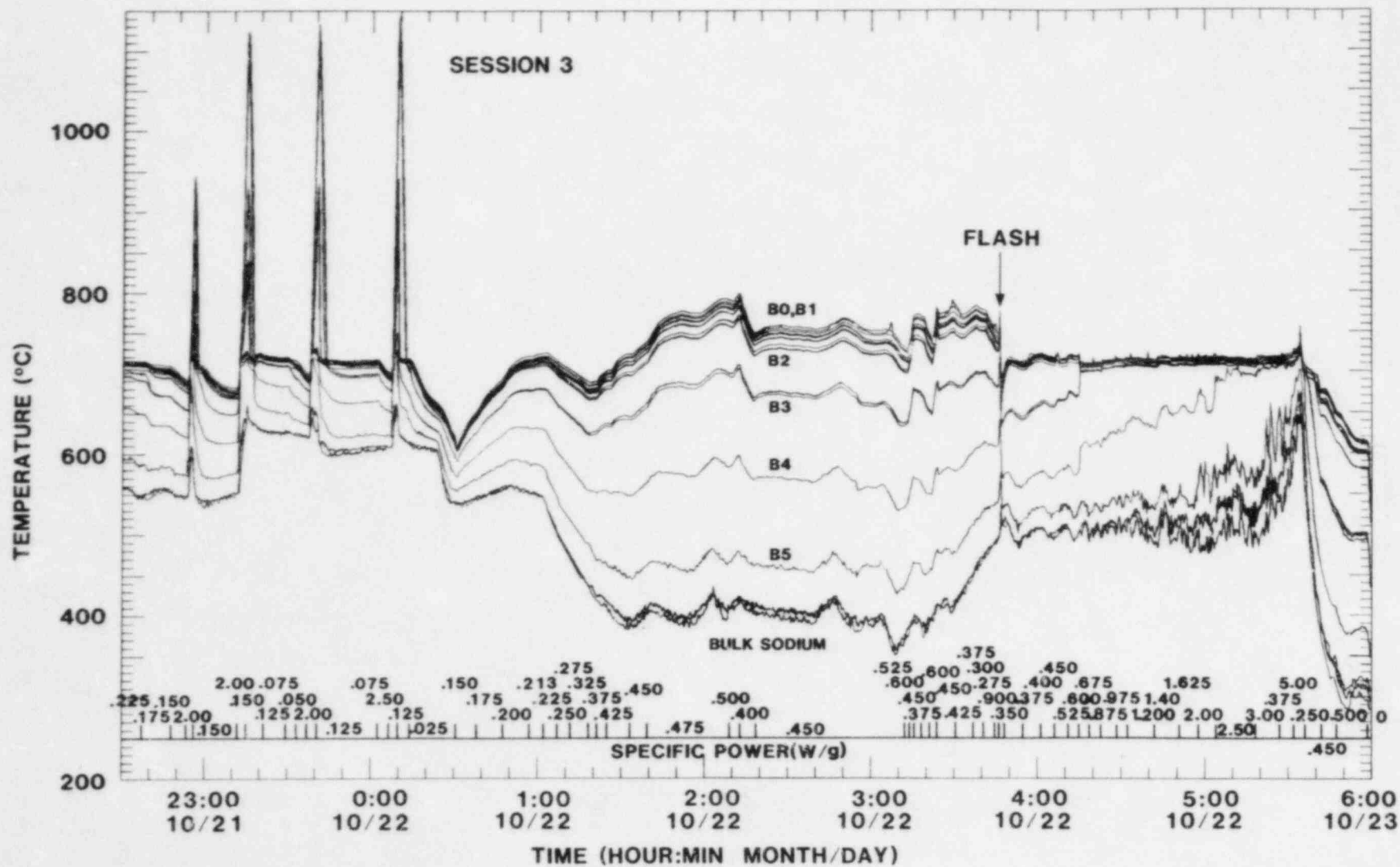
Figure 1.4-10.   Session 3 Superheat Flash and Subsequent Dryout

measurement in this test. Apparently the flashing event mixed the bed considerably thereby negating the detrimental effects of stratification. With a mixed bed, channels could penetrate to the bottom of the bed resulting in the dramatic increase in the dryout power.

c. Bed State at the End of Session 3

The control run at the end of session 3 showed that the bed height decreased to 65 mm or less (Figure 1.4-2). About half of this change occurred during the first large (90°C) flashing event and half during the strong boiling (with low subcooling) during the subsequent search for incipient dryout after the flash (Figure 1.4-10). This large change indicates that a sizable fraction of the original bed was outside of the crucible at the end of this session. The thermocouples below the crucible exhibited a large response to a step increase in power at the start of session 4. Their response was consistently much smaller prior to the 90°C flash. This supports the idea that there was fuel outside the crucible, and indicates that most of it left the crucible during the flash and the subsequent high-power boiling.

1.4.2.6 Session 4

The fourth session was concerned mostly with investigating the flashing phenomenon. As the third session revealed, a large flash could disrupt the bed to such an extent that the dryout power increased by a factor of 20. Hence, it was important to gain a better understanding of this phenomenon.

Many flashing events were initiated in this study. However, the maximum superheat attained was only 70°C. The 90°C flash could not be repeated. On the whole, the magnitude of the flashing events followed the theoretical curve if sufficiently long boiling times were used. If short boiling times were used, the superheat was substantially reduced.

a. Session 4 Dryout Measurements

A search for dryout was performed at the start of session 4 with 573 K (300°C) bulk sodium. Several channel events were observed as the power was increased. No dryout was observed up to 1.28 W/g. Higher powers were not attempted because experimenters suspected that vigorous channeled boiling would disrupt the bed more. But the 1.28 W/g limit demonstrated that the bed change caused by the 90°C flash at the end of session 3 was a permanent change.

b. Session 4 Flashing

Most of session 4 was devoted to investigating the superheat flashing phenomena. Figure 1.4-11 illustrates the measured superheats at which flashing occurred. The theoretical values are also plotted[1-15, 1-21]. Three classes of measurements are presented: those in which the saturation temperature was passed during a large-power-step test, and those involving only small power increments with either more or less than 15 minutes of boiling since the last flash.
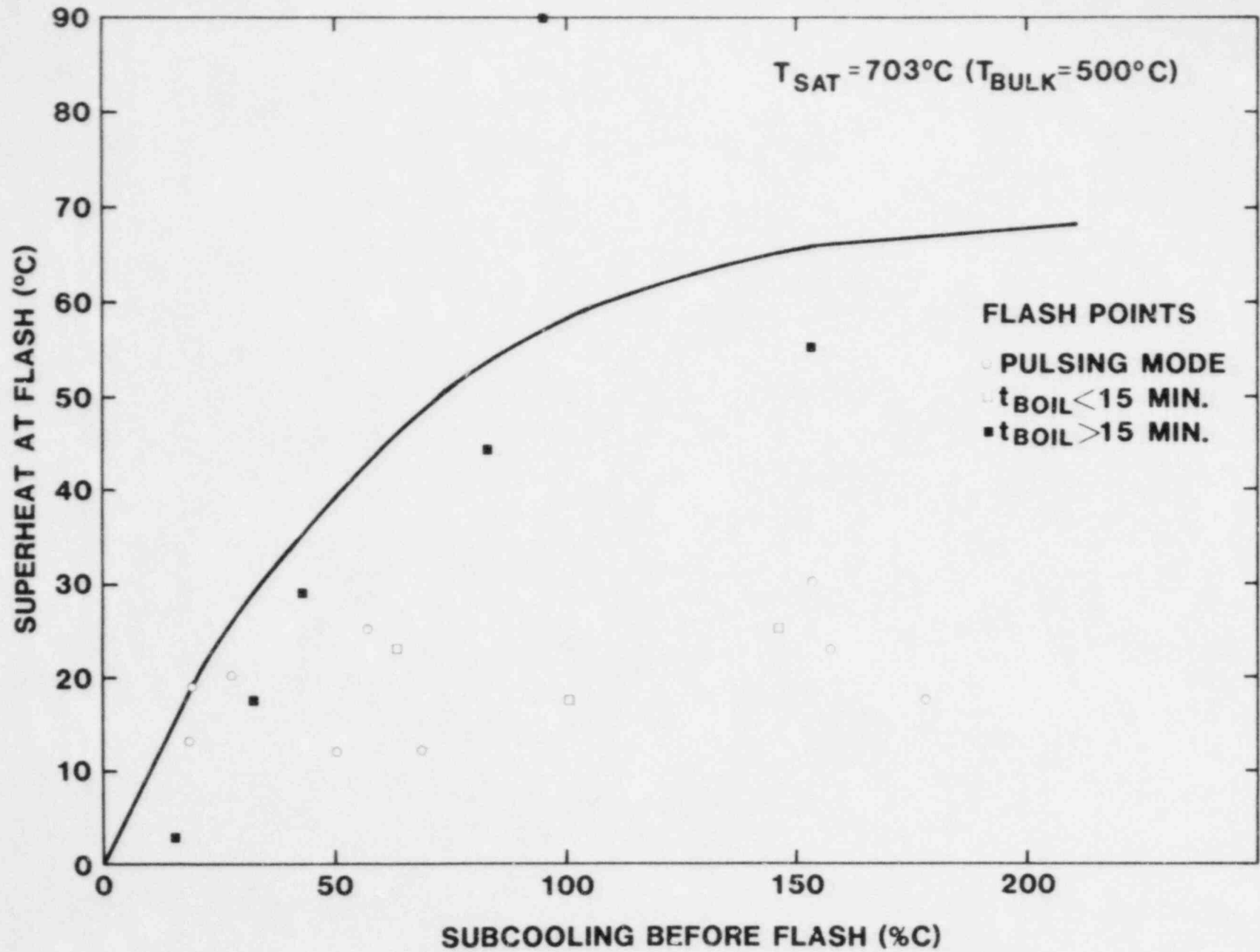
Figure 1.4-11 Superheat at Flashing

The measurements, which agree well with the prediction, were obtained with small steps after allowing the bed to boil for a period of time (15 minutes) before the flash. (Note that all these data occurred after many hours of initial boiling in session 1). The values which lie beneath the curve were either boiled for shorter times or subjected to large power steps. Apparently, both the boiling history and the heating mode are important for the creation of a large flashing event.

c. End State at the End of Session 4

The control run made at the end of the fourth session gave essentially the same results as the run at the start of the session. This indicates that the bed height ended session 4 at about the same value as it had at the start.

1.4.2.7 Summary

The D9 experiment consisted of four sessions. The first session showed that the dryout powers, which ranged from 0.10 to 0.64 W/g, were very close to incipient boiling, even at a low subcooling of 70°C. Sandia's one-dimensional boiling and dryout model[1-15, 1-16] predicted this. The saturation temperature experienced sudden drops at the lowest subcooling only. These events occurred at about the same subcooled-zone thickness as predicted for channel formation. However, they did not lead to an increase in bed coolability. Investigators postulate that the bed may have loosened because of capillary pressure at that point, but vapor did not penetrate the subcooled zone. However, higher powers subsequently yielded a thinner dry zone. This is believed to indicate channel penetration of the subcooled zone because such behavior was predicted for the channeled state. Note that channel penetration occurred only after dryout began, and that channeling did not cause a large increase in coolability.

Session 2 was devoted primarily to large power steps to simulate better the heating history in reactor accident debris bed. Steps up to 1.43 W/g were made (and higher steps in later sessions). Even though the steps exceeded the incipient dryout power by a factor of as much as 5 (and 10 in session 3), the dry zone thickness was less than 20 mm in most of the cases. Channel penetration is believed to have been responsible for this more coolable behavior. The dry-zone thickness in the channeled state was predicted to be limited to 20-mm.[1-15] Despite the many step tests, the incipient dryout power remained close to incipient boiling.

Session 3 investigated steady-state extended dryout. The dry-zone thicknesses were fairly close to those predicted by the one-dimensional model.[1-15, 1-16] In addition, a small increase in power yielded a collapse of the dry zone with low subcooling. This was the most direct indication of channeling in the experiment, was repeatable, and occurred at powers only slightly higher than predicted.

86

At the end of session 3, 100°C of liquid superheat was deliberately induced in the bed. This superheat was reduced and flashed at 90°C (for safety considerations) and resulted in a permanent change in the bed which increased the dryout flux (by a factor of 20) up to 4.4±0.6 W/g. The investigators believe that the flash mixed the bed sufficiently to overcome the detrimental effects of stratification.

The final session was devoted to the investigation of superheat flashing. Superheat could be achieved at the predicted levels[1-15, 1-21] only if the bed was sufficiently boiled, and was boiled between each flash. However, superheat in excess of 30°C could not be achieved with a large power step prototypic of heating in accident debris. Thus the benefits of flashing may not be applicable to reactor accidents.

1.4.3 Debris Bed Experiment D10/13

The D10/D13 experiment objectives, and experimental procedures to achieve those objectives, were reviewed during this quarter to allow completion of final designs and hardware ordering. The basic objective of the experiment is to investigate the effects of bottom cooling and high bed temperatures (up to 2500°C). Secondary objectives include the effects of rapid power increases, coolability at low subcooling, superheat disturbances, and the effect of pressure. Project personnel prepared a preliminary experimental procedure to meet these objectives and distributed it to program sponsors. This procedure included investigations of conduction, single-phase and two-phase heat removal in both a packed bed and a channeled bed, all conducted at relatively modest bed temperatures of 1473 K (1200°C). These investigations would be followed by extended dryout, with peak bed temperatures of 2773 K (2500°C).

Design drawings and fabrication techniques are undergoing review to increase the fabrication efficiency for all D10 components. Fabrication of some components that were previously in process continues. Investigators expect to initiate fabrication of all remaining components in January.

Project personnel have considered several design concepts for crucible fabrication, keeping in mind that they have not yet selected a material. These design evaluations are being conducted to minimize the procurement time once a material is selected. To eliminate questions of a bottom-fed bed, the D10 project staff considers a closed end crucible to be a design requirement. Current design concepts attempt to minimize the number of welds, especially in high temperature areas, and to eliminate stresses which would result from non-uniform thermal expansion.

Instrumentation for experiments D10/13 was reviewed from the viewpoint that with a closed end crucible, all instrumentation in the bed must penetrate from above and will therefore pass through the high temperature dry zone. Further, the temperature of the crucible wall must be well monitored to assure a high likelihood of crucible integrity during the experiment. Project personnel decided that ultrasonic

thermometers (UTs) should, if possible, be placed at radii of 15, 25, and 35 mm, that two high-temperature, C-Type thermocouples should be placed in the central regions of the bed to verify the ultrasonic data, and that six C-Type thermocouples would be used to monitor wall temperatures between 15 mm and 100 mm. Four K-Type thermocouples would be used to monitor bed temperatures between 120 and 150 mm. The locations of all bed thermocouples are summarized in Figures 1.4-12 and 1.4-13. Cover plate layouts to accommodate this instrumentation are being studied.

Sandia engineers with experience in stress analysis of components in high temperature service were consulted early in November. These meetings resolved questions about the interpretation of finite-element computer analyses performed for the D10 containment components.

Based on this review, the current design appears to be adequate for operation at maximum temperatures of 973 K (700°C), corresponding to maximum bed temperatures at the bottom of the bed of 1023 K to 1123 K (750°C to 805°C). Final computer runs were performed over the expected range of operating conditions to support the safety analysis. Some design improvements are also being investigated. These runs are expected to be completed soon, allowing procurement of containment components to be initiated in January.

In November and December, experimenters conducted the first two series of low-temperature tests on refractory material compatability. These tests were conducted at 573 K (300°C), 50 ppm O_2 and at 1073 K (800°C), 2 ppm O_2. No significant corrosion of any of the specimens was observed based on a visual observation of the test specimens. More detailed analysis of the specimens remains to be accomplished. An unforeseen difficulty in the oxygen loading procedure has delayed the tests with high-oxygen-content sodium. This difficulty is under investigation and should be resolved early in January, allowing the conduct of those tests.

Although some tubes have been delivered for the high temperature tests to be conducted at Los Alamos, most remain to be delivered. Initiation of the high temperature tests awaits delivery of the tubes and completion of the low temperature tests.

Sandia project-management-support personnel were contacted in November to assist in the preparation of a project flow chart for the D10/D13 experiments. This flow chart will be used to define required tasks, resources required to complete those tasks, to identify critical points for the timely progress of the D10/D13 project, and to provide a mechanism for monitoring the status of the project. A preliminary flow chart was prepared and, as expected, procurement of a suitable high temperature crucible directly determines the schedule of the project. Because a material has not yet been selected and will not be selected until February, the time required for fabrication cannot be determined precisely, making the overall project schedule somewhat uncertain. The flow chart will be continuously reviewed and updated as information becomes available and as tasks are completed.
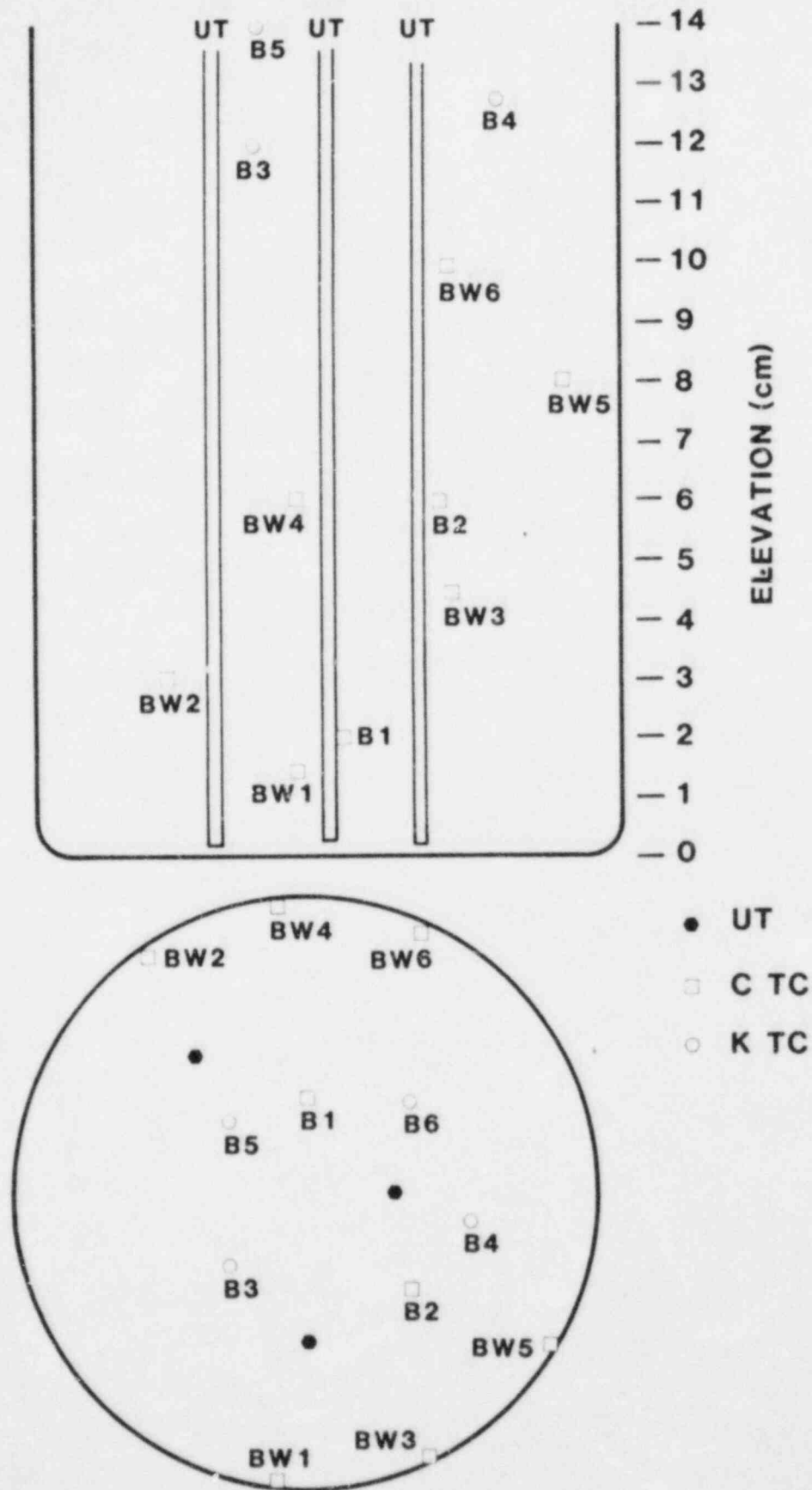
Figure 1.4-12. Thermocouple Locations (A)

89
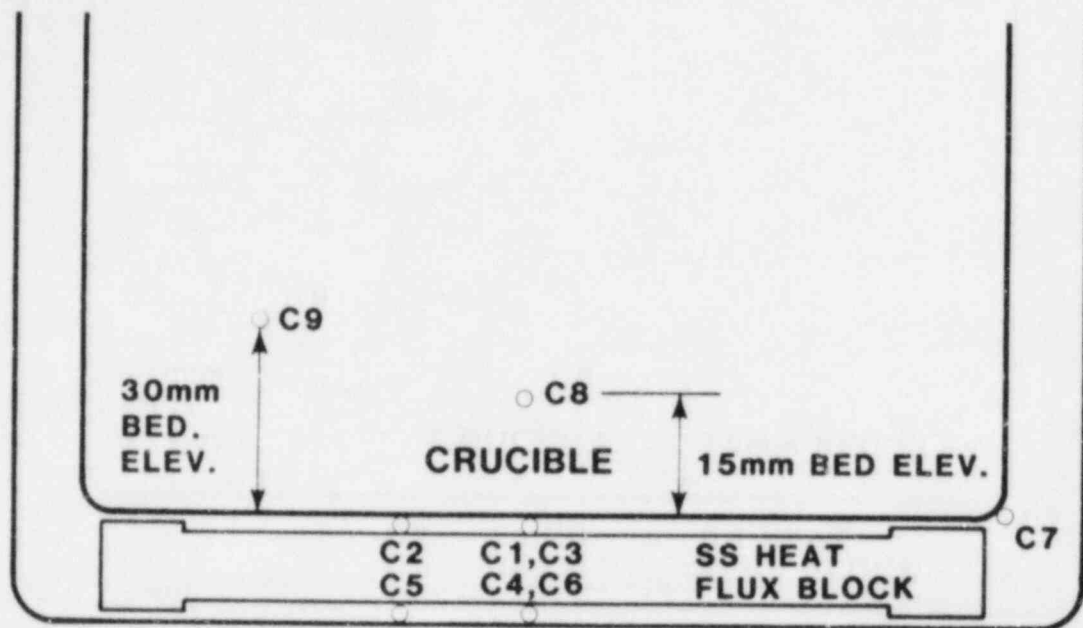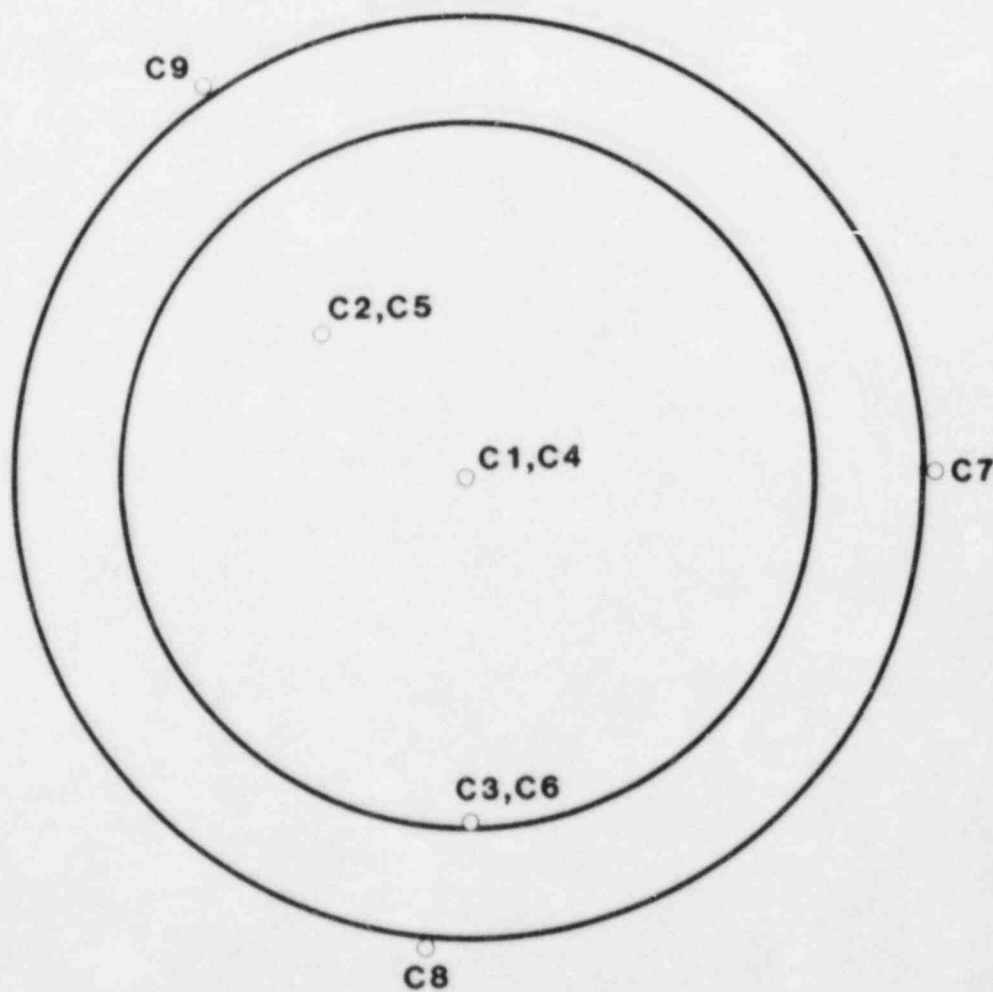
Figure 1.4-13. Thermocouple Locations (B)

Project personnel reviewed the status of the D10/D13 project with NRC sponsors in December. The materials compatability program, including current operations and anticipated schedule, was reviewed in detail. An overall program schedule was presented, with D10 occurring in February 1984 and D13 in May 1984. A large uncertainty exists in this schedule in that with selection of a crucible material remaining, the fabrication time for the crucible cannot be considered to be firmly established.

1.5 Dry Debris Coolability
(J. T. Hitchcock, 6421; J. E. Kelly, 6425)

1.5.1 Introduction

The Dry Capsule studies, the follow-on to the Molten Pool program, are using prototypic reactor materials to investigate experimentally the progression of a debris bed from dryout to melt and the interaction of the melt with structural and core retention material.

1.5.2 In-Pile Experiment Program

The DC 1 Experiment, the next in-pile test, will investigate the thermal characteristics of an internally heated UO_2 debris bed from 1273 K (1000°C) to melt and the phenomenology and thermal characteristics of a molten pool. During this quarter, project personnel completed the stress analysis on the containment design, the experiment plan was written and approved by both the ACRR Safety Committee and the Sandia Reactor Safety Committee (SRSC), and the fabrication of the experiment hardware was completed.

The containment design was shown to be structurally acceptable based on criteria of (1) survival for 4 hr without creep rupture and (2) a factor of safety greater than 4 for ductile rupture. Calculations were performed for both normal and postulated abnormal conditions. Abnormal conditions included failure of the primary vessel, failure of the secondary vessel, and loss of helium coolant flow. A final set of calculations considered a temperature 100°C above the expected values.

The experiment plan showed that the DC 1 experiment can be performed in a manner consistent with public and occupational safety. The plan was approved by both the ACRR Safety Committee and the SRSC contingent upon minor changes to the instrumentation.

1.5.3 Postdryout Debris Bed Modeling

The analysis of the postdryout behavior of reactor debris material is extremely important in reactor safety analyses. Special interest is attached to the progression of the debris to a molten state and the subsequent interaction of the core melt with structural and core retention materials. Current analyses rely heavily on experimental measurements, which are few in number because of the complexity of the phenomena. Consequently, analytical models would be desirable to predict the postdryout behavior of debris beds. Of

course, these models must depend implicitly on experiments that identify the important phenomena.

Sandia staff members are developing a one-dimensional model for analyzing the postdryout behavior of debris beds. This model, while still in a preliminary form, attempts to account for both the heat transfer within the bed and the motion of molten debris. By combining these phenomena, calculations can be performed that will predict the heatup and meltdown of debris beds.

The model is best described as a one-dimensional transient-heat conduction analyzer with the material motion overlayed. The heat transfer within the bed includes both radiation and conduction through the use of effective thermal conductivity models. Currently, the model assumes that convection can be ignored because it assumes that the gas (sodium vapor) is stagnant. The model also assumes that the gas and particulate are in equilibrium. With these assumptions, the mixture energy equation for the dry debris bed is given by

$$[(1 - \epsilon)(\rho C_{p_s}) + \epsilon (\rho C_p)_g] \frac{\partial T}{\partial t} = \frac{\partial}{\partial x}\left(k_e \frac{\partial T}{\partial x}\right) + (1 - \epsilon)\rho_s S \qquad (1.21)$$

where ϵ is the porosity, k_e is the effective thermal conductivity, S is the specific debris power (W/kg), ρ is the density, C_p is the specific heat, and T is the temperature.

Equation 1.21 is solved by establishing nodes for the bed and using a finite difference approximation for the equation. Porosity and particle size are allowed to be spatially dependent while the conductivity is temperature-dependent. Either constant temperature or specified heat flux can be used as boundary conditions. With these constraints, the temperature in the bed can be calculated as a function of time and space.

The unique feature of the model is its ability to calculate the melting and relocation of debris. The procedure the model uses is to solve mass and energy conservation equations for the molten debris. The motion of melt is prescribed from simple criteria that resulted from a parametric study using the PLUGM computer code.[1-14] Solution of these conservation equations, along with the prescribed motion, allows the melt to be redistributed throughout the bed.

The mass and energy equations simply require that mass and energy be conserved when molten material is transported. The main assumption of this model is that equilibration of the liquid and solid occurs instantaneously. This assumption is reasonable in view of the large surface area in a porous bed over which the liquid must flow. Because of the assumption, only one temperature needs to be calculated for each node.

The motion of the melt is the most difficult parameter to calculate. Uncertainties in both the physical properties, such as viscosity and surface tension, and the appropriate form of the momentum

equation contribute to this difficulty. Certainly, if the particle
diameter is small, the main force in the bed would be the capillary
force. This force tends to draw the melt into the bed in a spheri-
cally symmetric manner. Capillary force also tends to hold a certain
fraction of the liquid in the bed (i.e., the residual saturation).
Gravity tends to move the melt downward while viscous forces tend to
prevent penetration of the melt into the bed.

Except for the gravitational force, the other forces vary with
changes in either the porosity or the particle diameter. As the
particle diameter or the porosity decreases, the capillary force in-
creases. The viscous force also increases as either the particle
diameter or the porosity decreases.

For LMFBR debris beds being considered, the capillary force will
be the dominant force in the bed. When melt forms, it is rapidly
accelerated and drawn into the porous bed. However, once all the
liquid is within the bed, the driving force for capillary flow is lost
and the motion will quickly slow or stop. Of course, some downward
motion will occur because of gravity. Surface tension forces will
also hold back some of the liquid in the form of a film on the par-
ticles.

To estimate the penetration distance of the melt, a parametric
study was performed with the PLUGM computer model. This model solves
coupled mass, energy, and momentum equations for flow of a liquid
through a channel or porous medium. This model predicts freezing and
plugging of the flow channel. PLUGM was used to calculate the pene-
tration distance for a variety of test cases.

In these cases, a molten UO_2 reservoir was allowed to flow into a
porous bed. The porosity and temperature distribution of the bed were
varied about nominal bed values. The height of the reservoir was also
varied. The results of these tests indicated that the melt penetra-
tion was limited, either by plugging (i.e., freezing of liquid to
block the flow) or by depletion of liquid by film deposition on the
particles. In either case, the distance was limited to less than 1
cm. Consequently, this limit was taken for penetration of the melt
into the bed. The appropriateness of this limit will need to be
assessed in future work.

With the above prescribed motion of the melt, the model predicts
the meltdown sequence of a bed. The calculational procedure begins a
given time step with a known temperature and porosity distribution.
From these, material properties (conductivity, density, etc.) and the
power distribution are calculated. The energy equation is then
solved, resulting in a new temperature distribution. The size of the
melt zone (if any) is determined and the mass of melt is calculated.
Because the penetration by melt is nearly symmetric, half the melt is
moved upward and half is moved downward. As the melt moves into the
porous bed, it is equilibrated with the solid. If the upward-moving
melt plugs the bed (i.e., the local porosity goes to zero), then no
more liquid is moved upward. At the end of a time step. the new
porosity distribution is calculated and the temperatures are corrected

to reflect the equilibration procedure. The calculation continues, then, by advancing the time step and repeating the above steps.

One additional feature of the model is the void formation capability. As the center of a bed melts and the upward flow of the liquid plugs the bed, the melting solid can only move downward. If this occurs, a void will be left behind, provided the upper bed does not collapse. If the void forms, as it did in the MP-2 test, then radiation through the gas is included in the model. This void tends to insulate the melt from the upper boundary condition.

If constant-temperature boundary conditions are used, then a steady-state condition can be achieved. The results of such a calculation are shown in Figure 1.5-1. The figure shows that a porous layer exists on both the top and the bottom of the bed. The regions denoted as crust are those areas with zero porosity. Above the lower crust is a molten pool. Currently only conduction is considered in the molten pool. The modeling will need to be expanded to include natural convection effects within the pool. Nevertheless, this example shows the main features of the current model, which include the capability to heat the bed, melt and relocate mass, and form a voided region.

1.6 <u>References</u>

1-1. D. A. Powers and J. E. Brockmann, <u>Fission Product Release During Molten Core Debris Interactions with Concrete</u> (Albuquerque, NM: Sandia National Laboratories, to be published.)

1-2. D. E. Mitchell et al, <u>Intermediate Scale Steam Explosion Phenomena: Experiments and Analysis</u>, SAND81-0124, NUREG/CR-2145 (Albuquerque, NM: Sandia National Laboratories, 1981).

1-3. <u>Pressure Safety Practices Manual</u>, SAND76-0424 (Albuquerque, NM: Sandia National Laboratories, March 1979).

1-4. C. A. Tudbury, <u>Basics of Induction Heating</u>, Vol. 1 (New York: NY: John F. Rider Publishing, Inc., May 1960).

1-5. M. Slurzberg and W. Osterheld, <u>Essentials of Electricity-Electronics</u>, 3rd Ed. (New York, NY: McGraw-Hill Book Company, 1965).

1-6. L. S. Tong, <u>Boiling Heat Transfer in Two-Phase Flow</u> (New York, NY: John Wiley and Sons, Inc., 1965).

1-7. H. J. Ivey and O. G. Morris, <u>On the Relevance of the Vapor-Liquid Exchange Mechanism for Subcooled Boiling Heat Transfer at High Pressures</u>, AEW-R-137 (Dorset, England: UKAEA Winfrith, 1962).

1-8. W. W. Tarbell et al, <u>Sustained Concrete Attack by Low-Temperature, Fragmented Core Debris</u>, SAND82-2476, NUREG/CR-3024 (Albuquerque, NM: Sandia National Laboratories, 1982).
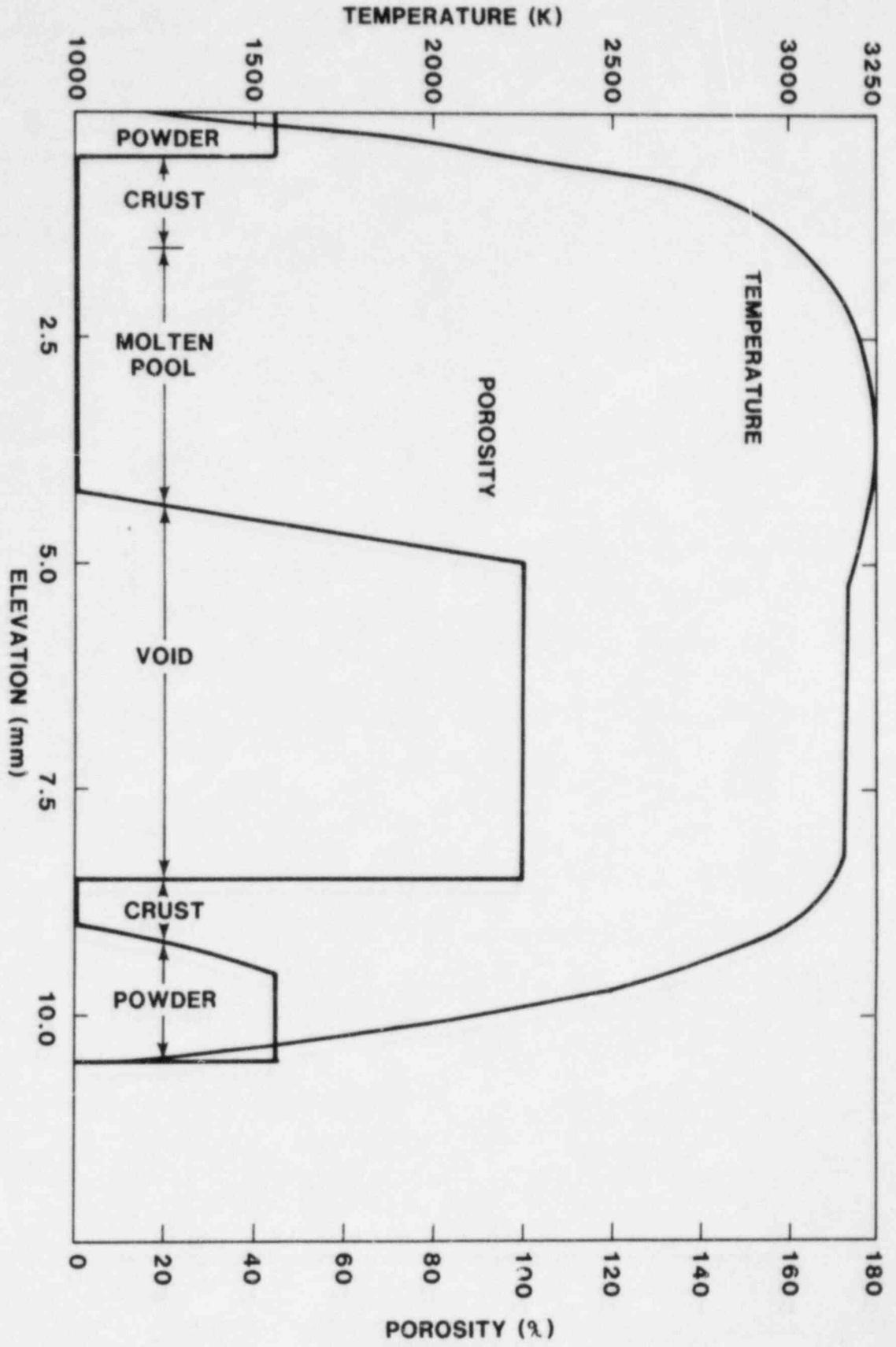
Figure 1.5-1. Steady-State Temperature and Porosity Distribution in a Partially Melted Debris Bed

1-9.   J. R. Welty, Engineering Heat Transfer (New York, NY: John Wiley and Sons, Inc., 1974).

1-10. F. P. Incropera and D. P. DeWitt, Fundamentals of Heat Transfer (New York, NY: John Wiley and Sons, Inc., 1981).

1-11. C. W. Keenan and J. H. Wood, General College Chemistry, 4th Ed. (New York, NY: Harper and Row Publishers, 1971).

1-12. Radiography in Modern Industry (Rochester, NY: Eastman Kodak Co., 1980).

1-13. Preliminary Assessment of Core Melt Accidents at the Zion and Indian Point Nuclear Power Plants and Strategies for Mitigating Their Effects, Vol. 1, NUREG-0850 (Washington, DC: US Nuclear Regulatory Commission, 1981).

1-14. M. Pilch and P. K. Mast, PLUGM: A Coupled Thermal-Hydraulic Computer Model for Freezing Melt Flow in a Channel, SAND82-1580, NUREG/CR-3190 (Albuquerque, NM: Sandia National Laboratories, to be published).

1-15. J. E. Kelly and R. J. Lipinski, "D9 Pre-Experiment Calculations," memo to C. A. Ottinger and G. W. Mitchell (Albuquerque, NM: Sandia National Laboratories, October 13, 1982).

1-16. R. J. Lipinski, A Model for Boiling and Dryout in Particle Beds, NUREG/CR-2646, SAND80-0765 (Albuquerque, NM: Sandia National Laboratories, 1982).

1-17. J. E. Gronager et al, PAHR Debris Experiment D-4, NUREG/CR-1309, SAND80-2146 (Albuquerque, NM: Sandia National Laboratories, 1981).

1-18. G. W. Mitchell et al, Heat Removal from a Stratified UO_2-Sodium Particle Bed, NUREG/CR-2412, SAND80-1622 (Albuquerque, NM: Sandia National Laboratories, 1982).

1-19. G. W. Mitchell and R. J. Lipinski, "Preliminary Report of the D7 Debris Bed Experiment," memo to Distribution (Albuquerque, NM: Sandia National Laboratories, June 21, 1982).

1-20. R. J. Lipinski, "D5 Interpretation and Speculation," memo to R. L. Coats (Albuquerque, NM: Sandia National Laboratories, March 10, 1982).

1-21. R. E. Holtz, The Effect of the Pressure-Temperature History upon Incipient Boiling Superheats, ANL-7184 (Argonne, IL: Argonne National Laboratory, 1966).

2. HIGH-TEMPERATURE FISSION-PRODUCT CHEMISTRY AND TRANSPORT
(R. M. Elrick, 6422; R. A. Sallach, 1846)

2.1 Introduction

The purpose of the High-Temperature Fission-Product Chemistry and Transport program is to establish the data base necessary to predict properly fission-product behavior during severe accidents. This experimental task is being pursued by three interrelated activities:

a. Definition of thermodynamic data and chemical reaction characteristics of particular fission products of interest.

b. Examination of the transport properties of fission products in prototypic environments of steam and hydrogen.

c. Comparison of the observed behavior of the fission products with predictions made by purely thermodynamic considerations.

Transport properties of the fission products are under study in the Fission-Product Reaction Facility (FPRF), developed as part of this program. The FPRF allows moderately volatile fission products to be generated in flowing steam and hydrogen mixtures at temperatures up to 1273 K (1000°C). The fission-product stream passes over alloys representative of structural materials in reactor cores. A Raman spectroscopy unit has been developed that allows determination of the chemical form of fission products in the vapor state.

2.2 Discussion of the Research

During this quarter, project personnel conducted the last test in the series to study the effect of cesium-iodine compounds on structural materials. This test involved CsOH in steam exposed to Inconel 600. A new series of tests began examining the chemistry of the control-rod material boron carbide (B_4C) exposed to steam only and then to steam and a fission product. Two tests were run, B_4C and steam (at 1000°C) in an Inconel-lined reaction tube, and then a similar run where CsOH was introduced into the steam downstream of the B_4C. Results of these tests will be reviewed.

The FPRF in which these experiments were conducted is described in earlier reports. It consists of a boiler to produce saturated steam, a critical orifice to regulate steam flow, a superheater to heat the steam, a method for mixing a controlled concentration of fission-products vapor with steam, a reaction tube in which the chemistry occurs, and a condenser.

97

To examine the reaction of CsOH vapor and steam at 1273 K (1000°C) in the presence of Inconel, vapor from CsOH heated to about 1003 K (730°C) was mixed with steam flowing at a rate of 1 g/min (a corresponding flow velocity of ~10 cm/s). The high-temperature sections of the facility were made of Inconel; the reaction tube was lined with a fresh sheet of Inconel, and Inconel coupons were placed along the tube. Typically, the steam system was brought to temperature and steam was introduced. After experimenters took several condensed steam samples, the CsOH was brought to temperature and held for about two hours. After the CsOH cooled, several more steam condensate samples were taken before the steam flow was stopped; steam flowed for about 4 hours.

Preliminary analysis consisted of atomic absorption spectroscopy (AA) on steam condensate samples and X-ray fluorescence on several coupons. Figure 2.2-1 shows a schematic of the apparatus with the results of these analyses. Using a standard timed exposure, fluorescence counts for the same element can be compared from coupon-to-coupon to give a measure of relative concentration. The background count is about 30.

Inconel coupons upstream of the injection point for CsOH vapor (position A) show no deposit of cesium but give 4500 counts from iron, 23,000 counts from nickel and 5200 counts from chromium. Downstream from the injection point (position B), there were 200 to 300 counts from cesium (not water soluble) 4500 from Fe, 25,000 from Ni, and 5000 from Cr. Investigators concluded from this that the CsOH had reacted to some extent with the Inconel. (The extent of reaction and the reaction rate will be estimated when quantitative concentration data are available.) However, some of the cesium remained in the steam, as indicated by the ~40 ppm of cesium found in the condensate by AA.

Figure 2.2-2 shows the experimental arrangement used for the series of B_4C experiments. Boron carbide particles about 0.07 cm in size were packed in a sieve that filled the 2.5-cm-diameter flow tube for about 1.2 cm of its length. (Particle surface area was measured by the BET method.) The particle bed, placed upstream in the reaction tube, provided a reaction-rate-limited geometry and distributed any reaction products uniformly across the flow cross section. Inconel and B_4C coupons were placed along the length of the reaction tube.

In the first experiment, steam at 1273 K (1000°C) flowed at the rate of 1 g/min for slightly more than 2 hours. Posttest analysis showed that the particle bed was fused with a hard shiny material which also coated the B_4C coupons. A plug of material formed in the condenser; it completely filled the 2.5-cm-diameter tube (Figure 2.2-3) but was porous to the steam and noncondensable gases. In general, the plug could filter aerosol particles and might react with some of the vapors. The steam-condensate samples contained, on the average, 1500 ppm of boron (by AA). The hard shiny coating on the B_4C was water soluble. Its removal from the coupons showed that reaction with steam had severely pitted the surface of the coupons (Figure 2.2-4). During the 2-hour exposure to steam, the 0.15-cm-thick coupons were reduced to half this thickness, and in spots the erosion perforated the coupon, as the figure shows. The complete reaction is

INCONEL COUPONS

SUPERHEATED
STEAM →

(A)

CsOH
IN

(B)

TO
CONDENSER →
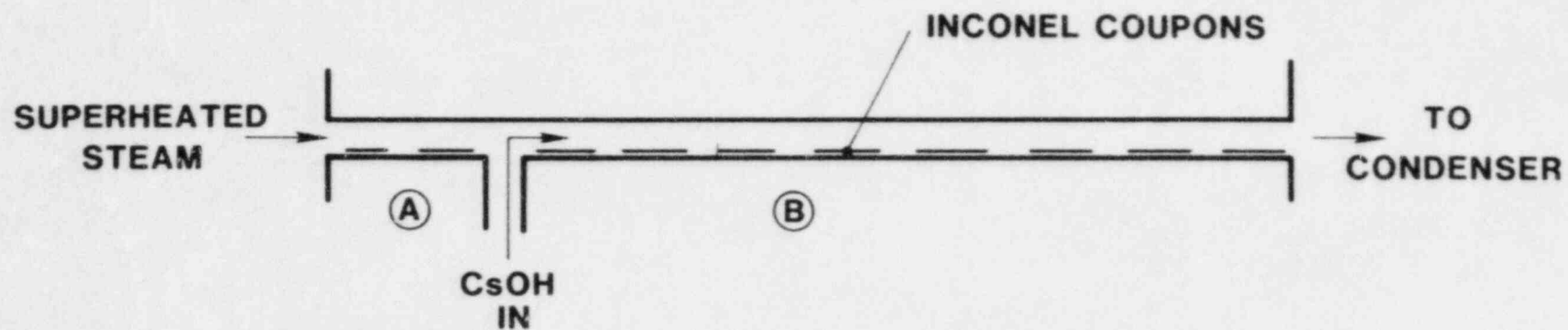
(A) INCONEL COUPON

Cs BACKGROUND
Fe 4,500
Ni 23,000
Cr 5,200

(B) INCONEL COUPON

Cs   200 TO 300
Fe 4,500
Ni 25,000
Cr 5,000

Figure 2.2-1.   Schematic of the Reaction Tube in the Experiment to
Examine the Effect of CsOH in Steam (1000°C) Exposed to Inconel 600.
(Results are normalized counts from X-ray fluoresence analysis of the
coupons; a background count is about 30.)
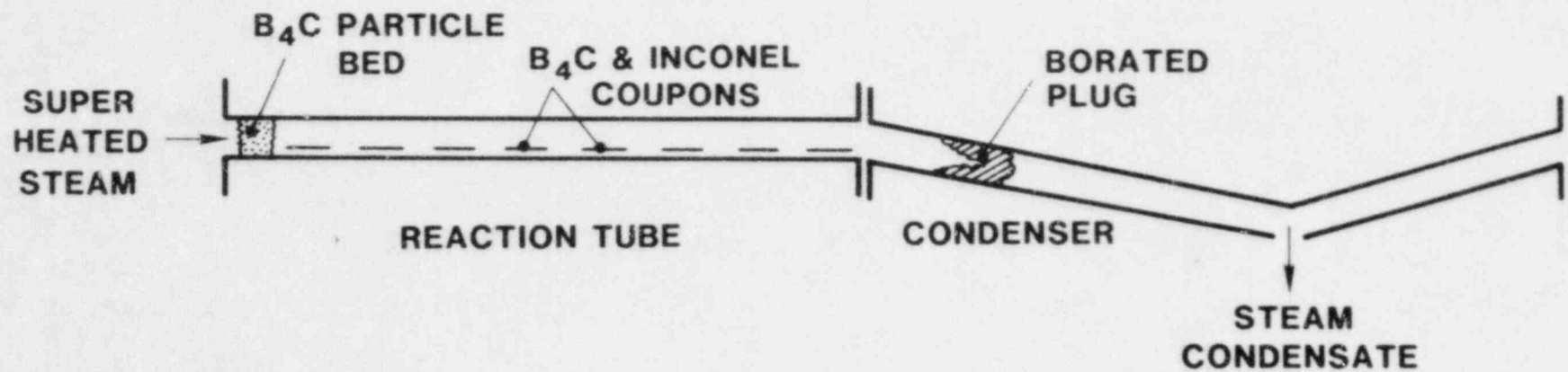
Figure 2.2-2. The Experimental Arrangement to Study the Reaction between Boron Carbide (B_4C) and Steam in an Inconel 600 System. (Position of the borated plug is indicated.)
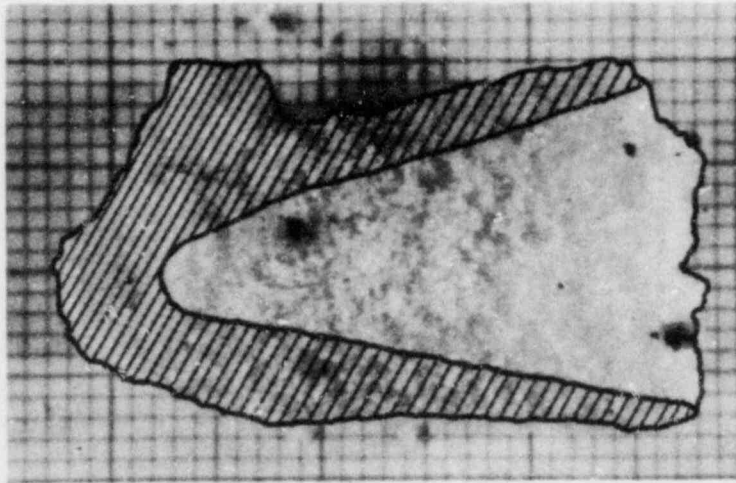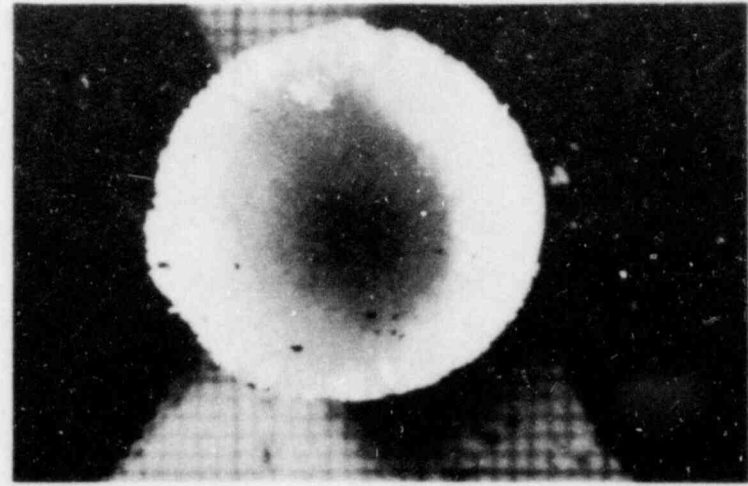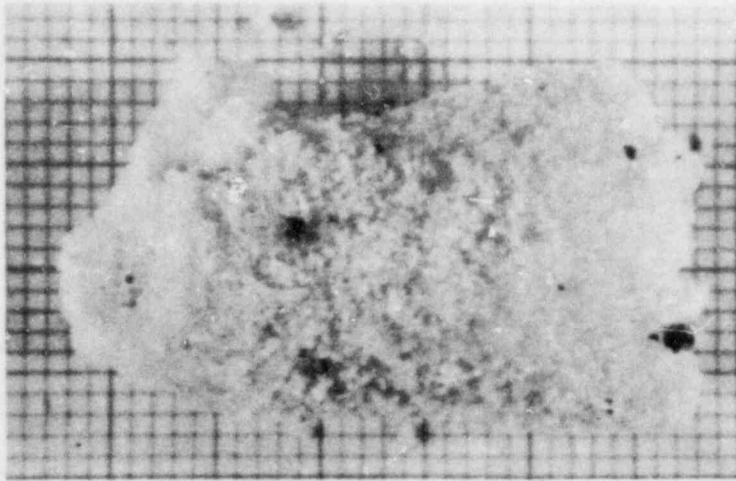
CROSS SECTION OF PLUG

Figure 2.2-3. The Boric Acids Produced from the Reaction of Boron
Carbide with Steam (1000°C) that Plugged the 2.5-cm-Diameter Condenser
Tube.
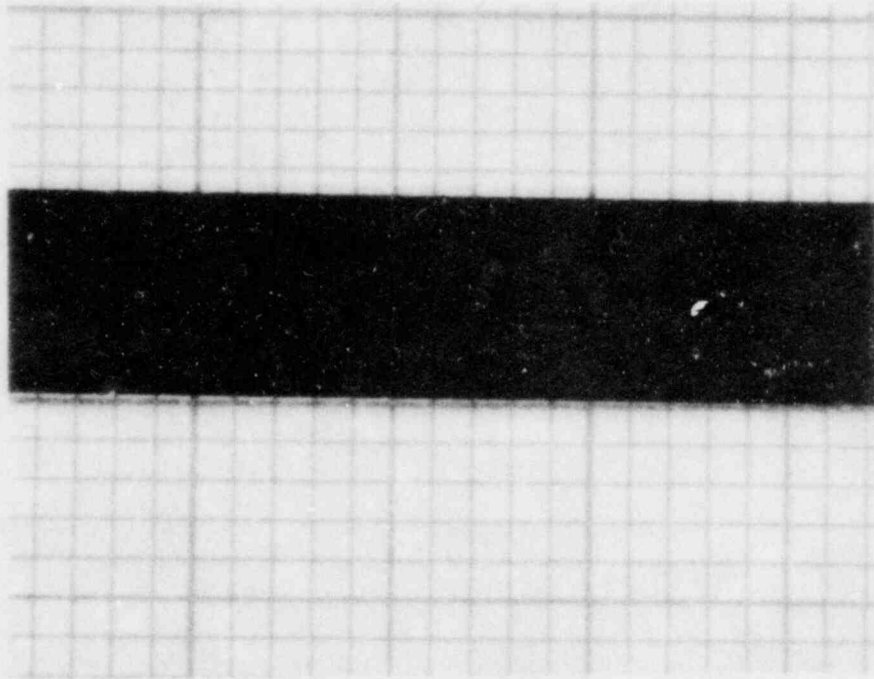
BEFORE   **AFTER**
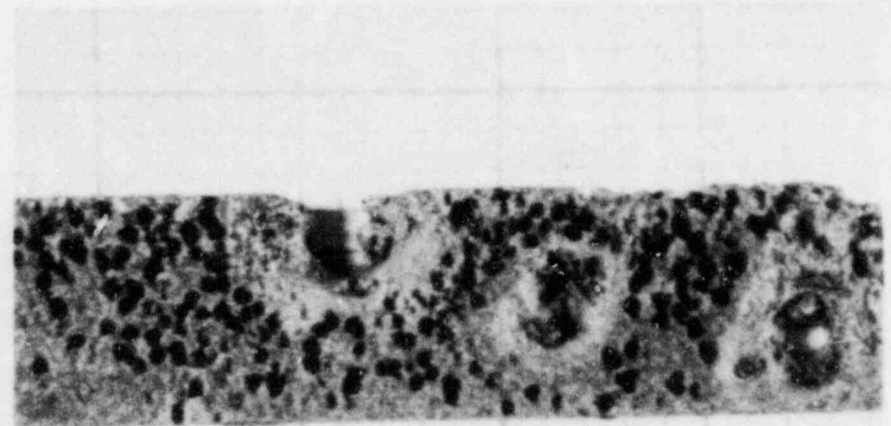
Figure 2.2-4. A Coupon of Boron Carbide Before and After Exposure to
Steam at 1000°C for 2 hr. (In some places, the pitting is seen to go
through the initially 0.15-cm-thick coupon.)

pictured as occurring in two steps. The steam reacts with the B_4C to form a fairly high-boiling-point oxide, B_2O_3 ($B_4C + 6H_2O \rightarrow 2B_2O_3 + C + 6H_2$) which is the water soluble deposit on the B_4C. The oxide then reacts with steam to produce some combination of more volatile boric acids (metaboric, HBO_2 and orthoboric, H_3BO_3):

$$B_2O_3 + H_2O \rightarrow 2HBO_2, \text{ and}$$
$$HBO_2 + H_2O \rightarrow H_3BO_3.$$
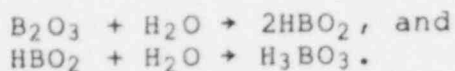
These are probably the boric acids that condense to form the borated plug in the condenser. They also account for the boron in the condensate.

Although addition of CsOH to the above system does not seem to alter the observed boron chemistry materially, the cesium reactions are significantly different from those of cesium in the CsOH, steam, and Inconel system. In the second experiment, performed with B_4C, the CsOH, heated to 923 K (650°C), was introduced into the 1273 K (1000°C) steam for about 2 hours. Figure 2.2-5 shows a schematic of the experimental arrangement and the results of posttest analysis by X-ray fluorescence and AA. No cesium could be detected on the Inconel, position B (compared to 200 to 300 counts in the CsOH, steam, Inconel system). Iron, nickel, and chromium counts on the Inconel (positions A and B) were similar to previous levels. A significant amount of cesium (2000 counts) reacted with the boric oxide on the B_4C coupons (position C). The oxide also acted as a flux and dissolved a rather large amount of Fe (6000 counts) and lesser amounts of Ni (200 counts) and Cr (40 counts). The borated plug formed again in the condenser, and about the same level of boron was measured in the steam condensate samples as was found in the B_4C, steam system. However, only 0.1 to 1 ppm of cesium was detected in the condensed steam compared to as much as 40 ppm before. The preliminary conclusions are:

a. CsOH reacts mildly with Inconel in the presence of steam.

b. In the presence of steam and boric acids, CsOH reacts with Inconel to a much lesser degree.

c. The presence of boric acids decreases the stability of CsOH vapor significantly. A very stable compound that might have formed as a result of this interaction is $CsBO_2$, according to the equation

$$CsOH + HBO_2 \rightarrow CsBO_2 + H_2O.$$

2.2 Presentations

a. R. M. Elrick and R. A. Sallach, "Fission Product Chemistry Experiments at Sandia", 10th Water Reactor Safety Research Information Meeting, Gaithersburg, MD, October 12-15, 1982.

b. R. M. Elrick and R. A. Sallach, "Status of Fission Product Chemistry Experiments at Sandia", US - German Core-Melt Information Exchange Meeting, Karlsruhe, Federal Republic of Germany, October 28, 1982.
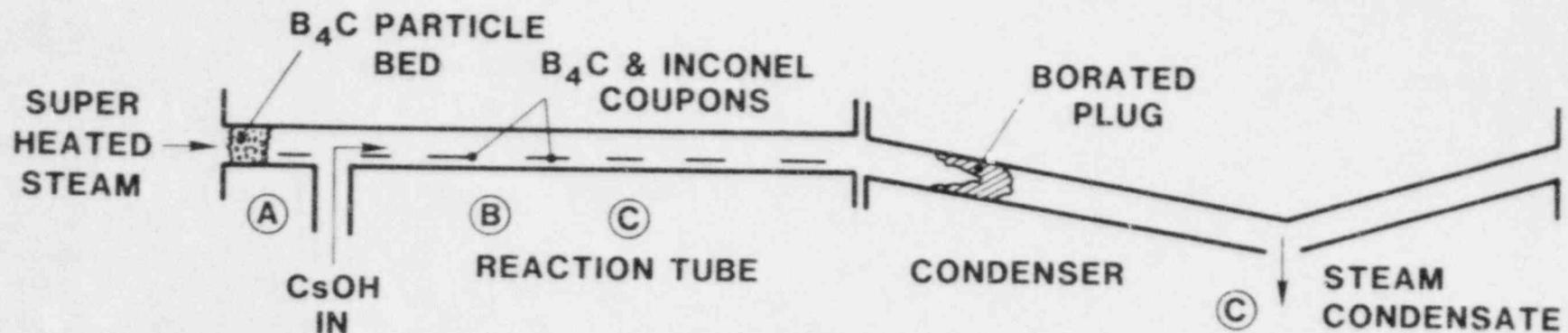
Figure 2.2-5. Experimental Arrangement to Study the Reaction between Boron Carbide (B_4C) in Steam with CsOH Vapor in an Inconel 600 System. (Results are normalized counts from X-ray flourescence analysis; a background count is about 30.)

3. CONTAINMENT ANALYSIS

(M. E. Senglaub, 6424; K. D. Bergeron, 6424;
P. Rexroth, 6424; W. Trebilcock, 6424; K. Murata, 6424;
F. W. Sciacca, 6424; M. J. Clauser, 6424)

The Containment Analysis programs are centered on the development, testing, and application of the CONTAIN code. CONTAIN is NRC's general-purpose computer code for modeling containment response to a severe accident and for determining the consequences thereof. It provides models, for both LWR and LMFBR systems, of phenomena occurring outside the reactor primary system and inside the containment building, including interactions between core debris and coolant or concrete, hydrogen combustion, thermal-hydraulics of the gases in the various compartments of the containment building, aerosol behavior, and fission-product transport. Major parts of CONTAIN are operational, and these are being extensively tested and applied to reactor accident analysis.

3.1 CONTAIN Code Development

a. MEDICI. In the interest of obtaining feedback and alternative models for the MEDICI ex-vessel debris/coolant interaction modeling project, a meeting was set up in Culham, England, with R. Peckover and R. Young from Culcheth, as well as F. Briscoe, B. Turland, and K. Moore from Culham. K. Bergeron (Sandia) presented a brief review of the MEDICI modeling efforts to date. An additional goal was to learn of ongoing UKAEA work that might be directly transferable to MEDICI. Although no new models are now available that might be suitable for adaptation to MEDICI, Turland and Moore are working on a time-dependent debris-bed dryout model that could help verify the simpler models anticipated for MEDICI. The UK representatives expressed interest and willingness to participate in the peer-review phase of the project.

A skeleton version of the MEDICI code is now being written. Enough models have been defined in the top-down design stage to write a program that accepts input, calls the various routines, and can be used as a driver for developing and debugging individual modules. A melt-release subroutine and several input subroutines have been completed.

Dr. M. Corradini of the University of Wisconsin, under contract to the MELCOR project, is assisting in developing several modules for MEDICI, implementing models he previously developed for fuel-coolant interactions. Dr. G. Moses, also of the University of Wisconsin, under contract to the CONTAIN code development project to assist in developing MEDICI, will work on numerical analysis and programming aspects of MEDICI. Sandia staff members met with Drs. Moses and Corradini to explain, demonstrate, and discuss the skeleton code.

b. Condensation on Structures. A major revision of the model for vapor condensation on structures has been completed as a result, in part, of the deliberations of an informal working group involving individuals from three different code projects at Sandia, CONTAIN,

HECTR, and MARCH. A significant feature of the new model, and of the code structure that implements it, is the flexibility to use a variety of heat transfer correlations for ordinary convective heat transfer in order to generate correlations for condensation heat transfer. A forced convection correlation can now be used, with different surface velocities (possibly time-dependent) for each structure in each cell. This type of capability is essential for treating initial phases of blowdowns and vessel-failure scenarios.

c. SINTER. The basic structure has been completed for the new version of SINTER, the LMFBR reactor-cavity model to be used in place of the model currently in CONTAIN. The initial phases of the development consisted of providing the interfaces to the source-physics routines characteristic of a debris pool, the basic differencing scheme, and a solution algorithm. The initial test consisted of a simple conduction problem with constant boundary conditions, and a second test added a volumetric heat source. The results of the tests agreed within fractions of a percent with the analytic results.

The next stage of development treats interfaces that move through the various layers of the problem being modeled. The required terms have been added to the model.

Stability checks were performed on the terms currently incorporated into the model, and indications are good that differenced equations are stable. A problem existed with large Nusselt numbers at layer surfaces, but a solution algorithm was developed that places no restrictions on the size of the surface Nusselt number in the solution of the model. An automatic coupling option was developed that will allow a tighter spatial coupling in the solution algorithm by re-specifying the number of nodes to be coupled. This will provide the ability to improve the coupling under flow reversal conditions where marching schemes have problems.

The terms necessary to treat moving interfaces in the ASWR (asymmetric weighted residual) solution algorithm have been incorporated into the stand-alone version of the revised SINTER model. This portion of the model is now undergoing testing.

d. Engineered Safety Systems Models. Fission-product and aerosol washout capability has been added to the containment-spray model in CONTAIN. Checkout and verification of the spray model are continuing.

e. CONTAIN-CORCON Link. Work was completed on a version of CONTAIN with a CORCON option, allowing the user to use CORCON instead of SINTER in one of CONTAIN's cells. A test case that uses SINTER on the pool of one cell and CORCON on the dry cavity of another cell has been run and gives reasonable results. Source tapes for both CONTAIN and CORCON for this version have been created and checked. A document has been completed that describes this version, gives the test-case input and some of the output, and describes the procedure for running this version from the source tapes.

f. MELCOR Physical Processes Assessment: Reactor Cavity Phenomena. The first major goal of the MELCOR project is to produce a major review of all the key physical phenomena that affect the progression of a severe LWR accident, and the consequent radiological effects. The task has been broken up into many components, a major one of which concerns physical processes occurring in the reactor cavity. These include fuel-coolant interactions, steam explosions, debris-bed formation, debris-bed heat transfer, core/concrete interactions, hydrogen generation, and aerosol generation and decontamination in pools. This review was initiated in December, and a first draft report will be completed in February. The report will consist of a review of phenomena and existing models, plus a recommendation for model selection for the MELCOR-1 code, as well as for MELCOR-2.

g. FORTRAN 77 Conversion. Project personnel are finishing a version of the code that incorporates the various modifications and improvements completed to date. For this version, several changes have been made to the input.

1. The input was restructured, and a MACHINE control block now must precede any other problem information.
2. The fission-product input is now specified only when fission products are used in the problem.
3. The CONTROL input block can now take either of two forms, one in which the parameters must occur in a prescribed order or one that uses individual keywords to specify the parameters. In the second form, the parameters may occur in any order, and omitted parameters are given default values.
4. Previously, the keyword FLOW was needed to turn on the atmospheric thermodynamic calculation; even in single-cell problems. Now, a new, more meaningful keyword, THERMO, also turns on the thermodynamics.
5. The routines that read input have been converted to FORTRAN 77. By using character variables, these routines should now function correctly on any computer, regardless of word length.

3.2 CONTAIN Testing and Validation

3.2.1 Testing

a. SINTER. A series of tests has been planned to investigate the handling of pool chemistry, pool sources, pool-heat transfer to structures and to the atmosphere, and fission-product heating by the existing (unrevised) version of SINTER. The test effort during this quarter concentrated on the areas of pool sources, pool chemistry, and pool-heat transfer. Previous efforts had indicated that the pool-chemistry testing simulating sodium/concrete interactions was quite complex. This testing was simplified by breaking it down into two test areas: pool sources and simpler chemical reactions.

All the pool-source tests conducted thus far have involved the addition or removal of materials from sodium pools. Some of the test variations included the following:

1. addition of materials at temperatures lower than that of the pool;
2. addition of materials at temperatures higher than that of the pool;
3. removal of sodium from the pool (negative source);
4. combinations of materials added and materials removed from the pool;
5. materials added with constant specific heats (per CONTAIN usage);
6. materials added with variable specific heats.

Where materials with constant specific heats were sources to the pool, results were generally quite good. The key parameters checked were pool-temperature change at specific times, for the cases where the source materials were cooler than the initial pool temperature, and time for the pool to reach its boiling point, for cases where materials were added at high temperatures. For the boiling cases, the CONTAIN predictions of sodium-boiling rates disagreed with the hand calculation predictions by about 30% to 40%. Tests in which materials with variable specific heats were sources to the sodium pool generally gave much poorer agreement with hand analysis results. For pool-cool-down cases, the disagreement regarding pool-temperature change at selected times was on the order of 15% to 20%. The pool-boiling cases showed deviations of about 30% to 40% between the calculated and CON-TAIN results for the time required for the pool to reach its boiling point. The net results of the pool source tests to date indicate that the source routines in CONTAIN work, but that the pool thermodynamics involving sources require further development.

The pool-chemistry test series included the following kinds of variations:

- pool sodium as a reactant;
- reactions not involving pool sodium;
- reactants with constant specific heats;
- reactants with variable specific heats.

The results of the pool-chemistry tests indicate that this rou-tine is at present not very trustworthy. Parameters, such as pool heatup and cooldown rates and time to reach boiling, vary considerably between CONTAIN and the hand calculations. The disagreement varies from very small to factors of about 4. The code appears to be handling the chemical reaction energy properly, and the errors appear to be related to the handling of pool-source and sink thermodynamics.

Early in this test series, the test results demonstrated the need to use a much tighter volume-fraction criterion for pool sources than is currently used in the unmodified CONTAIN coding. This criterion is used to determine which materials in the pool should be taken into account in the pool-heat balance and which should be ignored. The reference-volume-fraction limit below which materials are ignored is 10^{-6}. Even at this limit, poor heat balances were obtained. The volume-fraction limit was tightened to 10^{-10} in all of the cases noted

above. This improved the results but did not solve all of the problems. The default-volume-fraction criterion for pool materials should be made much tighter than the current value of 10^{-6}.

The present input routines require that either two or three reaction products be specified in the chemical reaction equations given in the input. Otherwise, subsequent input data is misread. Where a single reaction product was desired, this problem was circumvented by specifying 0.0 for the number of moles of an arbitrary second reaction product.

Tests were initiated in the area of heat transfer from the pool to surrounding structures. CONDUCT, a finite-difference, one-dimensional transient heat-conduction code, will be used to check the CONTAIN results for problems in this area. CONDUCT requires a relatively small amount of input and is fairly simple to use. The input for modeling the heat transfer from the sodium pool in the CRBRP reactor cavity to the surrounding structures was prepared. Volumetric heat sources representing the fission-product decay heat and the heat from the sodium/concrete interactions are included in the problem modeling.

b. _Aerosol Model_. CONTAIN aerosol calculations were compared directly with QUICK calculations for a check of the CONTAIN numerics and coding and for a comparison of QUICK's performance with that of the CONTAIN aerosol module. For these purposes the QUICK code was put into operation on the Sandia computers. The CONTAIN module ran appreciably faster than QUICK on a test problem while showing somewhat less sensitivity to variations in the number of particle-size classes in the range considered. The coding and numerical treatment in the module was verified by comparison to QUICK calculations for the AB1 and AB3 experiments in the containment systems test facility (CSTF) at HEDL.

3.2.2 Validation

a. _ABCOVE_. The CONTAIN blind prediction for the ABCOVE, AB5, experiment in the CSTF at HEDL was completed on schedule. Upon receipt of the preliminary sodium-aerosol data released by the CSTF project, the CONTAIN prediction and the experimental data were compared. Excellent agreement was found for the airborne mass concentration and the plated and settled mass. By inference, excellent agreement with the leaked mass would also be expected if the experiment leak rate were known. Qualitative agreement was also found for the particle-size distribution as a function of time, although further data analysis is required to assess the significance of the comparison for the size distribution. Comparison of one quantity (the median radius) with a raw data showed generally good agreement. Based on these results, CONTAIN (and MAEROS) appear to be in substantially better agreement with the experiment than any of the other codes.

b. _Visit to HDR Experimental Facility_. An important series of code and model validation experiments has been underway for the past year at the HDR experiment facility near Frankfurt, Germany. This is a decommissioned research reactor that is being used for full-scale

reactor blowdown experiments. CONTAIN is being used to model these experiments as part of its validation program. The facility was thoroughly inspected, and detailed photo-documentation was carried out. Important questions about the heat sink structures and flow paths were resolved. Further clarifications were obtained in subsequent meetings with the HDR plant manager and his staff, and with the HDR Project staff. These meetings also provided an opportunity to communicate to the Germans the differences between CONTAIN's models and more traditional design-basis-accident models. The use of a mechanistic aerosol model to treat the problem of liquid carryover from cell to cell (wet steam transport) was of considerable interest to the analysts.

Another important outcome of these meetings (and subsequent ones at KfK) was the realization that it was unlikely that CONTAIN could participate in the German Standard Problem effort, which is based on the HDR experiments but administrated by a separate organization, GRS, based in Garsching. This program can be viewed as a formal approval mechanism, akin to licensing, for computer codes used in German reactor safety analysis. The problem with CONTAIN's participation was that the deadline for submission of calculations was 22 November, earlier than the 31 January schedule that the HDR project itself was following (and on which CONTAIN's participation had been based from the beginning).

The first runs of the German HDR experiments involving the initial phase of a full-scale steam blowdown into containment were completed using a five-cell model for the complex containment building. Work is now underway to run the problem to 1500 s with a more realistic 14-cell model. This conversion is facilitated by some input-generating programs written for this specific purpose. Also to be added to the calculations is a treatment of wet steam as an aerosol, which should result in a more realistic treatment of the important "water carryover" program than is provided by any other code involved in the HDR code validation project. In addition, the new condensation model, including forced convection during blowdown phase, will be used.

Final calculations were completed on the CONTAIN code for the German code-validation experiment V44 at the HDR reactor facility. The experiment was a reactor-scale steam blowdown corresponding to a large LOCA in a complex configuration of cells and flow paths. It was the largest such validation experiment ever undertaken. Containment codes from several countries were used to predict the experimental results prior to release of the data. Although the experiment and most of the other codes participating involved only design-basis-accident phenomena, this "blind" code validation exercise represented an excellent opportunity to evaluate the adequacy of the relevant models in CONTAIN. The principal models involved were intercell flow, condensation/evaporation heat transfer, heat conduction in structures, and multicomponent thermodynamics. The configuration used for this calculation involved five control volumes and a new condensation/evaporation model that allowed both forced and natural convection regimes to be treated. The forced convection treatment was essential during

the blowdown because gas velocities were expected to be as high as several hundred meters per second during that period. A tape containing the code's predictions for 37 different sensors over a period of 1500 s was prepared according to the specifications of KfK, which is coordinating the validation exercise. These predictions included cell pressures, temperatures, gas densities, flow rates, structure temperatures, and heat transfer coefficients. Experimental data will be made available soon by KfK so that code predictions and measurements can be compared.

The HDR exercise not only was an opportunity to validate the relevant models in CONTAIN, but it also stimulated the development of some new features that should be useful for future applications. For example, a more flexible approach to output control was introduced, which keeps the amount of printed material down to the minimum the user needs. Also, a model for the effect of buoyancy on gas flow between cells of different elevations was developed and implemented (though it was not used in the final HDR calculations.)

c. Spray Washout of Radioisotopes. Testing and validation of the fission-product and aerosol washout features of the containment spray model continued. One of the containment systems experiments (CSE) performed at Pacific Northwest Laboratory (PNL) was modeled with CONTAIN. This experiment featured the spray washout of both iodine and aerosols from a heated and pressurized vessel. The spray-induced depletions calculated by CONTAIN compared well with the experimental values. A description of this calculation was prepared for the CONTAIN review meeting in Washington, D.C., in December.

3.3 Clinch River Containment Analysis

a. CRBRP Licensing. Sandia personnel met with NRC staff members on 13 October 1982, in Bethesda, Maryland, to discuss areas of technical assistance for the CRBRP licensing effort. Sandia personnel proposed three specific areas of technical assistance in which CONTAIN might be used:

1. evaluation of sodium/concrete interactions and the subsequent thermal and pressure loadings on containment;
2. evaluations of aerosol loads, overall aerosol effects, and fission-product release and transport;
3. evaluations of hydrogen accumulation and combustion.

The NRC staff generally agreed with the proposed technical assistance plan presented by Sandia personnel and offered several suggestions that were incorporated into the plan.

Part of Sandia's technical assistance to NRC on CRBRP licensing issues involves the assessment of aerosol behavior and aerosol effects following a vessel meltthrough accident scenario. To assist in this evaluation, both hand calculations and CONTAIN were used to establish the timing and rates at which sodium vapor might be entering the upper RCB for this event. The initial evaluations assumed an aggressive sodium/concrete interaction rate of 49 µm/s (7 in./hr) for the first

hour and then 7 μm/s (1 in./hr) for the remainder of the event. The nominal fission-product decay heat vs time was also used. The hand analysis did not account for heat transfer from the sodium pool to the reactor-cavity floor or walls, nor for sodium-vapor-condensation processes. Thus, the hand calculations give a conservative upper-bound estimate on the timing and extent of the entry of sodium vapor into the upper RCB. The CONTAIN analysis, however, includes heat transfer to the containment structures and allows for sodium-vapor condensation. These calculations have not yet been finalized.

b. <u>Aerosol Behavior</u>. The CRBR Project has used HAA-3B to predict the aerosol behavior in selected TMBDB scenarios for CRBR. CONTAIN predictions are being compared with the HAA-3B predictions, and significant differences between the two codes have been found. These are believed to result from the lognormal form assumed for the particle-distribution function in the HAA-3B code. The CONTAIN calculations shows a significant departure from a lognormal particle distribution when large aerosol densities occur. Previous comparisons between discrete and lognormal codes for small-scale experiments have shown differences similar to those observed for the TMBDB scenarios; the TMBDB calculations for full-scale containment under representative conditions may, however, show more directly the limitations of lognormal codes for containment analysis. Documentation of the differences in the code predictions and a thorough checking of the CONTAIN numerical algorithms are underway.

A prediction for the aerosol mass concentration for a CRBR TMBDB base case was initiated in order to compare CONTAIN results with the HAA-3B lognormal code under full-scale containment conditions and with a representative source term. By using CONTAIN in the same manner as in the ABCOVE prediction, sodium aerosol loading in the CRBR containment can be predicted. Specific calculations were made for a TMBDB base case in order to compare to HAA-3B calculations. The same CACECO-based source term was used for both HAA-3B and CONTAIN. The CACECO-based vent-rate table used in the HAA-3B calculations was not used, because CONTAIN normally would have only the provision for calculating venting in a mechanistic fashion. Instead, bounding calculations were performed at zero vent rate and at a vent rate near maximum. The conclusions reached were as follows:

1. For the duration of the source, the HAA-3B mass concentrations were a factor of 2 or 3 higher than the CONTAIN results.
2. Median particle sizes were typically a factor of 2 larger in the HAA-3B calculations.
3. The mass concentration was consistent with the expectation that HAA-3B would be conservative during the source.
4. Shortly after the end of the source, HAA-3B would be expected to underpredict the mass concentration seriously if the lognormal modeling were continued into this region and would overpredict the mass concentration if the Stirred Settling Model (SSM) were invoked at the end of the source. However, in the calculations, venting continued after the end of the

112

source at a rate sufficiently high to dominate natural re-
moval mechanisms shortly after the end of the source. In
this situation, inaccuracies in the lognormal modeling of
natural removal might not be severe even if lognormal model-
ing were used after the end of the source. In any case,
details of the way in which the source was cut off would have
to be known to make meaningful comparisons in this region.

3.4 LWR Containment Analysis

a. Aerosol Effects on Thermal-Hydraulics. A study of the
effects of coupling between thermal-hydraulic and aerosol behavior was
initiated. These calculations indicate that proper aerosol behavior
for the condensed water in the atmosphere is as important as surface
condensation in determining the course of LWR scenarios in which an
appreciable part of the primary system inventory is blown as steam
into containment.

Several CONTAIN calculations were performed that demonstrated
that the amount of water (mist) suspended in the atmosphere during a
severe accident can have a strong effect on the peak pressure result-
ing from a hydrogen burn or other strong source of heat. The peak
pressure can vary by a factor of 2 or 3 depending on the amount of
water remaining suspended. Accurate estimates appear to require the
use of CONTAIN's aerosol model. The results of these calculations
were presented at the CONTAIN Review Meeting at NRC, 13-14 December
1982.

b. Rainout of LWR Radionuclide Release Plumes. The aerosol and
fission-product models in CONTAIN treat the effects of moisture con-
densation, droplet formation, and rainout on the depletion of aero-
solized radionuclides within the containment building. J. Martin of
NRC has pointed out that, in the event the containment building fails
or otherwise releases saturated air at high pressure into the outside
atmosphere, the air becomes highly supersaturated at the lower pres-
sure, and rainout can occur in the vicinity of the reactor. To pro-
vide the appropriate source term for use in ex-plant atmospheric
dispersal codes such as CRC, containment codes such as CONTAIN need to
model these plume rainout effects. The effects are qualitatively
similar to those treated in CONTAIN but are sufficiently different in
detail to warrant a separate study. Effects that have been suggested
include plume depletion and far-field dose reduction resulting from
rainout effects, enhanced near-field ground contamination, and in-
creased plume buoyancy associated with the release of latent heat.

Several aspects of this problem are being addressed, using simple
scoping calculations, to gain insight into the order of magnitude of
certain key parameters and to determine which effects require more de-
tailed consideration in any comprehensive theoretical or experimental
treatment of this subject. Initial conditions considered included a
containment pressurized to 3 atm absolute, with 1 atm being air and 2
atm being water vapor. Since some containments (e.g., Zion) are
expected to fail only at much higher pressures, an initial pressure of
10 atm (1 atm air, 9 atm water vapor) is also considered. Initial
temperatures are taken to be the vapor saturation temperature.

Topics considered and results obtained are summarized as follows:

1. If condensation is ignored, postblowdown supersaturation ratios calculated are very large (>>10).
2. If condensation is assumed to occur until liquid water and vapor are in equilibrium following the blowdown, maximum fog densities are calculated to be 25 to 75 g/m^3 of liquid water.
3. Mixing of ambient air into the plume initially results in additional condensation, but the effect of this condensation upon fog density is compensated for by plume dilution, so that the mass of liquid water per unit volume of plume generally decreases monotonically. Relative humidity of the ambient air has a significant effect only if the ratio of admixed air to original plume material is large (> 10 to 100). In this case, high relative humidity increases both the condensed fraction and plume buoyancy. This effect of the released latent heat upon plume buoyancy is substantial until the condensed moisture largely reevaporates into the large volumes of admixed, unsaturated, ambient air.
4. In principle, the violent turbulence associated with the initial blowdown could break up any large droplets that might form. However, simplified analysis indicates that such effects will not significantly reduce rainout, assuming that rainout would occur in any case.
5. Turbulence can also increase rainout by enhancing agglomeration of small droplets. The effect is calculated to be significant for some, but not all, plausible values of the relevant parameters. Additional work will be required in order to draw useful conclusions as to the magnitude of this effect.

Work continued on evaluating the coagulation of aerosols (including fogs from condensing steam) in jets following failure caused by overpressurization, and blowdown of LWR containments. Attention was concentrated upon evaluating the inertial coagulation induced by the intense turbulence of the jet. An approach for evaluating the coagulation was developed based upon the relationship between the time integral of the turbulent energy dissipation (which controls the coagulation rate) and the initial-jet kinetic energy, which is ultimately dissipated by the turbulence. Several simplifying assumptions and approximations were introduced, which permit derivation of analytical expressions for the total coagulation to be expected.

The analytical results were evaluated for several representative sets of parameters, and the domains of validity of the underlying assumptions were examined. Results indicated that coagulation should be substantial for aerosols with a total concentration greater than 10 g/m^3 of suspended solids and liquids (including water) provided that initial particle diameters are 1 mm or larger. Calculations showed that concentrations as high as 25 to 75 g/m^3 of liquid water could result from steam condensation alone. Hence coagulation indeed may be important, and the subject should be pursued further.

c. LWR Sample Problem. The last of the problems in the LWR Sample Problem were rectified so that results could be presented at two conferences during October. The calculation involves a TMLB' sequence at a reactor modeled after the Zion plant, using MARCH for timing of primary system sources and CORCON for sources arising from the dry core/concrete interaction following vessel breach. Bugs identified in the course of setting up and running this problem have been corrected, and the latest version of the code runs the sample problem without the need for code changes. The real time modeled was 1300 min (about 21 hr), while the running time on the Cray computer was about 1 min. These statistics are preliminary, but they indicate that the mechanistic calculations used in CONTAIN can be run very fast on modern computers and can be used in PRA studies and in other cases where many short calculations are needed.

The input dataset and updates needed to run the LWR Sample Problem (station blackout in a large, dry PWR) were modified to run on the released version of the CONTAIN code. These updates and input sets were given to personnel at Battelle Northwest Laboratory who are interested in using the code for studies of the effect of engineered safety features on radioisotope release.

3.5 Presentations and Meetings

a. Presentations on CONTAIN for LWR Safety Analysis. During this quarter, papers were presented on the status of the CONTAIN code for LWR analysis at the 10th LWR Safety Research Information Meeting in Gaithersburg, Maryland, and the German-American BMFT/USNRC Core Melt Information Exchange Meeting in Karlsruhe, Germany. Both papers centered on three recent calculations that illustrate the current capabilities of the code and indicate some of the progress being made in code verification activities. The first calculation was a demonstration of the Engineered Safety Feature system, including models for containment sprays and fan coolers. A comparison with CONTEMPT calculations for the same problem showed very close agreement. A second calculation involved an aerosol experiment simulation and showed that CONTAIN is more capable of achieving significantly better agreement with experimental results, for both long and short times, than are lognormal codes like HAARM. The third calculation presented was the LWR Sample Problem (see 3.4c above), involving a TMLB' sequence in a large, dry PWR. The purpose of this calculation was not to provide a benchmark prediction for any particular plant (though this effort is expected to evolve in that direction) but rather to exercise as many operational features of the code as possible in a single, realistic, accident scenario. Phenomena modeled included heat transfer to structures, two-phase atmosphere thermodynamics, aerosol agglomeration and deposition, condensation on structures and aerosols, hydrogen burn, fission-product decay and transport, and intercell flow.

b. CONTAIN Review Meeting. A meeting held at NRC on 14 December to review CONTAIN's treatment of aerosol and radioisotope behavior in containment was attended by several NRC personnel and representatives of several NRC and DOE laboratories. Presentations covered the models

used in CONTAIN, experimental validation of these models, and applications of the code to reactor safety analysis. The main conclusions of the meeting were:

1. CONTAIN provides a mechanistic, fast-running model of containment phenomena.
2. Results to date of experimental validation are quite good.
3. Departures from lognormal size distributions (assumed in older aerosol codes) can change suspended-mass predictions by factors of 2 to 10 or more.
4. Aerosols can affect containment thermal hydraulics very significantly.
5. If containment integrity is preserved for several hours, secondary aerosols (from core/concrete interactions) may rapidly precipitate aerosols from the reactor vessel out of the containment atmosphere.

The following day (15 December) was devoted to a meeting generally reviewing aerosol research and modeling. One of the highlights of the meeting, from CONTAIN's viewpoint, was the report on the ABCOVE test by Bob Hilliard of HEDL. This test, in which six codes participated, consisted of a blind prediction of the aerosol behavior resulting from a sodium-spray fire in the CSTF vessel. The predictions of CONTAIN and MAEROS agreed very well with the measurements, not only for the suspended mass of aerosols, but also for the distribution of particle sizes. Moreover, CONTAIN appears to agree much better with the experiment than do HAARM-3, HAA-3, HAA-4, QUICK, or MSPEC.

4. ELEVATED TEMPERATURE MATERIALS ASSESSMENT

(C. H. Karnes, 1835; W. B. Jones, 1835)

The primary objectives of the Elevated Temperature Materials Assessment studies are (a) to determine how microstructures evolve due to thermomechanical history that results in mechanical property changes (b) to evaluate the validity of material damage rules used in design, and (c) to develop and evaluate nondestructive evaluation techniques.

4.1 Inconel 718 Characterization

The creep-deformed and thermally aged specimens of Inconel 718 from ORNL have been examined by transmission electron microscopy. The results indicate that neither time at temperature nor creep deformation at 866 K (593°C) produces significant changes in the fine-scale strengthening substructure. By contrast, exposure for about 1000 hr at either 977 K (704°C) was sufficient to alter the strengthening substructure. Specimens tested at 922 K (649°C) were requested from ORNL. A series of specimens of Inconel 718 from two different heats, thermally aged for varying times at 922 K (649°C) was prepared for examination by optical, scanning electron, and transmission electron microscopy. This series of specimens was provided to Sandia by INEL.

4.2 Biaxial Testing

The elastic response of the tubular biaxial specimen was measured under numerous multiaxial loading conditions to provide confirmation of the stress and strain measuring and calculating methods. Initial anomalous strain response to elastic loading at room temperature resulted from adiabatic heating of the gas by about 40°C during pressurization. This difficulty was eliminated by filling the specimen with vacuum pump oil. Testing at elevated temperatures will not require that the specimen be filled with a fluid because the induction heating using a feedback controller will provide a positive temperature control.

Computer programs have been written to impose several different biaxial loading paths on the specimen. These will control the test while the graphics terminal shows the actual test history plotted in biaxial stress space. The first exercise for these programs will be to develop yield surfaces at room temperature. Elevated temperature measurements will follow.

4.3 Deformation Modeling

Work in this area has shown that a back stress or kinematic hardening variable can be unambiguously determined from the strain transient dip test. Tests conducted on both an MTS servo-controlled hydraulic test machine and the specially designed dip test machine produced consistent results. These conclusions are, however, contingent on the use of a technique devised by W. Blum (Sandia) to reduce the dip test data. These data are necessary for application of any of the unified creep plasticity models that incorporate a kinematic hardening variable.

117

5. ADVANCED REACTOR ACCIDENT ENERGETICS

The Advanced Reactor Accident Energetics program is directed toward developing a data base for the understanding of the key in-core events, in a core disruptive accident, that determine the progression and severity of a reactor accident. For the advanced reactor, under-standing in-core events is particularly important because significant energy release from the core is possible. The magnitude of this energy release, and therefore the ultimate threat to the containment, is determined by the competing positive and negative reactivity effects caused by the motion and temperature of fuel, cladding, and coolant.

This program, currently focused on postulated CRBR accidents, in-volves experimental and analytical efforts to determine the magnitude and characteristics of these reactivity effects in the three phases of a core disruption accident in an advanced reactor. These phases are:

    a.   Initiation Phase -- Fuel Dynamics
    b.   Disassembly Phase -- Energetics
    c.   Transition Phase -- Fuel Freezing and Streaming.

5.1 Initiation Phase -- Fuel Dynamics
(S. A. Wright, 6423; P. K. Mast, 6425;
Erhart Fischer, Kernforschungszentrum, Karlsruhe, FRG)

5.1.1 Introduction

The final four experiments in the FD2/4 series were performed this quarter to complete the FD2/4 series. The experiments performed were FD 2.7, FD 2.8, FD 4.4, and FD 4.5.

The FD2/4 test series used reactor power history and fuel condi-tions as major parameters in the test matrix for investigating fuel disruption. The previous five experiments investigated the effects of power history on fuel disruption.[5-1, 5-2, 5-3] During this quarter, project personnel investigated the effect of fuel burnup. Burnup is an important parameter because it strongly affects the amount of re-tained fission gas that can influence the time and mode of fuel dis-ruption. Experiments FD 2.7 and FD 2.8 used fuel that had a burnup of 8.3 atomic percent (a/o). Experiment FD 2.7 reproduced the CRBR LOF-accident heating conditions, while experiment FD 2.8 examined the SNR conditions.

The behavior of fuel disruption for this high-burnup fuel was in-deed different from that observed in the moderate-burnup (4.0 to 5.0 a/o) fuel that was used in the previous experiments. In both experi-ments, fuel disruption began quite early in the form of solid-state swelling. The peak centerline temperatures were 2400 to 2500 K (2127° to 2227°C) and the temperatures in the unrestructured fuel were only 1900 to 2100 K (1627° to 1827°C). Copious amounts of volatile fission products were released as aerosols during the disruption process. These aerosols often obscured the view of the fuel pin.

In experiment FD2.7, the solid-state swelling was followed by liquid-state frothing, which produced large increases in volume, as in experiment FD2.6. In experiment FD2.8, fuel sputtering began shortly after the solid-state swelling. Investigators believe that this sputtering is analogous to the solid-state cracking and dispersion observed in experiment FD4.3. However, in the high-burnup case, the solid-state swelling relieved the fission-gas pressurization; therefore, the cracking was milder and appeared as sputtering rather than energetic dispersal.

The remaining two experiments FD4.4 and 4.5 investigated special cases of the solid-state cracking behavior that was observed in experiment FD4.3. FD4.4 produced solid-state cracking, but the heating was stopped before fuel melting. The fuel sample from this experiment is now available for postirradiation examination (PIE) analysis. Experiment FD4.5 investigated the cracking behavior in German fuel. This fuel was irradiated in the KNK-II reactor at KfK and had a burnup of 4.5 a/o and a linear heat rating of 43.5 kW/m. The major difference between this German fuel section and U.S. fuel is porosity. U.S. fuel typically has a porosity of 9% to 10% while this German fuel section had a porosity of 15%. It also had a slightly larger grain size (15 μm vs. 10 μm), which increased its gas content.

The results and analysis of experiments FD2.7 and FD2.8 are described below; however, the description of the last two experiments, FD4.4 and 4.5, will be left to the quarterly report for January-March, 1983.

5.1.2 Fuel Characteristics for Experiments FD2.7 and FD2.8

Experiments FD2.7 and FD2.8 used fuel sections from the middle of the PNL9-65 fuel pin. This fuel and its irradiation history are described in HEDL-TME-80-19.[5-4] Most of the data used in this report and analysis were taken from this HEDL report. The fuel pin had a peak burnup of 8.3 a/o and a peak linear heat rating of 15.1 kW/m. Destructive fission gas analyses made on neighboring fuel pins PNL9-63 and PNL9-59 indicated that 54% of the fission gas produced was released into the fission gas plenum. As a consequence, the PNL9-65 fuel pin has a retained fission gas content of 1.7×10^{26} atoms-Xe/m^3, or about twice that of any previous FD experiment.

The high fission-gas content resulted from a combination of the high burnup, low linear heat rating, and low operating temperatures (T (center) = 1726 K [1453°C]). An additional consequence of this low operating temperature was that no center void existed. However, the lack of a center void is not suspected to have altered the fuel disruption behavior significantly.

Additional fuel characteristics are described in Table 5-I. This table lists the local fuel characteristics for both experiments. Note that the fuel enrichment was 40.7%, and thus the reactor coupling factors were slightly lower than in the previous FD experiments. The coupling factors were determined by calorimetric measurements, as in all experiments, and are estimated to be accurate to ±3%.

Table 5-I

Fuel Characteristics for Experiments FD2.7 and FD2.8[5-4]

Fuel type	PNL9-65
Pellet numbers	
FD2.7	35-39
FD2.8	28-32
Burnup	8.3 a/o
Linear heat rating	15.1 kW/m
Fabrication density	90.9% TD
Theoretical density	11.0×10^3 kg/m^3
Fabrication enrichment	44.4%
Effective enrichment	40.7%
Pu/(Pu+U)	25%
% Fission gas retained	46%
ACRR coupling factor	11.62×10^3 J/kg/MJ

5.1.3 Results and Preliminary Analysis of Experiment FD2.7

Experiment FD2.7 used an ACRR power history very similar to that of experiment FD2.6. However, because of the lower coupling factor, and the high burnup and low linear heat rating of the fuel, this experiment reproduced the LOF accident heating conditions of the intermediate (rather than the lead) subassemblies in CRBR. These CRBR subassemblies have an end-of-life (EOL) burnup of 7.9 a/o and an average linear heat rating of 22.0 kW/m compared to the 8.3 a/o burnup and 15.1 kW/m of the PNL9-65 fuel pin.[5-5] Figure 5.1-1 shows the measured power history for this experiment. The power is given in terms of ACRR power and pin power.

The thermal and fission gas analyses were made with the SANDPIN and LANGZEIT codes.[5-6] LANGZEIT is a steady-state fission gas release code written and maintained by Lisa Vaeth at KfK. The code was run at Sandia by Erhart Fischer (KfK) to determine the initial inter- and intragranular fission gas distributions. The results of these analyses will be presented in future reports.

The results of the thermal calculations are illustrated in Figure 5.1-2. Figure 5.1-2a plots the fuel and clad temperature histories near the time of fuel disruption. Figure 5.1-2b plots the fuel temperature profiles at different times during the heating transient.

The major events of the fuel disruption are described in Table 5-II. The disruption began as solid-state swelling at t = 8.308 s. The power was about 1.8 x P_o and the peak fuel temperature was about 2500 K (2227°C). The swelling was observed as a vertical crack, about 10 mm long, in the clad, indicating that the fuel had swollen enough to contact the clad. Because the clad was about 90% through the heat of fusion and essentially molten, this contact caused it to separate.
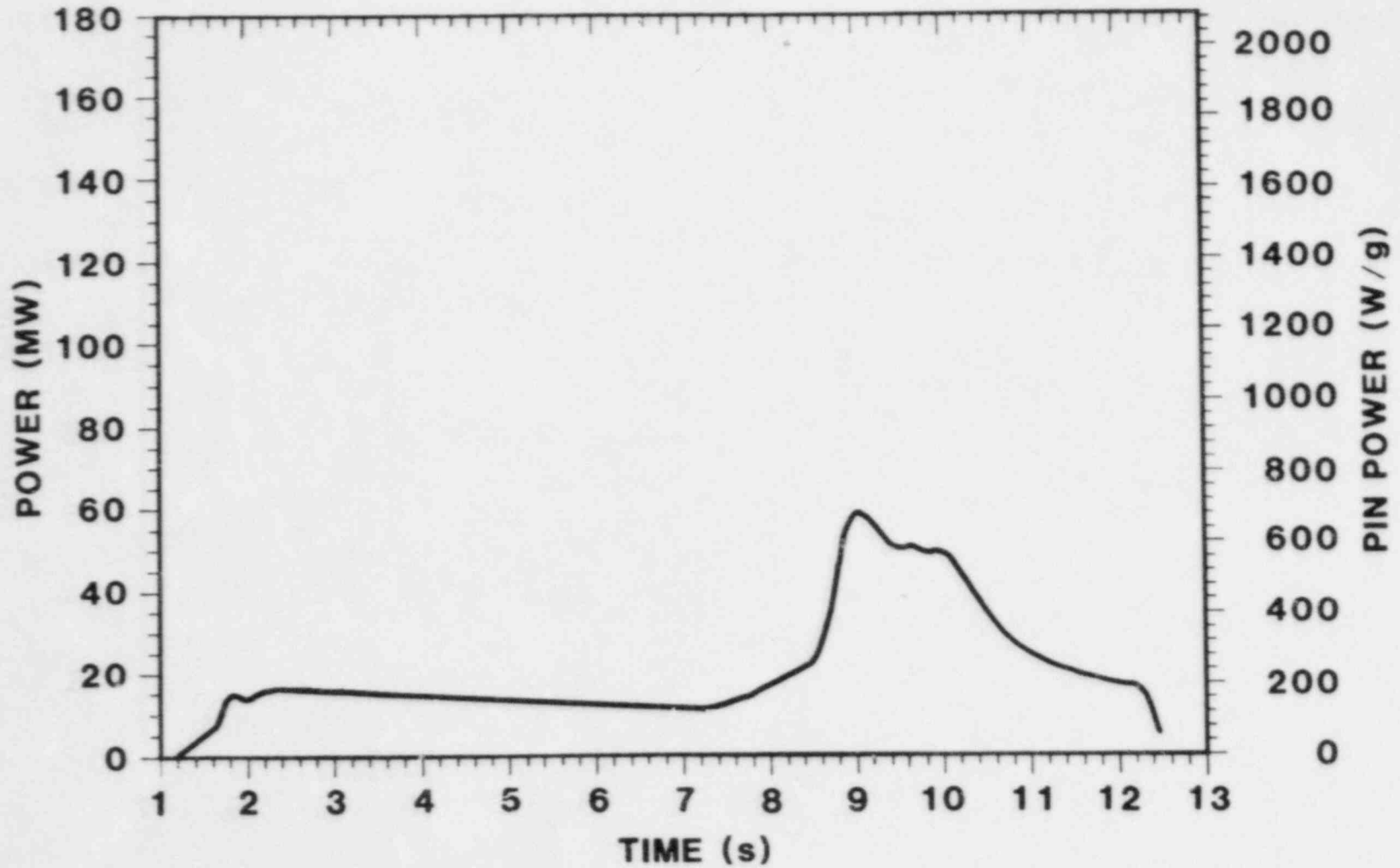
Figure 5.1-1.   Measured Power Transient, FD2.7, 8.3% Burnup
(CRBR LOF HCDA)
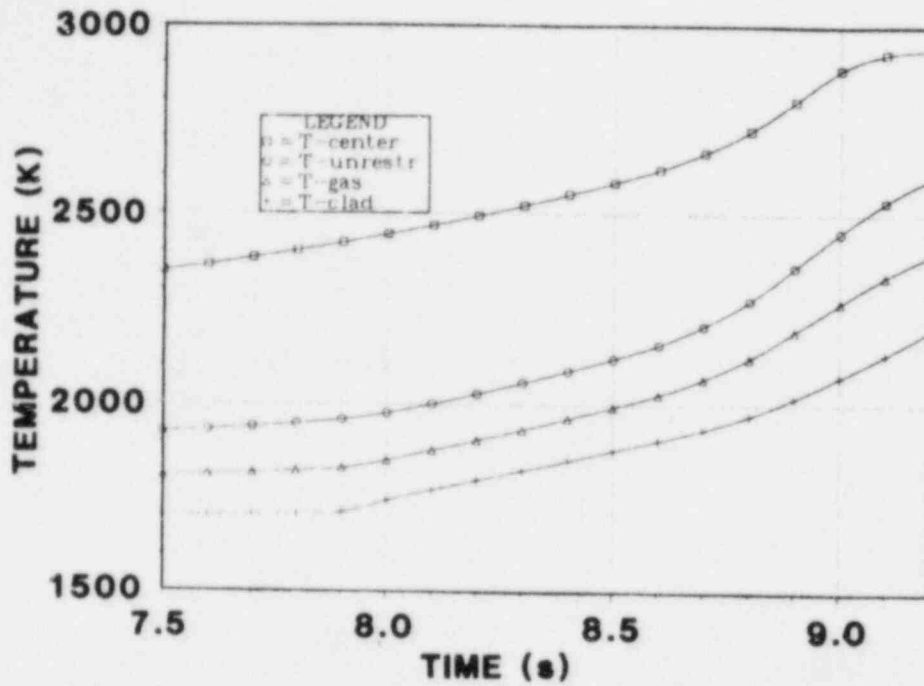
(a) FD2.7 TEMPERATURE HISTORIES
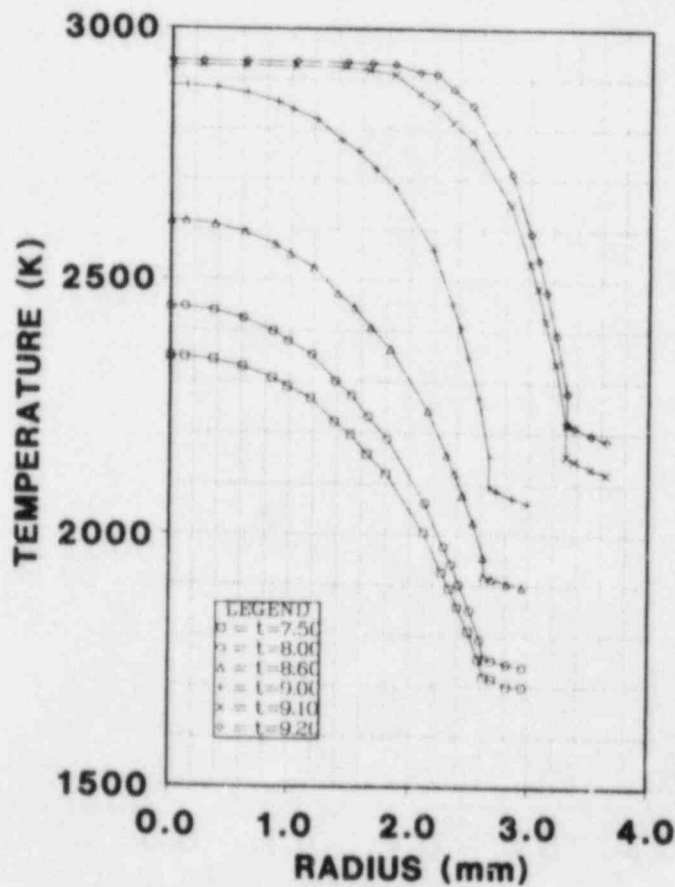
(b) FD2.7 TEMPERATURE PROFILES

Figure 5.1-2.   Results of Thermal Calculations for FD2.7

122

Table 5-II

Timing for FD2.7, "Intermediate Channel"
CRBR LOF Accident Simulation (Clean Fuel)

No.	Event	Time (Rod Timer)
0	Start of aerosol release, D = 5.84 mm	7.949
1	Continued mild aerosol release	7.989
2	Vertical crack in clad begins, start of solid state swelling, D = 6.05 mm	8.308
3	Crack in clad reaches full length of 6 to 7 mm, Solid state swelling continues, D = 6.25 mm	8.636
4	Aerosol masks view of pin, cont. swelling	8.845
5	Crack in clad widens, cont. swelling, D = 6.35 mm	8.891
6	Start of massive swelling and energetic gas release, 20% of fuel surface exposed through clad crack, D = 7.07 mm	9.004
7	Cont. massive swelling D = 9.33 mm	9.084
8	More gas release, 30% of fuel surf. exposed through clad, cont. rapid swelling, D = 10.45 mm	9.094
9	Start of fuel surface breakup, cont. swelling, D = 12.40 mm	9.113
10	Solid fuel chunks settle, D = 12.91 mm, clad 40% removed	9.125
11	Massive fuel settling, molten clad begins to drain, clad 50% removed	9.143
12	Massive clad relocation, clad 60% removed	9.177

(Although the clad was nearly molten, clad relocation had not begun.)
The swelling continued, and at t = 9.004 s, it began to accelerate.
At this time, the total observed solid-state swelling was 47% but
SANDPIN predicted a maximum volumetric swelling of 15%. SANDPIN also
predicted that the fuel centerline would be nearly molten, which is
probably why the swelling accelerated. Later at t = 9.113 s, the fuel
surface was observed to crack, probably because of interior liquid-
state frothing caused by fuel melting. The breakup continued and the
outer regions of the fuel began to slump, in the form of a collection
of solid chunks about 2 to 3 mm in diameter. Figure 5.1-2b shows that
the outer, unmolten region of the fuel pin was about 2 to
3 mm thick at this time. Thus, it is reasonable to expect the broken
chunks or particles would be about this same size.

The breakup and cracking observed here do not constitute the same
type of energetic grain-boundary cracking that was observed in exper-
iment FD4.3. Investigators believe this cracking to be caused simply
by the massive swelling or frothing that occurred in the interior of
the fuel pin when fuel began to melt.

This type of disruption was predicted by SANDPIN. The disruption
models in SANDPIN predicted no solid-state cracking (even though it
approached the cracking criterion within 20%) but did predict a mas-
sive liquid-state frothing. SANDPIN also predicted significant
amounts of solid-state swelling (15%), but the amounts observed were
far greater than predicted. This underprediction of the solid-state
swelling is illustrated in Figure 5.1-3, which is a plot of the
observed and calculated swelling as a function of time. In spite of
this underprediction of the solid-state swelling, SANDPIN does accu-
rately predict the time and magnitude of the liquid-state frothing
(see Figure 5.1-3).

In the SAS analysis the disruption was assumed to consist of
solid and molten fuel settling.[5-5] Table 5-III lists some of the
important thermal characteristics near the time of disruption assumed
by SAS. For comparison the experiment conditions are also given. The
SAS type settling was indeed observed in the experiment except that
the observed settling was preceded by massive swelling. The swelling
is enough to cause pin-to-pin interactions that would probably prevent
further settling in a bundle geometry. Thus, the power burst caused
by the settling, as predicted by SAS, would probably not occur, or if
it did occur, it would be dramatically reduced. This would, in turn,
increase the amount of fuel remaining in the core when the core
entered the transition phase.

5.1.4 Results and Preliminary Analysis for Experiment FD2.8

Experiment FD2.8 used an ACRR power history very similar to that
of experiment FD4.3. However, the pin power was slightly less because
of the lower coupling factor. The purpose of this experiment was to
investigate fuel-disruption behavior in cases where fuel and clad are
expected to disrupt coherently for high-burnup fuel and at relatively
high power levels (10 to 15 x P_o). Coherent disruption means that
fuel is disrupting while the clad is molten but before the clad re-
locates. Figure 5.1-4 shows the actual ACRR power history used in
experiment FD2.8. The pin power is also plotted.
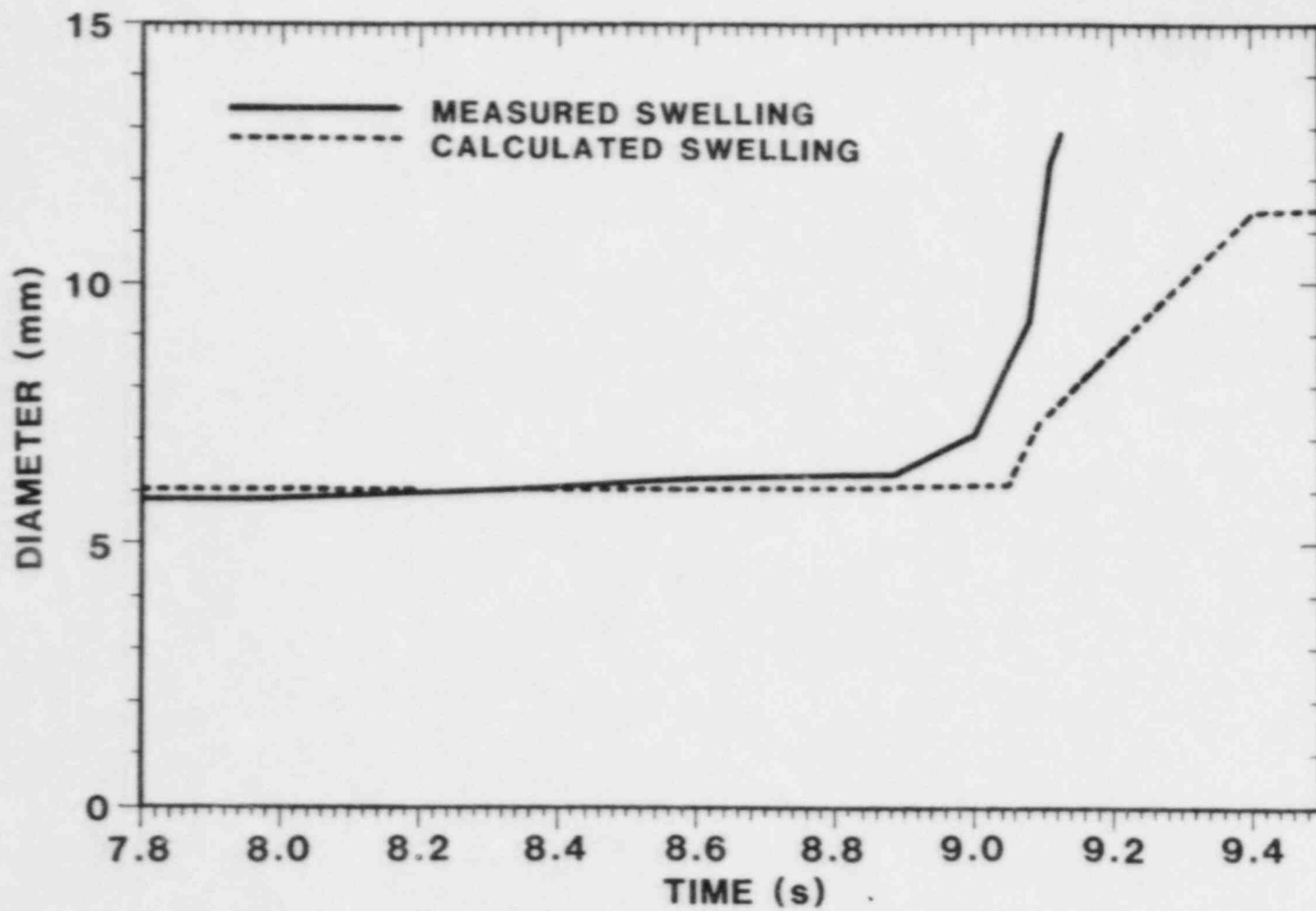
Figure 5.1-3. Swelling for FD2.7

Table 5-III

A Comparison of Thermal Conditions in Experiment FD2.7 with the
SAS LOF Accident Analysis for the Intermediate Channels.[5-5]
(The FD2.7 data are taken at time = 9.100 s, which corresponds
to the start of massive fuel centerline melting.)

Event	FD2.7, SANDPIN Calculations	CRBR Channel 2 SAS Calculations
Unrestructured* fuel zone temperature	2486 K (2213°C)	2540 K (2267°C)
Temperature gradient in the unrestructured* zone	955 K/mm	730 K/mm
Heating rate in the unrestructured* zone	790 K/s	---
Power level +	4.77 P_o^+	5 x P_o
Burnup	8.3 a/o	7.9 a/o
Retained fission gas	46%	44%

*The unrestructured fuel zone in SANDPIN at r/R_o = 0.865

+P_o = 26.5 kW/m

The results of the thermal analyses are shown in Figure 5.1-5.
Figure 5.1-5a plots the temperature history of the fuel and clad
around the time of fuel disruption, and Figure 5.1-5b plots the radial
temperature profiles at various times during the experiment.

The fuel disruption sequence as observed in the films is de-
scribed in Table 5-IV. The disruption began as solid-state fuel
swelling (t = 6.160 s) just as it did in experiment FD2.7. Again, the
swelling first appeared as a vertical crack in the clad. The swelling
continued for 70 ms and, at t = 6.233 s, sputtering began. The sput-
tering was superimposed upon the swelling. The observed volumetric
swelling at this time was 23% and the peak (centerline) temperature
was 2550 K (2277°C). The unrestructured fuel temperatures were 2100
to 2200 K (1827° to 1927°C). The velocity of the sputtered fuel
particles varied between 0.8 and 1.0 m/s. These particles had a
diameter of about 0.5 mm. The swelling and sputtering continued for
another 92 ms (t = 6.325 s), at which time very rapid swelling began,
probably the result of fuel melting. By this time the fuel had
swollen to five or six times its original volume. Slumping began 33
ms later (t = 6.358 s).
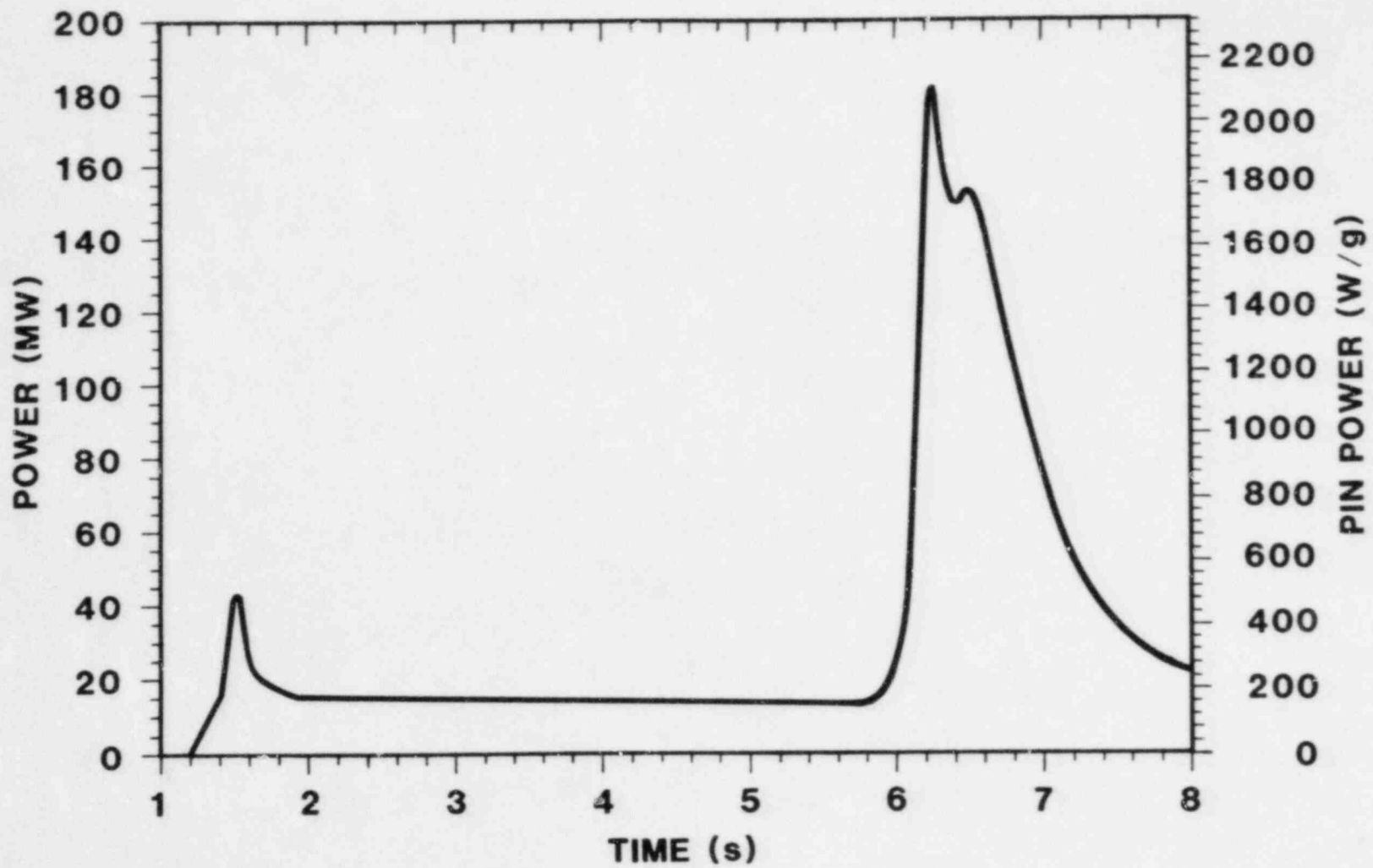
Figure 5.1-4.   Measured Power Transient, FD2.8, 8.3% Burnup
(Coherent Disruption LOF)

127
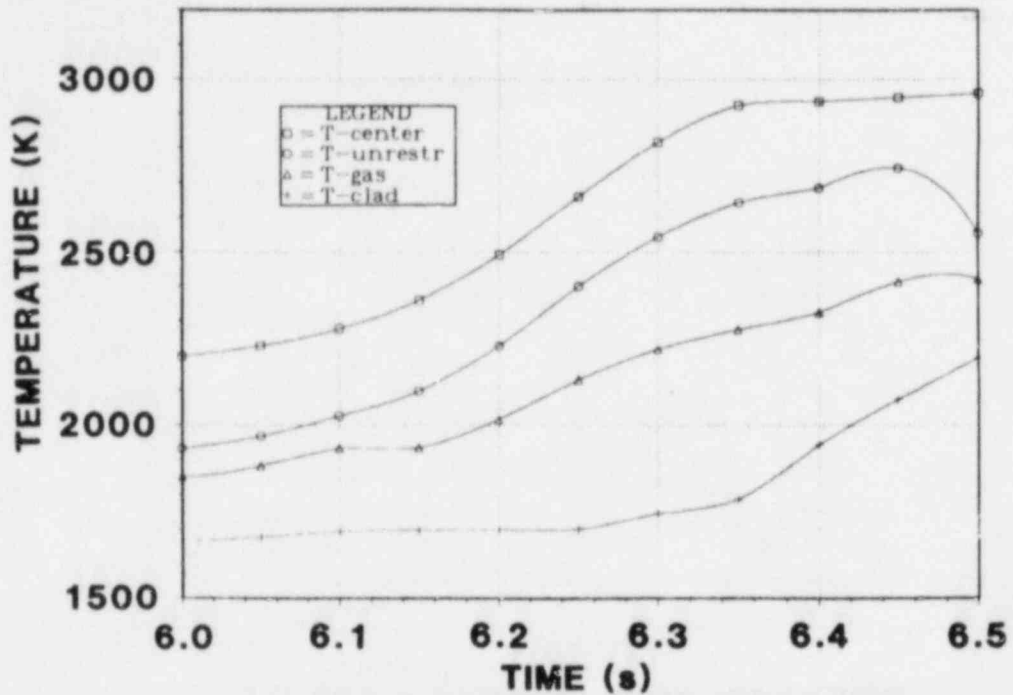
(a) FD2.8 TEMPERATURE HISTORIES
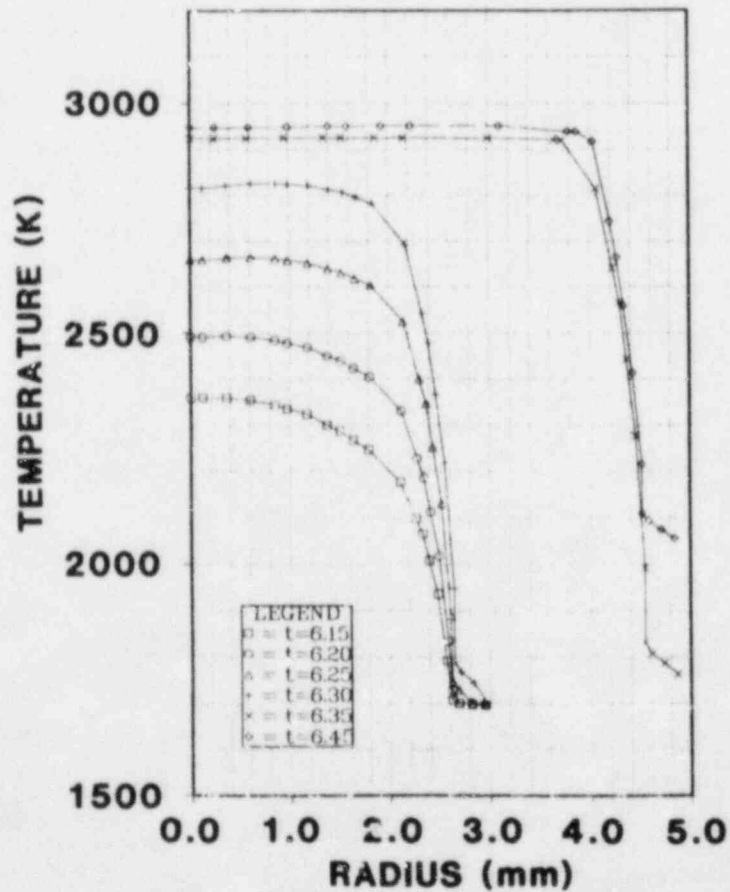
(b) FD2.8 TEMPERATURE PROFILES

Figure 5.1-5.   Results of Thermal Calculations for FD2.8

Table 5-IV

Timing for FD2.7, High-Burnup Coherent Fuel and Clad Disruption (Clean Fuel)

No.	Event	Time (Rod Timer)
0	Start of aerosol release, start of vertical crack in clad, D = 5.84 mm	6.160
1	Continued solid state swelling, clad crack widens and more aerosol release	6.171
1.5	Continued swelling, D = 6.20 mm	6.217
2	Start of solid state sputtering with jets of fission product release, D = 6.67 mm	6.233
3	Sputtering fully developed, v = 0.8 m/s, D = 6.67 mm	6.245
4	Start of massive fuel swelling, sputtering continues, D = 8.58 mm	6.313
5	Cont. rapid swelling, D = 9.06 mm	6.325
6	Start of slumping, cont. swelling, D = 16.2 mm	6.358
7	Start of clad relocation, cont. swelling, D = 22.2 mm	6.374
8	Rapid dispersion of slumped molten fuel, v = 1 m/s	6.476
9	Upper fuel pellet falls from crucible	6.601

The SANDPIN fission-gas calculations predicted all three modes of fuel behavior, solid-state swelling, cracking, and, upon fuel melting, large volume expansion. Just as in the previous experiment the fission-gas model underpredicted the solid-state swelling. SANDPIN predicted a peak solid-state swelling of 15% (8% total) and the observed swelling was 30%. Figure 5.1-6 shows the observed and calculated fuel diameters (measured at the fuel axial centerline where the maximum swelling occurs). Because these two experiments (FD2.7 and FD2.8) are the first FD experiments to use high-burnup fuel, investigators were not surprised to find that the SANDPIN fission-gas model underpredicted the swelling. Project personnel will have to look at the swelling models to investigate mechanisms that could explain the observed swelling.

The sputtering observed in this experiment is believed to be a direct result of the cracking predicted by SANDPIN. The sputtering occurred (rather than the rapid dispersal, as seen in experiment FD4.3) because the early solid-state swelling relieved the fission-gas pressurization and therefore reduced the potential for energetic cracking. The predicted time of cracking occurred 70 ms after it was observed. This delay could easily have been caused by an inaccurate description of the fission-gas initial conditions.

In terms of reactor safety analysis, the most important point is that if the fuel behavior, as observed in these experiments, is typical for an LMFBR LOF accident, then the fuel has a strong tendency to swell very early in the LOF power transient. This swelling is enough to close up the flow channels, thus removing paths for fuel to be ejected rapidly from the reactor. The nature of fuel movement under these conditions is not addressed by these experiments. However, it must be addressed in some mechanistic manner before the amount of fuel remaining in the core (and thus the potential for recriticality) upon entering the "transition phase" can be estimated.

Fuel and clad relocation will be addressed in the STAR series of experiments to begin in late FY83.
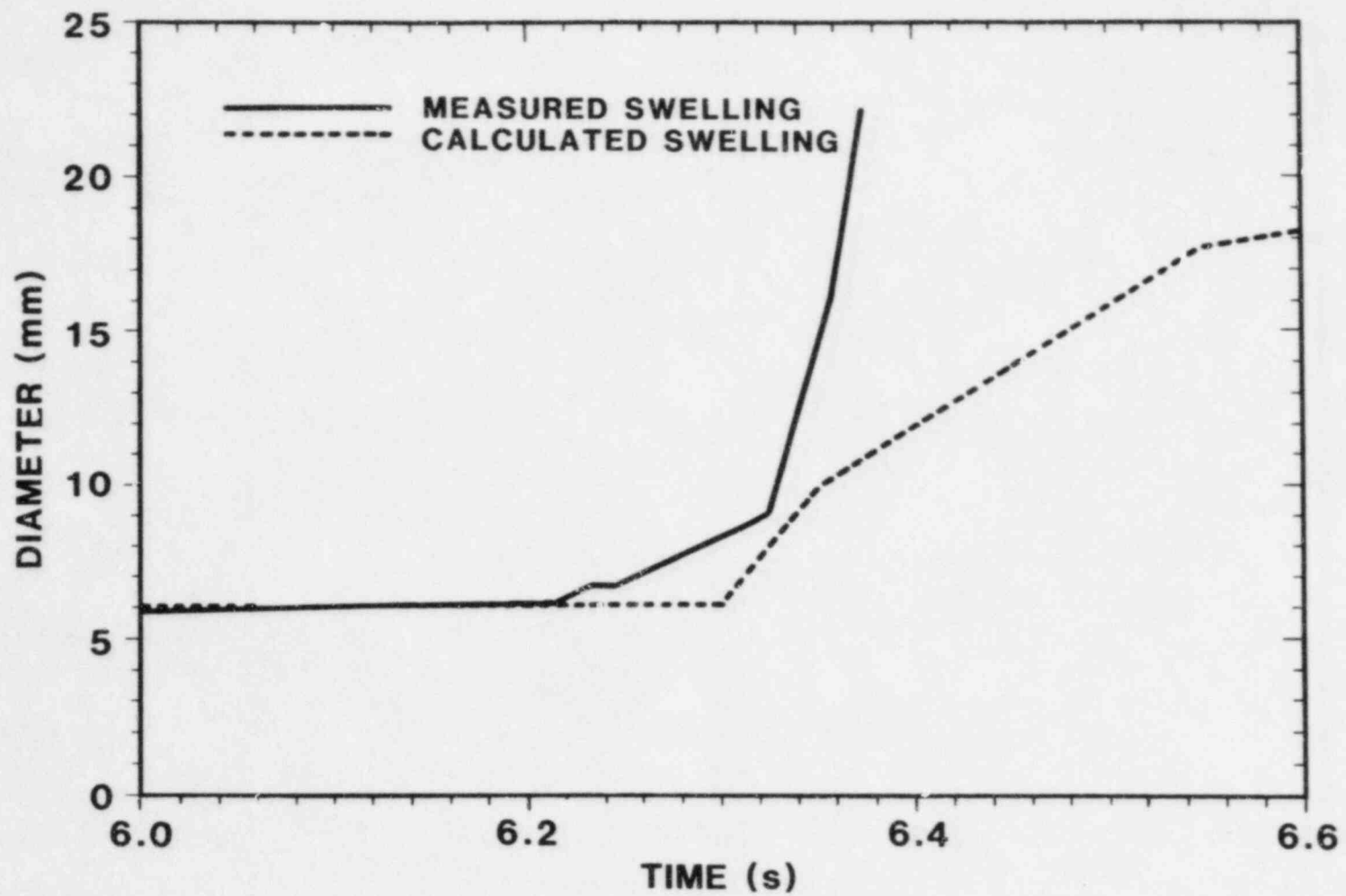
Figure 5.1-6.   Swelling for FD2.8

131

5.2 Disassembly Phase -- Energetics
(K. O. Reil, 6423; W. M. Breitung, 6425; M. F. Young, 6425)

This program is directed toward identifying the phenomena dominating the conversion of thermal energy into work energy and accurately modeling those phenomena for inclusion in accident analysis. The results of this work will be used to determine the work potential associated with core-disruptive accidents (CDA) in a CRBR-type reactor and to assess the magnitude of the threat to containment from this pressure source. This program currently emphasizes completion of the Effective Equation-of-State (EEOS) experiments and planning for the fuel coolant interaction (FCI) task. The jointly sponsored USNRC-KfK EEOS program is intended to characterize the pressure sources arising from fresh UO_2 and mixed oxide fuels.

During this quarter, work in the Disassembly Phase focused on completing the current series of EEOS experiments, planning for the coarse dispersed mixture (CDM) experiments, and development and documentation of the TEXAS multifield hydrodynamics code.

5.2.1 EEOS Experiments

Preparations for the remaining KfK-sponsored EEOS experiments were completed early in the quarter with package assembly and mass spectrometer calibration. The fifth and sixth experiments in the current EEOS series were conducted in late November. EEOS-5 provided confirmatory data on vapor pressure of high-purity UO_2. This experiment was similar to EEOS-4 except that the results extend to approximately 20% higher energy (≈ 7000 K). The EEOS-6 experiment was the first test to examine fresh "reactor-typical" UO_2. The UO_2 for EEOS-6 was derived from pressed and sintered pellets fabricated at Los Alamos.

The last three experiments in the EEOS experiment series were completed at the end of the quarter. EEOS-7 was a second experiment using reactor-typical UO_2 fuel and was the confirmatory repeat of EEOS-6. Experiments EEOS-8 and EEOS-9 were performed using reactor-typical fresh mixed oxide fuel (UO_2-PuO_2). The results of these final three experiments appeared to be consistent with the trends observed in EEOS-4, EEOS-5, and EEOS-6. Data relating pressure and energy up to ≈ 7000 K were obtained, with somewhat lower observed vapor pressures in UO_2 than were expected based on current EOS formulations. Data reduction and analysis must be completed before the implications of these results for the timing and magnitude of a CDA disassembly phase can be assessed.

The reduction and analysis of data from all these experiments is in progress at KfK, being performed by W. M. Breitung. Additionally, the Reactor Energy Analysis Program (REAP) code for use in EEOS analysis was completed and documented, and final studies of energy deposition in liquid fuel geometries were completed.

5.2.2 CDM Experiments

Planning and analysis activities for the CDM experiments con-
tinued with the completion of additional tests of the trigger mecha-
nism and the definition of parameters for the CDM trigger design.
Work also continued on the particle-dispersal-mechanism design to
achieve more uniform particle dispersions.

Because of resource constraints, imposed late in the quarter,
design and development activities for the CDM experiments were phased
down. CDM experiment package design will be documented, but the first
three CDM experiments, originally scheduled for late FY83, will be
postponed indefinitely.

5.2.3 TEXAS Hydrodynamic code

Development efforts on the TEXAS code were directed toward con-
sideration of a local boiling model, but the same resource constraints
that influenced CDM have curtailed TEXAS development. Activity is now
limited to documentation of the TEXAS code. The TEXAS model is suffi-
ciently general to be applicable to both LWR and LMFBR conditions and
development will continue only in conjunction with specific LWR
activities.

5.2.4 Conclusion

Experiment programs in support of CDA analysis will be limited to
Transition Phase (TRAN,GAP) and Initiation Phase (STAR) activities.
Because TEXAS documentation is forthcoming and EEOS analysis is under-
way in Germany, further reporting of Disassembly Phase in this series
of documents will occur on an "as-appropriate" basis only.

5.3 Transition Phase
     (D. A. McArthur, 6423; P. K. Mast, 6425)

5.3.1 Progress on TRAN Series II Experiments

5.3.1.1 Design of Fuel/Steel Pellets

   a. Heat Transfer within Pellets

   The use of pure fuel/steel melts in Transition Phase experiments
is of great interest because no data on the freezing and streaming of
fuel and steel have been obtained with pure reactor materials (UO_2/Mo
thermites differ significantly in microscopic thermal properties from
UO_2/steel melts). When a nuclear reactor is used to melt the fuel/
steel load, a radial variation of energy deposition results from
neutron self-absorption in the fuel. When experiments are being per-
formed at low driving pressures, this radial variation of energy
deposition could cause transient steel-vapor pressures at the outer
radius of the pellet that are larger than the driving pressure.
Although the turbulent nature of the melt flow would be expected to
mix melt regions of different temperature, this turbulent flow may not
be established early enough to assure that the flow is controlled by
the applied driving pressure. Therefore, during this quarter, much
effort was put into designing fuel/steel loads that would have an
acceptably uniform energy deposition.

   The two main approaches considered for reducing steel vapor pro-
duction in fuel/steel melts were described in the previous Quar-
terly (separation of steel from very hot fuel until the turbulent flow
is established or use of radial zones of different enrichment to
minimize variations in energy deposition).[5-7] For the first
approach, neutron transport and heat transfer calculations showed that
little steel vapor would be produced during the ~30 ms immediately
following the ACRR pulse, which should allow time for a turbulent flow
to be established. However, large uncertainties remained as to
whether the separate fuel and steel regions would become intimately
mixed during the flow. This first approach was discussed with the
analysts who would be responsible for interpreting the experimental
results. They felt that the mixing uncertainties would perhaps inval-
idate the analysis and greatly reduce the value of the experimental
results. Therefore the second approach, grading the fuel enrichment
to compensate for neutron absorption, was chosen.

   b. Design Criteria for Graded-Enrichment Pellets

   Within each radial zone of constant enrichment, the energy depo-
sition will be largest at the outer radius and will decrease toward
the pellet center (Figure 5.3-1). Because rapid mixing should occur
as the flow begins, the primary concern is achievement of the desired
average temperature at the same time that the peak deposition at the
outer edge of a zone produces less than 5 atm of steel vapor
(T < 3500 K), and the minimum deposition at the inner edge of a zone
produces complete melting of the mixture so that the flow is unimpeded
(T > 3138 K). Neutron-transport calculations were therefore performed
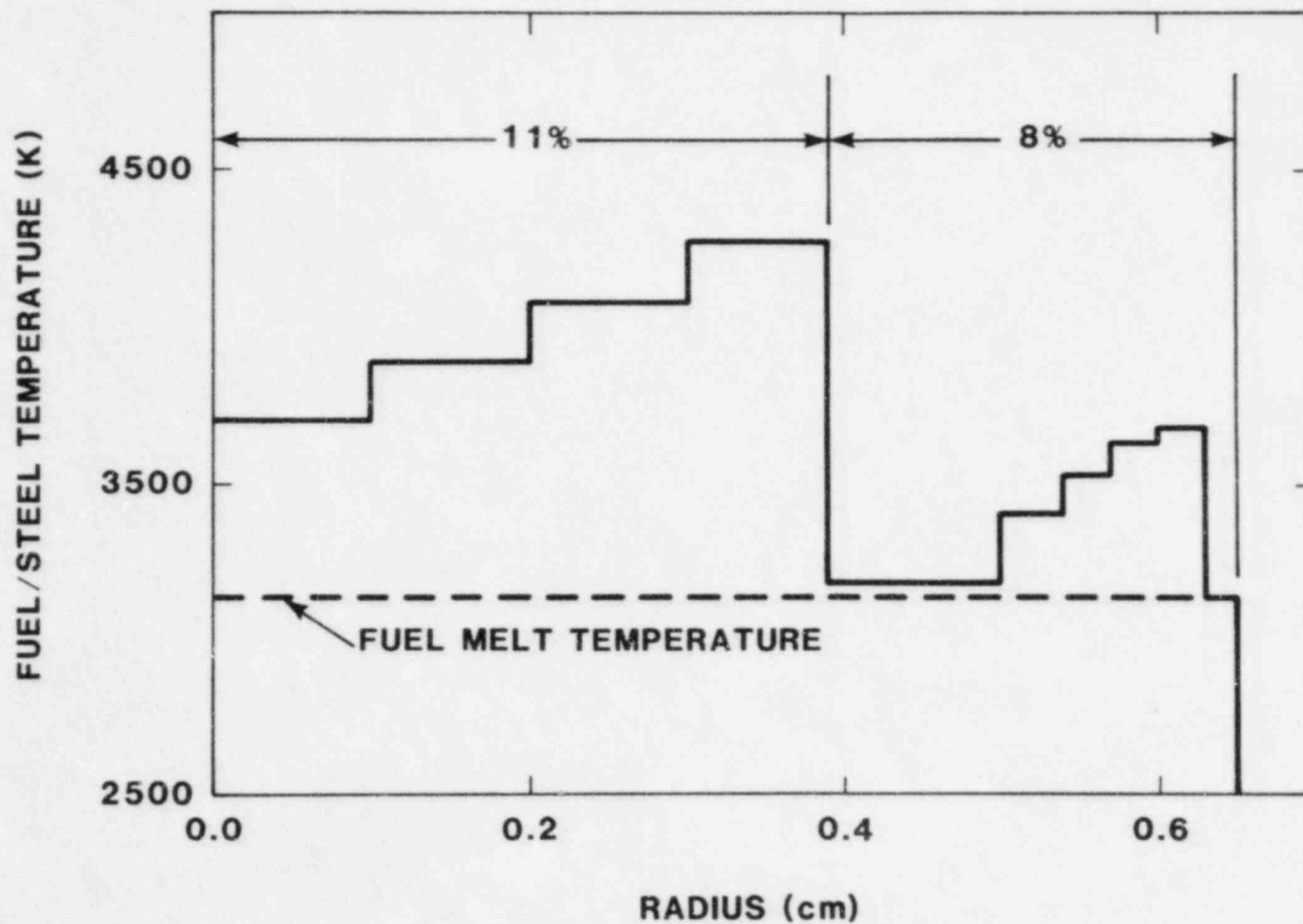
Figure 5.3-1. Typical Adiabatic Final Temperature Distribution for 1.3-cm-Diameter Fuel Pellet with Two Enrichment Zones (7.91 g/cm^3 UO$_2$, 0.42 g/cm^3 316 SS)

for three desired fuel/steel mixtures, assuming two zones of approximately equal radial thickness and varying the enrichment of each zone to achieve the above temperatures at the zone edges. A pellet density of 80% of the theoretical density was assumed, giving some volume for thermal expansion and expansion upon melting. Project personnel found that the design criteria could be achieved for pellets 0.8 cm in diameter, but three enrichment zones were required for 1.3-cm-diameter pellets.

c. Fuel/Steel Pellet Order to Los Alamos National Laboratory

Based on the preceding calculations, Sandia personnel ordered pellets of three fuel/steel compositions from Los Alamos, with the specifications shown in Table 5-V. The relative volume percentages of fuel and steel are given in the table, along with the enrichments of the inner (E1) and outer (E2) enrichment zones. A delivery date of mid-February 1983 has been estimated for these pellets, so fuel/steel experiments could begin at about that time.

Table 5-V

Fuel/Steel Pellet Specifications

Fuel (%)	Steel (%)	E1 (%)	E2 (%)
95	5	11	9
75	25	14	12
40	60	30	25

5.3.1.2 Fabrication of TRAN Series II Packages

a. Additional Diagnostics and Thermocouple Model

Measuring the fuel flow up the freezing channel has been difficult because of the high initial temperatures involved, the large radiation backgrounds present, and the need for thick containment walls. The Series II design offers more flexibility for diagnostic measurements because the freezing-channel wall and the containment wall are now separate. In the first Series II experiment, the annular channel experiment, a 316 SS wall surrounding the channel is thick enough to accommodate small-diameter thermocouples inserted in this wall to sense the flow of fuel up the channel.

The ideal thermocouple would probably be the Co-Ax design of Medtherm of Huntsville, Alabama. This type of thermocouple has a very accurately located junction area formed by a thin plating of known thickness. Heat transport calculations with TAC2D showed that a 0.013-cm-thick plating would probably be optimum for a rapid response

136

to molten fuel, yet the junction would survive long enough to provide some information about the initial heat flow into the junction. However, repeated phone calls to Medtherm over a period of 3 mo did not result in even a verbal quote. Therefore ordinary thermocouples were investigated as a possible diagnostic.

The primary questions involved with such a diagnostic are whether the thermocouples will be sensitive only to the main fuel flow, and whether their response times are short and consistent enough to measure, reliably, fuel-front velocities of the order of 10 m/s. Several preliminary experiments were performed in the laboratory to investigate these questions.

The manufacturer's quoted response times for 0.040-inch-diameter, grounded-junction Omega thermocouples are about 2 s, but the manufacturer did not clearly specify the method of measurement. In addition, a consistent onset of temperature rise is all that is necessary to sense the arrival of fuel front. Therefore, the response time of these thermocouples was measured by plunging them manually into a bath of liquid solder at 518 K (245°C) and recording both the temperature-rise behavior and the instant at which the thermocouple tip touched the molten solder. Figure 5.3-2 shows the simple apparatus used for these measurements. In this apparatus, the completion of an electrical circuit was used to record the instant of contact. Five randomly chosen Omega thermocouples were studied with this apparatus, and two examples of the measured response are shown in Figures 5.3-3 and 5.3-4. The responses approached final temperatures approximately exponentially, with a 10% to 90% pulse-rise time of between 105 and 155 ms. The roughly linear initial temperature rise occurred between 10.5 and 18.5 ms after the instant of contact. Some of these variations may be associated with variations in the speed with which the thermocouples were inserted into the solder bath.

The thermocouple-temperature behavior was modeled with the TAC2D heat-transfer code, using a fairly detailed model of the thermocouple geometry at the tip, and the known thermal conductivity of molten solder. The calculated variation of temperature agreed reasonably well with the measured behavior, indicating that the heat input to a thermocouple tip in an actual TRAN experiment might be deduced from such data.

The short delay in the onset of temperature rise and its relative consistency over several thermocouples has encouraged project personnel to attempt to measure fuel-front velocity on the annular channel experiment early in 1983. Two sets of thermocouples will be placed in the outer channel wall at axial locations 5 and 25 cm from the entrance to the annular channel. At each location, one thermocouple tip will be placed flush with the channel wall, while the other will be recessed a small amount in an attempt to reduce its response to any low-density debris that might precede the main flow.
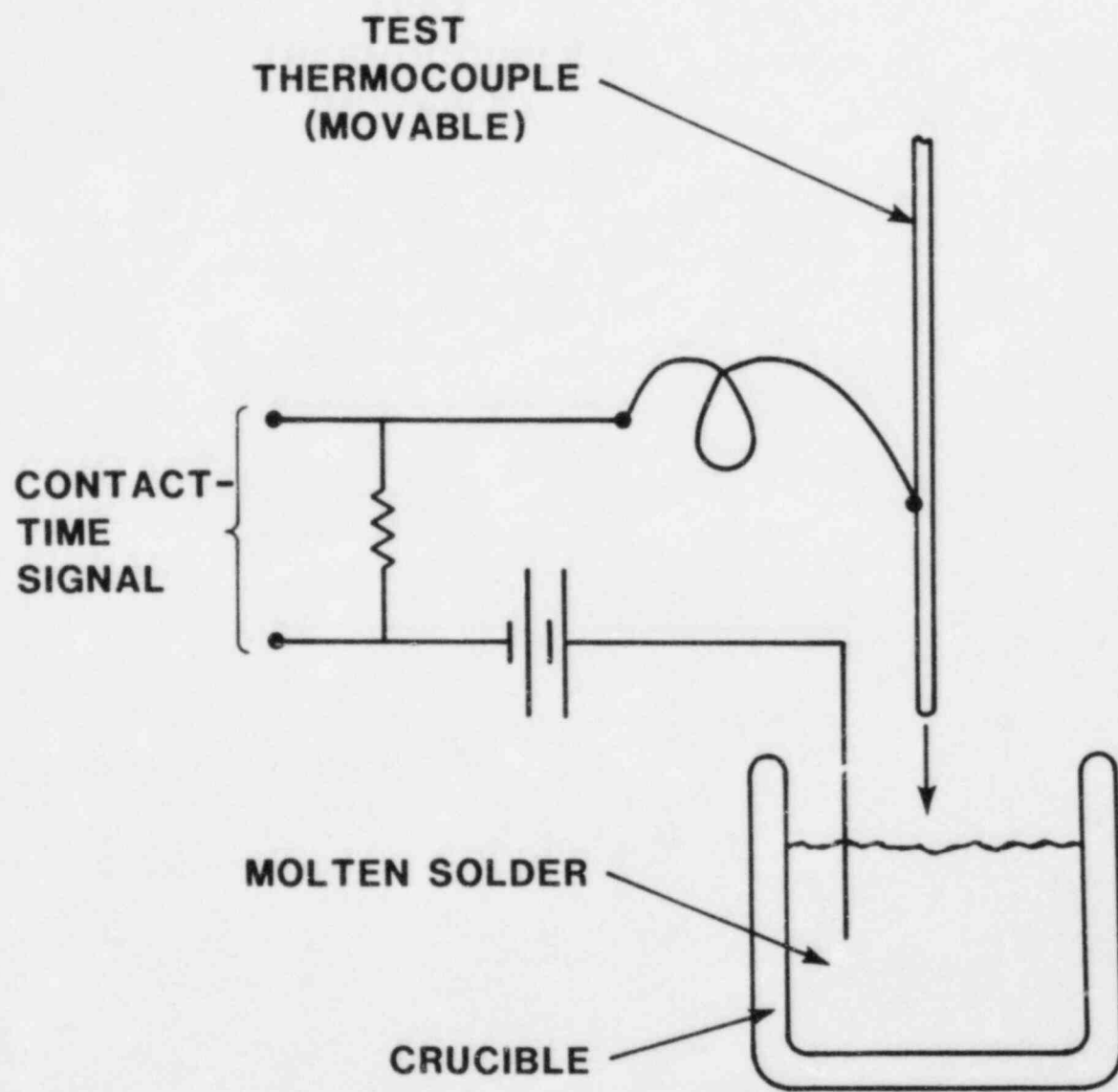
137

Figure 5.3-2.   Thermocouple Response Test Apparatus
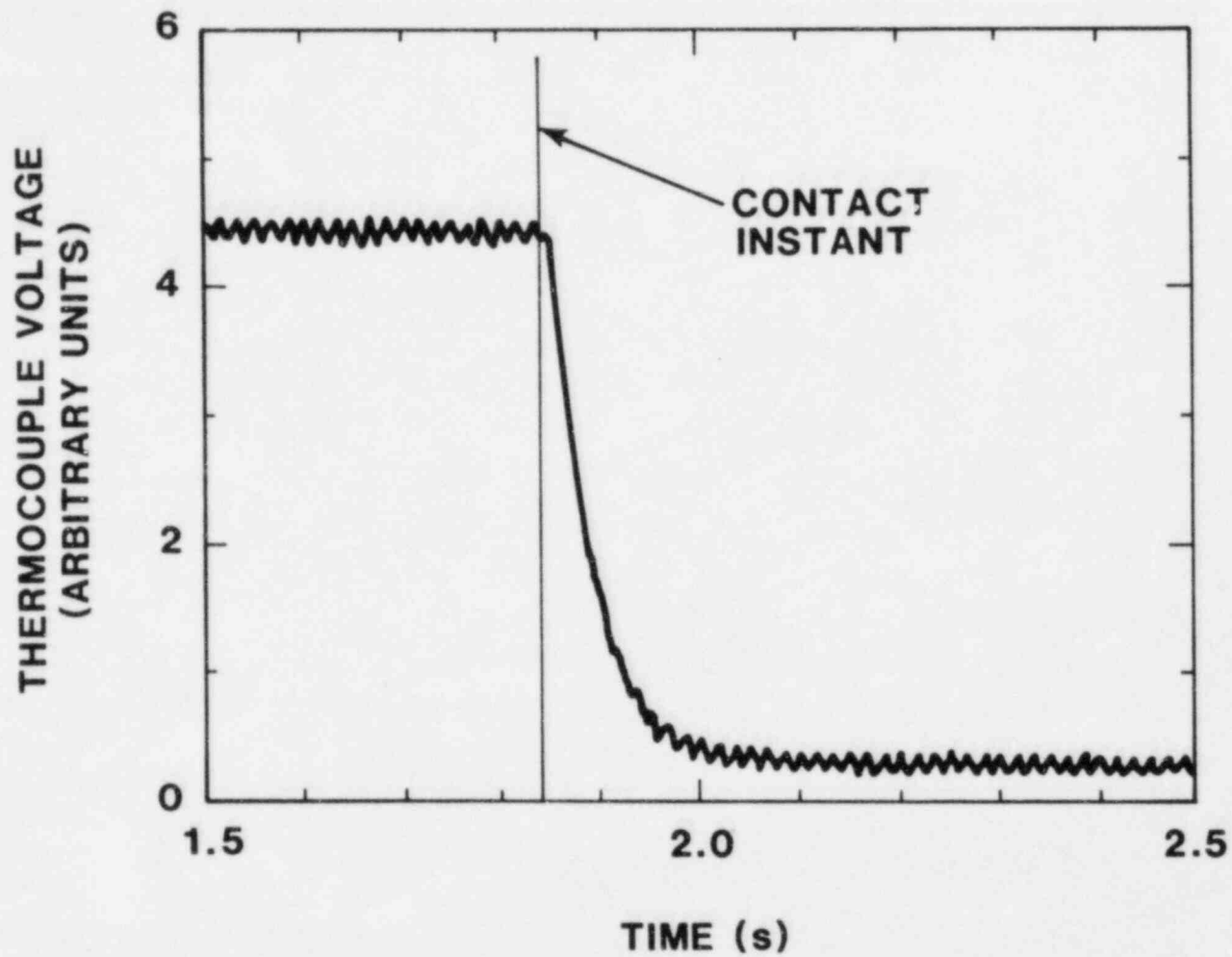
138

Figure 5.3-3.   Representative Response Curve for 0.040-in.
Chromel-Alumel Grounded-Junction Thermocouple
(First Example)

139
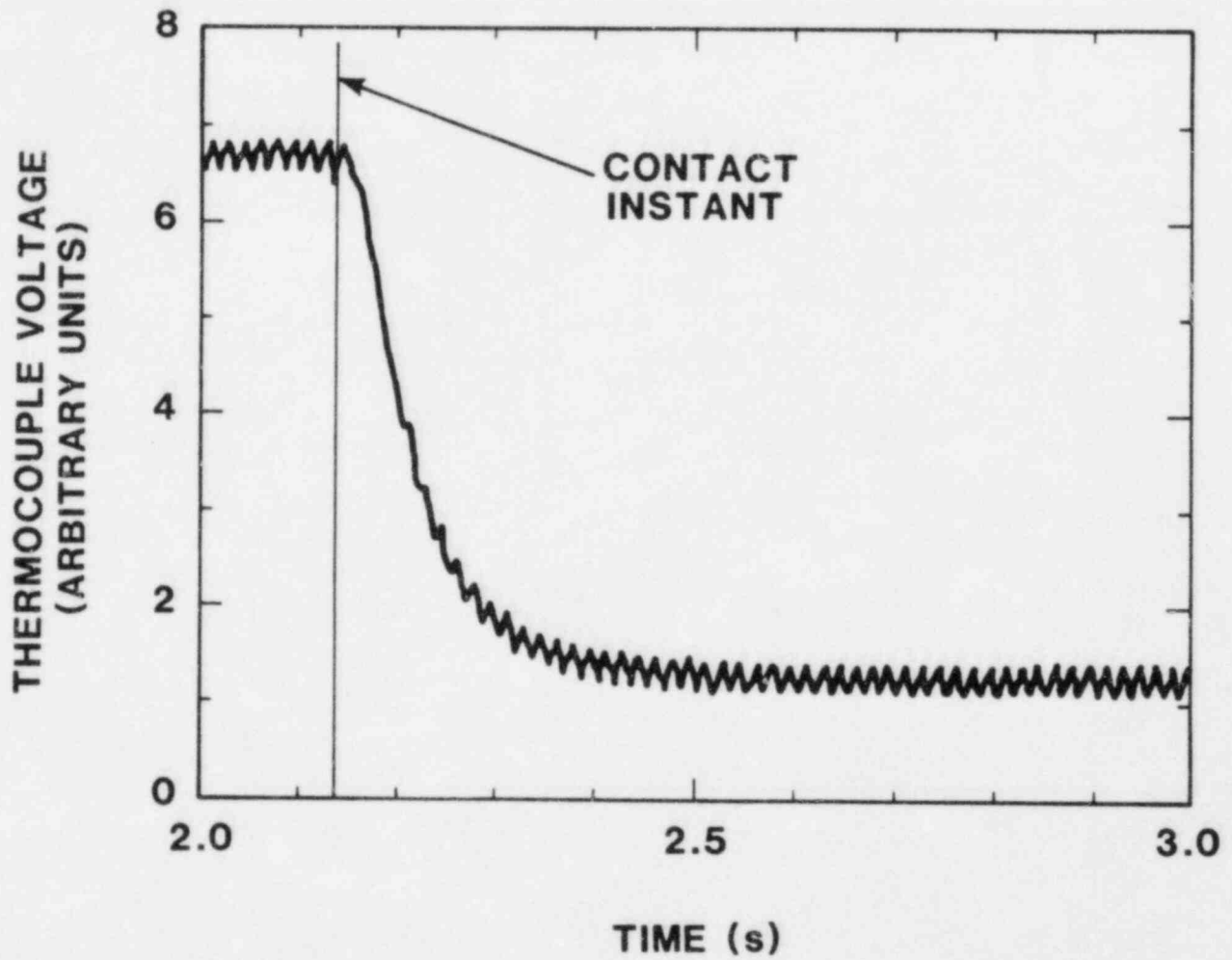
Figure 5.3-4.   Representative Response Curve for 0.040-in.
Chromel-Alumel Grounded-Junction Thermocouple
(Second Example)

b. Modifications of Package Design

The Series II package design was changed slightly because gun-drilling the entire length of the fuel melting chamber and matching the center of the freezing channel with sufficient accuracy proved difficult. The fuel housing for the TRAN Series II annular channel experiment contained a small asymmetry at the junction between the fuel melting chamber and the cone-shaped transition to the annular freezing channel. This asymmetry posed no safety problem and will not significantly affect the fuel flow.

The fuel-melting chamber area of future packages will be machined independently of the freezing channel, and the two sections will be joined by welding. Test welds are being performed and appropriate quality control procedures developed.

c. Experiment-Plan Issues (Thermal Stress Calculation)

For the case in which rapid plugging keeps essentially all the fuel in the melting chamber, project personnel investigated the problem of thermal stress in the walls of the melting chamber more closely. Elastic calculations show the possibility of wall rupture, so a plastic yield will have to be calculated. This calculation will help determine the desirability of a reduced initial temperature in the fuel-melting-chamber area.

d. Measuring Axial Variation of Energy Deposition

The axial variation of energy deposition over the larger TRAN Series II fuel load will be measured to check the calculational results. The calculated energy deposition varies by about 10% over the entire 22.9-cm length of the fuel load. This degree of axial variation might be acceptable without changes in the axial shape of the polyethylene moderator.

To verify the small axial variation, a uranium-loaded aluminum wire was inserted into a mock-up of the fuel melting chamber and irradiated with an ACRR pulse of approximately the same magnitude as that planned for the actual experiment. Because the uranium content may vary in this type of wire, the uranium content of the wire was preassayed at several points along its length by the dosimetry lab. The uranium content was found to be uniform within the statistical uncertainty of the measurements.

Figure 5.3-5 shows that the axial variation of energy deposition is approximately 19% rather than the 10% predicted by the calculations, and the peak of the energy deposition is not centered on the fuel load. Therefore, the package will be lowered 3 in. relative to the ACRR core, and the thickness of the polyethylene moderator will be decreased near the center of the fuel load and increased at the ends of the fuel load.
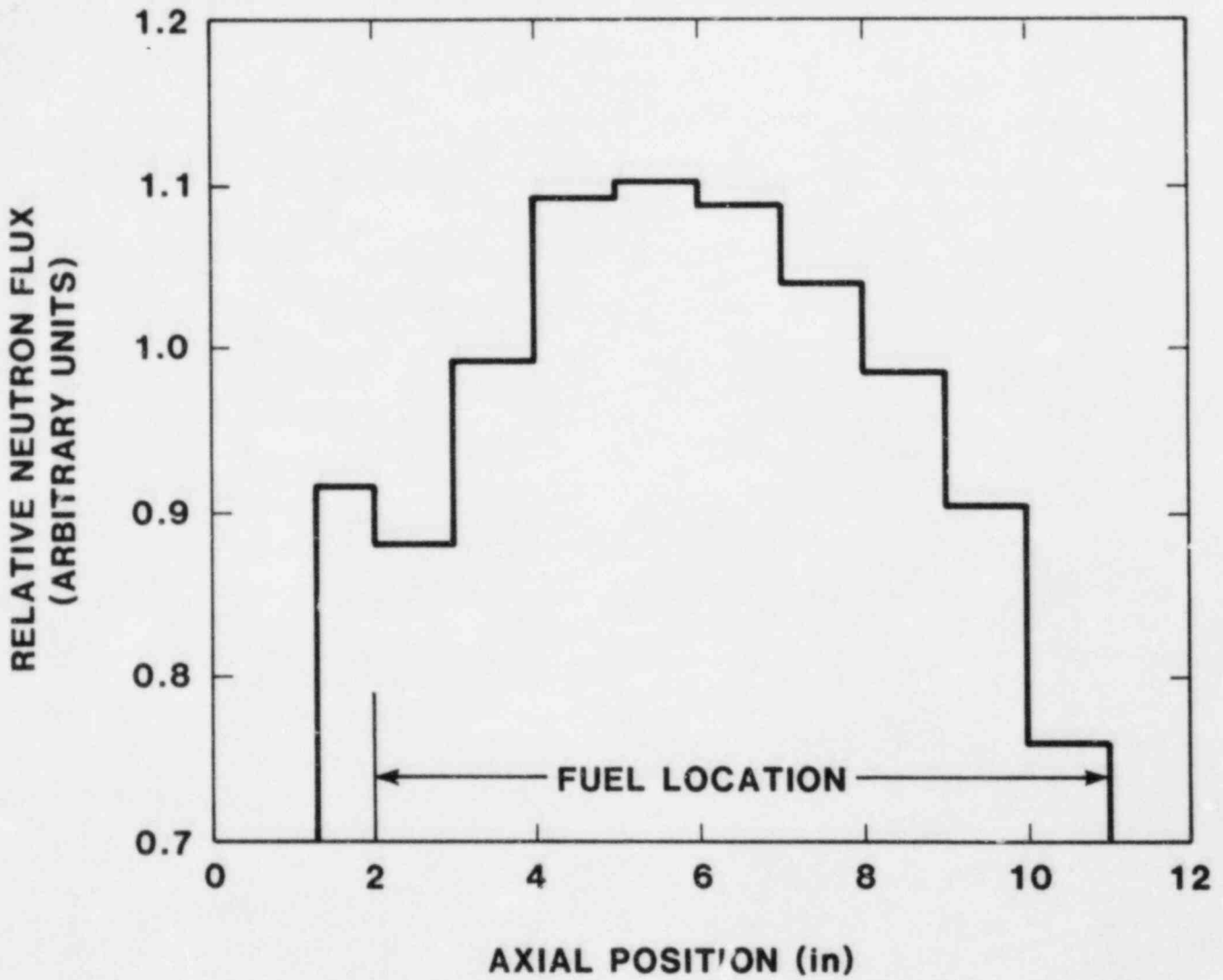
Figure 5.3-5. Axial Variation of Neutron Flux

142

e. Measuring Absolute Energy Deposition Coupling Factor

The success of the thermocouple model developed in 5.3.1.2a above should make possible a more accurate determination of the coupling factor between fuel temperature and ACRR energy. In previous measurements of this kind, the thermocouple was modeled as a single node, and few details of the energy transfer between the fuel and the thermocouple were included.

5.3.1.3 Posttest Examination of TRAN-2

a. Evidence of Steel in Leading-Edge Plugs

The nature of the leading-edge plugs observed in TRAN Series I experiment TRAN-2 has been of interest because their location at the leading edge suggests a bulk-freezing mechanism, yet the fuel penetration distance, about 90 cm, disagrees strongly with the bulk-freezing model. During this quarter, TRAN-2 was disassembled and studied in the hot cell facility, yielding information on the plug composition and details of the crust observed in TRAN-2.

Sections near the channel entrance show steel melting and ablation and a sheet of melted and refrozen steel surrounding a thick fuel crust. Although this geometry is superficially similar to TRAN-4 results, the boundary between the molten steel and the outside of the fuel crust is much more "jagged" in TRAN-2. A longitudinal section through the two plugs at the end of the TRAN-2 crust shows isolated areas of steel distributed throughout the fuel plug, suggesting an ablation-freezing type of mechanism with reduced heat transfer between the fuel and the steel, as compared to the traditional ablation-freezing model.

More complete studies of the crusts and the plugs are underway.

5.3.2 PLUGM Code Development and Application

5.3.2.1 Pretest Analysis of the Annular Channel Experiment (Series II)

The first TRAN Series II experiment is scheduled for February 1983. This test will use an annular freezing channel to investigate the stability of fuel crusts on steel surfaces of opposite curvature. The resulting information will help determine the applicability of stable-crust, conduction-freezing models to the freezing and plugging of fuel in noncircular flow channels. Arguments have been made in the past that in such flow channels (intersubassembly gaps, flow channels in the upper axial blanket) crusts may not be stable against the hydrodynamic forces associated with fuel flow. This annular channel experiment should determine whether the crust on the inside of a cylindrical surface (outer surface of the annulus) is more stable than the crust on the outside of a cylindrical surface (inner surface of the annulus).

Project personnel configured the geometry of the annular channel to be relevant to the analysis of fuel plugging and freezing in the CRBR upper axial blanket. Thus, the hydraulic diameter was chosen to be 3.2 mm and the inner diameter of the annulus was chosen to be 5.84 mm, the diameter of a CRBR fuel pin. This results in an outer annulus diameter of 9.04 mm. Experimenters want to prevent instantaneous wall melting at the time of fuel/steel contact, so the freezing channel will be preheated to a temperature of ~775 K (502°C). The results of this experiment should then be most directly comparable to the results of TRAN 1, 2, and 3. ACRR power pulse is planned that will heat the fuel up to an average temperature of ~3600 K (3327°C) prior to its injection into the freezing channel. This should assure that even with the axial power distribution in the ~23-cm-long fuel sample, the fuel at the leading edge of the flow will be above the liquidus temperature. The helium driving pressure (Δp) will be set at 10 bars.

A pretest analysis of the annular channel experiment (with the above defined parameters) was performed with the PLUGM code. A 100-g fuel sample is to be used in this first experiment. However, based on experience with the TRAN Series I experiments, project personnel anticipate that a substantial fraction of that 100 g will not be injected into the freezing channel. Thus, the PLUGM calculations were performed for assumed quantities of available fuel of 100, 75, and 50 g.

The results of the PLUGM calculations appear in Table 5-VI. As the table shows, instantaneous wall melting for this combination of steel and fuel initial temperatures is not predicted. As for experiments TRAN-2 and TRAN-3, however, the turbulent heat transfer from the superheated fuel to the wall does eventually raise the crust/wall contact temperature above the steel melting temperature. The extent of wall melting is somewhat less than that predicted for TRAN-2 and TRAN-3.

Table 5-VI

PLUGM Predictions for Annular-Channel TRAN-II Experiment

Initial Mass of Fuel	Mass in Freezing Channel	Axial Crust Length	Maximum Crust Thickness	Initial Contact Temperature	Axial Extent of Wall Melting
50 g	38.5 g	58 cm	0.15 mm	1540 K	~2 cm
75 g	59 g	79.5 cm	0.19 mm	1540 K	~6 cm
100 g	79 g	97 cm	0.24 mm	1540 K	~8 cm

If no blockage forms (TRAN-2), then calculations indicate that mass depletion of the original fuel mass by crust formation and film deposition will result in total crust lengths of 97, 79.5, and 59 cm for the cases of 100, 75, and 50 g, respectively, of initial fuel mass. The calculated masses of fuel in the freezing channel are 79, 59, and 38.5 g, respectively, for these three cases. The remainder of the fuel was calculated to be deposited (crust and film) in the melt chamber and in the transition region between the melt chamber and the freezing channel. The maximum calculated crust-plus-film thickness ranged from 0.15 to 0.24 mm, consistent with TRAN 1, 2, and 3 predictions.

5.3.2.2 PLUGM Code Development and Documentation

During this quarter, PLUGM development personnel drafted a topical report describing the code. This draft was distributed for internal Sandia review. Developers anticipate that the topical will be suitable for informal external distribution during the next quarter.

5.3.3 Design of TRAN Series III (GAP) Experiments

5.3.3.1 Heat Transfer from Fuel to Steel Containment Walls

The TRAN/GAP experiments are designed to study downward fuel penetration through planar channels representative of the gaps between adjacent blanket subassembly walls in a heterogeneous-core LMFBR. In these experiments, the melting of about 2 kg of pure UO_2 or UO_2/steel mixtures will occur, the melt being driven downward by low driving pressures (a few atmospheres at most). An annular cylinder of melt will be guided into the planar channel by a wedge-shaped transition. The melt load will probably be preheated to as much as 1173 K (900°C) to improve the uniformity of melt heating. The planar channel will be preheated to temperatures as high as 1173 K (900°C) to investigate conditions typical of accident scenarios.

One of the major safety questions in such an experiment is survival of the containment if the channel plugs rapidly and the hot fuel remains in the cylindrial form. Preliminary heat-transfer calculations showed that melting of the containment walls depends critically on the thickness of the fuel cylinder. Therefore, more detailed neutronic design of the experiment is required.

5.3.3.2 Neutronics Calculations

A range of fuel and moderator geometries was studied with the TWOTRAN neutron transport code. Based on these calculations, up to 2 kg of pure UO_2 can be heated with reasonable radial uniformity, provided that a hydrogeneous moderator is placed on the inside of the fuel cylinder. Since preheating of the fuel is planned, various methods of protecting the moderator from heat are being investigated.

5.3.4 TRAN Series I Topical Report Preparation

The TRAN Series I Topical Report was distributed to the coauthors for critical review, but busy schedules may delay this process considerably.

5.4 References

5-1.   *Advanced Reactor Safety Research Quarterly Report, July-September 1981*, NUREG/CR-2238 (3 of 4), SAND81-1529 (3 of 4) (Albuquerque, NM: Sandia National Laboratories, October 1982), pp. 5-1 to 5-8.

5-2.   *Advanced Reactor Safety Research Quarterly Report, October-December 1981*, NUREG/CR-2238 (4 of 4), SAND81-1529 (4 of 4) (Albuquerque, NM: Sandia National Laboratories, August 1983), pp. 225-236.

5-3.   *Advanced Reactor Safety Research Quarterly Report, April-June 1982*, NUREG/CR-2679 (2 of 4), SAND82-0904 (2 of 4) (Albuquerque, NM: Sandia National Laboratories, December 1983), Section 5.1.

5-4.   *Fabrication, Irradiation, and Postirradiation Examination of the PNL-9 Mixed-Oxide Fuel Pins*, HEDL-TME-80-19, compiled by R. E. Rowley (Hanford, WA: Hanford Engineering Development Laboratory, July 1981).

5-5.   S. K. Rhow and D. M. Switick, *An Assessment of HCDA Energetics in the CRBRP Heterogeneous Reactor Core*, CRBRP-GEFR-00523 (Sunnyvale, CA: General Electric Company, December 1981).

5-6.   L. Vaeth, "Current Status of Modeling Fission Gas Behavior in the Karlsruhe Code LANGZEIT/KURZEIT", PSB-Ber 742 (Karlsruhe, FRG: Kernforschungszentrum, Karlsruhe).

5-7.   *Advanced Reactor Safety Research Quarterly Report, July-September 1982*, NUREG/CR-2679 (3 of 4), SAND82-0904 (3 of 4) (Albuquerque, NM: Sandia National Laboratories, to be published).

6. LIGHT WATER REACTOR (LWR) DAMAGED FUEL PHENOMENOLOGY

Sandia's LWR Damaged Fuel Phenomenology Program includes analyses and experiments that are part of the integrated NRC Severe Fuel Damage (SFD) Research Program. Sandia will investigate, both analytically and in separate-effects experiments, the important "in-vessel" phenomenology associated with severe LWR accidents. This investigative effort will provide for three related research programs, the Melt-Progression Phenomenology (MPP) Program, the Damaged Fuel Relocation (DFR) Program, and the Damaged-Core Coolability (DCC) Program. These programs are key elements in the NRC research effort to provide a data base to assess the progression and consequences of severe core-damaging accidents.

The focus of these activities is to provide data and analytical models to support current NRC efforts in determining how to deal with accidents beyond the current design basis to include:

a. Reducing PRA uncertainties by improving methodology and codes.

b. Evaluating possible refinements in mitigation procedures and systems.

c. Planning for severe-accident management and emergency response.

d. Evaluating other regulatory decisions for accident conditions beyond the design basis.

6.1 Melt Progression Phenomonology
(J. B. Rivard, 6420A; M. F. Young, 6425)

The objective of this program is to provide balanced perspectives and capabilities applicable to that phase of severe LWR accidents starting with initial core damage and progressing through to breach of the reactor vessel and discharge of core materials into the containment environment.

The formal elements comprising this program are:

a. Core Damage Sensitivity Studies.

b. Severe Accident Uncertainty Analysis.

c. Melt Progression Model (MELPROG) Development.

6.1.1 Core Damage Sensitivity Studies

The core-damage sensitivity studies are directed toward identifying the most influential phenomena that govern the in-vessel core degradation process. The outline of Volume 1 of the sensitivity study report, Sensitivity Studies of Severe PWR Fuel Damage behavior, Vol 1,

Prequench Behavior, by R. O. Gauntt, J. B. Rivard, and M. F. Young, was prepared. Volume 2 of the report, to follow, will report on the quench behavior studies. The sensitivity matrix has been designed. Because exercising every combination of factors would call for more than 1200 computer runs, a two-level factorial approach is to be adopted. Doing this will reduce the computer runs to be correlated to less than 100.

This two-level factorial approach will permit project personnel to investigate the influence of six "external" factors:

a. Oxidation kinetics.

b. Void fraction model.

c. Sequence pressure.

d. Power level.

e. Hydrogen blanketing.

f. Axial power distribution.

Most of the two-level factorial study on the six external factors was completed and much of the preparation of the report documenting this work was also completed.

Additional work is now recognized as necessary in the preparation of the DFR-DQ matrix because of effects revealed by the exercising of the experiment simulation code and the necessity for limiting the experiment conditions, especially with regard to pressure, inlet superheat, and power distribution. A revised set of factors for the matrix may be necessary.

Sandia staff members have begun to analyze the air oxidation tests of K. T. Stalker (Sandia) using a modified version of the experiment code. The purpose of the analysis is to verify the heat transfer and oxidation models used in the DFR experiment design codes. Although the air oxidation test series is primarily intended for diagnostic development, the tests have achieved temperatures, under rapid oxidation conditions, of up to 2500 K (2227°C), providing a useful data base for design code verification.

6.1.2 Severe Accident Uncertainty Analysis (SAUNA)

The goal of this work is the quantification of the impact of phenomenological uncertainty on probabilistic risk analysis (PRA). It is a multiprogram effort at Sandia with a single working group.

Early in the quarter, the outline of the Phase 1 report, Severe Accident Uncertainty Analysis, was prepared, and Section 5.1, Uncertainty Analysis in Severe Core Damage Processes," was rough-drafted. Because of subsequent difficulties in satisfying all requirements, the

Phase 1 report contents were revised and the report retitled Identifi-
cation of Severe Accident Uncertainties. Except for Chapter 1,
"Introduction," and Chapter 8, "Factors, Concepts, and Recommenda-
tions," most of the preparation of this report is complete. A com-
plete consensus on overall treatment methodology is still lacking, but
the format for all tabular entries in the report was resolved.

6.1.3 Melt Progression (MELPROG) Code Development

The report, Modeling of LWR Coolant Systems During Severe Acci-
dents: MELPROG Prospective, was completed. Draft copies are cur-
rently undergoing review by Sandia management and the NRC. Some
revision is expected prior to issuance of the final report.

6.2 Light Water Reactor (LWR) Fuel Damage Experiment
(A. C. Marshall, 6423; K. O. Reil, 6423; K. T. Stalker, 6426; R. O. Gauntt, 6423)

6.2.1 Introduction

This program is directed toward examining the key phenomena that determine the core-damage configuration during the progression of a core melt sequence in an LWR core-uncovering accident. This program uses the information and perspectives gained in current LWR safety programs and focuses on the design of experiments which can contribute to the resolution of important severe-damage issues.

The two major areas of interest regarding in-vessel phenomena are:

a. The behavior of fuel and cladding during the stages of major core deformation from rod-bundle geometry to a severely degraded geometry and

b. The response of the severely damaged fuel to reintroduction of coolant from the emergency core cooling system (ECCS), especially the questions of redistribution of quenched material, short-term cooldown, increased steam generation, and oxidation reaction kinetics.

Information on the first item is necessary to predict the course and duration of core meltdown and associated effects in containment; resolution of the second provides the essential information to guide action that would terminate the accident and/or mitigate its consequences and to preclude action that could exacerbate the accident. Obviously, resolution of issues in (b), above, depends strongly upon knowledge of the phenomena implied in (a). Initial research priorities and the program proposed here focus on the behavior of fuel and cladding during major deformation sequences without introduction of additional liquid coolant.

The present work under this subtask focuses on the in-pile experiments because neutronic heating allows prototypic heat generation under severely damaged conditions.

During this quarter, project personnel performed analyses to evaluate operational parameters for the first DFR experiments, including the effects of phenomenological uncertainty in oxidation kinetics and hydrogen-blanketing behavior. They also performed preliminary analyses to evaluate the use of irradiated fuel in later DFR experiments.

6.2.2 Test Planning and Analysis

The DFRMOD3 code has been used to establish the operating parameters for the first in-pile severe-fuel-damage experiment. The desired range of relevant experiment conditions was first determined by using the PWRMOD2 codes to estimate PWR core conditions during a

150

core-uncovering accident. Two parameters were selected to provide the criteria for comparing experiment conditions to the PWR accident conditions. One parameter was the fraction of cladding oxidized at various axial locations as a function of local temperature. This parameter was chosen primarily because the fuel damage behavior depends upon the oxidation fraction and cladding temperature. The other parameter was the time-dependent axial temperature distribution in the fuel rods. Reasonable agreement between the experiment and PWR predictions for these two parameters was considered necessary to insure that the experiment will be performed in the phenomenological range of interest.

Calculations with the DFRMOD3 code established steam and fuel-rod power conditions for the DF-1 experiment, which will examine the phenomenology of cladding oxidation and fuel damage in a PWR core following a large-break LOCA. Sensitivity studies were also performed with the DFRMOD3 code. These studies showed the predicted behavior to be relatively insensitive to the inlet steam temperature and the axial fission-power distribution in the fuel rods. The behavior was moderately sensitive to the inlet steam flow rate and fuel-rod power level. As expected, the predicted behavior was very sensitive to the assumed Zircaloy/steam oxidation model.

The project staff investigated several different steam-starvation models for use in the DFRMOD3 code. These models were (1) a steam starvation-factor model, (2) the Chung surface adsorption model [6-1], and (3) a film-theory model. The steam starvation factor simply sets a limit on the fraction of available steam that can be used to oxidize Zircaloy at any given location. The Chung model represents the way in which hydrogen, in uniform steam-hydrogen mixtures, competes for chemical adsorption sites on the Zircaloy surface. The film-theory model is based on mass transport across a concentration boundary layer. The film-theory model agrees with the Chung measurements whereas the starvation factor does not. The Chung model does not allow for dependence on the mass flow rate and temperature whereas the film theory model does. The film-theory model is currently in use for all Zircaloy/steam oxidation calculations.

The DFR experiments will examine fuel conditions as one of the parameters that may affect the degree and mode of rubblization in severe-damage accidents. Sandia staff members anticipate that later DFR experiments will use irradiated fuel to allow correlation of fission-product release with the damage state. The first DFR tests, however, may use precracked fuel to represent some degree of irradiation effects on the fuel matrix. One way to achieve fuel cracking involves pulsing a fuel-rod bundle in the ACRR. The rod bundle will be contained in a canister filled with water. The induced thermal stresses, during or following the pulse, crack the fuel. This preconditioned fuel will then be available for the DFR or DQ experiments.

Project personnel have completed analyses to determine the conditions necessary for precracking the fuel. Neutronic, thermal-hydraulic, and stress calculations were required for this analysis. The staff concluded that severe fuel cracking will occur, in a fuel

rod bundle immersed in water, during cooldown following a relatively small ACRR pulse (≈100 MJ).

Project personnel are also evaluating the use of preirradiated fuel for the DFR experiments and a preliminary evaluation has been completed. The DFR tests could address several important issues related to fission products and aerosols, including fission-product release and early in-vessel chemistry, aerosol generation, magnitude, character, composition, transport, and plateout. BR-3 fuel rods from Belgium appear to be the most appropriate source of preirradiated fuel rods. The staff is checking several other potential sources for preirradiated fuel. No prototypicality problems associated with this preirradiated fuel have surfaced. Also, it appears that if the bundle γ-dose can be kept below 500 R/hr at 1 ft, and the capsule length does not increase substantially, current handling facilities can be used with relatively minor modifications. The suggested principal approach for measuring aerosols in irradiated-fuel experiments is a cold filter system.

6.2.3   In-Pile Experiment Apparatus

Project personnel have completed detailed drawings for the in-pile experiment capsule and have initiated purchasing procedures for all in-pile capsule hardware. Figure 6.2-1 illustrates the present capsule design.

Design of the optics for the in-pile experiments is nearly complete. The optical system, as currently planned, will include color and black-and-white motion picture filming, a color video system, a black-and-white video system for optical pyrometry, and a Raman/laser system for hydrogen monitoring. This system is illustrated in Figure 6.2-2.

An illustration of the entire DFR in-pile system is presented in Figure 6.2-3.

6.2.4   Out-of-Pile Tests

a.   Air Tests

Test number 9 in the out-of-pile air oxidation series was successfully completed. The test was designed to investigate further, for NRR, the possibility of propagating a zirconium "burn" in a drained spent-fuel pool but also served as a testbed for optimizing diagnostics for the in-pile series. The test geometry consisted of nine Zircaloy tubes filled with 1-cm-long pieces of silicon carbide to simulate fuel pellets. The tubes were placed in an insulating shroud and heated with an electrical heater representing the heat generated by other oxidizing clad bundles. A stainless steel plate separated the tubes such that six were on the heater side of the plate and three were on the unheated side. The experiment was observed with both video and still camera systems.
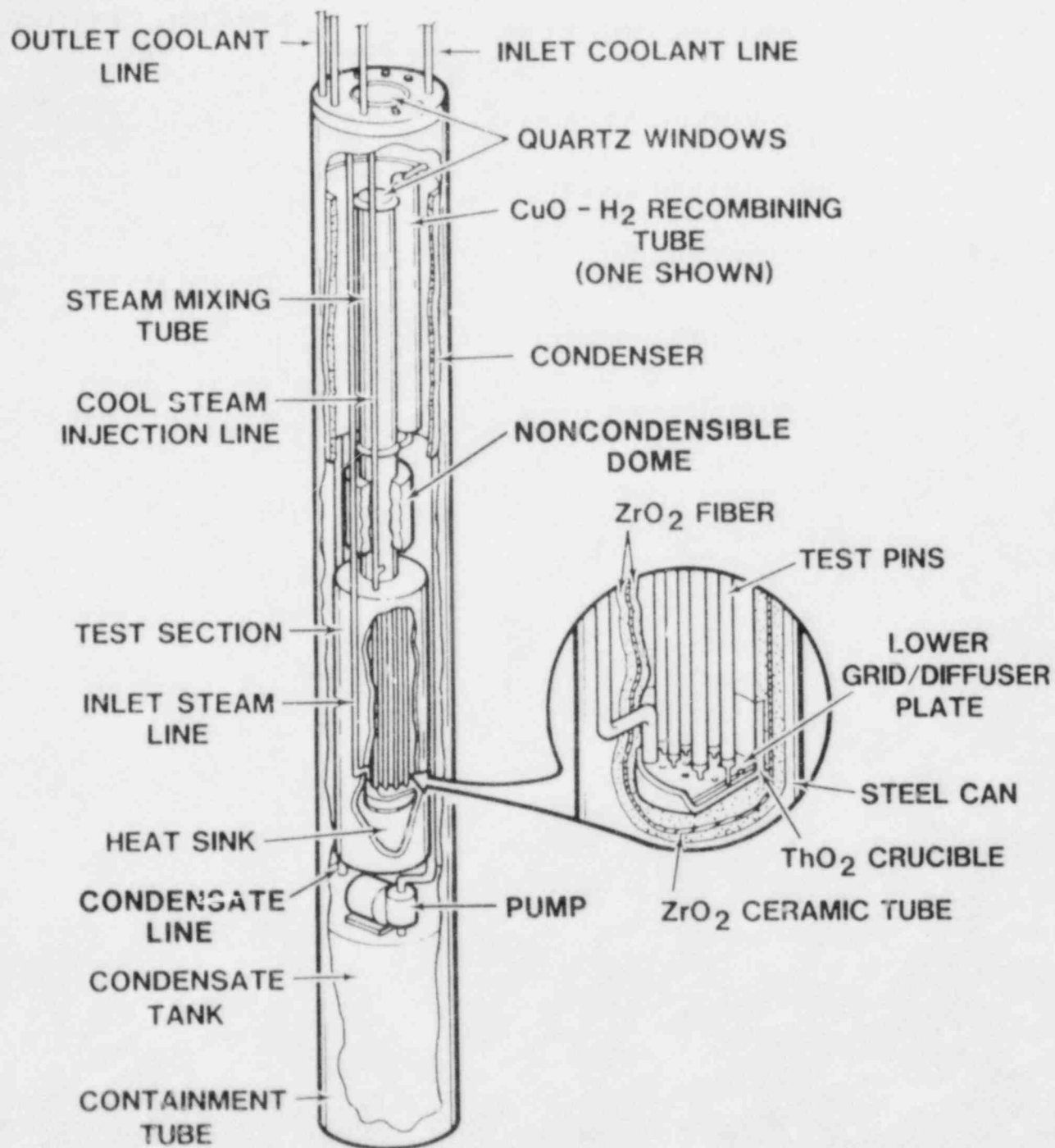
Figure 6.2-1.   DFR In-Pile Experiment Capsule

153

35 mm CAMERAS (COLOR AND B&W)

BEAM SPLITTERS

RADIOMETER

COLOR VIDEO CAMERA

UV LASER

TUBE

BEAM

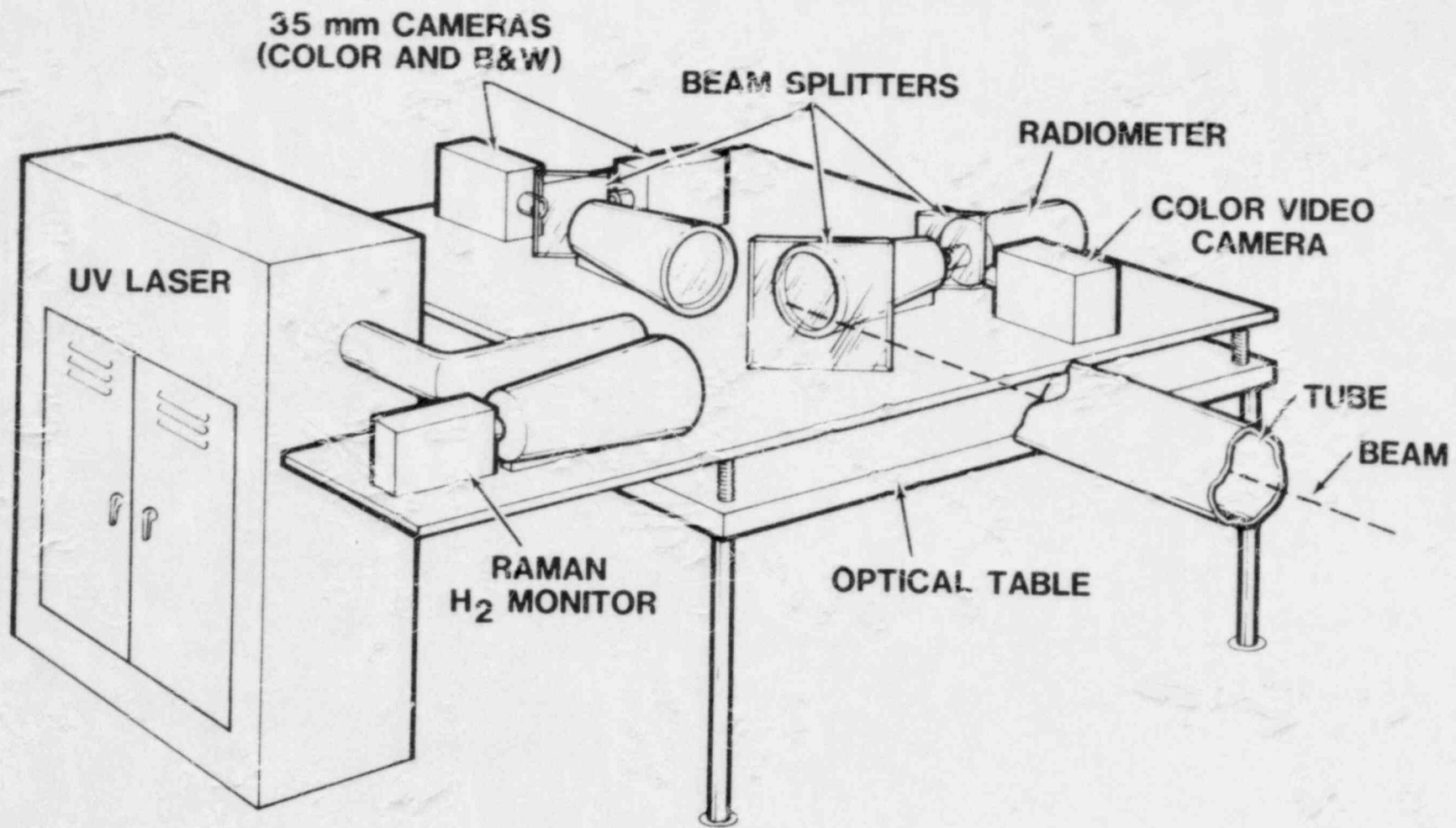RAMAN H$_2$ MONITOR

OPTICAL TABLE

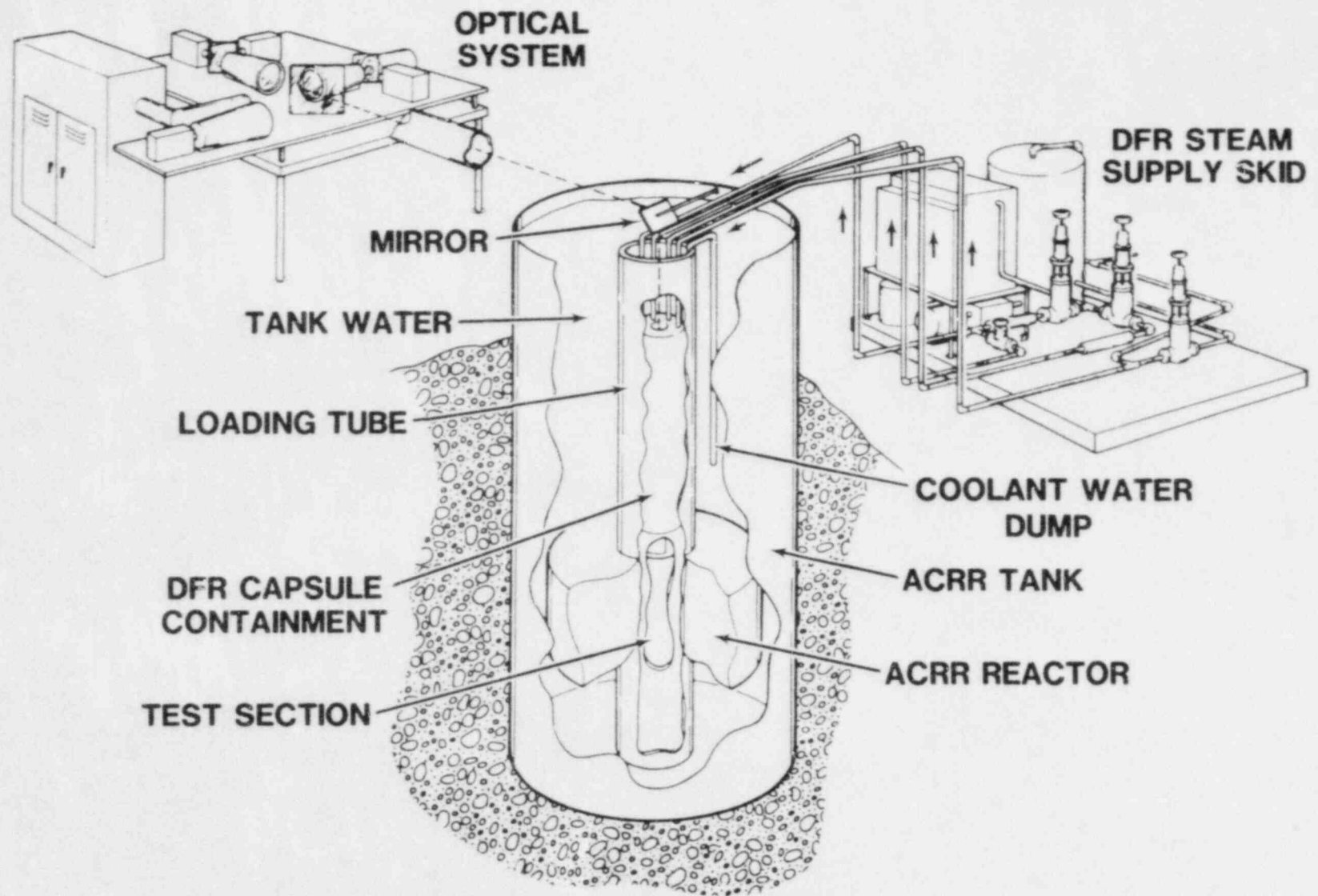154

Figure 6.2-2. Optical System (Simplified)

Figure 6.2-3.   DFR In-Pile Experiment Apparatus

The heater power was gradually increased from 500 to 1600 watts as the clad temperatures on the hot side increased to about 1273 K (1000°C) near the top of the rods. At this time, the air flow was 1.5 ft^3/min. The clad began to oxidize rapidly on the hot side of the plate, and the power to the heater was turned off. Subsequently, the plate began to melt, and rapid oxidation spread to the clad on the unheated side. The melting and flow of the steel plate can be seen very clearly in both the video tape and still photographs of the experiment. Thermocouple readings indicated that a peak temperature of about 1973 K (1700°C) occurred in the clad that was on the originally unheated side of the plate. The visual data also showed that the clad oxidized in place and did not melt away, and the pellets did not fall out of the clad. Workers at MIT and Sandia are analyzing the results of these air oxidation tests.

b. Steam Tests

Experimenters have completed the plumbing design for the out-of-pile steam system and have ordered all components. The design of a simple out-of-pile steam test section has been completed. This test section will permit the Raman hydrogen-monitoring approach to be tested under conditions similar to those found in the in-pile experiments. Development of the data acquisition and control system is continuing.

The plant electrical work required for the out-of-pile steam tests was completed. An optical test area is also being set up for the development of the visual diagnostics and the testing of the Raman hydrogen measurement technique.

To prevent possible flow oscillations in the DFR steam system, an orifice is required at the entrance to the condenser. Unfortunately, a fixed orifice cannot be used because the steam flow rate changes appreciably during the experiment; consequently, an orifice sized for the initial flow rates will produce a pressure drop, at a later stage of the experiment, that is too large because of the increase in flow velocity. Furthermore, no remote valves are available that will operate in the expected temperature range or fit within the space constraints of the DFR capsule. To satisfy the requirements for this orifice, a self-adjusting orifice was designed, based on the principle of a rotometer. The design consists of a steel ball in a tapered tube with a weight suspended from the ball by a steel rod. The choice of ball and weight size set the pressure drop across the float orifice. As the flow rate is increased, the ball rises in the tapered tube increasing the flow area, thereby maintaining a constant pressure drop. A float-orifice was fabricated and tested during this period. The orifice performed properly over the full range of steam flow rates expected for the first in-pile experiment.

6.3   Light Water Reactor (LWR) Degraded-Core Coolability (DCC) Program
      (K. R. Boldt, 6421; E. Gornam-Bergeron, 6425, P. A. Kuenstler,
      6452)

      Sandia National Laboratories is conducting a program to determine
the coolability of LWR degraded cores. The main purpose is to provide
an experimental data base for use in evaluating the applicability of
LMFBR coolability models to LWR-specific conditions. This will be
accomplished by performing a limited number of in-pile experiments
using fission heating of UO_2 rubble to simulate the source of decay
power in a severe-fuel-damage accident. For FY83, the scope of the
DCC program encompasses the following:

   a.   Continue design, acquisition of parts, and assembly of the
        first two DCC experiment packages.

   b.   Perform DCC-1, the first in-pile coolability experiment con-
        taining a UO_2 rubble bed in a water bath.

   c.   Analyze the DCC-1 results compared to current coolability
        models and develop and improve models where necessary.

6.3.1   LWR DCC Program - Experimental Activity

      During this quarter, the DCC experimental effort focused on the
following activities:

   a.   All components for the DCC-1 experiment and most components
        for the DCC-2 experiment were ordered. Those contracts that
        have already been placed were monitored to insure delivery on
        scheduled dates. The critical-path components for the DCC-1
        experiment are the primary and secondary pressure vessels
        with delivery expected in January 1983.

   b.   The liquid nitrogen storage tank and heat exchanger were
        assembled. Performance tests were completed and showed that
        the heat exchanger satisfied all required specifications.

   c.   Thermocouples for DCC-1 were received and sheath integrity
        (eddy-current) tests completed. Based on the eddy current
        test results and radiographs supplied by the manufacturer, 64
        thermocouples were selected for installation into the primary
        passthrough headers. This work is currently being performed
        by an outside contractor who will provide a glass-to-metal
        seal on each pair of thermocouple leads passing through the
        header.

   d.   Test equipment and auxiliary fixtures to be used in the DCC-1
        assembly were fabricated. These include a bell jar (0.5-m
        diameter and 3-m height) to be used for integral leak tests,
        a two-level assembly platform, and several handling fixtures.

   e.   The DCC fuel development testing program was completed. Of
        the candidate thermal neutron poisons (B_4C, B_2O_3, BN, B_2Zr

157

and Gd_2O_3), gadolinium oxide (Gd_2O_3) had the best retention
($>97\%$ during UO_2 processing) and also had the least impact on
the mechanical and chemical properties of the fuel. Neu-
tronics calculations for DCC-1 have been performed using
Gd_2O_3 and show that 1.0 a/o (1 atom Gd per 100 atoms of U)
concentration of gadolinium is sufficient to decouple the bed
power density from the liquid fraction in the bed. The
results of the neutronics calculations will be presented in
this quarterly.

Neutronics calculations for DCC-1 were performed using TWOTRAN.
[6-2, 6-3]   Figures 6.3-1 and 6.3-2 show the axial and radial power
profiles predicted for the DCC-1 experiment. The calculations were
performed with the following bed parameters:

a. UO_2 (density = 10.3 g/cm^3) with enrichment of 10%.

b.   One a/o of gadolinium in the form of Gd_2O_3 mixed homogen-
      eously in the bed.

c.   Bed porosity of 50% and totally flooded with water at 1 atm.

As Figure 6.3-1 shows, the axial power density profile is dominated by
the cosine flux distribution of the ACRR. A slight increase at the
top of the bed is caused by reflection and moderation of the neutron
flux in the water bath above the bed. Figure 6.3-2 shows that the
radial profile is strongly peaked at the outer edge of the bed. The
average power density and the overall peak-to-average ratios for a
totally wet and a dry bed are summarized as follows:

	Average Power Density (W/g/MW-ACRR)	Peak-to-Average Ratio
Totally flooded bed	0.48	1.7
Totally dry bed	0.44	1.7

The decoupling effect of the gadolinium is well demonstrated in these
predictions, showing less than a 10% decrease in power when the
flooded bed is totally dried.

To provide a basis for evaluating the reactivity effects of the
DCC-1 experiment on the ACRR core, several bounding bed configurations
were analyzed. Project personnel assumed that disturbances could
cause the bed to become void of liquid or be displaced entirely by
void or liquid. Table 6-I shows the results of these predictions for
the various bed configurations. As the table illustrates, no conceiv-
able bed configurations exist that would result in a reactivity inser-
tion of greater than +$1.00 (prompt critical). Because the assumed
bed configurations are bounding and not realistic, reactivity swings
of less than 50¢ would appear to be more appropriate for evaluating
the safety of the DCC-1 experiment. This analysis will serve as part
of the DCC-1 experiment plan to be submitted for safety review.
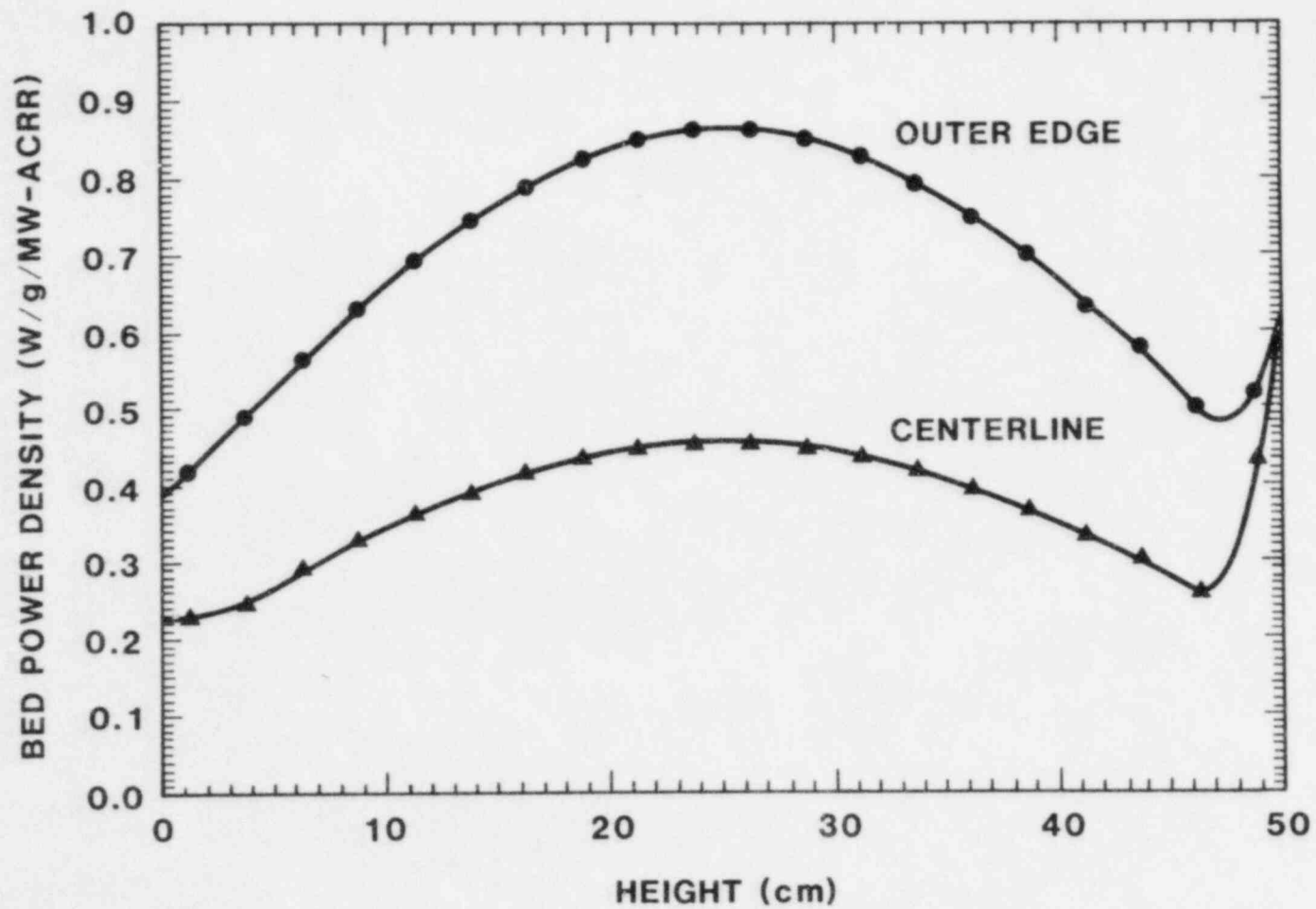
Figure 6.3-1. Axial Profile for DC   at Bed Centerline
and Outer Edge
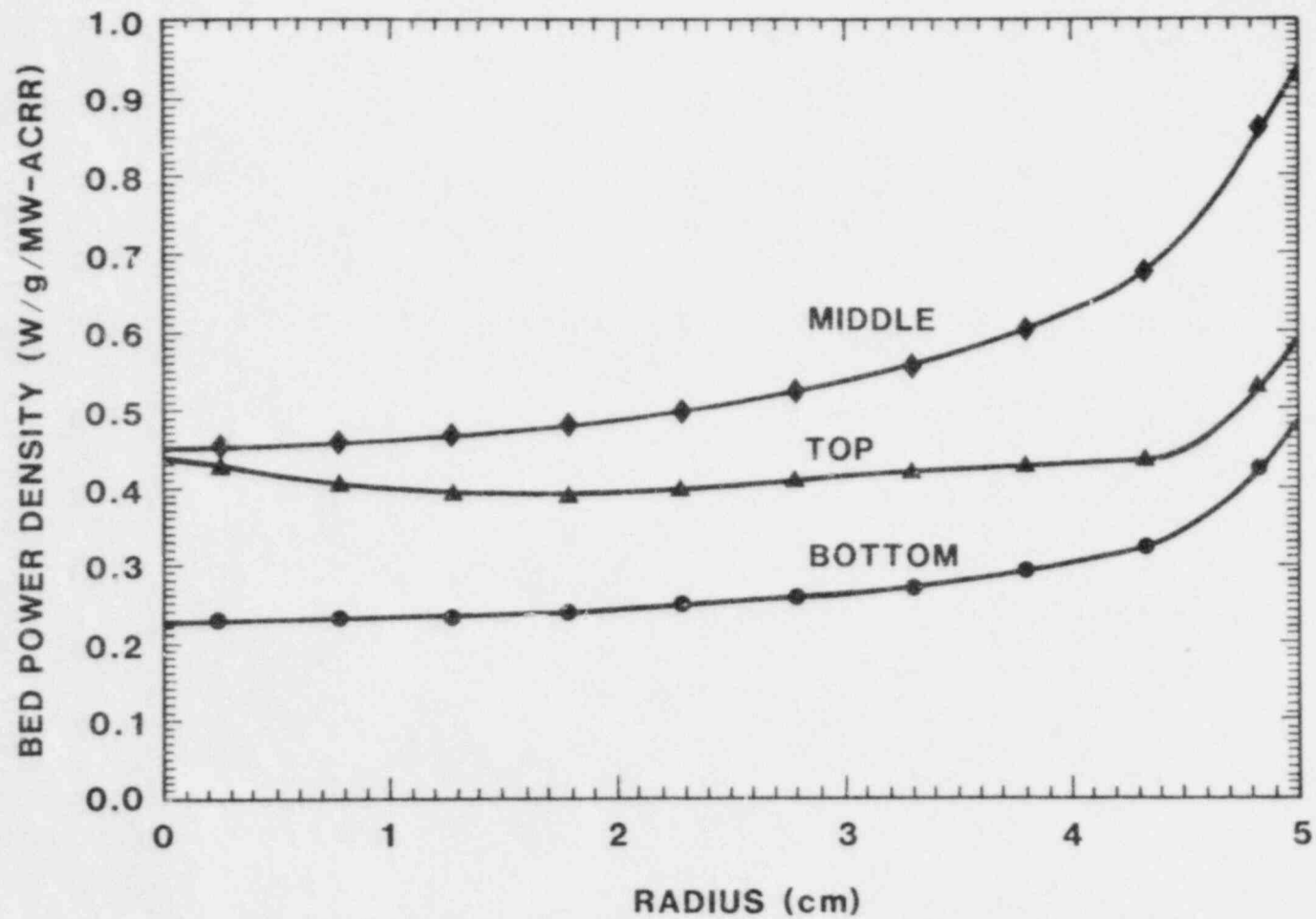
Figure 6.3-2. Radial Profiles for DCC-1 at Bed
Bottom, Middle, and Top

Table 6-I

Calculated Reactivity Worths for Various DCC Experiment Configurations

Configuration	k_{eff} TWOTRAN Calculation	Reactivity Worth Compared to Reference Reactor ($)	Reactivity Worth Compared to Reference Experiment ($)
(1) Reference ACRR: free field, no axial reflectors in cavity	1.112	0.0	+8.0
(2) Reference DCC Experiment (bed totally flooded)	1.049	-8.0	0.0
(3) DCC Experiment (bed totally dry)	1.053	-7.5	+0.5
(4) DCC Experiment (bed flooded, mid 4 in. of fuel and water replaced by void)	1.054	-7.3	+0.7
(5) DCC Experiment (entire bed replaced by void)	1.056	-7.1	+0.9
(6) DCC Experiment (entire bed replaced by water)	1.040	-9.1	-1.1

6.3.2 LWR Degraded Core Coolability (DCC) Program - Analysis

6.3.2.1 Particle Bed Fluidization

Particle bed fluidization phenomena relevant to LWR coolability questions were surveyed briefly during this quarter. Emphasis was on determining the main sources of uncertainty affecting the long-term coolability of degraded cores. The main conclusions of the survey are:

a. Bottom-Blocked Beds

For bottom-blocked heated beds in steady state, the liquid flows downward and the vapor flows upward. Thus, only the vapor has the potential to fluidize the bed particles. Some particles will be exposed to liquid flow exclusively, some to vapor flow exclusively, and some to both. If the porosity of the bed is uneven, for example, the vapor will flow preferentially through the regions of increased porosity. In heated beds, another complication is that the superficial velocities of both the liquid and the vapor vary as a function of height in the bed, the vapor velocity increasing with height. For beds of single-size particles in steady state at powers below or near the dryout power, the vapor flow is not large enough to fluidize the beds (except locally, at the tops of the beds, when channels are formed). The uncertainty for bottom-blocked beds in steady state involves whether, for mixed-size particle beds, the small particles will be fluidized and escape from the beds or relocate within the beds, what size particles will be fluidized, what the effect of bed height has on the escape potential of the small particles, and what is the effect on the dryout heat flux if some of the small particles escape from the top of the bed and remain fluidized. Gabor, ANL[6-4] noticed that the particles having diameters less than 0.1 mm fluidized out of his mixed particle-size beds when the coolant was sodium. No experiments with water were done that included particles of less than 0.1-mm size.

b. Bottom-Permeable Beds

For heated beds with forced flow of liquid through the bottom of the bed, both the liquid and the vapor can fluidize the bed. If the flow of liquid and vapor is large enough, the entire bed can be fluidized. The liquid flow required to fluidize a bed of either single- or mixed-particle size in the presence of flowing vapor can probably be estimated fairly accurately. Thus, the main uncertainties concern (as they did for the bottom-blocked beds) mixed particle-size beds where the liquid and vapor flows are not large enough to fluidize the whole bed but may be capable of relocating the smaller particles within the bed.

c. Transient Phenomena

Finally, the greatest uncertainty as well as potentially the most important fluidization phenomena probably occur during transient processes. Even when the bed bottom is blocked, liquid and vapor can be forced upward in the bed at high velocities for short periods of time by a number of means (such as superheat disturbances and step changes in power). Furthermore, even long periods of boiling have been observed to "loosen" the bed and produce a change in the dryout heat flux. Thus, a potential exists for temporary fluidization and subsequent stratification to occur. Whether beds that are temporarily fluidized can be kept in the fluidized state by high power generation within them remains uncertain.

6.3.2.2 Experimental Determination of Porosity of Particle Beds

Since September 1981, the DCC program and the Sandia University Research Program (SURP) have supported jointly a series of particle bed experiments being conducted under Dr. Mohamed El-Genk at the University of New Mexico (UNM). The experiments conducted thus far are particularly relevant to LWR severe accident analysis. They include measurements of the porosity of debris beds made from different size and shape particles, some of which are commonly used to investigate coolability limits of particle beds (i.e., spheres) experimentally and others of which are believed to be typical in shape and size to those that will be found in a degraded LWR core (i.e., granular particles and particles that are formed during a melt-water interaction). In the latter case, particles were obtained from Sandia's FITS experimental program.[6-5]

In the FITS tests, about 20 kg of molten iron-aluminum oxide were dropped into a pool of water. In the experiments where a single steam explosion occurred, the particulate typically had an average size of about 1 mm, a size distribution that was roughly lognormal, and a variance of about 1 (Figure 6.3-3).[6-5] Debris from FITS 9-B is a good example and was used in the UNM studies. In FITS 6-B and 7-B, no steam explosion occurred. For these tests, the debris also followed a lognormal size distribution, but with an average size of about 15 mm and a variance of about 2. In FITS 8-B, multiple steam explosions occurred. The particulate was very small, with an average size of 0.15 mm, and followed a lognormal size distribution. Debris from FITS 8-B and 6-B were provided to the UNM experimental team and were used in a few studies.

To simulate granular particles that might have been created during an LWR accident by the quenching and subsequent fragmentation of hot solids, fragmented steel spheres were used. Porosity was also measured for beds of spherical particles, the primary interest being to investigate the characteristics of particle beds most commonly used in experiments designed to determine the coolability limits of particle beds.

In a reactor accident, debris resulting from a melt-water interaction will eventually relocate downward and settle into beds of debris. These debris will almost certainly be spatially inhomogeneous in composition (according to particle size, density, chemical composition, shape, etc.), two possible extreme configurations being a homogeneous mixture and a mixture that is horizontally stratified (in layers) according to size. Thus, the porosity measurements were conducted on groups of particles that were uniform in size, representing a single layer of a stratified bed, or on a homogeneous mixture of particles.

The results of the porosity measurements are shown in Figure 6.3-4. To insure accuracy of experimental results, two different methods of measuring the porosity were employed. In the first, the water displacement method, a given volume of water was added to either a 4- or a 10-cm tube, then the particulate was gently dropped into the
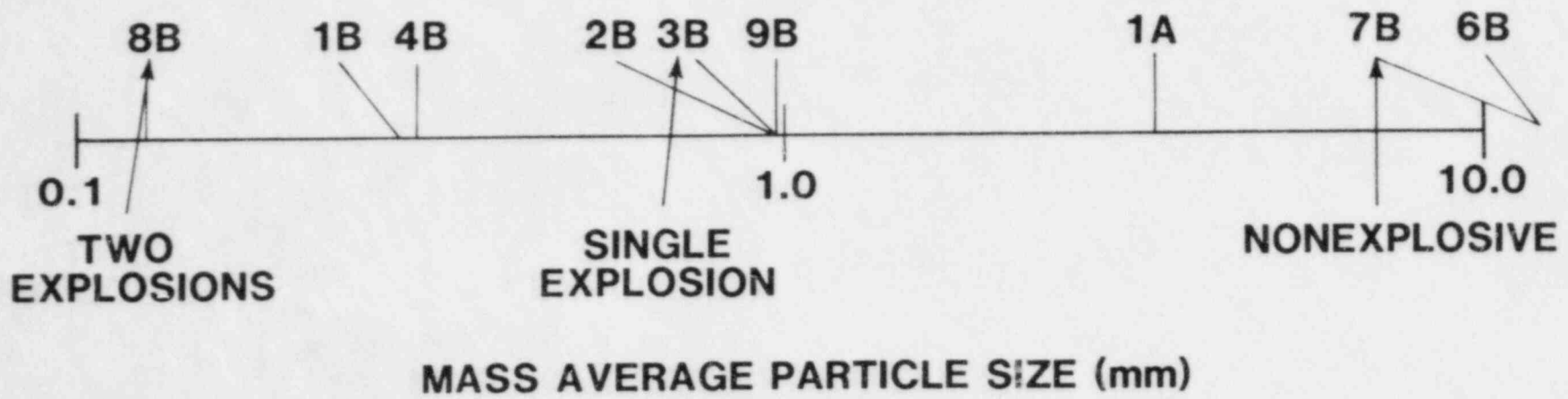
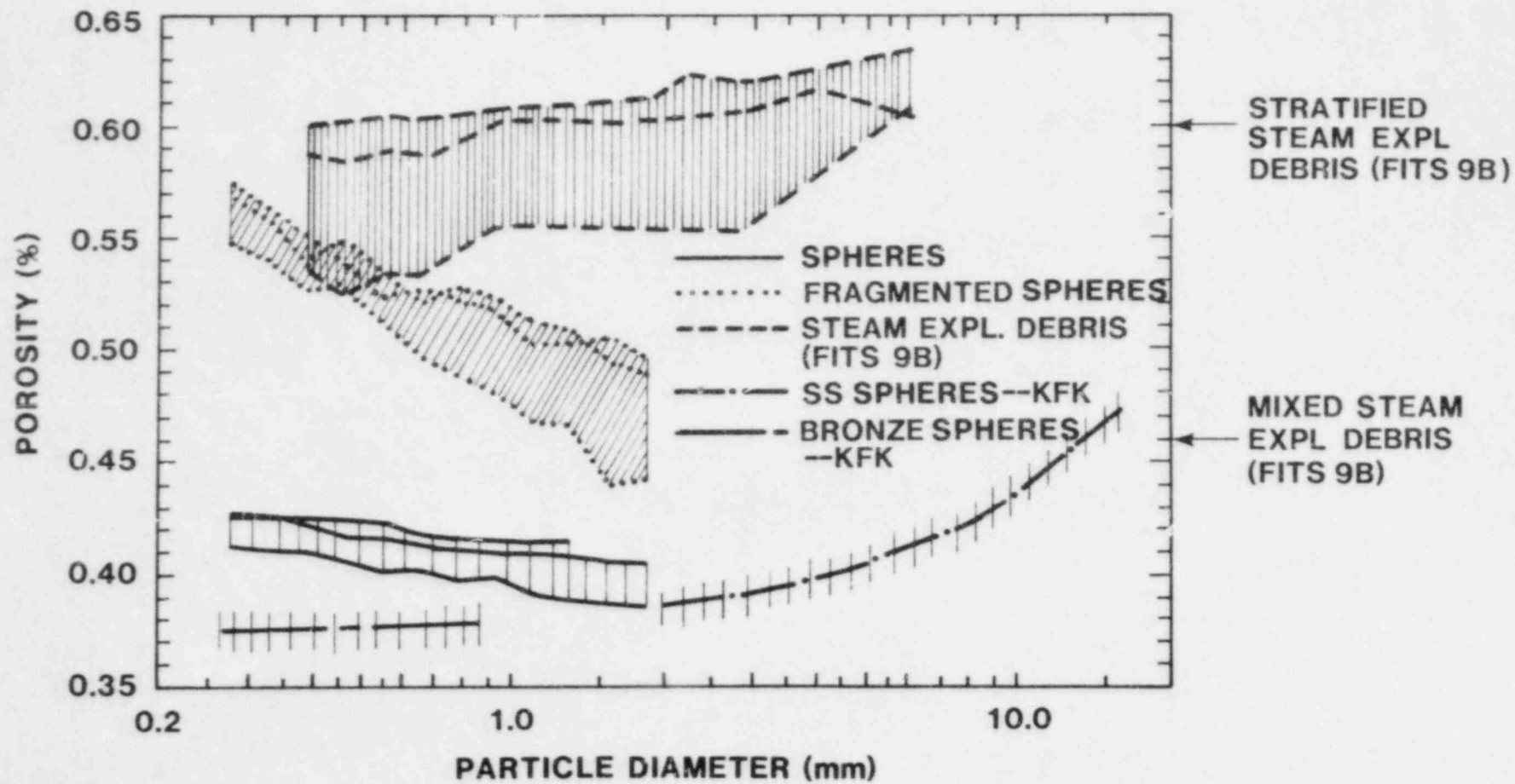Figure 6.3-3   Sandia-FITS Particle-Size Distributions

Figure 6.3-4 Porosity as a Function of Particle Size

water to form a bed. Measuring the bed height and the initial and final water heights allows measurement of the porosity of the particle bed, as long as a significant quantity of air has not been entrapped in the bed. Air entrapment was not observed to occur during the process of dropping the particles through the water. A second method to determine the porosity used only the height of the particle bed formed by dropping particles through air into the tube and a known value of the density of the material making up the particles. In addition, after an initial determination of the porosity was made for a particular bed, the bed was packed by giving sharp blows to the side of the tube. The porosity was then remeasured. The range of values of porosity, shown in Figure 6.3-4 for each bed of a given type and size of particulate, represents the range of values measured for packed and unpacked beds and both types of measurements. The results clearly show that:

1. Stratified beds of spherical particles will form with lower porosity than will beds of granular particles or FITS parti-cles, a typical value being about 0.4.

2. Stratified beds of granular particles will form with porosity that is higher than a similar bed of spheres but lower than a bed of FITS particles. The porosity of the small-particle layers (typically 0.56) will be larger than that of the large-particle layers (typically 0.48).

3. Stratified beds of particulate similar to FITS 9-B particles (formed during a single-triggered steam explosion) will form with a porosity larger than beds of spheres or granular particles. The porosity of the small-particle layers will be slightly less (typically 0.58) than the porosity of the large-particle layers (typically 0.62).

4. Homogeneous beds of particles of different sizes always form with a smaller porosity than they would if the same particles were strictly stratified in layers according to size.

The effect of the tube in which the bed is formed is to increase the average porosity of the bed when the size of the particles in the bed approaches 10% of the diameter of the tube. This is clear from the results of the porosity measurements made on beds of spheres (Figure 6.3-4).[6-6] In this case, the diameter of the tube holding the beds was 10 cm.

6.3.2.3 Measurement of the Capillary Heads of Particle Beds

Under the same funding programs as were described in the previous section, the capillary head of water in particle beds was measured. The particulate used for the beds was the same type as that described in the previous section. The experimental method employed was to fill a bed formed within a tube with water, set the tube in a shallow pool of water, then allow the water to drain through the permeable bottom of the tube until a stable water level was reached in the bed. The

capillary head is the difference between the water level in the tube and the water level in the outside pool. It is predicted to be[6-8]

$$H = \frac{1}{\rho g} \frac{6 \cos\theta}{\Omega} \frac{\sigma(1 - \epsilon)}{D\epsilon} ,$$ (6.1)

where σ is the surface tension in the liquid, θ is the contact angle between the particles and the liquid, ϵ is the bed porosity, ρ is the liquid density, g is the gravitational constant, and Ω is the shape factor. Figure 6.3-5 shows the results of the experiments and a comparison with the theoretical expression of Carmen for spheres and for particulate from FITS 9-B.[6-7, 6-8] A shape factor of 1 was used for both types of particulate. Clearly, from the figure, the results for the spheres follow the theoretical expression well. The data for the FITS 9-B particles do not, especially for small particulate. If the shape factor is adjusted so that the results fit the theoretical expression (Eq. 6.1), the values of the shape factor are as in Table 6-II. Table 6-II also includes results for granular particles.

A full description of the porosity and capillary head experiments and a catalogue of the results can be found in Reference 6-7.
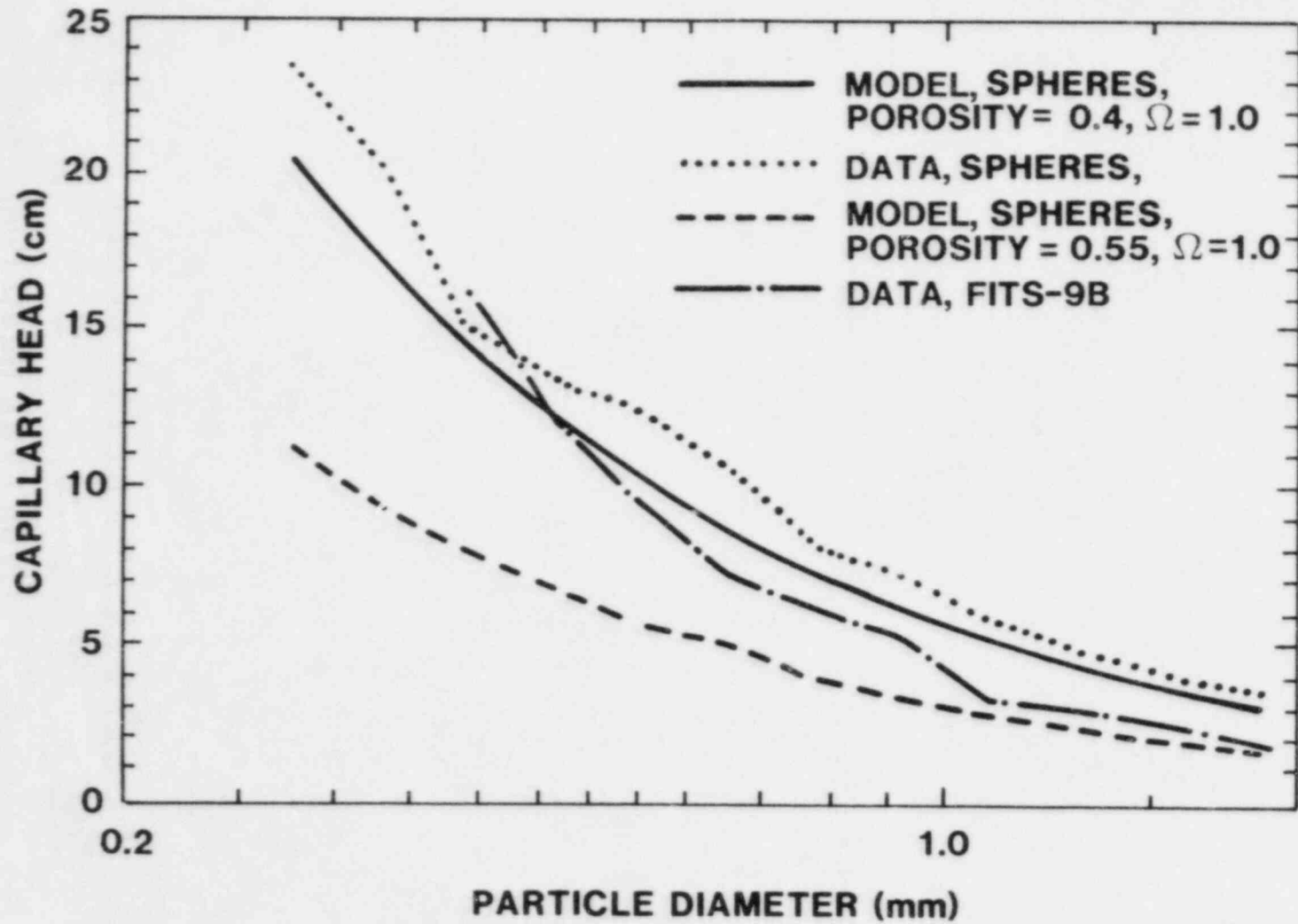
Figure 6.3-5   Measurement of Capillary Head as a Function
of Particle-Size Distribution

Table 6-II

Values of the Shape Factor

Avg. Particle Size (cm)	Shape Factor		
	Steel Shot	Steel Grit	FITS-9B Fragments
0.01	0.887	0.622	0.348
0.02	0.916	0.683	0.429
0.05	0.955	0.773	0.562
0.1	0.986	0.848	0.691
0.2	1.018	0.932	0.850
0.3	1.037	0.984	0.959
0.4	1.051	1.023	1.045
0.5	1.062	1.054	1.116
0.6	1.07	1.081	1.179

6.4 References

6-1. H. M. Chung and G. R. Thomas, "Rate Limiting Effects of Gaseous Hydrogen on Zircaloy Oxidation," Proceedings of the Workshop on the Impact of Hydrogen on Water Reactor Safety, 26-28 January 1981, Vol. 2 of 5, SAND81-0661 (Albuquerque, NM: Sandia National Laboratories, September 1981).

6-2. W. E. Nelson, private communications on DCC neutronics calculations, Sandia National Laboratories, October-December 1982.

6-3. K. D. Lathrop and F. W. Brinkley, Theory and Use of the General-Geometry TWOTRAN Program, LA-4432 (Los Alamos, NM: Los Alamos National Laboratory, May 1970).

6-4. J. D. Gabor et al, "Studies and Experiments on Heat Removal from Fuel Debris in Sodium," Proc. ANS Fast Reactor Safety Meeting, Beverly Hills, CA, 2-4 April 1974, CONF-740401, pt. 2, pp. 823-844.

6-5. D. E. Mitchell et al, Intermediate Scale Steam Explosion Phenomena: FITS-A and MD-Series Experiments and Analysis, SAND81-0124, NUREG/CR-2145 (Albuquerque, NM: Sandia National Laboratories, September 1981), and D. E. Mitchell, private communication.

6-6. L. Barleon et al, Particle Bed Experiment 82.2.3-3.15: Dryout Before Channel Penetration and Boiling-Induced, Irreversible Bed Changes, 01.02.15P81C (Karlsruhe, FRG: Kernforschungszentrum, Karlsruhe, June 1982).

6-7. M. S. El-Genk and D. Louie, Porosities and Capillary Heads Measurements in Particulate Beds, NE-94(82) SURP-080-6 (Albuquerque, NM: The University of New Mexico, November 1982).

6-8. A. E. Scheidegger, The Physics of Flow through Porous Media, 3rd Edition (Toronto, Canada: University of Toronto Press, 1960), p. 61.

7. TEST AND FACILITY TECHNOLOGY

7.1 ACRR Status
(T. F. Luera, 6451)

This section contains comments on the general status of overall ACRR operation and remarks concerning experimental activities involving the ACRR.

The ACRR is operating normally in support of weapons program research and advanced reactor safety experiments.

DISTRIBUTION:

US NRC Distribution Contractor (CDSI)
7300 Pearl Street
Bethesda, MD 20014
    (370 Copies for R3 and R7)

US Nuclear Regulatory Commission (4)
Division of Accident Evaluation
Office of Nuclear Regulatory Research
Washington, DC 20555
Attn: C. N. Kelber, Assistant Director
          Advanced Reactor Safety Research
       R. T. Curtis, Chief
          Analytical Advanced Reactor Safety Research, ARSR
       G. Marino, Chief
          Experimental Fast Reactor Safety
       R. W. Wright
          Experimental Fast Reactor Safety

R. W. Barber
US Department of Energy
Office of Nuclear Safety Coordination
Washington, DC 20545

US Department of Energy (2)
Albuquerque Operations Office
PO Box 5400
Albuquerque, NM 87185
Attn: J. R. Roeder, Director
          Operational Safety Division
       D. L. Krenz, Director
          Energy Research & Technology Division
          For: C. B. Quinn
                R. N. Holton

T. Ginsberg
Department of Nuclear Energy
Bldg. 820
Brookhaven National Laboratory
Upton, NY 11973

University of Michigan
Nuclear Engineering Department
Ann Arbor, MI 48104

General Electric Corporation (3)
Advanced Reactor Systems Department
PO Box 3508
Sunnyvale, CA 94088
Attn: K. Hikido, Mgr., Safety Engineering - M/C S-18
       D. M. Switick, Mgr., Plant Safety
       M. I. Temme, Mgr., Probabilistic Risk Assessment

DISTRIBUTION (Continued):

W. E. Nyer
PO Box 1845
Idaho Falls, ID 83401

W. Tarbell
K Tech Corp
901 Pennsylvania NE
Albuquerque, NM 87110

Projekt Schneller Brueter (4)
Kernforschungszentrum Karlsruhe GMBH
Postfach 3640
D75 Karlsruhe
West Germany
Attn: Dr. Kessler (2)
       Dr. Heusener (2)

UKAEA Safety and Reliability Directorate (4)
Wigshaw Lane
Culcheth
Warrington WA3 4NE
Cheshire
England
Attn: Mr. J. G. Collier, Director
       Dr. M. J. Hayn
       Mr. E. V. Gilby
       Dr. R. S. Peckover

AERE Harwell (2)
Didcot
Oxfordshire OX11 ORA
England
Attn: Dr. J. Gittus, AETB
       Dr. J. R. Matthews, Theoretical Physics Division

UKAEA (2)
Risley
Warrington WA3 6AT
Cheshire
England
Attn: Dr. B. Cowking, FRDD
       Dr. D. Hicks, TRDD

Dr. F. Briscoe
Culham Laboratory
Culham
Abingdon
Oxfordshire OX14 3DB
England

DISTRIBUTION (Continued):

Mr. C. P. Gratton
Division Head, SESD
Atomic Energy Establishment
Winfrith,
Dorset DTZ 8DH
England

A. J. Manley
EG&G Idaho, Inc.
T.S.B.
LWR Fuel Research Div.
PO Box 1625
Idaho Falls, ID 83415

K. S. Norwood
Mail Stop B 12
Bldg 4500 N
Oak Ridge National Laboratory
PO Box X
Oak Ridge, TN 37830

Joint Research Centre (3)
Ispra Establishment
21020 Ispra (Varese)
Italy
Attn: R. Klersy
        H. Holtbecker
        P. Fasoli-Stella

Power Reactor & Nuclear Fuel
  Development Corporation (PNC) (3)
Fast Breeder Reactor Development Project (FBR)
9-13, 1-Chome, Akasaka
Minato-Ku, Tokyo
Japan
Attn: Dr. Watanabe

Sandia National Laboratories
1230   J. E. Powell
1231   T. P. Wright
1510   D. B. Hayes
1530   W. Herrmann
1534   D. A. Benson
1541   W. Luth
1830   M. J. Davis
1835   C. H. Karnes
1840   N. J. Magnani
1846   R. A. Sallach
1846   R. K. Quinn
2150   C. M. Tapp
3141   C. M. Ostrander (5)
3151   W. L. Garner

3431	B. N.	Yates
6255	D. O.	Lee
6310	R. W.	Lynch (acting)
6350	R. M.	Jefferson
6400	A. W.	Snyder
6410	J. W.	Hickman
6412	J. W.	Hickman, acting
6415	D. C.	Aldrich
6420	J. V.	Walker (5)
6420	M. M.	Watkins
6420A	J. B.	Rivard
6421	T. R.	Schmidt
6421	K. R.	Boldt
6421	J. T.	Hitchcock
6421	G. W.	Mitchell
6421	C.	Ottinger
6422	D. A.	Powers
6422	J. E.	Brockman
6422	E. R.	Copus
6422	R. M.	Elrick
6422	J. E.	Gronager
6422	E.	Randich
6422	A. R.	Taig
6423	P. S.	Pickard
6423	A. C.	Marshall
6423	D. A.	McArthur
6423	K. O.	Reil
6423	S. A.	Wright
6425	W. J.	Camp
6425	D. R.	Bradley
6425	J. E.	Kelly
6425	R. J.	Lipinski
6425	P. K.	Mast
6425	K. K.	Murata
6425	M.	Pilch
6425	A.	Suo-Anttila
6425	A.	Wickett
6425	M. F.	Young
6427	M.	Berman (5)
6427	B. W.	Marshall
6427	L. S.	Nelson
6427	E. W.	Shepherd
6427	M. P.	Sherman
6427	S. R.	Tieszen
6427	C. C.	Wong
6430	N. R.	Ortiz
6440	D. A.	Dahlgren
6442	W. A.	Von Riesemann
6449	K. D.	Bergeron
6449	F. W.	Sciacca
6449	M. E.	Senglaub
6449	D. C.	Williams

DISTRIBUTION (Continued):

6450   J. A. Reuscher
6451   T. Luera
6452   M. Aker
6453   W. J. Whitfield
6454   G. L. Cano
6454   M. E. Field
6454   J. G. Kelly
6454   K. T. Stalker
7100   C. D. Broyles
7530   T. B. Lane (1)
        Attn: N. R. Keltner, 7537
               R. U. Acton, 7537
               T. Y. Chu, 7537
7550   F. W. Neilson (1)
        Attn: O. J. Burchett, 7551
               J. H. Gieske, 7552
8424   M. A. Pound

BIBLIOGRAPHIC DATA SHEET

1 REPORT NUMBER (Assigned by TIDC, add Vol. No. if any)
NUREG/CR-2679 (4 of 4)
SAND82-0904 (4 of 4)

2 Leave blank

3 TITLE AND SUBTITLE

Advanced Reactor Safety Research Quarterly
Report, October-December 1982, Vol. 24

4 RECIPIENT'S ACCESSION NUMBER

5 DATE REPORT COMPLETED
MONTH	YEAR

6 AUTHOR(S)

Advanced Reactor Research Program

7 DATE REPORT ISSUED
MONTH	YEAR
February	1984

8 PERFORMING ORGANIZATION NAME AND MAILING ADDRESS (Include Zip Code)

Sandia National Laboratories
Albuquerque, NM 87185

9 PROJECT/TASK/WORK UNIT NUMBER

10 FIN NUMBER A1016, A1054, A1172,
A1181, A1198, A1218, A1227,
A1250, A1263, A1264, A1335,
A1340, A1342, A1352

11 SPONSORING ORGANIZATION NAME AND MAILING ADDRESS (Include Zip Code)

Division of Accident Evaluation
Office of Nuclear Regulatory Research
U.S. Nuclear Regulatory Commission
Washington, DC 20555

12a TYPE OF REPORT
Quarterly Report --
Technical

12b PERIOD COVERED (Inclusive dates)
October - December 1982

13 SUPPLEMENTARY NOTES

14 ABSTRACT (200 words or less)

Sandia National Laboratories is conducting, under USNRC's sponsorship, phenomenological research related to the safety of commercial nuclear power reactors.

The overall objective of this work is to provide NRC a comprehensive data base essential to (1) defining key safety issues, (2) understanding risk-significant accident sequences, (3) developing and verifying models used in safety assessments, and (4) assuring the public that power reactor systems will not be licensed and placed in commercial service in the United States without appropriate consideration being given to their effects on health and safety.

Together with other programs, the Sandia effort is directed at assuring the soundness of the technology base upon which licensing decisions are made.

This report describes progress in a number of activities dealing with current safety issues relevant to both light water and breeder reactors. The work includes a broad range of experiments to simulate accidental conditions to provide the required data base to understand important accident sequences and to serve as a basis for development and verification of the complex computer simulation models and codes used in accident analysis and licensing reviews. Such a program must include the development of analytical models, verified by experiment, which can be used to predict reactor and safety system performance under a broad variety of abnormal conditions.

Current major emphasis is focused on providing information to NRC relevant to (1) its deliberations and decisions dealing with severe LWR accidents, and (2) its safety evaluation of the proposed Clinch River Breeder Reactor.

15a KEY WORDS AND DOCUMENT ANALYSIS	15b DESCRIPTORS

16 AVAILABILITY STATEMENT	17 SECURITY CLASSIFICATION (This report)	18 NUMBER OF PAGES
GPO Sales and NTIS	Unclassified	206
	19 SECURITY CLASSIFICATION (This page)	20 PRICE
	Unclassified	$

ORG.	BLDG.	NAME	REC'D BY*	ORG.	BLDG.	NAME	REC'D BY*

Sandia National Laboratories